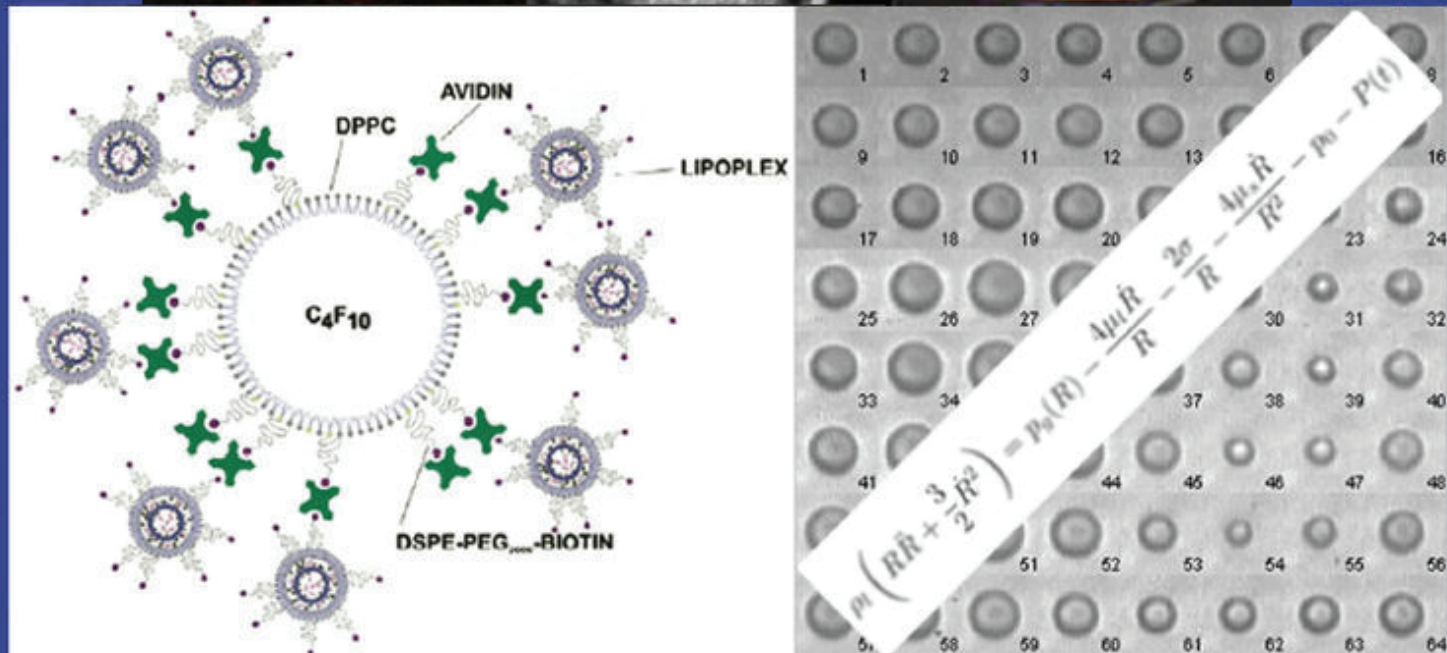
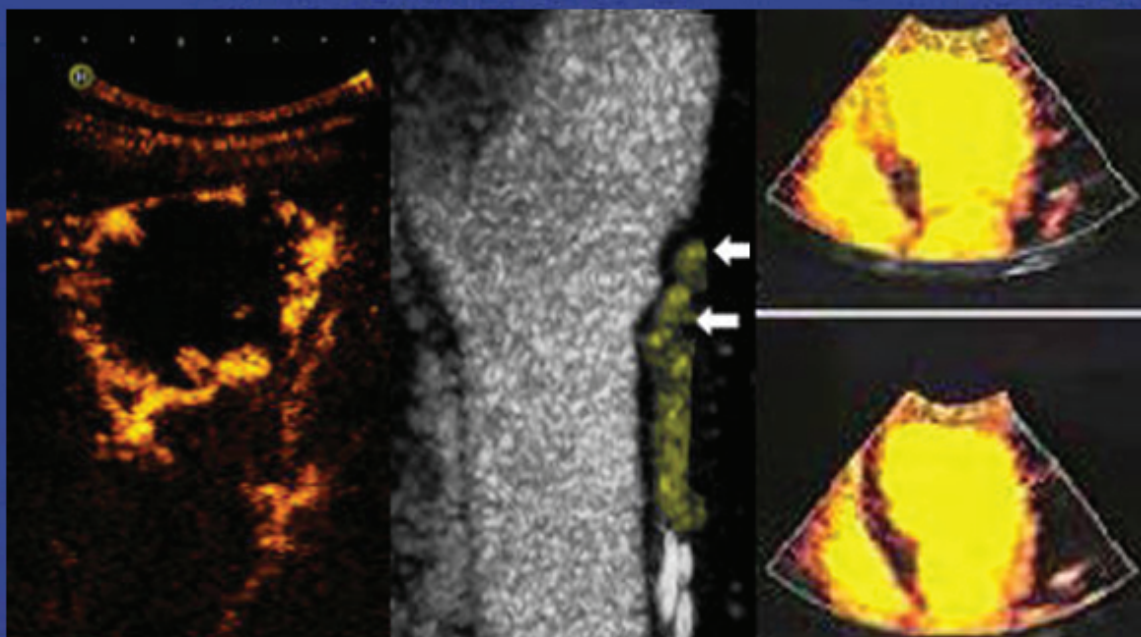


The 20th European Symposium on Ultrasound Contrast Imaging

- An ICUS Conference -



Abstract book

January, 22-23 2015, Rotterdam, The Netherlands
Organized by Arend Schinkel, Edward Leen, Nico de Jong
Erasmus MC Rotterdam - Imperial College London

20th EUROPEAN SYMPOSIUM ON ULTRASOUND CONTRAST IMAGING
22-23 JANUARY 2015, Rotterdam, The Netherlands

WEDNESDAY, 21 January 2015

15.30 PhD Defense Verya Daeichin (Erasmus MC)
 Micro-Ultrasound Molecular Imaging

18.00 – 20.00 Registration - Welcome Drinks

THURSDAY, 22 January 2015

Oral program

08.00 – 09.00	Registration	
09.00 – 09.10	Introduction and opening	David Cosgrove
09.10 – 09.30	HISTORY	Chairpersons: Folkert ten Cate & David Cosgrove
Nico de Jong	The bubble still vibrates as before but our understanding has changed dramatically since 1996	1
09.30 – 11.00	HIGH FRAME RATE IMAGING	Chairpersons: Stuart Foster & Hans-Peter Weskott
Peter Burns	High frame rate Doppler imaging with contrast	3
Claudia Errico	Transcranial functional ultrasound imaging of the rat brain using ultrafast doppler with microbubbles	5
Billy Yiu	High frame rate contrast-enhanced flow vectorgraphy with wide velocity estimation dynamic range	8
Charles Tremblay	An unbiased velocity mapping of tumour perfusion using multi-angle plane-wave contrast-enhanced imaging....	10
Guillaume Renaud	A novel contrast-enhanced ultrasound imaging technique with superior detection specificity based on the interaction of quasi counter-propagating wavefronts.....	14
11.00 – 11.30	Intermission	
11.30 – 13.00	CLINICAL APPLICATIONS	Chairpersons: Steve Feinstein & Jürgen Willmann
David Cosgrove	The future of contrast ultrasound	15
Hans-Peter Weskott	CEUS in lymph nodes – are there any indications?	17
Luciano Agati	Significant increase of flow kinetic energy in non-responders patients to cardiac resynchronization therapy	21
Paul Dayton	Updates on the progress of acoustic angiography high frequency contrast ultrasound	23
Steve Feinstein	3D Contrast-enhanced ultrasound (CEUS) imaging: Carotid artery atherosclerosis and intra-plaque angiogenesis	24
13.00 – 14.00	LUNCH	
14.00 – 14.30	Dutch Heart Foundation lecture.....	Chairperson: Otto Kamp
Nicola Gaibazzi	Clinical routine use of contrast during stress-echocardiography	26
14.30 – 16.00	THERAPY IN HUMANS AND THERAPY IN ANIMALS	Chairpersons: Eleanor Stride & Arend Schinkel
Helge Gilja	Therapeutic ultrasound in pancreatic adenocarcinoma.....	28
Jürgen Willmann	Ultrasound molecular imaging in inflammatory bowel disease: From small to large animals	30
Liza Villanueva	Targeted therapeutic gene knockdown using ultrasound and microbubble-mediated delivery of a transcription factor decoy.....	32
Ine Lentacker	Microbubbles as magic bullets in cancer immunotherapy.....	34
Rick Kwekkeboom	Ultrasound and microbubble induced delivery of miRNA-blockers in vitro, to mouse skeletal muscle and the mouse heart	37
16.00 – 16.30	Intermission	
16.30 – 18.00	DROPLETS AND BUBBLES	Chairpersons: Luciano Agati & Peter Burns
Michel Versluis	Acoustic droplet vaporization: physical insights from ultrahigh-speed microscopy at nanoseconds timescales.....	40
Marine Bezagu	High spatiotemporal control of spontaneous reactions using ultrasound-triggered composite droplets	43
Paul Sheeran	Evaluating in vivo contrast production from phase-shift droplets using a commercial small animal imaging system	46
Eleanor Stride	Fluorescence, fluidity and function – probing the microbubble surface.....	49
Stuart Foster	Borrowing from PET: A new approach for targeting ultrasound contrast agents using bioorthogonal chemistry....	51
18.30 – 22.30	SOCIAL EVENT (Incl. Dinner buffet)	

20th EUROPEAN SYMPOSIUM ON ULTRASOUND CONTRAST IMAGING
22-23 JANUARY 2015, Rotterdam, The Netherlands

FRIDAY, 23 January 2015

07.30 – 08.00

Registration

Poster sessions

07.30 – 09.00

MODERATED POSTER SESSION A: BIOLOGY

Moderator: Arend Schinkel

A1)	Annemieke van Wamel	Acoustic Cluster Therapy (ACT): a novel concept for targeted drug delivery – In vivo characteristics and proof of principle	54
A2)	Steve Feinstein	3D Contrast-enhanced ultrasound (CEUS) imaging of carotid artery plaques and intra-plaque angiogenesis.....	59
A3)	Katrien Vanderperren	Ultrasound and contrast-enhanced ultrasound imaging of mammary gland lesions in companion animal.....	61
A4)	Ine de Cock	Ultrasound and microbubble mediated drug delivery: Real-time imaging of co-administration vs drug loaded microbubble	65
A5)	Olga Koshkina	Poly-D,L-lactide-co-glycoside-perfluorocarbon nanoparticles for long-term ultrasound imaging	67
A6)	Yvo Kusters	Insulin-induced capillary recruitment in skeletal muscle is impaired in overweight individuals and associated with whole body insulin sensitivity	68
A7)	Alexander Klibanov	Ultrasound-triggered drug delivery: Tumor therapy in a murine colon adenocarcinoma model by insonation of doxorubicin-liposome-microbubble complexes in the tumor vasculature	70
A8)	Ilya Skachkov	Correlating sonoporation dynamics to reversible and irreversible sonoporation	72

07.30 – 09.00

MODERATED POSTER SESSION B: TECHNOLOGY

Moderator: Nico de Jong

B1)	Joshua Owen	Oxygen carrying microbubbles for enhanced sonodynamic therapy of hypoxic tumours	76
B2)	Avinoam Bar-Zion	Estimation of local contrast-enhanced ultrasound signals from non-uniform temporal samples.....	78
B3)	Jeong Yu Lee	Phase-shift protein-polymer nanodroplets for targeted drug delivery and ultrasound imaging	80
B4)	Anthony Novell	Optimization of multi-pulse sequences for nonlinear contrast agent imaging using a CMUT array	82
B5)	Tom van Rooij	The influence of binding on the radial excursions of lipid-coated microbubbles	85
B6)	Thomas Barré	Sonoporation for local and targeted delivery of a therapeutic antibody in colorectal cancer: in vivo proof of concept.....	88
B7)	Paul Sheeran	Threshold characterization of volatile phase-shift perfluorocarbon nanodroplets at pre-clinical frequencies	92
B8)	Chee Hau Leow	Plane wave ultrasound imaging and tracking of microbubbles in large vessels for flow quantification: Methods and initial evaluation on a carotid bifurcation phantom	94

Wednesday–Friday

POSTER SESSION C: NEW DIRECTIONS I

Election by the audience

C1)	Martynas Maciulevičius	Implicit dosimetry model for doxorubicin sonotransfer in vitro.....	97
C2)	Libertario Demi	Cumulative phase delay imaging – a new contrast enhanced imaging modality	100
C3)	Jean-Michel Escoffre	Microbubble-assisted ultrasound induced transient phosphatidylserine translocation	104
C4)	Dario Carugo	Changes in the physical properties of lipid membranes interacting with ultrasound-activated microbubbles	107
C5)	Jacopo Viti	Effectiveness and limits of plane wave contrast imaging for moving contrast agents	111
C6)	Anthony Novell	Dual frequency acoustic droplet vaporization detection for medical imaging	114
C7)	Paul Rademeyer	A multi-technique investigation of the effect of coating composition on microbubble behaviour	116
C8)	Marc Derieppe	Effect of the acoustic pressure on the uptake kinetics of sytox green model drug in sonopermeabilization	118
C9)	Sally Peyman	ON-CHIP production and characterisation of nanometer sized bubble populations	121

Wednesday–Friday

POSTER SESSION D: NEW DIRECTIONS II

Election by the audience

D1)	Ayache Bouakaz	Modeling of the dynamics of volatile phase-change contrast agents	123
D2)	Stefan Schalk	3D Contrast-ultrasound dispersion imaging by mutual information analysis in prostate cancer	125
D3)	Juan Rojas	In vivo contrast enhancement and circulation kinetics of low-boiling point phase-change contrast agents	129
D4)	Konstantinos Efthymiou	Acoustic interaction between a coated microbubble and a rigid boundary	133
D5)	Brandon Helfield	Physical insights into ultrasound-stimulated microbubble sonoporation	135
D6)	SimonaTurco	A new denoising method for improved parameter estimation in DCE-US	137
D7)	Naohiro Sugita	A numerical study on the natural frequency of a microbubble bound to a surface	141
D8)	Wing Keung Cheung	An automated algorithm for quantification of tissue perfusion in contrast enhanced ultrasound images: Initial evaluation in quantification of lower limb perfusion	143
D9)	Edyta Swider	Modifications of perfluorocarbon-loaded PLGA particles for ultrasound imaging	146

20th EUROPEAN SYMPOSIUM ON ULTRASOUND CONTRAST IMAGING
22-23 JANUARY 2015, Rotterdam, The Netherlands

FRIDAY, 23 January 2015

Oral program

09.00 – 10.30	BUBBLES AND IMAGING <i>Chairpersons: Dan Adam & Liza Villanueva</i>	
Yesna Yildiz	Correction of nonlinear propagation artefact in contrast enhanced ultrasound imaging: In vitro and in vivo evaluation	147
Jean-Marc Hyvelin	A new non-destructive method for the visualization and quantification of targeted microbubbles in ultrasound molecular imaging	151
Tim Segers	Acoustic characterization and modeling of sorted bubbles and the implications for contrast imaging	155
Klazina Kooiman	To buckle or not to buckle, that is the question – a fluorescence high-speed camera study	158
Alfred Yu	The biophysical facet of sonoporation: Dynamics at the cellular level	162
10.30 – 11.00	Intermission	
11.00 – 12.30	PERFUSION IMAGING <i>Chairpersons: Michel Versluis & Nicola Gaibazzi</i>	
Arnoud Postema	Contrast enhanced ultrasound parametric imaging for the detection of prostate cancer	163
Emmelie Stock	Assessment of the influence of propofol and butorphanol on contrast-enhanced ultrasonography of the feline kidney	165
Chloé Arthuis	Evaluation of placental perfusion using contrast enhanced ultrasound imaging	169
Francois Yu	Nitric oxide contributes to effective sonoreperfusion of microvascular obstruction	171
Heleen Dewitte	Theranostic mRNA-loaded microbubbles in the lymphatics of dogs: Implications for ultrasound-guided cancer vaccination	174
12.30 – 13.30	LUNCH	
13.30 – 14.00	COEUR LECTURE <i>Chairperson: Folkert ten Cate</i>	
Tom Porter	Microvascular thrombolysis: From in vitro to in vivo to clinical trials	177
14.00 – 16.00	COMPETITION: SONOTHROMBOLYSIS <i>Chairpersons: Tom Porter & Nico de Jong</i>	
Adam Dixon	Microbubbles produced by a catheter-based flow-focusing microfluidic device for sonothrombolysis.....	179
Adrien Poizat	Real-time control of ultrasound cavitation applied to extracorporeal ultrasound thrombolysis.....	183
Miguel Osmam Aguiar	Safety and feasibility of diagnostic ultrasound high mechanical index impulses in restoring epicardial flow in acute ST segment elevation myocardial infarction in humans	185
Sebastiaan Roos	Sonoreperfusion therapy for microvascular obstruction using microbubbles and low dose tPA	187
Christopher Accocia	A study of the micro-scale evolution of the erosion front of blood clots subjected to ultrasound stimulated microbubble treatments	189
Akash Goyal	Lowering acoustic requirements for effective sonoreperfusion of microvascular obstruction using ultra low dose tPA.....	192
Guillaume Lajoinie	On the controlled and directed local release from drug-loaded microbubbles for sonothrombolytic therapy	196
16.00 – 16.10	DISCUSSION AND CONCLUSIONS <i>Nico de Jong & Arend Schinkel</i>	
16.10	ADJOURN AND ANNOUNCEMENT OF THE WINNERS OF THE COMPETITION AND POSTER PRIZES	

SPONSORS

FIRST ANNOUNCEMENT 2016

The Scientific Board: Arend Schinkel, Edward Leen, Nico de Jong, Mike Averkiou, Folkert ten Cate, Paolo Colonna, David Cosgrove, Eleanor Stride

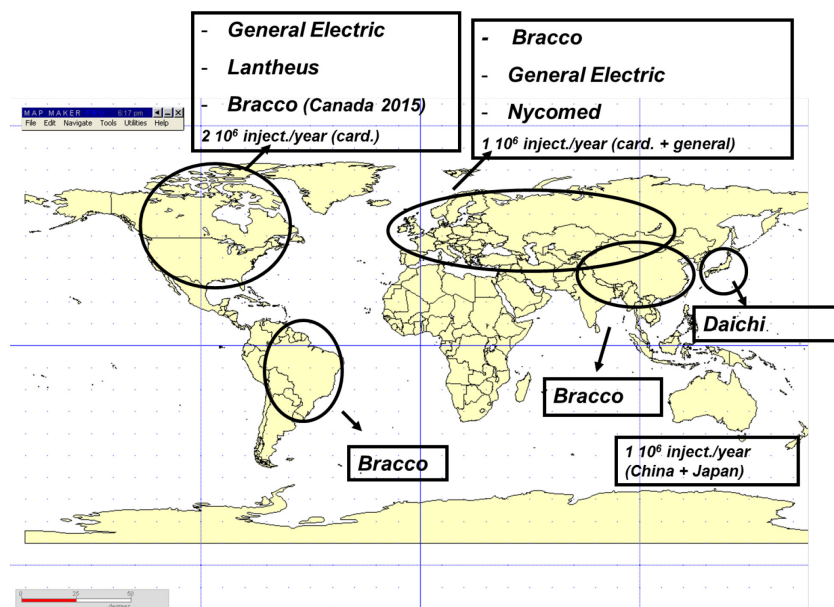
The bubble still vibrates as before but our understanding has changed dramatically since 1996

Nico de Jong

*Dept. of Biomedical Engineering, Thoraxcenter, Erasmus MC, Rotterdam, the Netherlands and
Laboratory of Acoustical Wavefield Imaging, Faculty of Applied Sciences, Technical University Delft,
Delft, the Netherlands*

It all started in the late eighties. Although echo images have improved substantially since their introduction in the early seventies, imaging of the blood pool and blood flow was still troublesome due to the very low scattering of the red blood cells. Only in larger cavities and vessels blood flow could be visualised with the so-called Doppler technique. There was a clear need for of an agent in order to increase the scatter amplitude. An obvious candidate was bubbles, since it was known that bubbles reflect ultrasound strongly. But, that was the *only* knowledge we had at that time. We hadn't the slightest idea about vibration modes of bubble, jetting, diffusion of the gases, temperature, pressure inside the bubble etc. etc. Nonlinearity was an unknown word. We had no idea about acoustic pressure generated by the ultrasound machine. The only thing we noticed was the high scatterer intensity of the bubbles and the medical community was very happy that the first commercial available contrast agents could pass the lung circulation and could be observed in the left ventricle cavity and in other organs like liver, kidney and brain. But, the "Holy Grail" in cardiology to use contrast agents for myocardial perfusion was not yet achieved. Contrast was very promising, not only for clinicians but

also for start-up companies and some larger pharmaceuticals. The sky was the limit and large profits on the horizon. NOW, twenty years later this all has changed. We understand more or less the vibration, including buckling and thresholding at low acoustic pressure. For medium pressures we take advantage of the second, sub and ultra



harmonics and we know that the bubble is destroyed at high but still diagnostic pressures. Further, the modeling has more and more evolved indicating our understanding of the complicated bubble vibration. BUT, we know almost nothing about the only thing that matters: The bubble behaviour in the human

body. At which bubbles are we looking at, what is the influence of the 37° degrees, what about the diffusion process after intravenous administration, what is the behaviour in small capillaries nearby red blood cells and for newer application the vibration of the bubbles if targeted or drug loaded. Currently we get nice contrast images due to advanced detection schemes, but the exact source of the response is still full of question marks. The market has also changed substantially. The numerous smaller companies have disappeared and only a few agents are on the market. The market is growing slow but steady as indicated in the figure. In addition the contrast agents have proven to be safe.

The last 20 years major steps have been taken, although much smaller than anticipated in the early nineties. For the coming 20 years we aim for a full understanding of these tiny bubbles in order to extend the ultrasound technology further for molecular imaging and therapeutic applications.

High frame rate Doppler imaging with contrast

Charles Tremblay-Darveau[†], Ross Williams[†], Matt Bruce^{*}, Peter N Burns[†]

[†]*Dept Medical Biophysics, University of Toronto, Imaging Research, Sunnybrook Research Institute, Toronto*

^{*}*Supersonic Imagine, Aix-en-Provence*

Current contrast imaging modes detect bubbles in a way which is largely independent of the speed at which they are flowing with blood. While this has advantages for perfusion imaging, it means that measuring flow velocity in blood vessels, or sometimes even just visualising blood vessels, requires a separate examination using a non-contrast Doppler mode. Various attempts have been made to integrate colour Doppler into contrast modes, with only limited success. The principal challenge is acquisition time: the short pulse sequences (often only three pulses) used in contrast imaging do not provide sufficient data for wall filtering and velocity estimation and longer ensemble lengths drop the framerate to unacceptable values. We have shown that by using plane-wave excitation, where the framerate becomes effectively equal to the PRF, we can perform linear and nonlinear Doppler processing, with phase and/or amplitude modulation, and detect coherent ensemble lengths of around 100 and produce contrast Doppler images at framerates of 50-100Hz. This clearly opens up new possibilities for the combination of colour Doppler and contrast modes, but also presents some new challenges. Doppler is fundamentally a narrow-band detection process: the Doppler shift translates into a velocity if we are able to attribute a value for the carrier frequency in the Doppler equation. Ambiguity in this value creates uncertainty in the velocity estimate. Bubbles have the inconvenient tendency to give broadband echoes even if excited with a narrowband pulse. In the extreme case, bubble disruption gives rise to a broadband echo that is mirrored in a wide spectrum of Doppler shifts from a single target velocity. This is the white streak we see in the vertical (frequency) axis of a single gate pulsed Doppler spectrum when a bubble passes by and is disrupted. How can we detect a Doppler shift from such a broadband echo? In conventional pulsed Doppler systems, this problem is seen as an intrinsic tradeoff between axial resolution (RF bandwidth) and velocity resolution (1/Doppler bandwidth), and is often described as a fundamental location/velocity ‘uncertainty principle’: the only way to get a good velocity estimate is to give up image resolution. In fact, this is only a limit of a one-dimensional velocity estimator: by performing a 2-D Fourier transform in the space defined by RF (fast-) and Doppler (slow-) time we show that velocity can be estimated from broadband bubble echoes by measuring a gradient in 2-D frequency space. While this may be an appropriate way to process bubble Doppler signals, it is computationally prohibitive. A neater solution is to perform a set of rotating projections in this time domain space provided by the radon transform. We show that this has the effect of eliminating spectral broadening from bubble signals acquired at these very high rates.

In the meantime, the same nonlinear bubble behaviour that creates a challenge for one aspect of Doppler solves another: while pulse inversion and amplitude modulation Doppler provide segmentation between the linear and nonlinear components of the bubble echo, they do not separate the tissue harmonic in the nonlinear spectrum, limiting the contrast-to-tissue ratio. Even with long filter lengths, this can be a difficulty. However, we show that a bubble-specific phase behavior under AM can provide simple and effective segmentation of the bubble components of the high speed Doppler image.

Transcranial functional ultrasound imaging of the rat brain using ultrafast doppler with microbubbles

Claudia Errico*, **Bruno-Félix Osmanski***, **Sophie Pezet**, **Olivier Couture***, **Zsolt Lenkei^t**,
Mickael Tanter*

* Institut Langevin (ESPCI, CNRS UMR7587, INSERM ERL U979) 1 rue Jussieu, 75005, Paris

^t Laboratoire de Neurobiologie (ESPCI, CNRS UMR 7637) 10 rue Vauquelin, 75005, Paris

Introduction

Functional Ultrasound (fUS) has been validated as a novel imaging technique capable of measuring the brain activity through the neurovascular coupling with a high spatio temporal resolution (1ms, 100µm). It relies on the high sensitivity ultrafast Doppler based plane wave imaging. However, due to the attenuation of the skull, this method requires a cranial window (thinning skull or craniotomy) which is a highly invasive surgical procedure. In this work, we propose to perform transcranial fUS by enhancing the blood signal with contrast agents.

Methods

In-vivo experiments were performed on n=6 rats following three different imaging protocols: bilateral thinned-skull window (A), unilateral thinned-skull window (B) and full transcranial (C) imaging. The functional ultrasound acquisitions were achieved at the anteroposterior reference coordinates of Bregma -0.6 mm, containing the hind limb primary sensory cortex (S1HL). We delivered, every 10 minutes, a maximum of 11-13 bolus of 200µL of microbubbles (2×10^7 SonoVue /ml), corresponding to a maximum of 2.6mL of the initial suspension. In-vivo activations of the brain were achieved by sending, alternatively, 5 electrical stimulations on the left and right sciatic nerves following an on/off pattern (5s ON and 20s OFF). Preliminary experiments established that the concentration of microbubbles was stable one minute after each injection, time at which the functional ultrasound acquisition was initialized. The fUS sequence consisted in insonifying the brain at 500Hz using a compounded sequence with three tilted plane waves (PRF=1500Hz) with a 15MHz probe (128 elements) connected to an ultrafast clinical scanner (SSI, France). The entire acquisition lasted 150s to recover the five delivered stimuli.

Results and discussion

The backscattered signals from the rat brain are a superposition of signals coming from the blood containing microbubbles and from the slow moving tissue, which was removed by using a high-pass filter with a cut-off frequency of 75Hz. In order to correctly place the probe above the SHL1, vascular maps were acquired performing an ultrafast Doppler scan of the brain for each protocol (A, B, C). As

shown in figure 1, we had no access to the vascularization network of the brain when transcranial imaging is performed without an injection of ultrasound contrast agents (Fig.1B). The ventricle of the choroid plexus, highly recognizable on the Bilateral and Unilateral thinned-skull window (Fig.1A, D, E), became visible through the intact skull only after injecting a bolus of 150 μ L of microbubbles (Fig.1C). The activated areas, shown in figure 2 as color overlays, are extracted by correlating the increase in the cerebral blood volume with the targeted electrical stimulation pattern. Strong activation in the corresponding sensory-motor cortex could be observed under the thinned hemispheres (Fig.2 A2, A3 and D2) with no injection of contrast agents. However, because of high attenuation due to the skull, the activation could not be observed without microbubbles transcranially (Fig2 B2, B3, and D3). With the addition of microbubbles, activation could be observed without the skull (Fig2 C2, C3 and E3). The reproducibility of the activation was exploited by calculation the Pearson coefficient, leading to a correlation coefficient of $\rho=0.7\pm0.1$.

Our work has demonstrated that the combination of ultrafast Doppler and ultrasound contrast agents allows transcranial functional imaging. Hence, stimuli-induced changes in the cerebral blood volume deep within the rat cortex can be assessed through the intact skull. This approach leads to a non-invasive functional imaging of the rat brain, facilitating longitudinal studies.

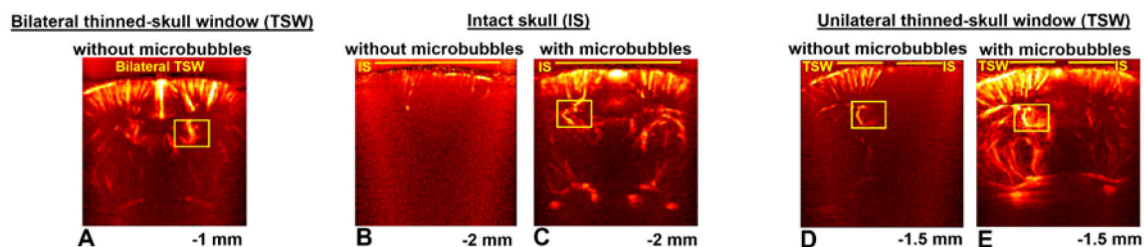


Figure 1. The ventricle of the choroid plexus (boxed in yellow) was easily accessible on the gold standard technique of the bilateral thinned-skull window protocol without injecting microbubbles (A) and on the unilateral TSW configuration without (D) and with the use of contrast agents (E). Without delivering any ultrasound contrast agents the vascularization network of the brain through the intact skull was not accessible (B). On the contrary, after the injection of 150 μ L of SonoVue microbubbles, we achieved a clear distinction of the choroid plexus (C), followed by correct placement of the probe above the S1HL.

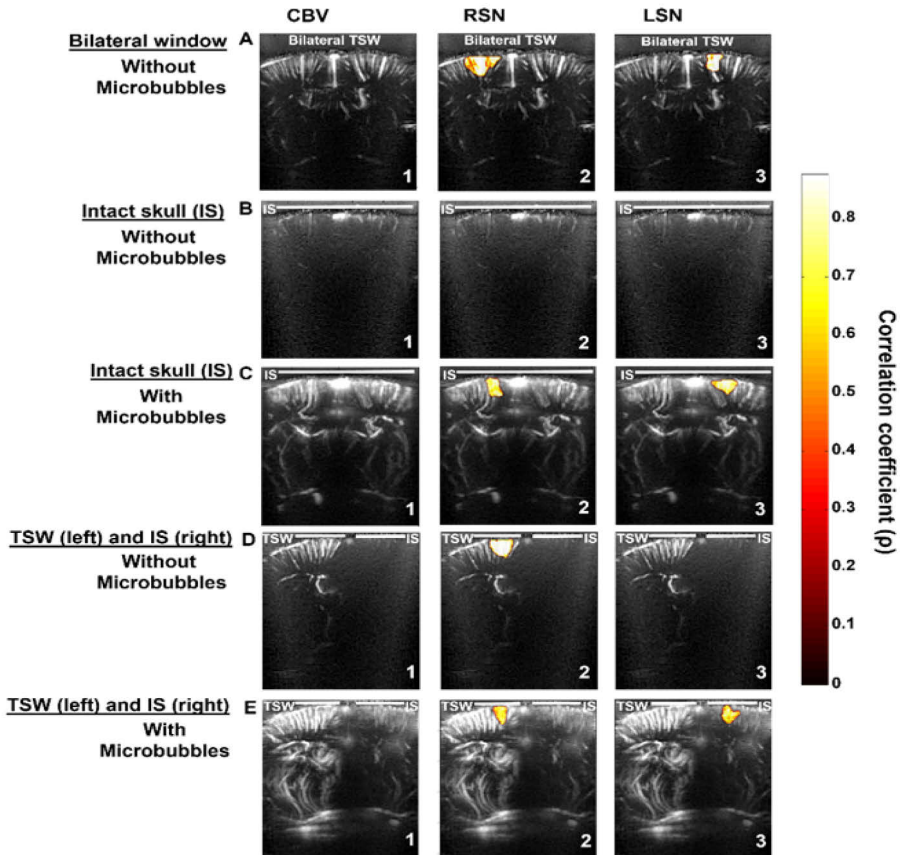


Figure 2: Contralateral activations of the sensory-motor cortex (A.1, B.1, C.1, D.1, E.1). Vascularization maps acquired with Ultrafast Doppler representing the cerebral blood volume (CBV) are observed under the bilateral and unilateral thinned-skull window (TSW) after electric stimulation of the sciatic nerves with or without injection of a vascular contrast agent Whereas, under the intact skull (IS) after activation of the left sciatic nerve, the cortical activation could only be detected with the injection of microbubbles (IS side after left sciatic nerve stimulation).

High frame rate contrast-enhanced flow vectorgraphy with wide velocity estimation dynamic range

Billy Y. S. Yiu and Alfred C. H. Yu

Medical Engineering Program, The University of Hong Kong

Background, motivation and objective

Although high frame rate ($>1,000$ fps) mapping of flow vector fields has recently been demonstrated to be feasible, its efficacy in deriving accurate estimates in diagnostic scenarios with significant spatiotemporal variations in flow patterns remains to be proven. From an engineering standpoint, what is lacking is a robust flow vector computation solution with high estimation dynamic range such that both slow and fast flow velocities can be tracked consistently. Here, we report a new contrast-enhanced ultrasound flow vectorgraphy framework that can enable high-dynamic-range flow vector estimation based on multi-angle vector Doppler estimation from contrast-specific echoes. Central to this new approach is the design of a multi-harmonic processing algorithm that can achieve fine slow-time resolution needed for slow-flow detection and effectively account for Doppler aliasing of fast flow.

Methods

To estimate flow vectors with high estimation dynamic range and at high frame rates, our new framework has leveraged three technical principles: (i) high-frame-rate broad-view data acquisition (steered plane wave firings); (ii) contrast echo processing innovations (multi-harmonic slow-time analysis); (iii) flow vector estimation via a multi-angle, least-squares estimation algorithm. In our prototype implementation, we have adopted a three-angle plane wave steering configuration (-10° , 0° , $+10^\circ$; 10 kHz PRF), and a 9 MHz transmit frequency was used to excite circulating microbubbles inside the vasculature to elicit their harmonic echoes. It was experimentally realized on our lab's channel-domain research scanner that comprises an L14-5 linear array transducer, a SonixTouch programmable transmit front-end, a SonixDAQ pre-beamformed data acquisition tool, and a GPU high speed processing platform. At each pixel position in the beamformed image frame (computed using GPU), multi-harmonic slow-time processing was carried out as follows for each Tx-Rx angle pair. First, a filter bank was implemented to extract the contrast-specific subharmonic echoes (five spectral bands set between 4-9 MHz; in 1 MHz increments). Second, for each filter bank channel, mean Doppler frequency estimation was performed using the lag-one autocorrelation phase algorithm (with a sliding window of 64 ensembles). Linear regression was then performed on the Doppler estimates of different bands to derive the unaliased Doppler estimate for that Tx-Rx angle pair. To derive the flow vector, the unaliased Doppler estimates from all combinations of Tx-Rx angle pairs are fitted onto a least-squares model that considers the vector computation process as an N-equations, two-unknowns problem. The

process was repeated at different sliding window time points to obtain high frame rate cineloops of contrast-enhanced flow vectorgraphy.

Experimental results

To evaluate the efficacy of our framework, calibration experiments were conducted using a 4.4 mm dilated diameter vessel with pulsatile flow resembling the carotid pulse. With a peak flow rate of 5ml/s, our proposed framework was able to estimate flow vectors whose direction is aligned with the vessel orientation (average absolute angle difference: <1 deg). Also, the estimated peak centerline flow velocity was 55 cm/s, which is consistent with the theoretical value derived from fluid mechanics. In contrast, flow vectors estimated from non-contrast flow echoes showed significant deviation from the expected value because of aliasing (generally faltered for velocities above 25 cm/s for the imaging configuration used). These inconsistencies in flow vector estimation resulted in spurious errors in visualization. We have examined this issue further in a carotid bifurcation imaging scenario with 50% eccentric stenosis at the entrance to the internal carotid artery branch (pulsatile flow; peak flow rate: 15 ml/s). Our contrast-enhanced flow vectorgraphy framework produced high frame rate cineloops that are in line with the expected flow profile derived from CFD simulations, whereas various visualization errors are evident in flow vector maps produced without using contrast. The peak flow jet velocity measured using our framework was 100 cm/s, and the recirculation flow speed was as low as 2.5 cm/s. Corresponding cineloops will be shown at the conference.

Acknowledgements

This work is funded in part by the Research Grants Council of Hong Kong (GRF 785811M) and the Hong Kong Innovation and Technology Fund (GHP/025/13SZ).

An unbiased velocity mapping of tumour perfusion using multi-angle plane-wave contrast-enhanced imaging

*Charles Tremblay-Darveau¹, Ross Williams², Paul Sheeran¹, Laurent Milot²,
Matthew Bruce³ and Peter N. Burns^{1,2}*

¹*Department of Medical Biophysics, University of Toronto, Ontario, Canada*

²*Sunnybrook Health Sciences Centre, Toronto, Ontario, Canada*

³*Supersonic Imagine, Aix en Provence, France*

Introduction

Ultrasound plane-wave imaging increases the imaging frame rate by up to two orders of magnitude over conventional line-by-line imaging, enabling duplex Doppler and microbubble contrast-enhanced imaging without sacrificing flow sensitivity [1]. A limitation of plane-wave imaging is the absence of focussing of the incident acoustic pulse, resulting in a low contrast image. One way to recover image quality is to sum coherently many low resolution images using plane waves emitted at different insonation angles [2]. The downside is that coherently summing the signal of a moving scatterer causes constructive or destructive interference in the resulting Doppler spectrum, which can bias velocity estimations [3]. In this work, we propose a simple inverse filter, which can be integrated to the wall-filter, that permits the recovery of an unbiased velocity estimate. It is shown that the Doppler spectrum computed from a multi-angle acquisition is then similar to the spectrum acquired using a single insonation angle. Lastly, a high resolution mapping of an intramuscular VX-2 tumour is produced using multi-angle compounded plane-wave Doppler.

Theory

Adding coherently the moving RF signal has the effect of applying a low-pass filter on the Doppler spectrum. For a scatterer moving with a Doppler shift $\Delta\phi$ between adjacent pulses, the summed signal from Na angles can be expressed as:

$$z_{\text{summed}}(t) = z_o(t) \left(\frac{e^{i\Delta\phi Na} - 1}{e^{i\Delta\phi} - 1} \right) \quad (1)$$

where the summation acts as a transfer function (H) on the Doppler signal. The initial data, non-corrupted by the coherent summation, can then be recovered by applying the inverse transfer function. Because H has zeroes at $\text{PRF}/Na * n \mid n \in [1, 2, \dots, Na]$ where PRF is the pulse repetition frequency, we

must ensure that the inverse of H doesn't diverge at these points, which would otherwise amplify the noise floor. This can be accomplished with a Wiener filter.

Method

The Doppler spectrum of flowing Definity microbubbles (Lantheus Medical Imaging Inc., N. Billerica, MA, USA) contained within the wall-less vessel of a commercial flow phantom (523A custom model, ATS Laboratories, Bridgeport, CT, USA) was assessed using plane-wave Doppler sequences based on 1 and 10 insonation angles. The Doppler vector was acquired by cycling periodically through the various angles at constant PRF. The high resolution cine-loop was recovered by repeatedly replacing the oldest low resolution image with a new one (i.e. a moving window), hence maintaining an imaging rate equivalent to the PRF. The Doppler vector was then compensated by multiplying the inverse transfer function (eq. 1) with the wall-filter.

The perfusion in a VX-2 tumour was assessed with amplitude modulation Doppler (AMD) [4]. VX-2 tumour cells, which are a poorly differentiated squamous cell carcinoma, were injected into the thigh muscles of the hind limbs of New Zealand white rabbits. Plane-waves of 1 cycle at 4.5 MHz center frequency were emitted using an Aixplorer scanner (Supersonic Imagine, Aix-en-Provence, France) with an 8MHz center frequency linear array probe.

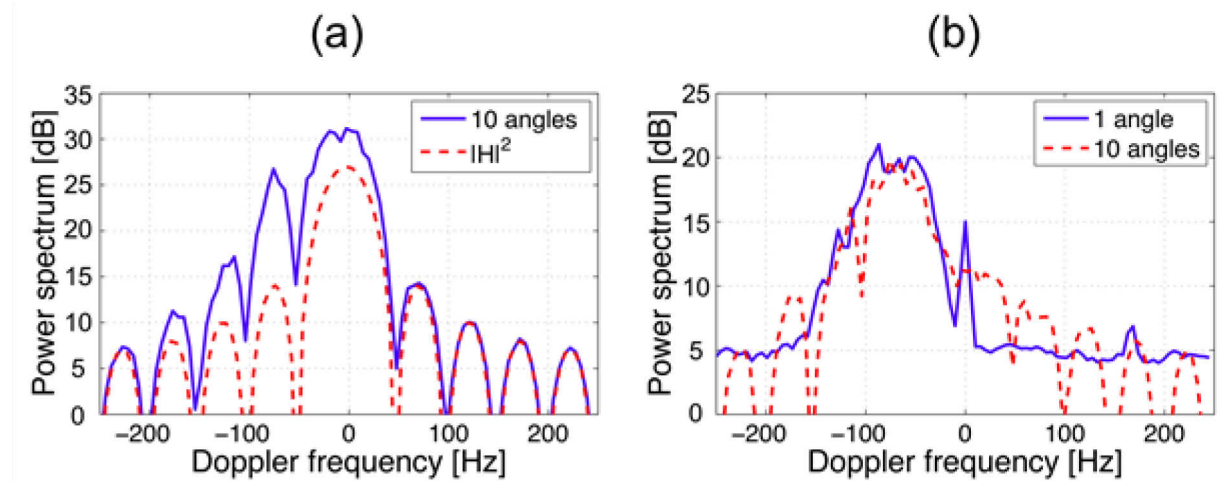


Figure 1. (a) Doppler spectrum of flowing microbubbles using an acquisition compounded with 10 angles at a PRF of 500Hz (solid blue). Most information outside of the -50Hz to 50Hz range is lost due to interference. The transfer function estimated in the theory section is shown as the dashed red line. (b) Compensated 10 angles spectrum (dashed red) compared to the spectrum acquired with a single transmission angle (solid blue). Both the 1 angle and 10 angles estimations then agree.

Results and discussion

1) In-vitro validation:

Fig. 1a shows a strong reduction of the original Doppler signal occurring for Doppler frequencies higher than PRF/Na as a result of motion interference. Renormalizing the Doppler spectrum (using

equation 1) realigns the Doppler signal such that a similar spectrum to the one of a single insonation angle is measured. The proposed method compensates for the bias in the velocity measurement as expected, but the information located at the zeroes of the transfer function cannot be recovered.

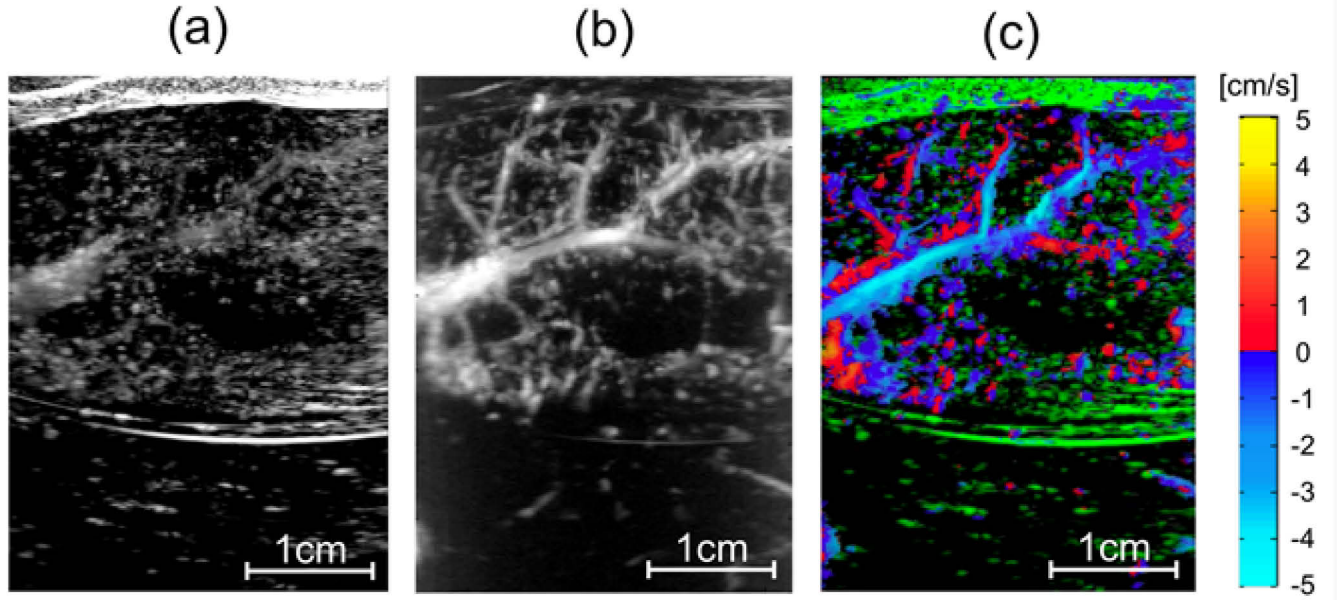


Figure 2. (a) AM, (b) AM power Doppler and (c) AM colour Doppler overlay on the contrast-enhanced image (green) of a VX-2 tumour perfused by microbubbles. The AM and Doppler contrast-enhanced images are complementary in identifying the conduit vessels and the capillary bed. (a) and (c) are produced at a frame rate of 80Hz. A PRF of 2kHz was used.

2) Perfusion measurement in an *in-vivo* VX-2 tumour:

The perfusion in a VX-2 tumour was assessed using a multi-angle adaptation of AMD. The contrast-enhanced image (i.e. conventional AM, Fig. 2a) shows a mostly hyperechoic tumour with some hypoechoic regions, and little information about the vascular morphology. In contrast, the power Doppler image (Fig. 2b), created using the same data, reveals the detailed conduit flow morphology. Both methods were combined into a single image in Fig. 2c, depicting the perfusion and flow within the tumour.

Conclusion

A simple signal processing scheme was implemented to compensate for the bias present in plane-wave Doppler using multi-angle coherent compounding. It was then possible to produce an image of high contrast and resolution without sacrificing the accuracy of the velocity estimation. The perfusion of a VX-2 tumour was then imaged using compounded contrast-enhanced plane-wave Doppler. To our knowledge, this is the first time such detailed images of the tumour vasculature have been acquired using ultrasound and an acquisition lasting much less than a second.

References

1. Tremblay-Darveau et al. *Combined Perfusion and Doppler Imaging Using Plane-Wave Nonlinear Detection and Microbubble Contrast Agents*. IEEE Trans. Ultrason. Ferroelectr. Freq. Control (2014) vol. 61 (12) pp. 1988-2000
2. Montaldo et al. *Coherent plane-wave compounding for very high frame rate ultrasonography and transient elastography*. IEEE Trans. Ultrason., Ferroelect., Freq. Contr. (2009) vol. 56 (3) pp. 489-506
3. Denarie et al. *Coherent Plane Wave Compounding for Very High Frame Rate Ultrasonography of Rapidly Moving Targets*. IEEE Trans. Med. Imag. (2013) vol. 32 (7) pp. 1265-1276
4. Tremblay-Darveau et al. *Adapting amplitude modulation to plane-wave non-linear Doppler imaging*. IEEE Ultrasonics Symposium (2012) pp. 1742-1745

A novel contrast-enhanced ultrasound imaging technique with superior detection specificity based on the interaction of quasi counter-propagating wavefronts

G. Renaud^{1,2}, J. G. Bosch¹, A. F. W. van der Steen^{1,3} and N. de Jong^{1,3}

¹*Biomedical Engineering, ThoraxCenter, Erasmus Medical Center, Rotterdam, The Netherlands*

²*Laboratoire d'Imagerie Biomédicale, UPMC – CNRS UMR 7371 – INSERM UMR S 1146, Paris, France*

³*Acoustical Wavefield Imaging Research Group, Delft University of Technology, Delft, The Netherlands*

Contrast detection methods implemented in present clinical ultrasound scanners show high sensitivity but a poor specificity due to pseudo-enhancement produced by nonlinear wave propagation in regions containing contrast agent (even at low transmit pressure). They all require linear propagation to detect nonlinear scattering of contrast agent microbubbles. As a consequence, tissue can be misclassified as contrast agent microbubbles, and contrast agent concentration can be overestimated. This artifact hinders development of contrast-enhanced ultrasound imaging towards reliable quantitative measurement of local contrast agent concentration, and hence blood perfusion of tissue. We propose in this work a new detection method, with specific beamforming and pulsing scheme, that produces contrast images with highly reduced pseudo-enhancement due to nonlinear propagation in contrast agent. It is based on the interaction of the two wavefronts broadcasted by two separate sub-apertures of a linear array probe. The contrast image is formed line by line, one single image line is the line segment bisector defined by the centers of the two sub-groups of transmitting elements. The method was implemented in a programmable ultrasound system, the proof of principle is shown in vitro. It is shown that the amplitude of the artifact relative to true contrast signal amplitude can be reduced by up to 13 dB.

The future of contrast ultrasound

David Cosgrove

Imperial and King's Colleges, London

Microbubbles have proven to be extremely useful as diagnostic agents for ultrasound in cardiology and radiology, notably for the liver. However, they have the potential for a far wider range of uses, both in unmodified form (thus minimising regulatory barriers) and in new forms. New methods to image and modify them are also under development. These future uses may be divided into diagnostic and therapeutic categories.

For Diagnosis, one approach is to develop targeted agents that attach preferentially to cell surface molecules of interest. Since conventional microbubbles with micron diameters cannot escape from the blood pool, the initial targets are processes involving the blood vasculature. Two main areas are being explored in man, neovascularisation (in tumours and chronic inflammation) and thrombus. Ligands to VEGF1 can be attached to phospholipid microbubbles; numerous preclinical studies have shown these to be effective ways to image malignant neovascularisation and the first human trial in prostate cancer has been completed. A difficulty has been the relatively poor binding power of the targeted microbubbles, especially in the non-immunogenic form for human use. The same strategies that are used for molecular imaging in nuclear medicine and MR can be deployed: change the formulation to increase the specific binding or wait for clearance of the unbound agent from the blood stream. The delay has to contend with the progressive loss of signal over time of both bound and unbound microbubbles, so this approach is not very successful with microbubbles. Another approach makes use of the fast time resolution of ultrasound and tries to recognise which micron bubble population are fixed and which are moving, thus enabling the bound population to be selectively imaged. Efforts have also been made to detect differences in the echoes from free versus bound microbubbles.

An important advance in allowing access to tissue beyond the endothelium is the development of nanodroplets, made by cooling and pressurising microbubbles – since they are around 200nm in diameter, they are able to cross the endothelium, especially where it is leaky. Sonication with acceptable ultrasound intensity can be used to reform the original microbubbles, with their ligands intact. This opens the way to imaging beyond the endothelium.

New microbubble-specific imaging modes promise to improve the detection of microbubbles. Chief among these is plane wave imaging which allows for very high PRFs so that multiple pulses could be sent along an imaging line with varying phase and amplitudes. This could improve tissue suppression

and give cleaner images.

The simplest approach to therapy employing microbubbles is to make use of their mechanical effects upon disruption and this has been used to accelerate thrombus breakdown to promote revascularisation in the middle cerebral artery and is being assessed from the coronary arteries in myocardial infarction. The risk of inducing brain haemorrhage has slowed implementation and this risk is compounded if tissue plasminogen activators (TPA), used on their own =in conventional stroke therapy, are administered at the same time.

An interesting approach uses low frequencies and low intensities along with microbubbles to ‘massage’ the endothelium or other surfaces, relying on the effect of acoustic radiation force impulses (ARFI) to move microbubbles away from the beam. This may allow temporary opening of the blood-brain barrier so that i.v. drugs could penetrate better.

Co-administration obviates some of the regulatory barriers and has been used to augment chemotherapy of pancreatic cancer with gemcitabine; remarkably in this Norwegian trial, low MIs were used, as for diagnostic real time contrast studies. Further such trials are anticipated. Microbubbles might also be used to augment high intensity focussed ultrasound (HIFU) which would speed up the method, thus removing one of the main barriers to its wider use: the slow rate of heating that makes for inordinately long treatment sessions.

The most direct approach to treatment with microbubbles is to tag them with active drugs such as chemotherapeutic agents; breaking these microbubbles with high MI pulses releases the agent so that high concentrations can be achieved locally. This has been shown in small animals to minimise the cardiotoxicity of adriamycin, a cytotoxic drug often used against breast cancer. This therapeutic avenue could be combined with the nanodroplets method and with endothelial ‘massage’ to facilitate entry into the interstitial space and thereby access to tumours and other pathologies.

CEUS in lymph nodes – are there any indications?

Dr. Hans-Peter Weskott

Head of Central Ultrasound Department, Klinikum Siloah, KRH, Hannover, Germany

Ultrasound is most useful in detecting and characterizing peripheral and abdominal lymph nodes (LN). Whenever scanning conditions allow, high frequency probes should be used. B-mode criteria such as size, shape, number, architecture, echogenicity and delineation of margins are the basis for characterizing lymph nodes. In addition color-coding techniques such as color Doppler, B-Flow™ and CEUS are used to evaluate the LN vasculature [1,4-9].

CEUS contributes to the detection of the sentinel or secondary LN and to evaluate the nodal vasculature and vessel architecture. Directly subcutaneous injection of contrast agent can be used to detect the sentinel [2,3] and secondary lymph nodes (Fig 1).

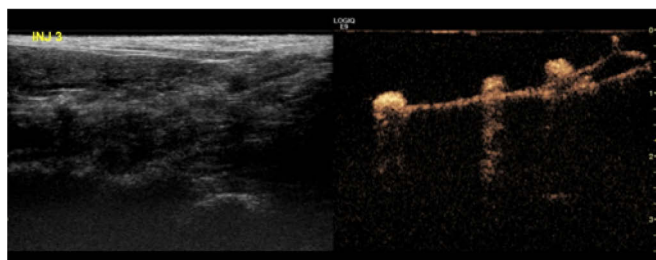


Figure 1: Contrast image of a lymphatic vessel and three lymph nodes

While reactive and LN in NHL show a regular tree like branching of the intra-nodal vessels, metastatic LN destroy the vascular network and build up their own chaotic vasculature. Tumor vessels have no muscle layer, absent or malfunctioning pericytes, show irregular branching, a tortuous course, dilatation with sudden change of diameter and regional changes of microvessel density. The fenestration of the vessel wall results in pores of different sizes from 7nm to 850nm [2]. The size of these pores most probably relate to the leakiness of tumor vessels, thus causing an increase of the intra-nodal pressure leading to local ischemia and thus stimulate neoangiogenesis. With an increasing pressure intranodal veins are compressed and cannot be detected with CDI, and if the pressure is increases even more no vasculature can be seen and a mostly central ischemia and necrosis develops (Fig. 2, 3).

The vasculature in Non Hodgkin lymphoma is mostly preserved, but due to the densely packed tumor cells peripheral resistance is high leading to a hilar amputation with no detectable peripheral vessels (Fig.4).

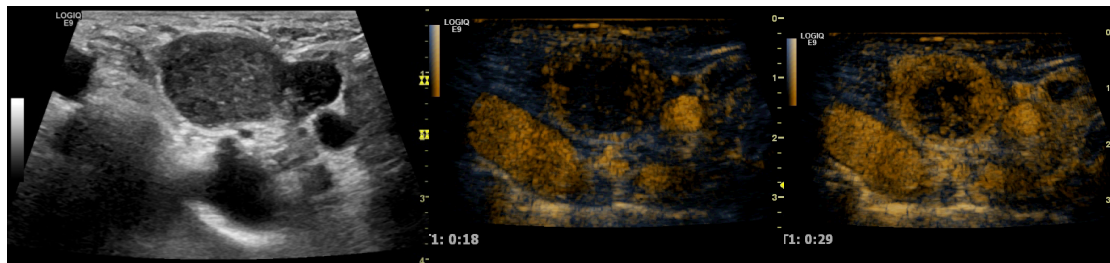


Figure 2: Centripetal enhancement starting at the peripheral zone of the LN metastasis (lung cancer met of the neck)



Figure 3: Hematogeneous spread of breast cancer into two breast cancer metastases in the liver hilum. Central ischemia (metastases), enhancement starts from the subcapsular area, probably the intact cortex



Figure 4: Non Hodgkin lymphoma. Quick centrifugal enhancement with the LN periphery remaining unenhanced ("hilar amputation") Contrast still frames taken at 11s, 18s, and 30s

In contrast, cancerous LN show a centripetal enhancement and an uneven distribution of tumor vessels, recognized as areas of different contrast enhancement levels. Additionally micro-bubbles are washed quickly.

As the direction of enhancement often appears quickly a high frame rate is needed, especially in abdominal LN.

Ultrasound may add value in US guided punctures. Negative LN biopsies are often caused by focal necrosis, especially in fast growing tumors. The additional use of contrast agent is helpful in guiding needle puncture of viable tumor tissue when necrosis is likely (Fig. 5).

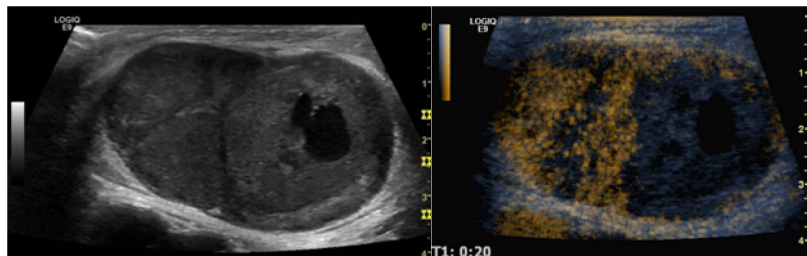


Figure 5: Three LN metastases demonstrating one of them being complexly necrotic (malignant melanoma)

CEUS can be used as well for proving residual viable tissue after chemo- or radiation therapy. The therapeutic effect of chemotherapy or radiation therapy can reliably be proved by CEUS as well.

In case of infiltration or destruction of the LN capsule CEUS is beneficial to prove peri-nodal hyper-enhancement as an indicator for tumor infiltration of the surrounding fatty tissue.

After LN dissection of cancerous LN local infiltration of tumorous cell nests may not be detected in B-Mode. CEUS helps in difficult post surgical situation to detect local tumor infiltration.

Indications for CEUS can be:

Detection of the sentinel/secondary LN

Discriminating reactive from cancerous LN

Discriminating LN of NHL from cancerous LN

Helps to demonstrate cancerous infiltration of peri-nodal fatty tissue

Proving necrotic LN areas, especially after chemo- or radiation therapy

Helps to locate viable and necrotic areas of a LN before biopsy

May prove tumor infiltration of the adjacent fatty tissue

References

1. Weskott HP. [B-flow-a new method for detecting blood flow](#). Ultraschall Med. 2000 Apr;21(2):59-65.
2. Sever AR, Mills P, Jones SE, et al. Preoperative sentinel node identification with ultrasound using microbubbles in patients with breast cancer. AJR 2011; 196:251–256
3. [Sever AR, Mills P, Weeks J, Jones SE, Fish D, Jones PA, Mali W](#). Preoperative needle biopsy of sentinel lymph nodes using intradermal microbubbles and contrast-enhanced ultrasound in patients with breast cancer. [AJR Am J Roentgenol](#). 2012 Aug;199(2):465-70. doi: 10.2214/AJR.11.7702
4. Weskott HP. [Ultrasound in the diagnostic management of malignant lymphomas](#). Radiologe. 2012 Apr;52(4):347-59. doi: 10.1007/s00117-011-2254-3
5. Weskott HP, Shanshan Yin. [Ultrasound in the Assessment of Lymph Node Disease. In small parts and Superficial Structures](#). Ultrasound Clinics Vol 9, Number 3. ed. N Dahiya. 2014

6. Ahuja A, Ying M. Sonographic evaluation of cervical lymph nodes. *AJR* 2005;184:1691-1689
7. Alvarez S, Anorbe E, Alcorta P, Lopez F, Alonso I, Cortes J. Role of sonography in the diagnosis of axillary lymph node metastases in breast cancer: a systematic review. *AJR* 2006; 186:1342–1348
8. Chang DB, Yuan A, Yu CJ, Luh KT, Kuo SH, Yang PC. Differentiation of benign and malignant cervical lymph nodes with color Doppler sonography. *Am J Roentgenol* 1994;162:965-8
9. Khanna R, Sharma AD, Khanna S et al.: Usefulness of ultrasonography for the evaluation of cervical lymphadenopathy. *World Journal of Surgical Oncology* 2011 9:29-
10. Hobbs SKI, Monsky WL, Yuan F, Roberts WG, Griffith L, Torchilin VP, Jain RK. Regulation of transport pathways in tumor vessels: role of tumor type and microenvironment. *Proc Natl Acad Sci U S A.* 1998 Apr 14;95(8):4607-12
11. Dähnert W. Radiological Review Manual. 520-522. Lippincott Williams & Wilkins. 2011
12. Dwebury KC. The Lymph nodes. In: Abdominal and General Ultrasound. Ed. Meire, Cosgrove, Dewbury. Churchill Livingstone. 401-411
13. Lunt SJ, Kalliomaki TM, Brown A, Yang VX, Milosevic M, Hill RP. Interstitial fluid pressure, vascularity and metastasis in ectopic, orthotopic and spontaneous tumours. *BMC Cancer.* 2008 Jan 7;8:2
14. Rubaltelli L, Beltrame V, Scagliori E, Bezzon E, Frigo AC, Rastrelli M, Stramare R. Potential Use of Contrast-Enhanced Ultrasound (CEUS) in the Detection of Metastatic Superficial Lymph Nodes in Melanoma Patients. *Ultraschall Med.* 2013 Jul 16
15. Solbiati L, Rizatto G, Bellotti E, Montali G, Cioffi V, Croce F.. High resolution sonography of cervical lymph nodes in head and neck cancer: criteria for differentiation of reactive versus malignant nodes. *Radiology* 1988; 169: (Suppl. P) 113
16. Tschaumler A, Ott G, Schang T, Seelbach-Goebel B, Schwager K, Hahn D. Lymphadenopathy: differentiation of benign from malignant disease—color Doppler ultrasound assessment of intranodal angioarchitecture. *Radiology* 1998; 208:117-123
17. Tzankov A, Heiss S, Ebner S, Sterlacci W, Schaefer G, Augustin F et al. Angiogenesis in nodal B cell lymphomas: a high throughput study. *J Clin Pathol.* 2007;60(5):476-82
18. Voit C, Schoengen A, Schwürzer-Voit M, Weber L, Ulrich J, Sterry W, Proebstle TM. The role of ultrasound in detection and management of regional disease in melanoma patients. *Semin Oncol.* 2002 Aug;29(4):353-60
19. Weskott HP. Emerging roles for contrast-enhanced ultrasound. *Clin Hemorheol Microcirc.* 2008;40(1):51-71

Significant increase of flow kinetic energy in non-responders patients to cardiac resynchronization therapy

L Agati¹, S. Cimino¹, F. Cicogna¹, D. Cantisani¹, M. Trivigno¹, C. Caira¹, G. Pedrizzetti², G. Toni³

¹Sapienza University of Rome, Department of Cardiov. & Respiratory Sciences, Nephrology & Geriatrics, Rome, Italy

²University of Trieste, Department of Civil and Environmental Engineering, Trieste, Italy (3) S.S. Annunziata Hospital, Sulmona, Italy

Background

Blood motion in the left ventricle (LV) is characterized by a vortical blood motion. In the recent years, several studies evidenced the presence of a close relationship between cardiac function and quality of intra-ventricular fluid dynamics. The wall motion abnormalities in dilated or ischemic cardiomyopathies lead to a lack of efficiency in the blood-tissue dynamical interaction, that may be associated to adverse clinical outcome. We hypothesize that maladaptive intra-cardiac vortex dynamics participates to the development of LV remodeling and therefore influences the response to cardiac resynchronization therapy (CRT). Aim of this study was to demonstrate that the Echo-PIV-derived flow pattern inside the LV could represents a sensitive and reliable marker of cardiac mechanics abnormalities with the potential to become an important clinical tool for the assessment of cardiovascular outcome in patients treated with CRT. Methods: We enrolled 20 heart failure patients who underwent to CRT. All patients underwent 2D echocardiography exam, and fluid dynamics assessment at baseline (CRT-ON) and during a temporarily discontinued state (CRT-OFF). Patients were divided in two groups: "responders" to CRT (increase in LVEF>20% after CRT) and "non responders".

Results

In "responders" patients we observed a significant change between CRT-OFF and CRT-ON in vortex shape: vortex area and vortex length decrease significantly, respectively, 0.23 ± 0.02 vs 0.19 ± 0.01 , $p=0.002$, and 0.58 ± 0.05 vs 0.5 ± 0.04 , $p=0.043$. Moreover, Kinetic energy fluctuation decrease significantly (1.24 ± 1.07 vs 1.07 ± 0.34 , $p=0.039$). In "non responders" patients we observed a significant increase in energy dissipation (0.54 ± 0.16 vs 0.76 ± 0.32 , $p=0.004$), vorticity fluctuation (0.82 ± 0.05 vs 0.87 ± 0.05 , $p<0.001$) and kinetic energy fluctuation (1.36 ± 0.32 vs 1.6 ± 0.5 , $p=0.002$).

Conclusion

Our data show a slight improvement in LV flow indexes derived from vortex ring analysis in "responders" patients and a significant worsening in "non responders" patients treated with CRT. In

particular a significant increase in energy dissipation was observed in "non responders" patients. These findings evidence the importance of a proper selection of patients to treat before establishing an invasive and potentially harmful treatment. Further studies with a larger sample are necessary to understand if LV blood flow parameters can contribute to the selection of CRT-"responders".

Updates on the progress of acoustic angiography high frequency contrast ultrasound

**Paul A. Dayton, Sarah Shelton¹, Brooks Lindsey¹, Ryan Gessner¹, Yueh Z. Lee⁴,
Stephen Aylward², Mike Lee³, Emmanuel Cherin³, F. Stuart Foster³**

¹*Joint Graduate Department of Biomedical Engineering, University of North Carolina and
North Carolina State University, NC, USA*

²*Kitware Medical Imaging, 101 East Weaver Street, Carrboro, NC*

³*Department of Medical Biophysics, Sunnybrook Health Sciences Centre, Toronto, ON, Canada*

⁴*Department of Neuroradiology, University of North Carolina at Chapel Hill, Chapel Hill, NC
27599*

Contrast ultrasound has shown substantial utility in many clinical and pre-clinical imaging applications where there is desire to assess blood flow or molecular markers. However, to date, most contrast imaging is performed below 20 MHz. We hypothesize that this is partially due to the poor nonlinear response of microbubble contrast agents when excited with frequencies far above their resonance (<10 MHz) and challenges with pulse customization using high frequency transducers. However, it has been known for over a decade that when excited near resonance, microbubbles can produce an extremely broadband acoustic response that can exceed even 45 MHz. The challenge to taking advantage of this broadband response is that commercial ultrasound transducers do not have a bandwidth that can excite contrast agents near resonance and receive higher order (ie 3-5) harmonics. Thus, our team has been developing and evaluating multi-frequency transducers to take advantage of this broadband bubble response. Imaging with dual-frequency transducers designed to capture higher order harmonics from oscillating microbubbles at 15-45 MHz has since demonstrated the capability for very high resolution imaging with very effective tissue suppression due to non-overlapping tissue echoes and receive bandwidths. The resulting images resemble x-ray angiography, leading us to refer to this technique as “acoustic angiography” (Figure 1). In this talk, we review our recent findings utilizing this new imaging approach in-vitro, in-animals, and in patients.

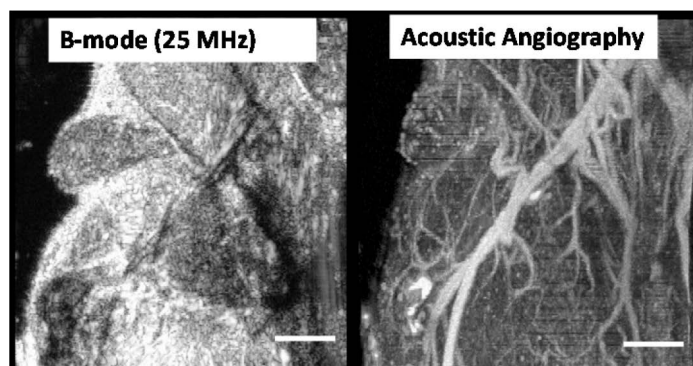


Figure 1: Traditional B-mode ultrasound imaging of a mouse abdomen (right) compared to acoustic angiography (left) which shows microvasculature in high detail (illustrating right iliac and femoral vasculature, and associated smaller vessels).

3D contrast-enhanced ultrasound (CEUS) imaging: Carotid artery atherosclerosis and intra-plaque angiogenesis

**Sandeep Saha¹, Venu Gourineni¹, David M Mills², Kirk D Wallace², Boris M Shur¹,
Frank Yamout¹, Aaron M Dentinger², Adele Liuzzo¹, Vijaya Reddy¹, Dirk R Padfield²,
Chad Jacobs¹, Robert March¹, Walter McCarthy¹, Kunlin Cao², Jing Jin², Dan Adam³,
Marshall Goldin¹, Steven Feinstein¹**

¹Rush University Medical Center, Chicago, IL, USA

²GE Global Res, Niskayuna, NY, USA

³Israel Inst of Technology, Haifa, Israel

Introduction

The vulnerable plaque is characterized by the presence of increased intra-plaque vascularity and hemorrhage leading to deleterious CV events (MI, CVA and death). Multiple investigators have shown that the identification of the vulnerable plaque using CEUS techniques serves as predictive model of adverse outcomes. Currently, only qualitative imaging using 2D CEUS is available for clinical practice. The primary limitation associated with 2D CEUS revolves around the issue of registration; the 2D imaging plane does not represent a volumetric characterization of the carotid vessel. The goals associated with the use of a 3D CEUS examination include: (1) rapid image acquisition, (2) reduction in operator dependence, (3) avoidance of ionizing radiation, (4) reduction in downstream diagnostic testing, (5) accurate volumetric assessment of carotid plaque atherosclerosis, (6) quantification of intra-plaque angiogenesis, and (7) economical use of health resources.

Therefore, this is the first clinical trial using 3D CEUS to assess carotid stenosis, intra-plaque angiogenesis, in patients with clinically significant plaques undergoing carotid endarterectomy.

Methods

Data were acquired on 15 patients asked to participate in this IRB-approved, clinical trial prior to undergoing surgery. All patients received carotid artery MR and/or CT angiogram per their clinician. Post-operatively, the patient's carotid artery plaque histology was reviewed with a pathologist.

Each CEUS carotid image was acquired using a GE LOGIQ E9, RSP6-16 4D probe using an ultrasound contrast agent. To assess plaque stenosis and vascularity, semi-automatic image analysis algorithms were developed to segment the lumen, plaque, and intra-plaque vessels. Measurements derived from 3D CEUS images were validated against the patient's CT, MR.

Results

The data from our clinical trial will be presented and include lumen measurements (CCA, ICA, and ECA) from the 3D CEUS as compared to the patient's MR or CT scans.

Conclusion: The results to date provide promising support for the use of 3D CEUS registration of the carotid anatomy, thus providing a basis to pursue quantitative, volumetric imaging of the carotid artery plaque and intra-plaque angiogenesis.



Clinical routine use of contrast during stress-echocardiography

Nicola Gaibazzi, MD PhD

Department of Cardiology, Parma University Hospital, Parma, Italy

This presentation will address the way contrast-enhanced ultrasound (CEUS) is currently applied in today's cardiology practice in many centers worldwide to enhance imaging during rest and stress-echocardiography.

Clinical Stress-echocardiography has been revolutionized by the availability of stable gas-filled microbubbles that, using a simple peripheral venous injection, may portend the following multifaceted advantages:

a) Opacify heart chambers, making wall motion assessment of the left ventricle:

- more *reproducible* among different readers
- slightly but significantly more *accurate* and
- raising its *feasibility* to almost the totality of patients, comprising the small but existing percentage of technically inadequate patients, in whom stress-echocardiography was previously precluded, and stress-MRI the only alternative for wall motion assessment.

Morphologic assessment is made also much more reliable, easily uncovering and better defining cardiomyopathies (apical hypertrophy or non-compaction cardiomyopathies) difficult to be studied with standard echocardiography

b) Enhance color-Doppler imaging of the mid-distal left anterior descending artery (LAD), by so doing increasing feasibility up to almost 100% of coronary flow reserve measurement even by non-experts or in very difficult patients. Additionally, this may ultimately lead to the interesting possibility of visualizing long tracts of the mid-distal LAD by Color-Doppler imaging, with the additional capability to detect apparently rare entities such as myocardial bridges or intramyocardial course.

c) Assess myocardial perfusion, which, although technically demanding and often adequate for most but not all 17 segments of the left ventricle, boosts very significantly sensitivity to diagnose coronary artery disease in all coronary territories, although with minor loss in specificity, compared

with isolated assessment of wall motion; myocardial perfusion also demonstrates incremental accuracy for prognostication compared with standalone wall motion assessment.

This multiparametric approach to diagnosing suspect coronary artery disease increases accuracy and operator confidence, making stress-echocardiography very competitive with other more costly and complicated techniques, such as cardiac magnetic resonance or PET imaging.

Therapeutic ultrasound in pancreatic adenocarcinoma

Spiros Kotopoulos^{1,2}, Georg Dimcevski^{1,3}, Dag Hoem⁴, Michiel Postema^{1,2} and Odd Helge Gilja^{1,3}

¹National Centre for Ultrasound in Gastroenterology, Haukeland University Hospital, Bergen, Norway

²Department of Physics and Technology, University of Bergen, Bergen, Norway

³Department of Clinical Medicine, University of Bergen, Bergen, Norway

⁴Department of Surgery, Haukeland University Hospital, Bergen, Norway

Background

There are over 217 000 new cases of pancreatic cancer each year. Pancreatic cancer is very difficult to treat due to aggressive biology, late diagnosis, encasement of large blood vessels and/or the presence of metastasis; hence surgery is rarely an option. Chemotherapy produces modest responses but is not curative in this setting, mainly because its use is severely hampered by toxic effects to vital organs. As a result, the survival is very low. The mortality of the inoperable patients is 50% within 3 months and 90% within 12 months

Objectives

The aims of this Phase I study were to investigate the safety and the ability of inducing sonoporation in a clinical setting, using commercially available technology, to increase the patients' treatment cycles and to possibly increase the overall survival in patients with pancreatic adenocarcinoma.

Methods

10 Patients were treated using a customized configuration of a commercial clinical ultrasound scanner (GE LOGIQ 9) over a time period of 31.5 min following standard chemotherapy treatment with gemcitabine. SonoVue was injected intravenously during the treatment with the aim of inducing sonoporation. To ensure microbubbles were present throughout the whole treatment, 0.5 ml of contrast agent followed by 5 ml saline were injected every 3.5 min, i.e., at $T = 30.0, 33.5, 37.0, 40.5, 44.0, 47.5, 51.0, 54.5$, and 58.0min. A single vial (4.5 ml) was used throughout each treatment. Treatment was stopped at $T=61.5$ min. The total cumulated ultrasound treatment time was only 18.9 s. Gemcitabine was administered by intravenous infusion at a dose of 1000 mg/m² over 30 min.

Results

Using the authors' custom acoustic settings, the 10 patients were able to undergo an increased number of treatment cycles; from an average of 8 cycles, to an average of 14 cycles when comparing to a historical control group of 80 patients. In the first two out of five patients treated (published data, ref below), the maximum tumor diameter was temporally decreased to $80 \pm 5\%$ and permanently to $70 \pm$

5% of their original size, while the other patients showed reduced growth. Compared to historical data, there was increased survival with 60% of patients surviving 12 months.

Conclusions

It is feasible to combine ultrasound, microbubbles, and chemotherapy in a clinical setting using a commercially available clinical ultrasound scanner to increase the number of treatment cycles. Our study also indicates increased survival in patients with inoperable pancreatic adenocarcinoma.

Reference

Medical Physics, Vol. 40, No. 7, July 2013

Ultrasound molecular imaging in inflammatory bowel disease: From small to large animals

**Huaijun Wang, Stephen A. Felt, Steven Machtaler, Ismayil Guracar, Richard Luong,
Thierry Bettinger, Lu Tian, Amelie M. Lutz, Jürgen K. Willmann, MD**

Inflammatory bowel disease (IBD) is a group of chronic relapsing disorders, including Crohn's disease and ulcerative colitis, with extensive inflammatory changes in the small and large bowel. Current therapies of IBD with immunosuppressants and immunomodulators are not disease-specific and may have major side effects. Ongoing research explores inexpensive, widely available, safe, and noninvasive methods for the quantitative assessment of the disease extent that allow better individualization of treatment regimens by earlier identification of non-responders from responders and by minimizing drug doses in patients responding to a certain treatment. The purpose of our study was to evaluate the feasibility and reproducibility of ultrasound molecular imaging using dual P- and E-selectin-targeted contrast microbubbles for assessment of inflammation in a porcine acute terminal ileitis model, using histology as a reference standard.

Acute terminal ileitis was established in 19 pigs; 4 pigs served as controls. The ileum was imaged with clinical grade dual P- and E-selectin-targeted microbubbles ($\text{MB}_{\text{Selectin}}$) at increasing doses (0.5x, 1x, 2.5x, 5x, 10x, and $20 \times 10^8/\text{kg}$ b.w.) and with control non-targeted microbubbles ($\text{MB}_{\text{Control}}$). To test reproducibility, scans were repeated twice following $\text{MB}_{\text{Selectin}}$ and $\text{MB}_{\text{Control}}$ injections. After imaging, scanned ileal segments were analyzed *ex vivo* for both inflammation grading on H&E staining and for expression of selectins using quantitative immunofluorescence.

Our results showed that ultrasound molecular imaging signal significantly increased linearly between a dose of 0.5×10^8 and $5 \times 10^8/\text{kg}$ b.w. ($P < .001$) and plateaued between a dose of 10×10^8 and $20 \times 10^8/\text{kg}$. Ultrasound molecular imaging was reproducible ($\text{ICC} = 0.70$) and administration of $\text{MB}_{\text{Selectin}}$ in acute ileitis resulted in a significantly higher ($P < .001$) imaging signal compared to control ileum and to $\text{MB}_{\text{Control}}$. *Ex vivo* inflammation histological grading correlated well with *in vivo* ultrasound signal ($\rho = 0.79$, $P < .001$). Also, expression levels of P-selectin ($P < .001$) and E-selectin ($P = .04$) on inflamed capillaries in acute ileitis were significantly increased compared to control ileum.

In conclusion, the results of our study suggest that ultrasound molecular imaging with dual selectin-targeted microbubbles can be translated from small to large animal imaging in an acute terminal ileitis model in pigs using current clinical ultrasound equipment. This is a critical further step towards future clinical translation of this imaging approach for accurate and objective quantification of inflammation

in the abdomen. Since ultrasound is widely accessible, relatively inexpensive, and does not involve ionizing radiation, ultrasound molecular imaging may have significant future clinical utility as a complementary imaging modality for the diagnosis and management of patients with IBD.

Targeted therapeutic gene knockdown using ultrasound and microbubble-mediated delivery of a transcription factor decoy

Jonathan A. Kopechek, Andrew R. Carson, Xucai Chen, Charles F. McTiernan, Bima Hasjim, Malabika Sen, Jennifer R. Grandis, Flordeliza S. Villanueva

Center for Ultrasound Molecular Imaging and Therapeutics, University of Pittsburgh, Pittsburgh, PA

Background

Ultrasound (US)-based therapies using microbubbles (MB) have the potential for targeted delivery of molecular therapies. Preclinical studies demonstrate that daily intratumoral injection of a STAT3 decoy inhibits STAT3 signaling and growth of squamous cell carcinoma (SCC), but daily tumor injection is invasive, cumbersome, and not clinically feasible. Thus, we tested the hypothesis that MB loaded with STAT3 decoy + US inhibit STAT3 signaling and tumor growth with *in vitro* and *in vivo* models of murine SCC.

Methods

Cationic lipid MB were loaded with STAT3 or mutant decoy as a control (10 µg decoy per 1×10^9 MBs). Therapeutic US was delivered using a clinical scanner (1.3 MHz, MI setting=1.6, 4 frames/burst, pulse interval 2 sec). Cultured SCC-VII cells expressing luciferase (luc) under a STAT3 responsive promoter were treated with US as MB were infused into the cell suspension over 5 min. Luc activity was measured 8 hrs post treatment. For *in vivo* studies, mice with subcutaneous SCC-VII tumors were treated with US during 20 min i.v. MB infusion every 3 days (total 3 treatments). Tumor volume was tracked with 3D US. Other control mice (no US) received i.v. infusions of 10 µg free STAT3 decoy or saline only.

Results

Compared to mutant decoy-loaded MB (n=13), US treatment of cells *in vitro* with STAT3 decoy-loaded MB (n=14) reduced luc expression by $28 \pm 11\%$ ($p < 0.001$). US treatment of tumor-bearing mice with STAT3 decoy MB (n=6) reduced expression of STAT3 downstream target genes by 34-39% compared to mutant decoy (N=8, $p < 0.05$). In addition, US treatment with STAT3 decoy MB significantly increased tumor doubling time (DT) compared to control groups (n=7-8; $p < 0.05$, Figure 1). Compared to control groups, US and STAT3 decoy MB treated tumors were 31-40% smaller on day 4 ($p < 0.02$), 51-61% smaller on day 7 ($p < 0.02$), and 44-64% smaller on day 10 ($p < 0.02$). Further, the amount of radiolabeled STAT3 decoy detected in tumors eight hours after treatment was greater with UTMD

compared to controls infused with STAT3 decoy alone, or infused with STAT3 decoy loaded microbubbles but without ultrasound treatment.

Conclusions

US/MB treatment delivers a transcription factor decoy to selectively knock down gene expression and inhibit tumor growth. This approach has the potential to deliver small molecular weight therapeutic nucleic acids to target tissues in a range of diseases, including cancer and cardiovascular diseases.

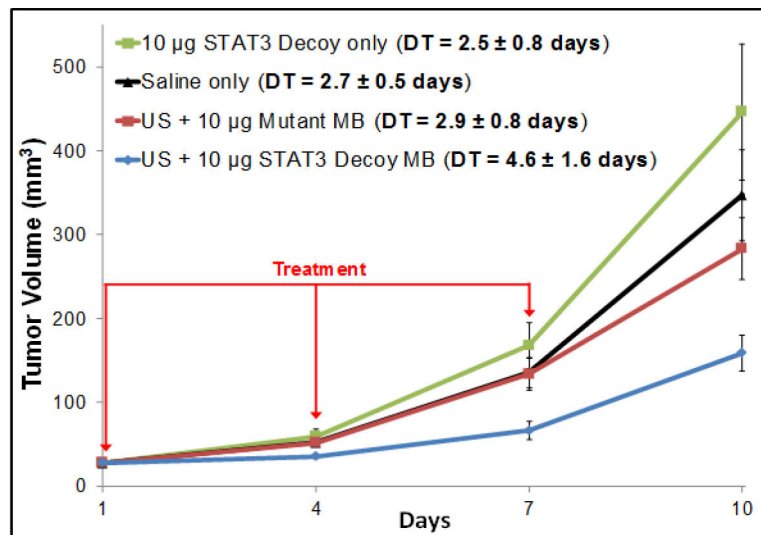


Figure 1: Tumor volume plotted as a function of time for each treatment group. Tumor growth was significantly inhibited after US + STAT3 decoy MB treatment compared to control groups ($p = 0.02$, $N=6-8$ per group). DT represents tumor doubling time.

Microbubbles as magic bullets in cancer immunotherapy

Heleen Dewitte^a, Sandra Van Lint^b, Katrien Vanderperren^c, Hendrik Haers^c, Emmelie Stock^c Stefaan C. De Smedt^a, Karine Breckpot^b and Ine Lentacker^a

^aLab for General Biochemistry and Physical Pharmacy, Faculty of Pharmacy, Ghent University, Ghent, 9000, Belgium

^bLaboratory of Molecular and Cellular Therapy, Department Immunology-Physiology, Medical School of the Free University of Brussels (VUB), 1090, Jette, Belgium

^cDepartment of Veterinary Medical Imaging and Small Animal Orthopaedics, Faculty of Veterinary Medicine, Ghent University, Merelbeke, Belgium

Ever since dendritic cells (DCs) first emerged as the most potent antigen presenting cells and key initiators of immune responses, they have paved the way for DC-based immunotherapy^{1,2}. These cells are specialized in taking up antigens, and presenting them to naïve T cells. If the T cells recognize the antigen as non-self, they become activated, proliferate, and differentiate into effector T cells. Once active, these T cells will selectively target and destroy cells expressing the antigen.

This capacity of DCs to trigger antigen-specific immune responses can be used to our benefit: When DCs are modified to present tumor associated antigens (TAAs), specific anti-tumor immune responses can be evoked. As an alternative to the currently used strategies for antigen-loading of DCs, we have used mRNA loaded microbubbles for ultrasound guided transfection of dendritic cells (**figure 1**).

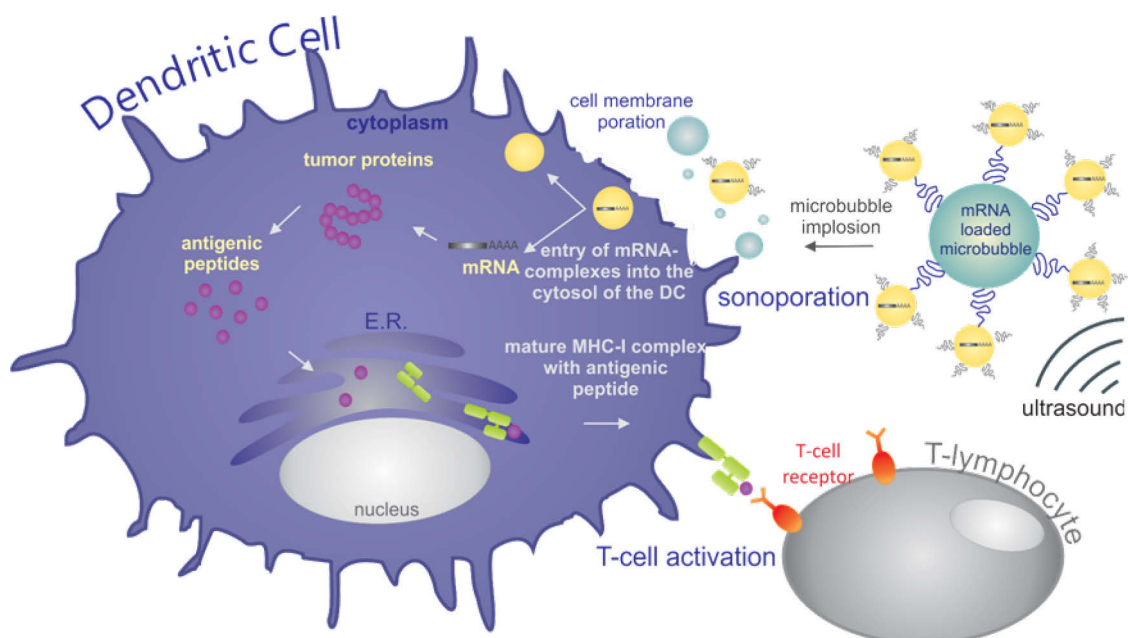


Figure 1: Using mRNA-sonoporation, DCs can be modified to present tumor-associated antigens to T cells. Upon T cell activation, an antigen-specific immune response is generated.

Previously, we showed that sonoporation can be used to transfect dendritic cells *in vitro* and that these transfected DCs were able to translate the TAA encoding mRNA resulting in T-cell activation³. This presentation will focus on our latest results where we have performed a therapeutic tumor vaccination study in mice where we used *in vitro* sonoporated DCs as a vaccine in tumor-bearing mice. E.G7-OVA-bearing mice were intradermally injected with different types of mRNA-sonoporated DCs : (a) DCs sonoporated with control mRNA (eGFP mRNA); (b) DCs sonoporated with OVA mRNA (model TAA) and (c) DCs sonoporated with OVA+Trimix mRNA. TriMix is a mixture of 3 mRNAs that encode proteins that will modulate the function of the DCs, resulting in more mature DCs, and hence in better T-cell activation⁴. When OVA mRNA-sonoporated DCs, but especially OVA+TriMix-sonoporated DCs were used, tumor growth was significantly reduced. For OVA+TriMix, tumors even completely regressed in 30% of the animals (**Figure 2A**). Moreover, rechallenge with tumor cells did not lead to tumor growth, indicating long-lasting immunological protection (**Figure 2B**)⁵.

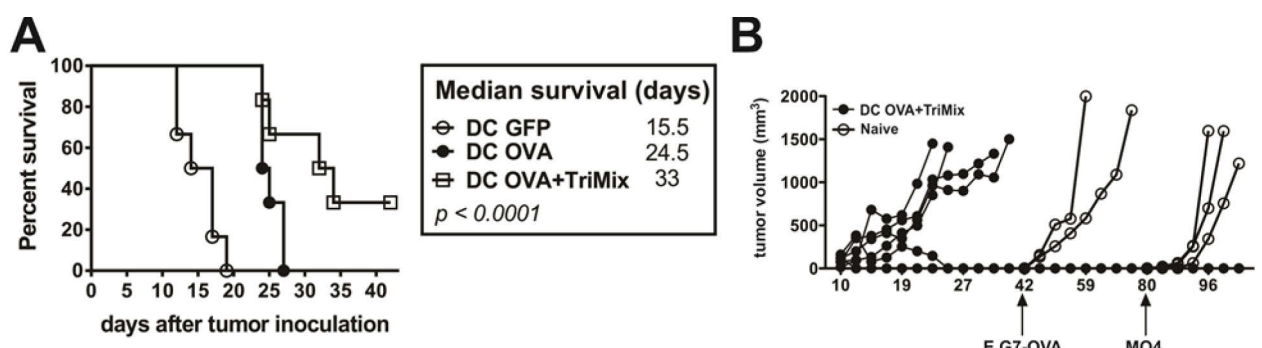


Figure 2: Therapeutic vaccinations with mRNA-sonoporated DCs.

Current clinically used DC immunotherapies make use of a very complex and expensive procedure in which *ex vivo* transfected patient-specific DCs are administered to the patient. Currently we are evaluating whether sonoporation can be applied to achieve an *in vivo* transfection of lymph node resident DCs. At first instance we evaluated the spontaneous drainage of mRNA loaded microbubbles to the lymph nodes after intradermal injection. **Figure 3** shows that we were indeed able to visualize the lymph vessels and lymph nodes with contrast ultrasound in dogs⁶.

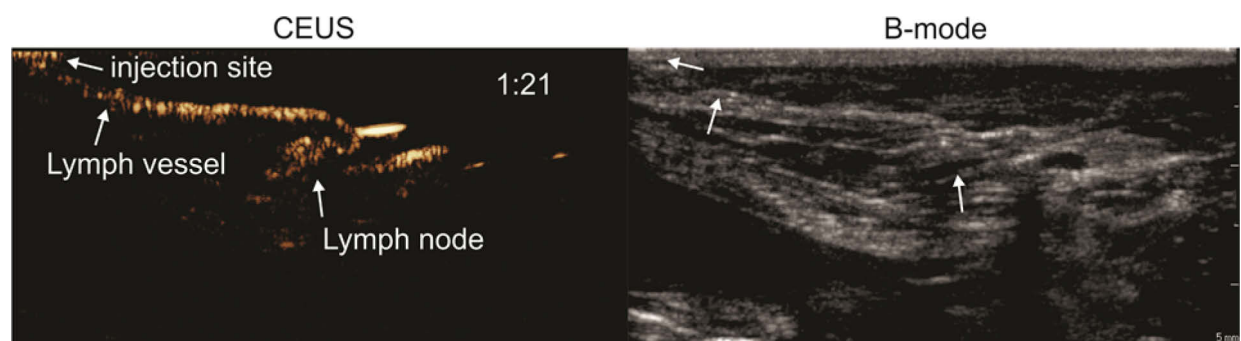


Figure 3: Contrast agent migration from the injection site into the lymph vessels and nodes in dogs.

In conclusion, mRNA sonoporation shows to be a promising tool in DC-based cancer immunotherapy.

Acknowledgements

Ine Lentacker is a postdoctoral fellow of the Research Foundation Flanders, Belgium (FWO-Vlaanderen). Heleen Dewitte is a doctoral fellow of the Institute for the Promotion of Innovation through Science and Technology in Flanders, Belgium (IWT-Vlaanderen).

References

1. Steinman, R.M. & Cohn, Z.A. *Identification of a novel cell type in peripheral lymphoid organs of mice*. *Journal of Experimental Medicine* 137, 1142-1162 (1973)
2. Steinman, R.M. & Dhodapkar, M. *Active immunization against cancer with dendritic cells: the near future*. *International Journal of Cancer* 94, 459-473 (2001)
3. De Temmerman, M.-L. & Dewitte , H. et al. *mRNA-Lipoplex loaded microbubble contrast agents for ultrasound-assisted transfection of dendritic cells*. *Biomaterials* 32, 9128-9135 (2011)
4. Van Lint, S. et al. *Preclinical Evaluation of TriMix and Antigen mRNA-Based Antitumor Therapy*. *Cancer Research* (2012)
5. Dewitte, H. et al. *Theranostic mRNA-loaded microbubbles in the lymphatics of dogs: implications for drug delivery*. *Theranostics* 5, 97-109 (2015)
6. Dewitte, H. et al. *The potential of antigen and TriMix sonoporation using mRNA-loaded microbubbles for ultrasound-triggered cancer immunotherapy*. *Journal of Controlled Release* 194, 28-36 (2014)

Ultrasound and microbubble induced delivery of miRNA-blockers *in vitro*, to mouse skeletal muscle and the mouse heart

Rick F.J. Kwekkeboom¹, Zhiyong Lei², Sylvia J.P. Bogaards¹, Eric Aiazian^{3,4}, Otto Kamp⁴, Walter J. Paulus¹, Joost P.G. Sluijter², René J.P. Musters¹

¹*Department of Physiology, VU University Medical Center, Van der Boechorststraat 7, 1081 BT, Amsterdam, the Netherlands*

²*Department of Experimental Cardiology, University Medical Center Utrecht, P.O. Box 85500, 3508 GA, Utrecht, the Netherlands*

³*Axle International, Nieuwe Uitleg 28, 2514 BR, the Hague, the Netherlands*

⁴*Department of Cardiology, VU University Medical Center, De Boelelaan 1117, 1081 HV, Amsterdam, the Netherlands*

MicroRNAs are involved in many pathological processes and are a promising class of molecules to target therapeutically. Different classes of miRNA-blockers exist, e.g. the anti-miR and the antago-miR. In the present study, ultrasound (US) -responsive microbubbles (MB) were investigated for their capability to locally deliver anti-miR and antago-miR to endothelial cells *in vitro* and the skeletal and heart muscle in mice to increase local concentration and decrease off-side effects.

Endothelial cells were treated *in vitro* with anti-miR or antago-miR in combination with MB and US at 1 MHz and a peak negative pressure of 0.2 MPa. After treatment, anti-miR could be found in the nucleus of the cell up to 24 h after treatment. The antago-miR could be found both in the nucleus and cytosol up to 24 h after treatment. The delivery of anti-miR led to a 50% knockdown of the target miRNA whereas the delivery of antago-miR did not have an effect on target miRNA levels.

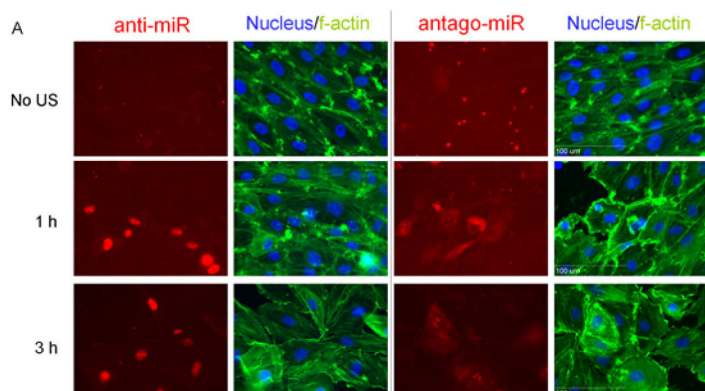
For *in vivo* delivery of miRNA-blockers to skeletal muscle, first a small pilot study was performed to determine what US-protocol was most feasible for delivery of miRNA-blockers. We found that low pressure US (mechanical index (MI) of 0.2) at 1 MHz does not increase local delivery of miRNA-blockers where high pressure (MI of 1.8) at 7 MHz does increase local delivery (the same was true for 2 MHz at an MI of 1.4). Subsequently, mouse skeletal muscles were treated with US at 7 MHz with an MI of 1.8 after an i.v. bolus injection of cationic MB and antago-miR. This leads to increased delivery of antago-miR to the capillaries of these muscles and caused extravasation of antago-miR to the extracellular space. Treatment with US at 7 MHz and an MI of 1.8 after an i.v. bolus injection of cationic MB and anti-miR did not lead to increased delivery of anti-miR.

Subsequently, cationic MB and US were tested for their capability to deliver antago-miR to the heart. For US treatment, a Philips Sonos 5500 machine was used with an s12 or s3 transducer operating in

angio contrast mode. Treatment protocols with both transducers were confirmed to cause MB destruction. Treatment with both transducers led to an increased delivery of antago-miR to the heart. Antago-miR could be found inside the cardiomyocytes 30 min, 24 h and 48 h after treatment. In addition to an increase in antago-miR delivery, treatment with US, MB and antago-miR lead to an acute disturbance of the mouse ECG, ventricular wall thickness, ejection fraction and lung function.

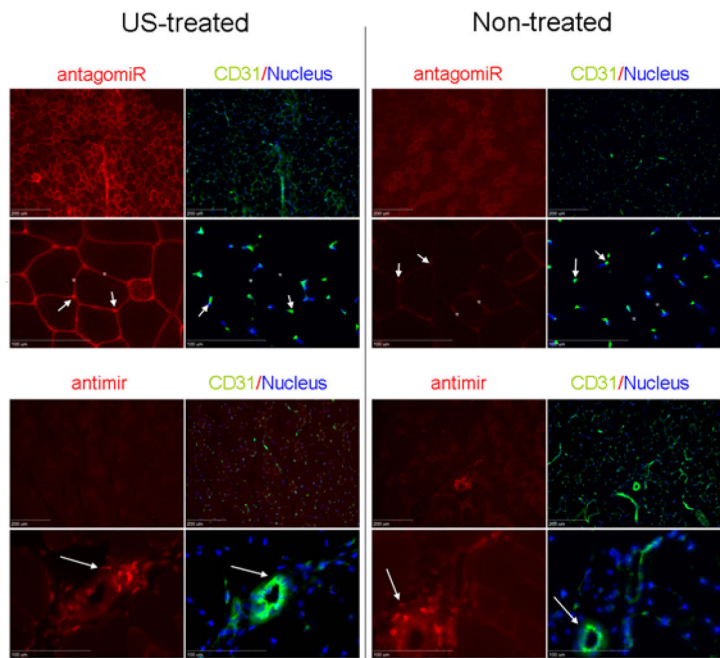
In conclusion, US and MB can be used to deliver anti-miR and antago-miR intracellularly *in vitro*. Only delivery of anti-miR leads to knockdown of the specific miRNA target. US-protocols that worked *in vitro* did not increase local delivery *in vivo* and MB destruction seems necessary. Additionally, MB and US can increase local delivery of antago-miR to the skeletal muscle but not of anti-miR. The processes which drive *in vitro* success are different from the processes which drive *in vivo* success making translation of *in vitro* results to *in vivo* drug delivery difficult. Additionally, we studied local delivery of antago-miR to the heart of mice. We found that local delivery of antago-miR to skeletal muscle results in increased delivery to the capillaries and extravasation. In the heart, antago-miR could only be found in the cardiomyocytes. The different nature of the muscles might cause different delivery patterns after similar treatment regimens with US and MB.

Figure 1: In vitro delivery of anti-miR and antago-miR to endothelial cells



Fluorescence microscopy images of anti-miR and antago-miR transfection in HUVECs without US-treatment and 1h, and 3h after US-treatment

Figure 2: In vivo delivery of antago-miR and anti-miR to skeletal muscles of mice



Fluorescence microscopy images (10x and 40x magnification) of cryosections of treated semimembranosus muscles of mice stained for CD31 (green) and nucleus (blue), anti-miR and antago-miR are red. Antago-miR could mostly be found in the capillaries (white arrows) and at myocyte-myocyte junctions (white stars), US-treatment (left panel) increased antago-miR delivery. Anti-miR could mostly be found around arterioles (white arrows), US-treatment (left panel) did not have effect on anti-miR delivery or tissue distribution. Images are representative images for several experimental mice per group

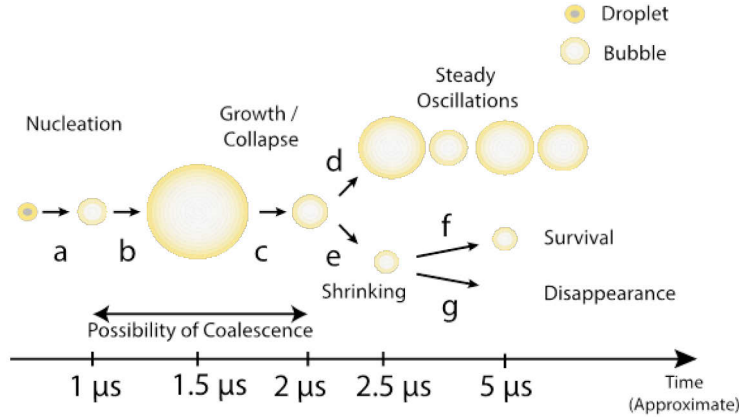
This research forms part of the Project **P1.05 LUST** of the research program of the **BioMedical Materials** institute, co-funded by the **Dutch Ministry of Economic Affairs**. The financial contribution of the **Nederlandse Hartstichting** is gratefully acknowledged.

Acoustic droplet vaporization: Physical insights from ultra high-speed microscopy at nanoseconds timescales

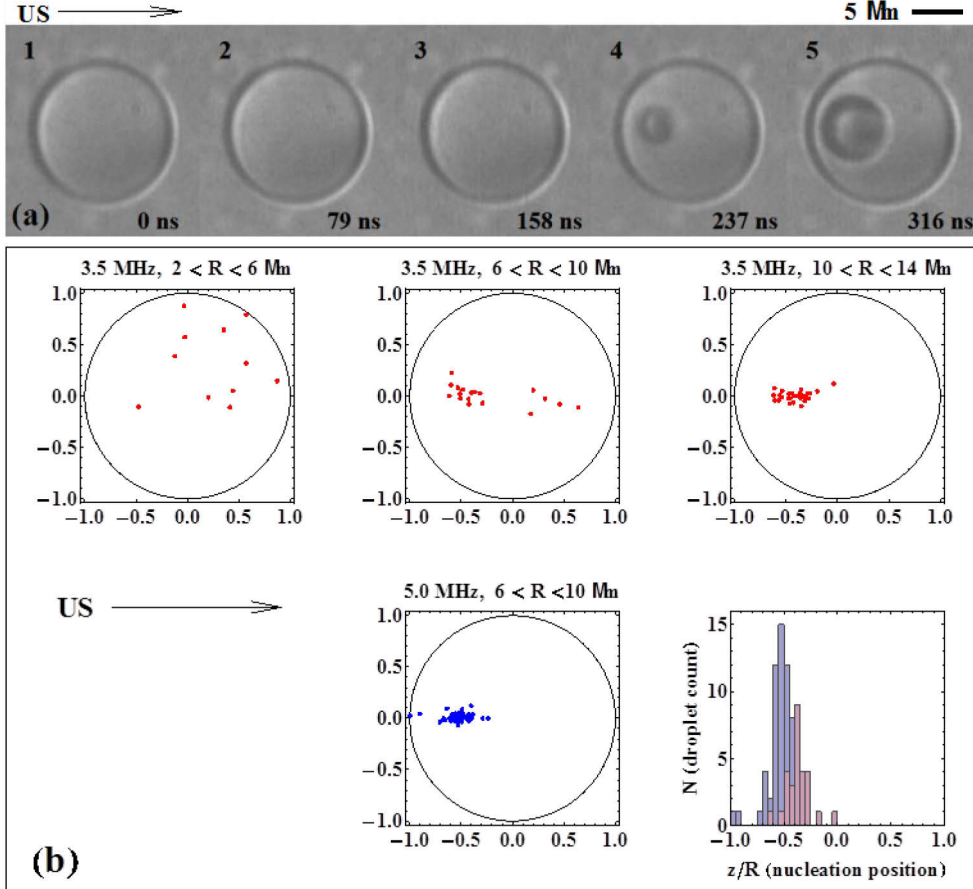
Michel Versluis

Physics of Fluids group, MIRA Institute for Biomedical technology and Technical Medicine and MESA+ Institute for Nanotechnology, University of Twente, Enschede, The Netherlands

The interaction of droplets and bubbles with ultrasound has been studied extensively in the last 25 years. Microbubbles are broadly used in diagnostic and therapeutic medical applications, for instance, as ultrasound contrast agents. They have a similar size as red blood cells, and thus are able to circulate within the blood vessels. Perfluorocarbon liquid droplets can be a potential new generation of microbubble agents, as they can be triggered with ultrasound converting them into gas bubbles. Prior to activation, they are at least 5 times smaller in diameter than the resulting bubbles. Together with the violent nature of the phase-transition the droplets can be used for local drug delivery, embolotherapy, HIFU enhancement and for tumor imaging. Here we study the ultrasound-focusing concept within a droplets sphere, droplet shaking due to media compressibility, and droplet phase-conversion dynamics. We observe the vaporization of submicron PFC droplet for the first time at a nanoseconds timescale. This examination of the droplets revealed interesting phenomena that could not be detected at lower imaging frame rates. The results have shown effects of shell material retention by the bubbles after vaporization. We estimated that the efficiency of conversion of droplets into bubbles when exposed to an acoustic pulse within the diagnostic range is at least 10%. In this chapter we also show that submicron droplets may undergo coalescence or fragmentation during the initial oscillations following droplet vaporization. Bubble coalescence, effectively increasing the shell material concentration on the bubble surface, increases the chances of bubble survival. An increase of the initial droplet concentration, leading to a reduced inter-droplet separation distances, hence, is beneficial for the production of stable microbubbles. Thus, the efficiency of initial droplet vaporization, and the efficiency of stable bubble production may be very different, depending on the excitation conditions.



A study into the origin of acoustic droplet vaporization mechanism is presented. The Brandaris ultra high-speed camera is used to investigate nucleation within the droplets in the parameter space of the droplet size and acoustic parameters such as pressure amplitude and frequency. We show that ADV is initiated by the focusing of the superharmonics of a non-linearly distorted acoustic wave within the droplet. In the parameter range considered, the focusing leads to up to a ten-fold increase of the incident peak negative pressure in a well-defined focusing spot. The location of the focusing spot as well as the focusing strength depends on the frequency of the incident wave and on the size of the droplet. A higher frequency and a larger droplet radius, i.e. a smaller wavelength compared to the droplet size, leads to a more pronounced focusing effect and consequently leads to smaller pressure amplitudes required for activation. Nonlinear propagation is shown to have a crucial role in ADV. It causes distortion of the pressure waveform and the resulting superharmonics are highly focused within the spherical droplet. Thus, the transducer geometry, as well as the parameters for nonlinearity of the propagating medium have an effect on the focusing strength and the position of focusing.



Finally, the Brandaris ultra high-speed camera is used to investigate the radial dynamics of acoustic droplet vaporization. Acoustic microdroplet vaporization was imaged for the first time at a nanoseconds time scale with a sampling rate of 3-5 images per cycle, being able to capture pre-nucleation, nucleation, during ultrasound and post ultrasound, all for a single vaporization event. With the proposed method of pressure restoration it was shown that the inception of nucleation occurs during the peak negative half cycle of ultrasound and slightly shifted towards the end of it. Following nucleation, the physics of the vapor bubble expansion is shown to be heat transfer limited. The vapor bubble expansion was observed to have two components, one monotonic with a typical velocity of expansion of 5-10 m/s and a second oscillatory component with the typical amplitude of 1.2 μm associated with the applied ultrasound. The vapor bubble growth is increased by acoustic activation and through a simple physical model it was shown to be the result of rectified heat transfer when the ultrasound is forcing the vapor bubble.

High spatiotemporal control of spontaneous reactions using ultrasound-triggered composite droplets

Marine Bezagu,^{†,§} Claudia Errico,[‡] Victor Chaulot-Talmon,[§] Fabrice Monti,[§] Mickael Tanter,[‡] Janine Cossy,[†] Patrick Tabeling,[§] Stellios Arseniyadis,[†] Olivier Couture[‡]

[†]Laboratoire de Chimie Organique, Institute of Chemistry, Biology and Innovation (CBI) – UMR 8231 – ESPCI, ParisTech/CNRS/PSL* Research University, 10 rue Vauquelin, 75231 Paris Cedex 05, France

[‡]Institut Langevin, ESPCI ParisTech, CNRS (UMR 7587), INSERM (U979), Paris, France

[§]Laboratoire de Microfluidique, MEMS et Nanostructures, ESPCI ParisTech, CNRS (UMR Gulliver 7083), Paris, France

Background, Motivation and Objective

Achieving high spatial and temporal control over a spontaneous reaction is a particularly challenging task with potential breakthroughs in various fields of research, including surface patterning and drug delivery. In this context, we previously established that perfluorocarbon composite droplets comprised of a nanoemulsion of water loaded with fluorescein and encapsulated in a perfluorohexane matrix (4 μm in diameter) could release their content by acoustic vaporization (Couture *et al.* *Medical Physics*, **2011** and **2012**). Following these initial results, we implemented the use of these microdroplets to allow spatial and temporal control of a chemical reaction by isolating two reactants (**A** and **B**) and releasing them using acoustic pulses. This method of control allows the formation of the product (**C**) specifically at the focal zone upon vaporization of the perfluorocarbon matrix (Figure 1). The steep threshold of release of these droplets (1.7 MPa PNP at 5 MHz) allows the triggering of a chemical reaction with a high spatial (mm) and temporal resolution (ms).

Statement of Contribution/Methods

The demonstration was achieved by encapsulating a solution of azidocoumarin (**A**) in DMSO into composite droplets of perfluorohexane and releasing the content into the external flow containing a reactive alkyne (**B**). Most importantly, the product of the reaction of **A** and **B** is fluorescent ($\lambda_{\text{ex}} = 350$ nm, $\lambda_{\text{em}} = 430$ nm). The two solutions (**A** encapsulated + **B** in solution) were injected in a microfluidic channel where a 2.25 MHz transducer was focused. A single pulse of 30 cycles was emitted while a camera (10 fps) mounted on a fluorescent microscope (10X, DAPI) recorded the fluorescence induced during the reaction.

We also demonstrated the ability to control the reaction using a standard clinical scanner. Hence, the same droplets that contained a solution of **A** were injected in a cell-culture plate filled with a solution of **B** and placed under a 4 MHz, 196-element probe connected to a clinical ultrasound scanner. The latter was used to emit a single pulse of 2 cycles on each spot of the release and the distance between the

different spots is equal to the pitch number of the transducer (0.3 mm). Release spots could be selected anywhere on the plate using a software interface. The chemical cloud was eventually excited with a UV light thus allowing to observe the release-pattern through a UV filter.

Results/Discussion

Interestingly, a single acoustic pulse was able to vaporize several droplets within the microfluidic channel, leading to the release of their content in the surrounding medium. As shown on Figure 1, in the following 100 ms upon release, the fluorescence intensity within the focus zone was multiplied by a factor of 10 (**A + B**) compared to the control experiment. As the fluorescence is specific to the reaction product, this allowed to demonstrate the subsequent formation of the product **C** immediately after ultrasound release.

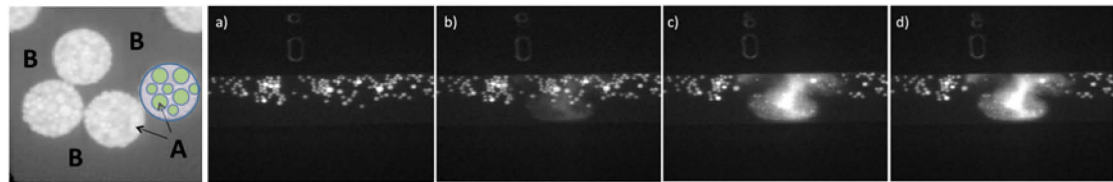


Figure 1: Microscope images of the ultrasound-induced chemical reaction. The release pulse happened between the first and second images (100 ms apart). a) $t = -100$ ms; b) $t = 0$; c) $t = 100$ ms; d) $t = 200$ ms.

By remotely scanning the focus zone of the ultrasound clinical system, several spots of release could be generated over each line, initiating the chemical reaction in specific zones of the plate. Thus, a 3 cm high representation of a landmark of Paris could be created point-by-point within 6 seconds (Figure 2).

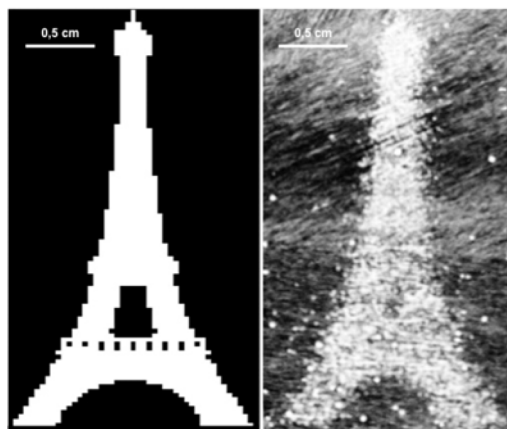


Figure 2: Drawing generated by focusing pulses according to the pattern (left) with an ultrasound scanner within a plate filled with droplets of **A** in a medium of **B**. Photography made under UV light (histogram equalized) a few seconds after the end of the release.

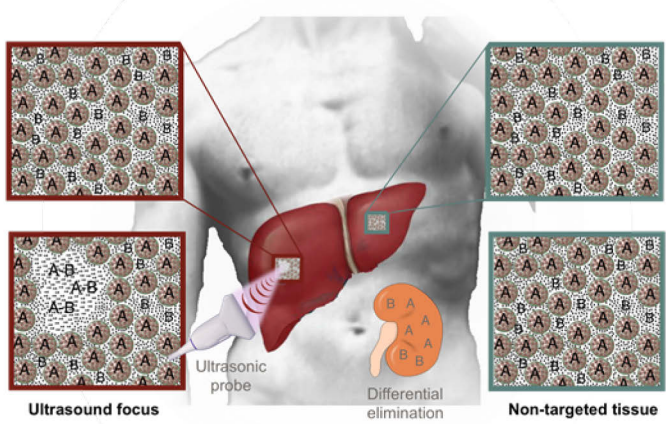


Figure 3: Perspective of this work

Evaluating *in vivo* contrast production from phase-shift droplets using a commercial small animal imaging system

Paul S. Sheeran¹, Yasaman Daghighi², Ross Williams² and Peter N. Burns^{1,2}

¹*Department of Medical Biophysics, University of Toronto, Toronto, Ontario, Canada*

²*Sunnybrook Research Institute, Toronto, Ontario, Canada*

Introduction

Ultrasonically vaporized phase-shift perfluorocarbon droplets provide a unique solution to several problems in medical diagnostics and therapeutics. To date, investigations have largely focused on evaluating vaporization conditions that optimize bubble production at depths relevant to human medicine (through several centimeters of attenuating tissue)¹, resulting in the use of ultrasound frequencies predominantly in the 1 – 10 MHz range. Very recently, researchers have begun to push toward clinical implementation by combining droplet activation and contrast production monitoring within the same system using a single transducer^{2,3}. However, extending these concepts to small animal ultrasound imaging systems (i.e. high frequency) would allow for more effective preclinical evaluation of phase-shift droplets, and would allow researchers to easily add this class of agents to ongoing preclinical investigations. In this study, we explore *in vivo* droplet activation and imaging using standard settings on a commercial small animal ultrasound scanner.

Methods

Phospholipid-encapsulated phase-shift decafluorobutane (DFB) droplets were produced by a ‘microbubble condensation’ method⁴ to form polydisperse distributions with peaks on the order of 200 to 300 nm. Doses consisting of 100 µL DFB droplets followed by 100 µL saline were administered at a rate of 100 µL/min to the tail vein of C3H mice. Both healthy and tumour-bearing mice (KHT cell hindlimb xenografts) were imaged using a VisualSonics Vevo 2100 high frequency imaging platform with a 40 MHz center frequency probe. All imaging and activation were accomplished using single cycle B-mode sequences at either 2% output power (manufacturer reported PNP ≈ 0.89 MPa) or 100% power (manufacturer reported PNP ≈ 4.48 MPa) with 20-22 dB image gain and an imaging threshold of 65 dB. Contrast resulting from droplet vaporization was evaluated in various organs, including liver, superficial tumours, carotid artery, kidney, and *ex vivo* whole blood gathered from cardiac puncture. Data were evaluated both in single-plane configurations and whole-organ volumetric measurements obtained by mechanically scanning the transducer at 0.032 mm intervals in the elevational dimension. Imaging data were exported and analyzed offline in MATLAB by manually drawing regions-of-interest over the images and evaluating the linearized pixel values relative to agent-free baseline and pre-activation baseline.

Results and Discussion

B-mode imaging on the Vevo2100 at 40 MHz, 2% power provided high-resolution, detailed images of the target organ at pressures lower than the droplet vaporization threshold, while increasing the power to 100% caused a high amount of bubble formation localized around the axial pulse foci. The degree of contrast production varied both with target organ and time after injection (**Fig. 1**). In linear B-mode imaging, median contrast increase was on the order of 20-22 dB relative to agent-free baseline in the liver 5 minutes after injection, whereas enhancement in tumours at the same time point was on the order of 14 dB, depending on tumour size. Clearance of droplets in circulation manifested as decreases in contrast production at later time points. Qualitative differences in clearance of the bubbles resulting from droplet vaporization between the liver and other target organs suggests liver contrast may partly result from droplets vaporized after uptake by macrophages while in circulation. Whole-blood, liver, and tumour measurements demonstrated the long circulation properties of the injected droplets, with contrast production continuing past the 1 hour mark – significantly longer than possible with conventional microbubble contrast agents such as Definity or MicroMarker. Droplets were well tolerated with no adverse events observed in all animals tested at the injected dose.

Conclusion

Evaluating contrast production and circulation properties of low boiling point phase-shift droplets can be accomplished on high-frequency scanners such as the Vevo 2100 using standard imaging settings and pulse parameters. The high-resolution imaging capabilities allow new approaches to evaluate droplet performance as a function of formulation – both in terms of contrast production and longevity in circulation. Here, it was shown for the first time that phase-change droplets formed from DFB can persist in circulation for more than 1 hour. Future customization of the pulse-sequences and adaptation to contrast imaging modes may provide new possibilities for preclinical goals.

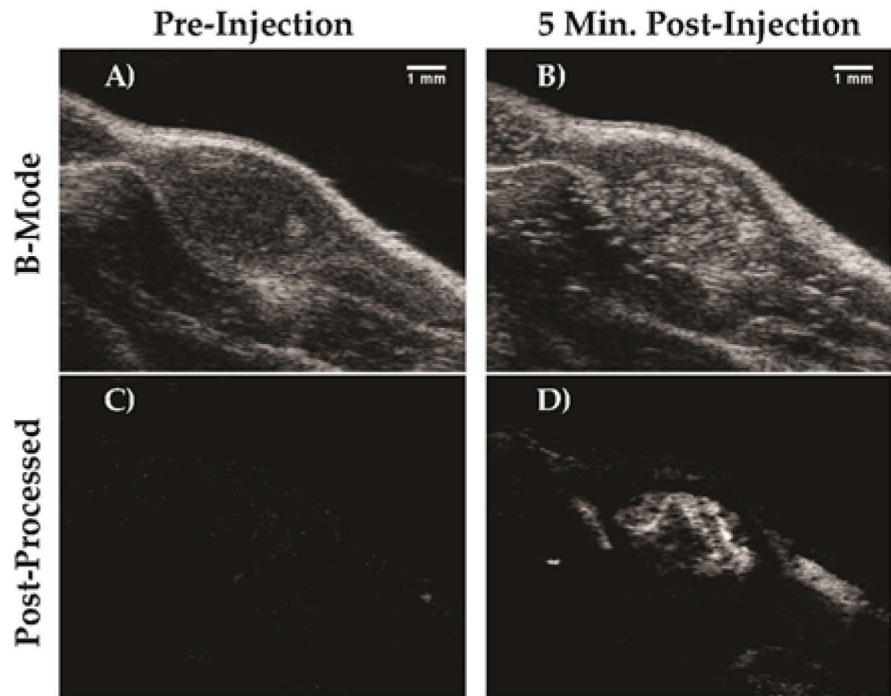


Figure 1. B-mode images of superficial KHT-C xenograft tumours in mice exposed at 100% power output on a VisualSonics Vewo 2100 (40 MHz linear array) (A) prior to injection of DFB droplets, and (B) 5 minutes post-injection. Vaporization of circulating droplets manifests as newly generated bubbles. (C and D) Post-processed images showing cumulative variation captures the localization of the ongoing droplet activation by first applying sequential frame subtraction and integrating the resulting frames (here for 75 sequential vaporization frames).

References

1. Williams, R. et al. Characterization of Submicron Phase-change Perfluorocarbon Droplets for Extravascular Ultrasound Imaging of Cancer. *Ultrasound Med. Biol.* **39**, 475–489 (2013)
2. Couture, O. et al. In vivo targeted delivery of large payloads with an ultrasound clinical scanner. *Med. Phys.* **39**, (2012)
3. Sheeran, P. S. et al. Contrast-Enhanced Ultrasound Imaging and In Vivo Circulation Kinetics with Low Boiling Point Nanoscale Phase-Change Perfluorocarbon Agents. *Ultrasound Med. Biol.* **In Press**, (2014)
4. Sheeran, P. S., Luois, S. H., Mullin, L. B., Matsunaga, T. O. & Dayton, P. A. Design of ultrasonically-activatable nanoparticles using low boiling point perfluorocarbons. *Biomaterials* **33**, 3262–3269 (2012)

Fluorescence, fluidity and function – Probing the microbubble surface

Dario Carugo¹, Richard Browning¹, Paul Rademeyer¹, N. A. Hosny², Erdinc Sezgin³, Jorge Bernadino de la Serna³, Christian Eggeling³, Marina Kuimova² and Eleanor Stride¹

¹*Institute of Biomedical Engineering, University of Oxford, UK*

²*Department of Chemistry, Imperial College London, UK*

³*MRC Human Immunology Unit, Weatherall Institute of Molecular Medicine, University of Oxford, Oxford OX3 9DU, UK*

Characterisation of both the physical and bio-chemical properties of microbubble agents has been the focus of intensive research over the last two decades. Quantifying the relationship between microbubble characteristics, ultrasound exposure conditions and their performance in both diagnostic and therapeutic applications has become increasingly important with the development of techniques such as perfusion mapping, targeted drug delivery and gene therapy. In terms of their clinical utility, it is desirable to maximise the stability of the microbubbles and their circulation time; their echogenicity, in particular their nonlinear response; and their ability to mediate therapeutic effects.

Invaluable insights into microbubble dynamics have been provided by ultra high speed video microscopy. Similarly, electron and scanning confocal microscopy have yielded important findings as to the mechanisms underlying microbubble induced bioeffects. The aim of the work presented in this paper is to utilise quantitative fluorescence microscopy techniques as a complementary approach to investigate the relationship between microbubble characteristics and the nanoscale structure and physical properties of their surface coatings.

Through the use of specifically engineered molecular probes it is possible to determine how the molecular concentration or “packing” of surfactant molecules on the microbubble surface and the resulting membrane potential and viscosity are affected by coating composition and/or the surrounding environment. Results will be presented indicating how these parameters are affected by: (i) varying the components of the microbubble coating, including the addition of functional nanoparticles (ii) the fabrication technique (sonication or microfluidic) and (iii) exposure to ultrasound (Figure 1)¹.

¹ Hosny et al. PNAS 2013 **110**:9225-9230

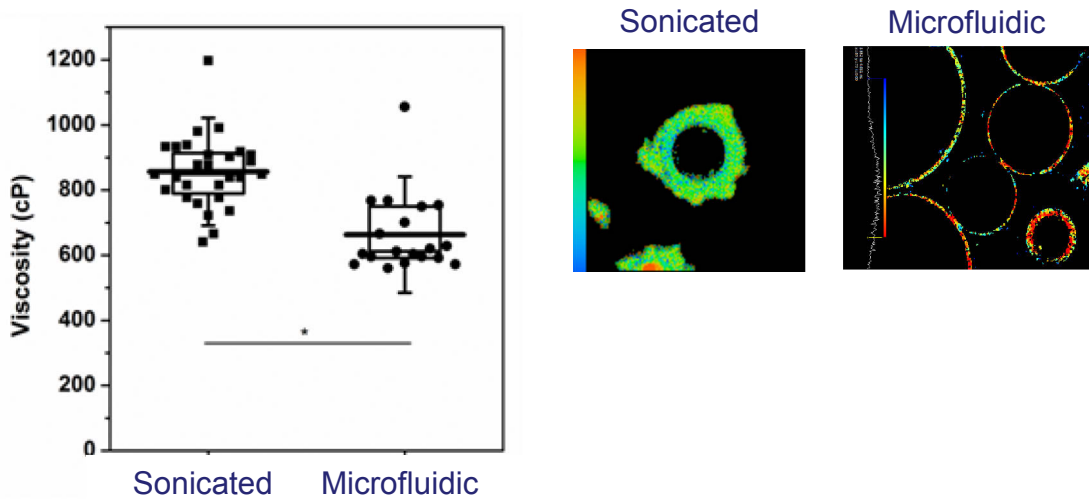


Figure 1: Fluorescence lifetime measurements of surface viscosity from phospholipid microbubbles prepared by sonication and microfluidics (left). Representative images from the experiment (right).

In addition surface homogeneity and the uniformity of surface properties within a bubble population will be examined and the results compared to measurements of microbubble stability and acoustic response. The potential for developing new microbubble compositions and manufacturing methods and/or optimisation of ultrasound exposure conditions to improve microbubble performance and consistency of response will be discussed.

Borrowing from PET: A new approach for targeting ultrasound contrast agents using bioorthogonal chemistry

Aimen Zlitni¹, F. Stuart Foster² and John Valliant¹

¹Department of Chemistry and Chemical Biology, McMaster University, Hamilton Ontario, Canada

²Sunnybrook Health Sciences Centre, and Department of Medical Biophysics, University of Toronto,
Toronto Ontario, Canada

Targeted microbubbles (MB's) enable ultrasound (US) to be used to visualize specific molecular targets. Contrast agents of this nature have traditionally been prepared by linking ligands to the shell of MB's through either covalent ligation or biotin – streptavidin type binding. We describe here a new approach to US molecular imaging that employs covalent and highly selective capture of functionalized MB's *in vitro* and *in vivo* through the use of bioorthogonal chemistry. The results to be presented are unique examples of bioorthogonal capture of MB's and represent the first demonstration of pre-targeting strategies for US molecular imaging. The methodology involves exploiting the rapid and highly selective reaction between tetrazines and transcyclooctene (TCO). A TCO-conjugated antibody is allowed to accumulate at the target of interest and clear from non-targeted organs. Upon subsequent administration, tetrazine functionalized MB's (MBTz) selectively couple with the TCO groups *in vivo*. As a proof of concept, the approach was used to visualize vascular endothelial growth factor receptor 2 (VEGFR2) in comparison to conventional VEGFR2 targeted MB's. MBTz was prepared using a biotinylated derivative of a commercially available tetrazine which was combined with streptavidin coated MB's (MicroMarker Target-Ready contrast agents, VisualSonics). TCO-conjugated antiVEGFR2 was prepared by incubating an excess of commercially available (E)-cyclooct-4-enyl-2,5-dioxopyrrolidin-1-yl carbonate (TCO-NHS) with antiVEGFR2 at 4°C overnight at pH 9-9.5 resulting in an average of 2.7 TCO groups per/antibody. Adhesion of MBTz to VEGFR2(+) tumor cells was evaluated *in vitro* in a parallel plate flow chamber adhesion assay under flow conditions mimicking that found in tumor capillaries. The results showed substantially higher retention of MBTz to VEGFR2(+) cells that were treated with TCO-antiVEGFR2 compared to untreated VEFGR2(+) cells. Through semi-quantitative analysis of the relative areas covered by the MB's over the area covered by the cells, MBTz binding to treated VEGFR2(+) cells was over an order of magnitude higher than the signal obtained in VEGFR2(-) cells. *In vivo* contrast enhanced US images obtained in VEGFR2(+) tumor-bearing mice using MBTz showed a 4 fold greater signal enhancement when mice were treated with TCO-antiVEGFR2 before imaging compared to those who were not treated with antibody. The approach offers the opportunity to use one microbubble construct with any antibody that can be modified with TCO; a procedure which is simple and that employs commercially available reagents.

Conclusion

Our results show the potential of this new MB contrast paradigm to greatly simplify the development of new targeted US contrast agents and facilitate the use of ultrasound in antibody drug development



Thursday, January 22, 2015

Social Event

Brewery "DE PELGRIM"
Aelbrechtsekolk 12 Rotterdam

Tours: between 19.00 and 20.00 hrs
Buffet: around 20.00 hrs

Coaches will be leaving from the Hilton at 18:30 and will be back there around 22:30

Acoustic Cluster Therapy (ACT): a novel concept for targeted drug delivery – In vivo characteristics and proof of principle

***Annemieke van Wamel¹, Andrew Healey², Per Christian Sontum², Svein Kvåle²,
Nigel Bush³, Jeff Bamber³ and Catharina de Lange Davies¹***

¹*Dept. of Physics, NTNU, Trondheim, Norway*

²*Phoenix Solutions AS, Oslo, Norway*

³*Joint Dept. of Physics, ICR, London, UK*

Introduction

Heterogeneity of tumor vasculature often makes it difficult to realize a sufficient level of medical drugs throughout the whole tumor without reaching a toxic overdose for normal tissue. The current paper presents a novel approach to solve this problem: Acoustic Cluster Therapy (ACT) – an acoustically active formulation system comprising microbubble-microdroplet clusters, currently developed by Phoenix Solutions AS (Oslo). ACT is a triple action system designed to facilitate localized: 1) delivery of drugs, 2) increased drug retention time, and 3) improved vascular extravasation and tissue distribution.

The ACT™ concept is based on a formulation system where positively charged, micron sized oil droplets (μd) and negatively charged microbubbles (μb) are mixed to form a dispersion of small, free flowing $\mu b/\mu d$ -clusters. A drug payload may be dissolved in the oil component or, optionally, be co-administrated with a non-loaded cluster dispersion. Upon local exposure using regular diagnostic ultrasound (DUS), the microbubbles transfer acoustic energy to the attached microdroplets and the oil undergoes an instant liquid-to-gas phase shift, releasing its payload. The activated system produces bubbles that expand to approximately 30 μm , transiently blocking the local microvasculature, reducing or pausing blood flow, significantly enhancing local drug retention time at high concentration. Post activation, the deposited bubbles are insonated with low frequency, low MI ultrasound resulting in moderate bubble oscillations that increases local vascular extravasation and tissue distribution. Compared to existing state of the art alternative approaches s.a. regular contrast microbubbles + DUS, the proposed concept offers several unique attributes that may enhance clinical utility significantly:

- High loading capacity; loading a droplet volume vs. a thin stabilizing membrane.
- Deposit properties; trapping the drug within the targeted pathology, avoiding rapid wash out after release.
- The large trapped bubbles guarantee close contact of the bubble with the endothelial wall.

In the current paper we report results that confirm the use of regular diagnostic ultrasound for activation of the μ b/ μ d clusters, and the transient, local deposition of activated bubbles in tumor tissue. Moreover, we show Proof of Principle through significantly improved extravasation and accumulation of co-injected vascular dyes in tumor tissue.

Material & Method

Animals

All experimental animal procedures were in compliance with protocols approved by the Norwegian National Animal Research Authorities. Female Balb/c nude mice (Taconic, Denmark) were purchased at 8-10 wk of age. Animals were anesthetized during all injections and imaging procedures.

Tumor model

50- μ L suspension containing 3×10^6 PC-3 prostate adenocarcinoma cells was slowly injected subcutaneously on the lateral aspect of one hind leg between the hip and the knee. Tumors were allowed to grow for 3–6 wk until the diameter of the tumor was between 5 and 10 mm.

Test items

The ACT compounds investigated were kindly provided by Phoenix Solution AS, Oslo, Norway. A non-loaded μ b/ μ d-clusters formulation without a molecular payload dissolved in the μ d oil phase, for investigations of effects on uptake of co-administered compounds. For comparison studies, Sonazoid contrast agent was used.

In vivo imaging

The cluster dispersion was injected intravenously and activated by local insonation of tumor tissue for 75 seconds using regular diagnostic ultrasound (DUS). For activation a VScan system (GE Healthcare) was used with a center frequency of 2.25 MHz and nominal MI of 0.8 (measured to be approx. 0.45 in the insonated tumor volume). Imaging was performed with a small animal ultrasound imaging system (Vevo2100) at 16 MHz during the activation procedure and continued post activation in Bmode, Linear and Nonlinear Contrast imaging modes.

Evans Blue extravasation assay

Immediately after Evans blue (50 mg/Kg) i.v. injection, the cluster dispersion was injected and activated for 45s with DUS as stated above. After activation, the tumor was exposed to low frequency (500 KHz, 8 cycles, 1kHz p.r.f.) US (LFUS) for 5 minutes. 30 minutes after LFUS treatment, tumor and other tissues were harvested, Evans Blue was extracted as described in by Bekeredjian, R., et al (2007)[1], and samples were analyzed using a spectrophotometer at 620nm. For LFUS, MIs of 0, 0.1, 0.2, 0.4, and 0.8 where tested. The results were compared to control treatment groups; “cluster dispersion + DUS only” and “microbubbles only + DUS/LFUS”.

Infra-red dye 800CW PEG fluorescent contrast agent extravasation assay [2]

Immediately after CW800-PEG (5 pmol/g) i.v. injection, the cluster dispersion was injected and activated for 45s with DUS as stated above. After activation, the tumor was insonated for 5 minutes LFUS at an MI of 0.2. Directly after LFUS treatment and at intervals up to 9h, whole animal Near Infrared Fluorescent (NIF) images where recorded using a Pearl® Impulse whole animal imaging system. The 800CW-PEG accumulation c.q. the signal intensity ratio between the treated tumor leg and control leg was compared between groups; “cluster dispersion, no US”, “cluster dispersion + DUS” and “cluster dispersion + DUS/LFUS”.

Results

Diagnostic ultrasound generated ACT bubbles.

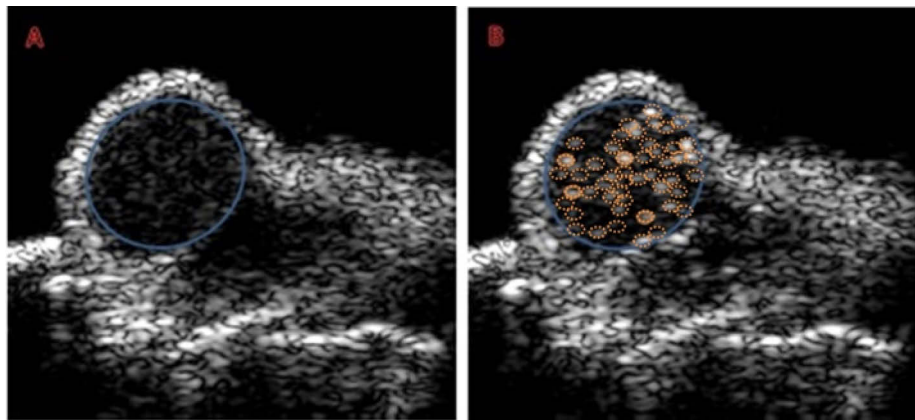


Figure 1: Vevo2100 images of PC3 tumor marked by blue line. A) ultrasound image before diagnostic ultrasound and injection of the μ b/ μ d cluster dispersion. B) ultrasound image after injection of the μ b/ μ d cluster dispersion and 75s diagnostic ultrasound. Large, activated and deposited bubbles are marked by orange circles.

Compared to control groups with “microbubbles only + DUS” or “microdroplets only + DUS”, cluster composition + DUS treated tumors had 8 to 10 times higher echo intensity directly after treatment (fig. 1). Activated and deposited bubbles could be individually observed up to 5 minutes after DUS treatment. No significant differences in tumor perfusion between pre and post activation and bubble deposition could be observed by CEUS. Time intensity curves confirmed deposition of bubbles (fig. 2).

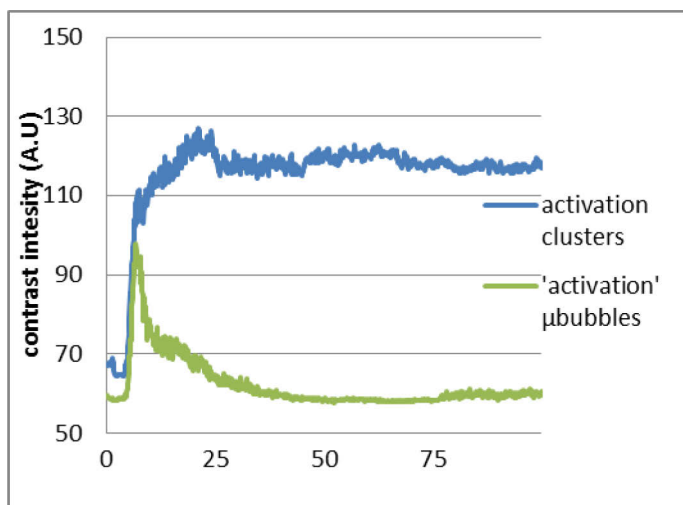


Figure 2: Vevo2100 Time intensity curves of inflow of activated cluster dispersion (blue) and microbubbles (green) into tumor tissue. During the first 25 seconds of DUS medicated activation of the cluster dispersion, an increase of contrast intensity was found after which the signal was constant. In contrast, for DUS medicated activation of the microbubbles only, an increased contrast intensity signal was found during the first 10 seconds after which the signal decreased to background level after 40 seconds.

Evans blue accumulation

Compared to cluster dispersion activation with no additional LFUS treatment, applying 45s DUS followed by 5 minutes LFUS using an MI of 0.1 and 0.2 increased Evans Blue accumulation in tumor tissue by 53% and 61%, respectively. No significant differences in Evans Blue accumulation were found between the different treatments in heart, liver, or control muscle tissues. We found no significant enhancement of Evans Blue accumulation in tumors treated with microbubbles only after insonation for 5'45'' with DUS.

Infra-red dye 800CW PEG fluorescent contrast agent accumulation

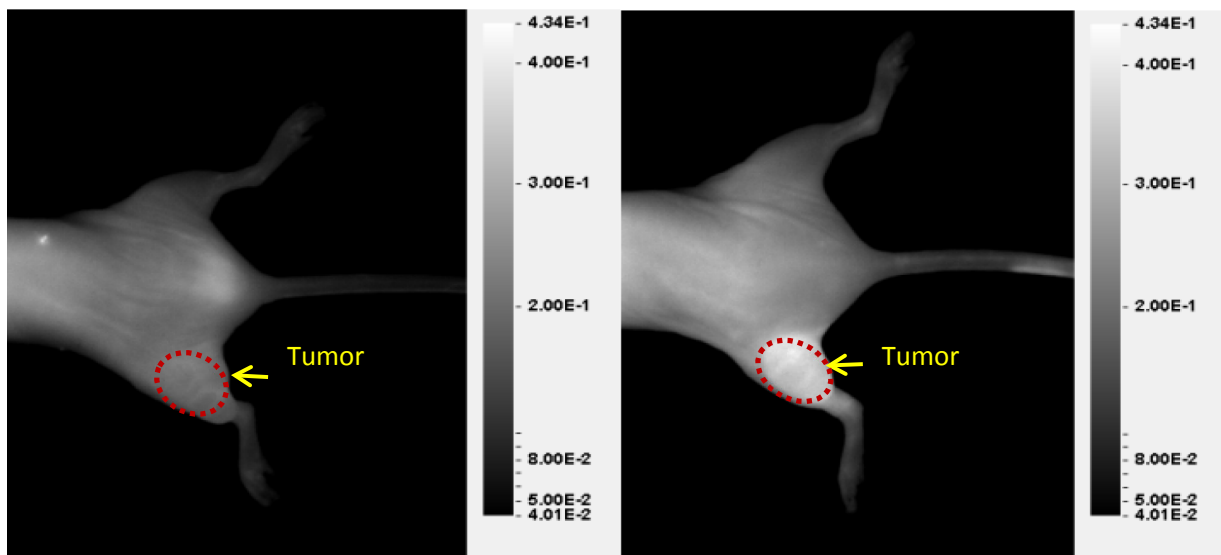


Figure 3: 800CW-PEG accumulation 1 hour after treatment. Typical NIF images of animals receiving 800CW-PEG, with no additional treatment (left) and animals receiving 800CW-PEG + cluster composition + DUS/LFUS (right).

Directly after treatment with “cluster composition + DUS” and “cluster composition + DUS/LFUS”, and up to 9 hours after treatment, 800CW-PEG accumulation was significantly higher ($p<0.01$) compared to “cluster composition without US” treatment tumors. 1 hour after treatment, the tumor-to-control leg ratio was 1.10 (± 0.15) and 1.65 (± 0.13) for the untreated and treated tumor, respectively (fig. 3). After 9 hours still a significant difference ($P<0.004$) was found with ratio values of 1.5 (± 0.05) for untreated and 1.8 (± 0.10) for the treated tumors. For tumors treated with “cluster composition + DUS only” (no LFUS) this ratio was 1.3 (± 0.04) and 1.7 (± 0.23) for 1 and 9 hours, respectively.

Conclusion

In this study, we have demonstrated Proof of Principle for the ACT concept in a relevant pre-clinical tumor model. We have shown transient deposition of large bubbles in tumor tissue after activation of $\mu b/\mu d$ clusters using regular diagnostic US. Furthermore, we showed that deposition and low MI insonation of activated bubbles results in a significant increase in local accumulation of a co-administered vascular agent, and that a molecular payload incorporated into the formulation is locally released and taken up in targeted tissue. As a general platform for targeted delivery of drugs the ACT concept offers a number of unique attributes which may enhance therapeutic efficacy significantly. Studies to demonstrate this are under way.

References

1. Bekeredjian, R., et al., Ultrasound targeted microbubble destruction increases capillary permeability in hepatomas. *Ultrasound Med Biol*, 2007. **33**(10): p. 1592-8
2. Billaud, M., et al., A new method for *in vivo* visualization of vessel remodeling using a near-infrared dye. *Microcirculation*, 2011. **18**(3): p. 163-71.

3D Contrast-enhanced ultrasound (CEUS) imaging of carotid artery plaques and intra-plaque angiogenesis

Venu Gourineni, Sandeep Saha, David M Mills, Kirk D Wallace, Boris M Shur, Aaron M Dentinger, Vijaya Reddy, Dirk R Padfield, Frank Yamout, Adele Liuzzo, Chad Jacobs, Robert March, Walter McCarthy, Kunlin Cao, Jing Jin, Dan Adam, Marshall Goldin and Steven Feinstein

Introduction

Vulnerable plaque is marked by increased intra-plaque vascularity, hemorrhage and is associated with cerebrovascular (CV) events. Current use of 2D CEUS carotid imaging does not provide a true volumetric representation of the intra-plaque angiogenesis. Therefore, this is the first clinical trial using 3D CEUS to assess intra- plaque angiogenesis, in patients with clinically significant plaques prior to carotid endarterectomy (CEA).

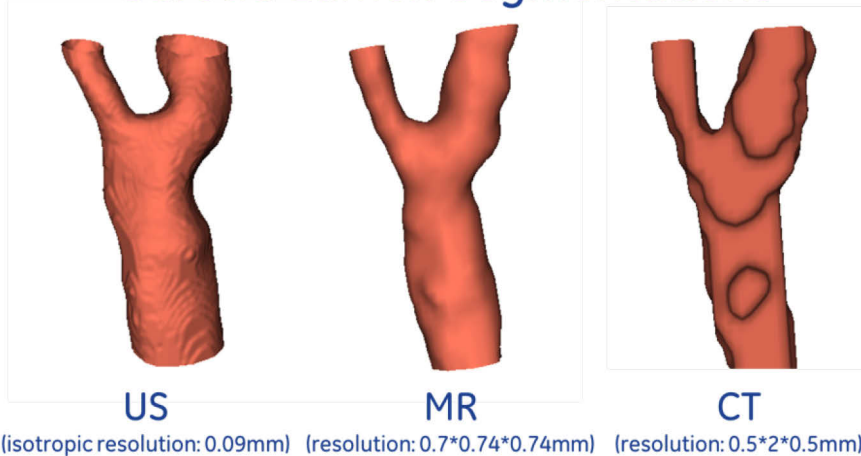
Methods

Data were acquired on 11 patients that were asked to participate in this pilot study prior to CEA. All patients had MR and/or CT angiogram as part of their standard care and all carotid artery plaque specimens were collected and sent for histologic evaluation. CEUS volumes were acquired using a GE LOGIQ E9, RSP6-16 4D probe and Optison. In order to assess plaque vulnerability, semi-automatic image analysis algorithms were developed to segment the lumen, plaque, and intra-plaque vascularity. Measurements derived from 3D CEUS images were validated against CT, MR, and histology.

Results

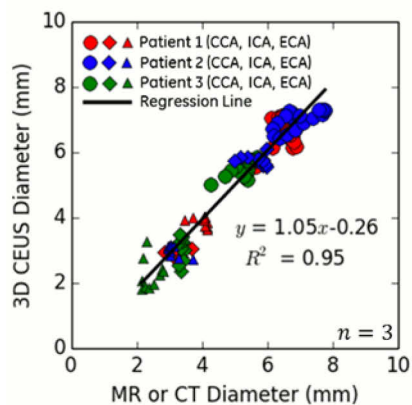
Preliminary results from 3 patients were analyzed and lumen volumes were segmented from all available modalities (figure shows CEUS example). Lumen measurements of the CCA, ICA, and ECA from 3D CEUS were compared to MR or CT. High correlation is shown in the figure for these patients ($R^2=0.95$). Further analysis of the 3D CEUS images demonstrates that we can identify intra-plaque vascularity (see segmentation from one patient). Initial results from CEUS showed 7-11% vascular density within the plaque and histology showed 10% from a single slice.

Carotid Lumen Segmentations

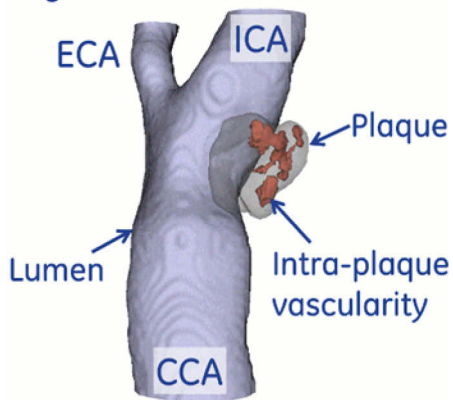


(isotropic resolution: 0.09mm) (resolution: 0.7*0.74*0.74mm) (resolution: 0.5*2*0.5mm)

Correlation of 3D CEUS w/ MR or CT



Segmentation from 3D CEUS



Conclusion

These results demonstrate that it is feasible to use 3D CEUS for quantitative, volumetric imaging of the carotid artery and intra-plaque angiogenesis in patients scheduled for CEA. Future work will extend this analysis to all patients and make a quantitative comparison of intra-plaque vascular density from 3D CEUS vs. multiple histology slices.

Ultrasound and contrast-enhanced ultrasound imaging of mammary gland lesions in companion animals

K. Vanderperren¹, E. Stock¹, H. Haers¹, E. Van der Vekens¹, M. De Ridder², N. Sanders³, H. de Rooster², JH Saunders¹

¹ Department of Veterinary Medical Imaging and Small Animal Orthopaedics, Faculty of Veterinary Medicine, Ghent University, Merelbeke, Belgium

² Department of Medicine and Clinical Biology of Small Animals, Faculty of Veterinary Medicine, Ghent University, Merelbeke, Belgium

³ Laboratory for Gene Therapy, Faculty of Veterinary Medicine, Ghent University, Merelbeke, Belgium

Introduction & aim

Abnormalities of the mammary gland include neoplasia, cysts, inflammation and/or infection.¹ Mammary gland tumours are very common in dogs and constitute more than half of all tumours that affect bitches.^{2,3} Approximately 50% of the canine mammary tumours are malignant,² whereas most feline mammary tumours are malignant.⁴ It is essential to distinguish the type and stage of the tumour as they influence treatment and prognosis.⁵

Ultrasonography (US) has been used to assess the tissue composition and vascularity of canine mammary tumours.⁶ B-mode US characteristics such as heterogeneity of the tumoral tissue, irregular surface border, unclear margins and calcifications may indicate malignancy.^{7,8} However, benign and malignant mammary tumours cannot be differentiated based on their B-mode US appearance. Similarly, no correlation was found to differentiate between benign and malignant mammary gland tumours based on the presence of vascularization and its characteristics.⁸

Contrast-enhanced ultrasound (CEUS), using microbubble contrast agents, has recently been proposed as a new imaging modality to quantify tissue perfusion.⁹ It uses tiny, gas-filled microbubbles, stabilized by an outer shell, that are injected intravenously. Microbubbles remain strictly intravascular, with no interstitial diffusion or urine excretion.⁹ Therefore, they can be viewed as blood pool markers enabling functional vascular imaging.

The objective of this study was to describe the contrast-enhanced ultrasonographic appearance of various canine mammary gland lesions and whether CEUS can aid in distinguishing between benign and malignant lesions.

Material and Methods

Thirteen bitches of various breeds and 1 cat with mammary gland lesions were examined. Average age was 10 years and the dogs weighed between 2.5 and 78 kg with a mean weight of 26 kg. All patients underwent B-mode US, CEUS and surgical removal of the mammary gland lesions. A final diagnosis was obtained by histopathology.

Ultrasonography was performed using a linear 17-5 or 12-5 MHz transducer. Contrast-enhanced US was performed using a linear transducer of 12-5 MHz on a dedicated machine (Philips iU22 xMATRIX, Philips Medical systems, Bothell, Washington, USA) with contrast-specific software. Microbubble contrast agent SonoVue® (Bracco, Milan, Italy) was injected three to four times (depending on the amount of mammary gland lesions) intravenously as a 0.4 ml/10kg bolus followed by 2-4 ml of sterile saline flush (NaCl 0.9%). Two-minute digital video clips of the enhancement of the mammary lesions were obtained. The first injection with Sonovue® was not used for further evaluation.

The following parameters were evaluated on B-mode images: tumour margin (sharp/unsharp, smooth/irregular), echogenicity, and calcifications (presence or absence). The resulting CEUS images were reviewed subjectively during the early arterial and late parenchymal phase. The following characteristics were evaluated on CEUS images: contrast enhancement (absent, homogeneous or heterogeneous), flow pattern (central, peripheral or mixed central/peripheral), and focal defects (presence or absence).

Results

In total, 24 mammary gland lesions were diagnosed in 13 dogs and 1 cat. The histopathological diagnosis was benign in 14 mammary gland lesions (6 cysts, 1 inflammation, 3 simple adenomas, 2 complex adenomas, 2 nodular hyperplasia) and malignant in the remaining 10 mammary gland lesions (6 adenocarcinomas (grade I= 3; grade III= 3); 1 complex adenocarcinoma; 1 cystadenocarcinoma; 2 inflammatory carcinomas). On B-mode US, substantial overlap was present between the US features of benign versus malignant lesions. Twelve of the benign mammary gland lesions showed sharp margins, 2 unsharp margins, 10 smooth borders and 4 irregular borders. Of the malignant tumours, all 10 showed sharp margins, 6 smooth borders and 4 irregular borders. The parenchymal echotexture of 7 benign lesions and 2 malignant tumours was homogeneous, while 7 benign and 8 malignant lesions showed heterogeneous parenchymal echotexture. Calcifications were present in 5 malignant lesions and in 3 benign lesions.

With CEUS, all (adeno)carcinomas and adenomas were well-vascularized and showed heterogeneous contrast enhancement. However, a difference in flow pattern could be observed between these two entities. All (adeno)carcinomas had peripheral flow during the arterial phase. In 6 (adeno)carcinomas, the contrast went slightly centripetally in the parenchymal phase without reaching the center of the lesion (Figure 1); whereas the cystic adenocarcinoma showed a fast complete centripetal fill-in with the presence of a non-enhancing area representing a cystic lesion. Three adenocarcinomas only showed circumscribed peripheral flow during both phases. Contrary, the adenomas showed mixed central and peripheral flow pattern during both arterial and parenchymal contrast phases (Figure 2). Four

adenocarcinomas and all adenomas also showed focal non-enhanced defects. Tortuous vessels were detected in 4 adenocarcinomas and in 2 adenomas.

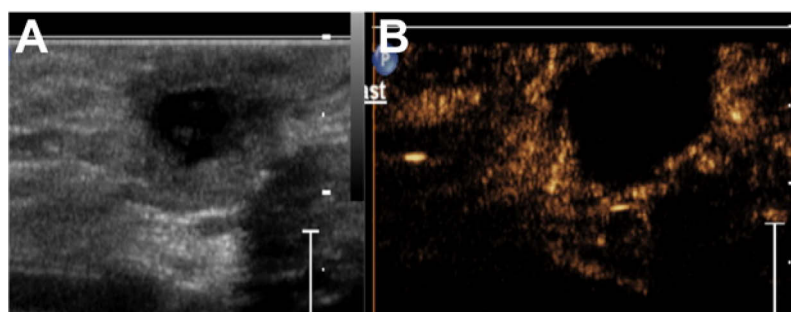


Figure 1: US image (A) en corresponding CEUS image (B) of an adenocarcinoma grade III.

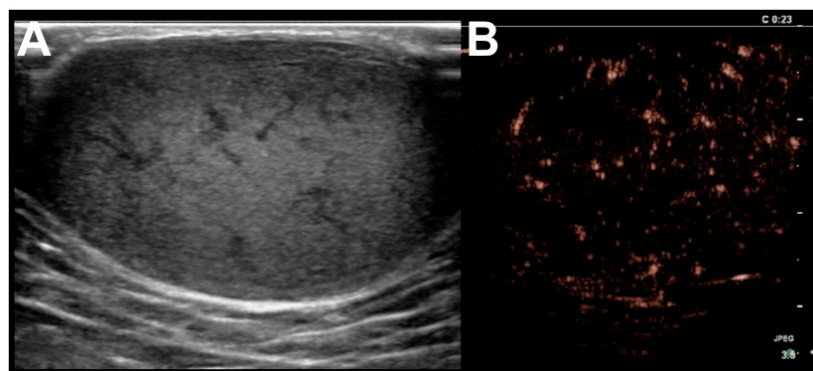


Figure 2: US image (A) en corresponding CEUS image (B) of an adenoma.

With CEUS, the benign cysts were characterized by a non-enhancing lesion with a ring sign (flow surrounding the lesions border) (Figure 3). Similarly, nodular hyperplasia did not show any contrast enhancement. The inflammatory lesion appeared as increased enhancement of the normal mammary gland tissue showing a homogeneous mixed central and peripheral enhancement.

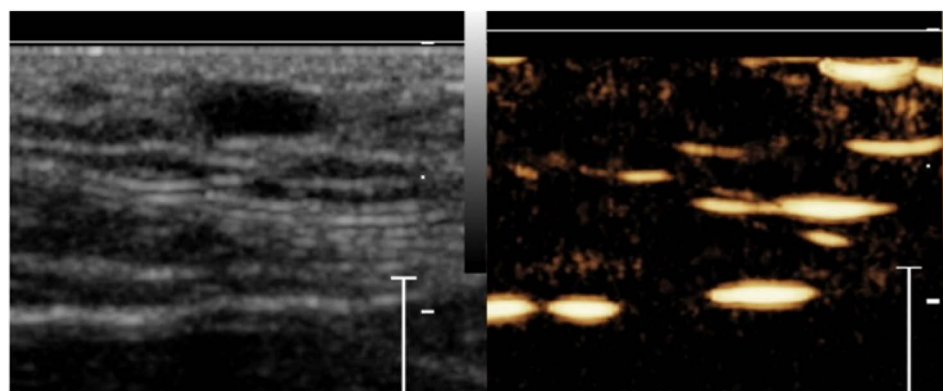


Figure 3: US image (A) en corresponding CEUS image (B) of a cyst (+).

Conclusions

Benign and malignant mammary gland lesions were nonspecific and could not be differentiated based on their B-mode US appearance, which was in agreement with the literature.⁶ During CEUS, histologically confirmed benign and malignant lesions showed different contrast enhancement and flow patterns. Therefore, CEUS could have potential as diagnostic tool for the differentiation between benign and malignant lesions. Future work is necessary to establish the role of CEUS in the assessment of mammary gland lesions.

References

1. Hecht S: *Female reproductive tract*. Pennick D and d'Anjou MA (ed): *Atlas of Small Animal Ultrasonography*, Wiley-Blackwell, 2008; 397-416
2. Queiroga F, Lopes C: *Canine mammary tumors – new perspectives*. Annals of Congress of Veterinary Science, Oeiras, Brazil 2002; 183-190
3. Moe L: *Population-based incidence of mammary tumors in some dog breeds*. J Reprod Fertil-Suppl 2001; 57: 439-443
4. Viste JR, Myers SL, Singh B, Simko E: *Feline mammary adenocarcinoma: tumor size as a prognostic indicator*. Can Vet J 2002; 43(1): 33-37
5. Cassali GD, Lavalle GE, De Nardi, AB et al: *Consensus for the Diagnosis, Prognosis and Treatment of Canine Mammary Tumors*. Braz J Vet Pathol 2011; 4(2): 153-180
6. Nyman HT, Nielsen OL, McEvoy FJ, et al: *Comparison of B-mode and Doppler ultrasonographic findings with histologic features of benign and malignant mammary tumors in dogs*. Am J Vet Res 2006; 67(6): 985-991
7. Paulinelli RR, Vidal CS, Ruiz AN, et al: *Prospective study of the ultrasound features in the diagnosis of solid breast lesions*. Revista Brasileira de Ginecologia e Obstetrícia 2002; 24: 195-199
8. Feliciano MAR, Vicente WRR, Silva MAM: *Conventional and Doppler ultrasound for the differentiation of benign and malignant canine mammary tumours*. J Small Anim Pract 2012; 53: 332-337.
9. Haers H, Saunders JH: *Review of clinical characteristics and applications of contrast-enhanced ultrasonography in dogs*. J Am Vet Med Assoc 2009; 234 (4): 460-470.

Ultrasound and microbubble mediated drug delivery: Real-time imaging of co-administration vs drug loaded microbubbles

De Cock I., De Smedt S., Lentacker I.

Laboratory for General Biochemistry and Physical Pharmacy, Ghent University, Ghent, Belgium

Introduction

In ultrasound mediated drug delivery, drugs are usually co-administered with the microbubbles. More recently, novel approaches to load microbubbles with drugs are being explored. For example, gene nanoparticles can be attached to the microbubble surface, leading to successful gene transfection [1]. However, it remains unclear how exactly transfection is achieved. Previously, we have shown that co-administration of microbubbles and dextrans can enhance dextran delivery across the cell membrane by creating aspecific pores or by stimulating endocytic uptake [2]. Moreover, acoustic pressure played a major role in which uptake mechanism was involved. We wanted to investigate if the same mechanisms apply when large nanoparticles are used and when they are loaded onto the microbubble surface. Therefore, we studied how nanoparticles enter cells when they are co-administered with or loaded onto microbubbles via real-time confocal imaging during ultrasound exposure.

Methods

BLM cells were labeled red with CellMask® Deep Red Plasma membrane Stain. Green fluorescent polystyrene beads of 100 nm were used as a model for gene nanoparticles. The beads were co-administered with red fluorescent lipid shelled microbubbles or attached to the microbubble surface via biotin-avidin bridging. By mounting the ultrasound setup on a swept field confocal microscope, release of beads from loaded microbubbles and microbubble-cell interactions could be imaged in real-time at a relatively high frame rate (24 fps). The following acoustic parameters were used: centre frequency 1 MHz, pulse length 1000 cycles, PRF 100 Hz, exposure time 5 sec and acoustic pressure from 100 to 300 kPa.

Results

In case of co-administration, the beads close to microbubbles were transported along with the microstreamings created by microbubble cavitation. These microstreamings consist of vortical flow structures surrounding the microbubble [3] (Figure 1A). Figure 1B displays the trajectory of beads in these microstreamings, as analysed by ImageJ. The dotted line represents the cell border, while the full line indicates a microbubble cluster. The trajectories (indicated by the arrows) show that the beads are moving away from the cell. We could not detect transport towards the cell, although this movement

might be out of focus. As a consequence of the microstreamings, the contact between the beads and the cell membrane is too short to stimulate endocytosis. In addition, the chance that the large beads (100 nm) can enter the cell through a pore is smaller when they are transported at the relatively high speed of the microstreamings. When beads were loaded on microbubbles, beads moved over the microbubble surface without being released at low acoustic pressures. At higher acoustic pressures the beads were released and deposited on the cell membrane. Figure 2 shows an example of this bead deposition. The green fluorescent beads are attached to the red fluorescent labeled microbubble surface. The cell borders are indicated by the dotted line. When the microbubble (indicated with the arrow) is exposed to ultrasound, it enters the cell, while releasing and depositing the beads on the cell membrane.

Conclusion

Co-administration of microbubbles and drugs is less favorable, especially for larger molecules such as gene nanoparticles, since they are transported in the fast moving microstreamings. Microbubbles loaded with gene complexes can deposit the cargo immediately on the cell membrane, although higher pressures are needed to induce release.

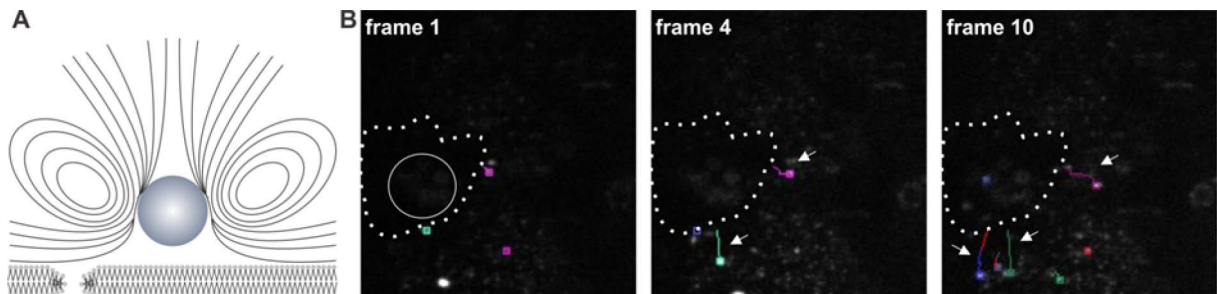


Figure 1: (A) Schematic representation of microstreamings created by microbubble cavitation. (B) The beads co-administered with microbubbles are transported along with these microstreamings. The trajectories of the beads are indicated with the arrows. A microbubble cluster is encircled, while the cell border is marked with the dotted line. Images were acquired at a frame rate of 24 fps.

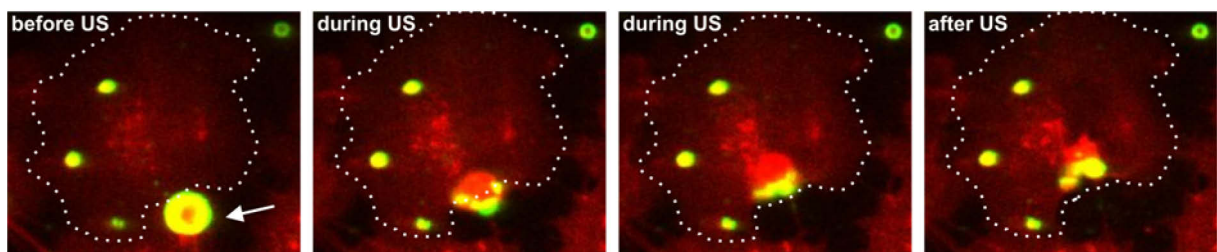


Figure 2: Upon ultrasound exposure, the microbubble indicated with the arrow penetrates the cell (marked with the dotted line), while releasing the green fluorescent beads and depositing them directly on the cell membrane.

References

1. De Temmerman et al. (2011). *Biomaterials*, 32, 9128-9135
2. De Cock et al. (2015). *J. Control. Release*, 197, 20-28
3. Luan et al. (2014). *Ultrasound in Med. & Biol.*, 40, 1834-1846

Poly-D,L-lactide-co-glycoside-perfluorocarbon nanoparticles for long-term ultrasound imaging

**Olga Koshkina, Edyta Swider, Eric van Dinter, Carl Figdor, I. Jolanda M. de Vries,
Mangala Srinivas**

Radboud University Medical Center (RadboudUMC), Department of Tumor Immunology,
Radboud Institute for Molecular Life Sciences (RIMLS), 6500HB Nijmegen, The Netherlands

Dendritic cell (DC) therapy has great promise in the treatment of cancer. One of the main advantages of this method is that it uses body's own immune system for treatment. Long-term tracking and the quantification of DCs, or other therapeutic cells, *in vivo* is essential to effectively optimize such therapy. Cell tracking with ultrasound is especially attractive, as it is already widely used. However, most currently available contrast agents, are not sufficiently stable over time and therefore not suitable for long-term cell tracking.

Here we present multifunctional poly-d,l-lactide-*co*-glycoside (PLGA) and perfluorocarbon (PFC)-based nanoparticles, which can be tracked with ultrasound for at least several days [1-3].

We prepared the nanoparticles, which are 200 nm in diameter, by ultrasonication-solvent-evaporation method using PLGA and different perfluorocarbons. Aiming at the production of multimodal imaging agents, additional components, e.g. fluorescent dyes, can be incorporated during the formulation process. To obtain general information on the properties of the particles, we characterized the particles by electron microscopy, dynamic light scattering, X-ray scattering, fluorescence spectroscopy and calorimetric methods. Furthermore, we quantified the amount of encapsulated PFC by ¹⁹F NMR. These results indicate that the interior structure of our contrast agents is fully different from the structure of microbubbles or nanodroplets. In particular, no gaseous or vaporizing component appears to be present. To prove the ultrasound performance of our agents, we carried out high resolution ultrasound *in vitro* and *in vivo*, using particles or labeled DCs for injections *in vivo*. The results of ultrasound imaging were confirmed by ¹⁹F MRI and fluorescence microscopy revealing the colocalization of all three labels.

We are now studying the impact of different synthesis parameters on the structure and function of these imaging agents. Our results indicate that the combination of PLGA and PFC can result in particles with unique structure and properties. We expect PLGA-PFC particles to go into clinical testing shortly.

References

1. M. Srinivas, L. J. Cruz, F. Bonetto, A. Heerschap, C. G. Figdor, I. J. de Vries, *Biomaterials* 2010, 31, 7070-77
2. L. J. Cruz, P. J. Tacken, R. Fokkink, B. Joosten, M. Cohen Stuart, F. Albericio, R. Torensma, C. G. Figdor, *Journal of Controlled Release* 2010, 144 118–126
3. M. Srinivas, I. J. de Vries, J. L. Cruz, C. G. Figdor. *Contrast agents for imaging (pending patent application, filed Sep. 14, 2012). Application Number 12184562.2-1216*

Insulin-induced capillary recruitment in skeletal muscle is impaired in overweight individuals and associated with whole body insulin sensitivity

Y.H.A.M. Kusters^{1,2,3}, C.G. Schalkwijk^{1,2,3}, A.J.H.M. Houben^{1,2}, J. Op 't Roodt^{1,3}, P.J. Joris^{3,4,5}, R.P. Mensink^{3,4,5}, C.D.A. Stehouwer^{1,2}

¹*Department of Internal Medicine, Maastricht University Medical Center, PO Box 616, 6200 MD, Maastricht*

²*Cardiovascular Research Institute Maastricht (CARIM), PO Box 616, 6200 MD, Maastricht*

³*Top Institute Food and Nutrition, PO Box 557, 6700 AN, Wageningen*

⁴*Department of Human Biology, Maastricht University Medical Center, PO Box 616, 6200 MD, Maastricht*

⁵*School for Nutrition, Toxicology and Metabolism (NUTRIM), PO Box 616, 6200 MD, Maastricht*

Objectives

Obesity is increasingly prevalent and is associated with insulin resistance and an increased risk for the development of type 2 diabetes and cardiovascular diseases. An important effect of insulin is its ability to increase the number of perfused capillaries in skeletal muscle, thereby enhancing its own delivery, and that of glucose, to myocytes. It has been suggested that the insulin-induced increase in perfused capillaries is an important driving factor in whole body insulin sensitivity. Therefore, we investigated whether insulin-induced capillary recruitment is impaired in overweight individuals as compared to lean individuals and whether capillary recruitment is associated with whole body insulin sensitivity.

Methods

During a hyperinsulinaemic, euglycaemic clamp we measured whole body insulin sensitivity by means of glucose infusion rate (GIR), and examined the effects of insulin on capillary recruitment in forearm skeletal muscle in 25 lean (defined as waist circumference < 94 cm) men and 53 overweight (defined as waist circumference between 102 and 110 cm) men. Individuals were non-diabetic, non-smokers, free of cardiovascular disease, aged between 18 and 65 years, and did not use medication influencing vascular or metabolic measurements. Using contrast-enhanced ultrasound (SonoVue, Bracco, The Netherlands) in a fasted and hyperinsulinaemic state, we determined the insulin-induced capillary recruitment by means of change in microvascular blood volume (ΔMBV).

Results

Lean men had a mean age of 47.0 ± 17.7 years and mean body mass index (BMI) of $23.3 \pm 1.8 \text{ kg/m}^2$ compared to 50.1 ± 12.8 years and $30.0 \pm 2.1 \text{ kg/m}^2$ in overweight men. Mean insulin sensitivity (GIR) was substantially reduced in overweight individuals as compared to lean individuals (4.05 ± 1.31 vs. $6.76 \pm 1.79 \text{ mg/kg/min}$; $p < 0.001$). Body mass index was inversely correlated to GIR ($r = -0.587$, $p <$

0.001). In lean individuals, insulin increased microvascular blood volume by $48.3 \pm 71.8\%$, compared to $-3.3 \pm 28.0\%$ ($p < 0.01$) in overweight individuals. Moreover, ΔMBV was correlated with GIR ($r = 0.429$, $p < 0.001$).

Conclusions

Insulin-induced capillary recruitment in forearm skeletal muscle is impaired in overweight individuals and is associated with whole body insulin sensitivity. These findings support the hypothesis that insulin-induced capillary recruitment is impaired in obesity and contributes to whole body insulin resistance.

Ultrasound-triggered drug delivery: Tumor therapy in a murine colon adenocarcinoma model by insonation of doxorubicin-liposome-microbubble complexes in the tumor vasculature

Alexander L. Klibanov, Zhongmin Du, Galina B. Diakova

*University of Virginia Cardiovascular Division, Robert M. Berne Cardiovascular Research Center,
PO Box 801394, Charlottesville VA 22908 USA*

Introduction

Triggered release of drugs from carrier systems *in vivo* is widely investigated for targeted tumor therapy. During the past decade, an ultrasound-sensitive liposome-microbubble pendant drug carrier system has been developed: microbubbles, decorated with liposomes that carry e.g., doxorubicin, have been shown to release the drug in response to insonation. However, due to low drug load, those pendant particles were only successful for suppressing tumor cell growth *in vitro*, in cell culture models. In this study, we were able to prepare particles with high doxorubicin load, using liposomes larger than the standard 80 nm Doxil/Caelyx formulation, and achieved successful inhibition of tumor growth in a subcutaneous murine tumor model.

Methods

Decafluorobutane microbubbles were stabilized with a shell consisting of DSPC, PEG stearate and biotin-PEG-DSPE (20:20:1 mass ratio). Liposomes carrying ammonium citrate were prepared from DOPC, cholesterol and biotin-amidocaproyl-DSPE; liposomes were purified from external ammonium citrate by repeated centrifugation. Remote loading of citrate-containing liposomes with doxorubicin from external HEPES buffer was performed at elevated temperatures, to achieve efficient drug entrapment inside the liposome inner aqueous core. Streptavidin linker was used to affix biotinylated liposomes onto the surface of biotinylated microbubbles, with pendant complex formation.

C57BL/6 mice were injected subcutaneously in the hind leg with MC38 colon carcinoma cells (a generous gift of J. Schlom, NIH); therapy has been initiated when tumors have reached 4-5 mm size. Doxorubicin-liposome-microbubble complexes were injected intravenously (doxorubicin dosage 6 mg/kg); all animal studies were performed under isoflurane inhalation anesthesia, on a warm pad to maintain animal body temperature. Contrast ultrasound imaging with Sequoia 512 (15L8 probe, nondestructive CPS imaging, 7 MHz, MI 0.2) was used to monitor the particles in the tumor vasculature. Therapeutic ultrasound treatment with Birtcher Megason physical therapy apparatus transducer pointed at the tumor was initiated immediately after complex injection and performed for 10

min (0.6 W/cm², 1 MHz continuous sine wave applied repeatedly, for 3 s with 10 s intervals between ultrasound pulses to ensure replenishment of drug complexes in the vasculature).

Results and Conclusions

Doxorubicin-liposome-microbubble complexes have been prepared. These pendant particles demonstrated excellent drug load (>1 pg doxorubicin per complex, an order of magnitude higher than what had been demonstrated earlier with Doxil or Doxil-like liposome-based complexes). Thus, administering 6 mg/kg doxorubicin became feasible. Treatments were performed repeatedly, three times a week, for the course of two weeks; ultrasound imaging confirmed tumor perfusion with drug carrier microbubbles. Mice demonstrated normal behavior during the course of the treatment; serious side effects were not observed. Following doxorubicin-liposome-microbubble pendant complex particle administration combined with insonation, significant suppression of tumor growth was achieved, as compared with control untreated animals ($p<0.05$). Some of the tumors have reduced size in response to the combination of ultrasound and drug-microbubble administration. Untreated control animals, as well as mice repeatedly injected with doxorubicin-liposome microbubble complexes but not subjected to ultrasound treatments, have all demonstrated rapid tumor growth over the course of the study. Fluorescence microscopy of frozen tissue sections confirmed enhanced doxorubicin deposition in the tumor in response to ultrasound treatment.

In conclusion, repeated administrations of doxorubicin-liposome-microbubble pendant particles combined with ultrasound treatments of the tumor under ultrasound imaging guidance resulted in a significant suppression of tumor growth in a subcutaneous murine tumor model.

Acknowledgements / Funding Sources:

This study was supported in part via NIH R21/33 CA102880 and R21 EB016752.

Correlating sonoporation dynamics to reversible and irreversible sonoporation

*Ilya Skachkov¹, Tom J.A. Kokhuis^{1, 2}, Tom van Rooij¹, Ying Luan¹,
Antonius F.W. van der Steen^{1, 3}, Nico de Jong^{1, 3}, Klazina Kooiman¹*

¹*Dept. of Biomedical Engineering, Thoraxcenter, Erasmus MC, Rotterdam, the Netherlands*

²*Interuniversity Cardiology Institute of the Netherlands, Utrecht, the Netherlands*

³*Laboratory of Acoustical Wavefield Imaging, Faculty of Applied Sciences, Technical University Delft, Delft, the Netherlands*

Background

Vibrating microbubbles (MB) can increase cell membrane permeability, also known as sonoporation, which can be exploited for therapy. Sonoporation can be either reversible or irreversible. When irreversible, it causes severe cell damage and death. When reversible, the created pore will close and as a consequence drug uptake will stop [1]. Different therapeutic approaches may require different grades of sonoporation and there may be a balance between effectiveness and cell damage. The aim of this study was to investigate how targeted MB (tMB) and non-targeted MB (ntMB) effect cell membrane permeability at different ultrasound (US) settings. We investigated sonoporation real-time by studying propidium iodide (PI) uptake dynamics.

Methods

Human umbilical vein endothelial cells (HUVECs) were cultured in OptiCells as previously described [2]. Lipid-coated MB were made by sonication [2, 3]. For tMB, CD31 antibody was conjugated to the MBs [2]. MB were added 5 min prior to sonication at a ratio of 4 MB per cell. Sonoporation dynamics were studied at 150, 300, and 500 kPa peak negative acoustic pressure (P_A ; n=3). A 1 MHz single pulse was applied with varying amount of cycles (500, 1,000; 2,000; 5,000; 10,000; 20,000; and 50,000 cycles). PI was used to assess cell membrane permeability and PI uptake was studied for up to 3 min after insonification (at 5 sec intervals) with an AxioCam MRC camera (Carl Zeiss). For every field of view (FOV), the fluorescence intensity changes in every cell were analyzed using ImageJ [4] (~2500 cells per FOV). The data were analyzed in two ways: 1) the time it took for the fluorescence intensity to reach 90% of its maximum, and 2) the fluorescence intensity change was fitted to the model of Fan et al [5] that describes the diffusion through re-sealable pores:

$$F(t) = \alpha \cdot \pi D C_0 \cdot r_o \cdot \frac{1}{\beta} (1 - e^{-\beta t}) \quad \text{Equation 1}$$

where $F(t)$ is the experimentally measured fluorescence intensity per cell over time, α is the coefficient that relates the amount of PI molecules with PI-RNA and PI-DNA fluorescence intensity measured by

the microscopic imaging system used in the experiments, D is the diffusion coefficient of PI, C_0 is the extracellular concentration of PI, r_0 is the radius of the pore, β is the resealing constant of the pore, and t is time. Cell viability was assessed 1 hour after ultrasound treatment by adding Calcein-AM 30 min after treatment.

Results

Depending on the applied pressure and the amount of cycles, we observed a sonoporation efficiency ranging from $0.15 \pm 0.04\%$ (150 kPa, 500 cycles, tMB) to $44.9 \pm 13.4\%$ (500 kPa, 50.000 cycles, ntMB). As shown in Fig. 1A for 500 kPa, 50,000 cycles, and ntMB, the maximum fluorescence intensity in the nucleus varied a factor of 140 amongst cells. The time to reach 90% of maximum intensity also varied between cells: from 5 seconds to 3 minutes. The same data were also fitted to Eq. 1. Two sonoporated cell populations could be identified, illustrated by the red and blue dots in Fig. 1B. The red dots illustrate the group that has large pore sizes in combination with a low ability for pore resealing (i.e. low pore resealing coefficient), whilst the blue group contains cells with smaller pore size coefficients and high pore resealing coefficient (blue dots). For each acoustic setting, the amount of “red” and “blue” cells in the population is plotted in Fig. 2A for ntMB at 500 kPa. With increasing P_A , the amount of blue cells reached a plateau, whereas the amount of red cells kept increasing. Interestingly, the amount of red cells correlated well with the amount of dead cells as shown in Fig. 2B. For 300 kPa and ntMB, the same trend was observed, accept that the plateau for the blue cells was already reached at 5,000 cycles. No difference between red and blue cells for ntMB could be distinguished at 150 kPa for all studied cycles. Also, no plateau was reached. The only difference between ntMB and tMB is that the plateau for the blue cells was reached at higher cycles, namely 20,000 for both 300 kPa and 500 kPa.

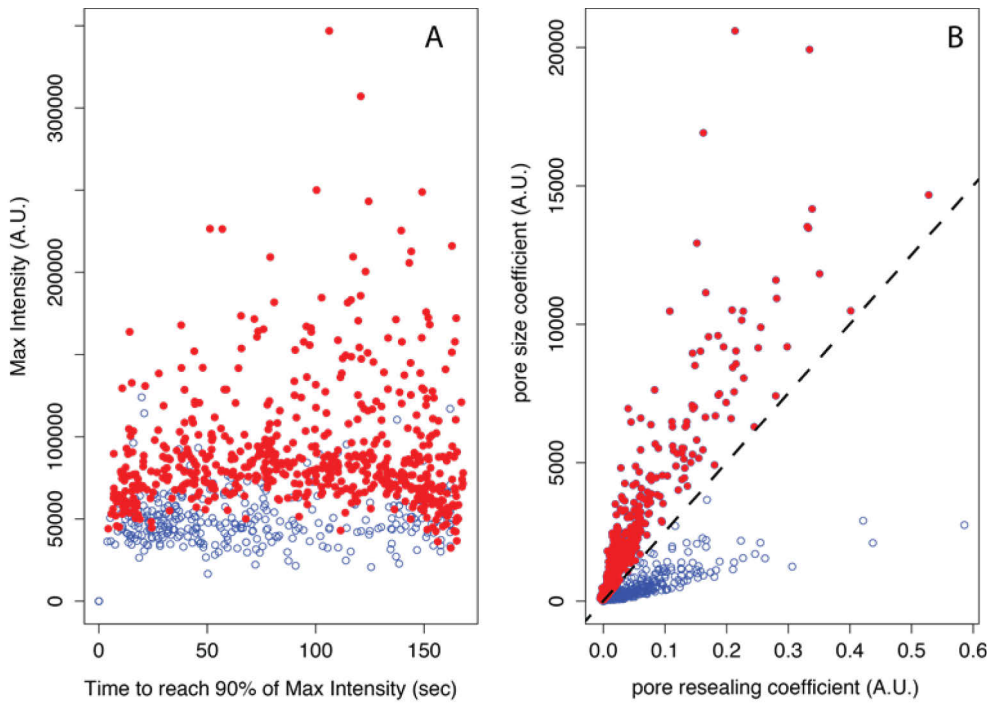


Figure 1: Nuclear propidium iodide uptake dynamics for ntMB at P_A 500 kPa, 50,000 cycles. (A) The time it took for the fluorescence intensity to reach 90% of its maximum intensity for the sonoporated cells; (B) The pore size coefficient ($\alpha \cdot \pi \cdot D \cdot C_0 \cdot r_0$) as a function of the pore resealing coefficient (β) as derived from equation 1; black dashed line indicates cut off level between two cell populations, determined as a middle line between the side lobes of the two populations by linear least square fitting. Every dot represents one cell; the red and blue color coding is the same in graph A and B.

Conclusion

This study shows the feasibility of real-time sonoporation measurements using time-lapse fluorescent recordings in combination with a diffusion model. Different patterns of PI uptake derived from this model highly correlate with cell viability and could be used to estimate cell death in studies when direct cell viability essays are not applicable. The fact that blue cells reach the plateau with increasing amount of cycles suggests that lower ultrasound pulse durations should be used for drug delivery, where a high level of cell viability is required.

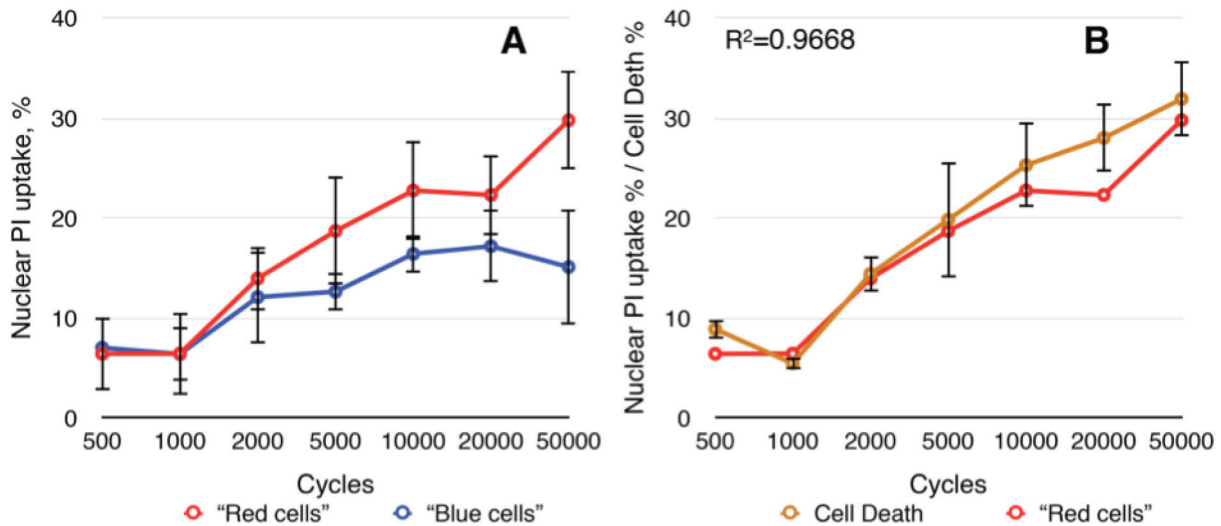


Figure 2: (A) The amount of the two different color coded sonoporated cells populations for ntMB insonified at 500 kPa as a function of the applied acoustic cycles. (B) Red sonoporated cell population and cell death as a function of the applied acoustic cycles.

Acknowledgements

Authors would like to thank, Michiel Manten, Robert Beurskens, Geert Springeling and Frits Mastik from the department of Biomedical Engineering, Erasmus MC for their technical assistance.

References

1. Hernot, S. and A.L. Klibanov, Microbubbles in ultrasound-triggered drug and gene delivery. *Advanced drug delivery reviews*, 2008. 60(10): p. 1153-1166
2. Kooiman, K., et al., Sonoporation of endothelial cells by vibrating targeted microbubbles. *J Control Release*, 2011. 154(1): p. 35-41
3. Klibanov, A.L., et al., Detection of individual microbubbles of ultrasound contrast agents: imaging of free-floating and targeted bubbles. *Invest Radiol*, 2004. 39(3): p. 187-95
4. Schindelin, J., et al., Fiji: an open-source platform for biological-image analysis. *Nature methods*, 2012. 9(7): p. 676-682
5. Fan, Z., et al., Spatiotemporally controlled single cell sonoporation. *Proc Natl Acad Sci U S A*, 2012. 109(41): p. 16486-16491

Oxygen carrying microbubbles for enhanced sonodynamic therapy of hypoxic tumours

Conor McEwan¹, Joshua Owen², Eleanor Stride², Colin Fowley¹, Heather Nesbitt¹, David Cochrane¹, Constantin. C. Coussios², M. Borden³, Anthony P. McHale¹ and John F. Callan¹

¹*Biomedical Sciences Research Institute, University of Ulster, Coleraine, Northern Ireland, U.K.
BT52 1SA*

²*Oxford Institute of Biomedical Engineering, University of Oxford, UK, OX3 7DQ*

³*Department of Chemical Engineering, Columbia University, 500 W 120 ST, New York, NY 10027,
USA*

Hypoxia within solid tumours is a key determinant of the effectiveness of radiation- and chemotherapy-based treatments, with high levels being associated with poor prognosis. It arises as a consequence of the atypical vasculature that is characteristic of growing tumours which results in the development of areas within the tumour where oxygen demand outstrips oxygen supply. Hypoxic fractions ranging from 10 to 30 % are present in most solid tumours regardless of size.

A promising technique for the treatment of recalcitrant tumours is Sonodynamic Therapy (SDT) which involves the use of a sensitising drug, molecular oxygen and ultrasound to produce reactive oxygen species within the tumour resulting in cytotoxic effects. However, as oxygen is a key substrate for SDT, the reduction of oxygen within the tumour environment caused by hypoxia again reduces treatment effectiveness. The aim of this study was to investigate the potential for using oxygen filled microbubbles to increase the local oxygen concentration in the tumour environment to facilitate SDT.

Phospholipid-stabilised microbubbles containing either oxygen (O_2) or sulphur hexafluoride (SF_6) were produced by sonication and conjugated to a sonosensitiser (Rose Bengal) via an Avidin-Biotin linker. Both *in vitro* and *in vivo* experiments were performed to compare the yield of reactive oxygen species generated and the cytotoxic effect of the microbubbles. A four-fold increase in the effect upon the viability of pancreatic cancer cells (BxPc-3) was seen with the O_2 compared with the SF_6 microbubbles (Figure 1) for the same ultrasound exposure conditions (30s exposure of 3.0Wcm^{-2} at 1MHz centre frequency, 100 Hz pulse repetition frequency and 50% duty cycle).

Similar results were seen *in vivo*. Tumours were induced in BALB/c SCID mice again using the BxPc-3 cell line and exposed to ultrasound for 3.5 mins (3.5 Wcm^{-2} at 1MHz centre frequency, 100 Hz pulse repetition frequency and 30% duty cycle) following injection of either O_2 or SF_6 microbubbles. Five days after treatment a 45% reduction in tumour volume was seen in the mice receiving the O_2 bubbles, compared with a 35% increase in volume for those receiving the SF_6 microbubbles. As shown in Figure

2, the control groups (no ultrasound) showed an increase of 180% in tumour volume over the same period.

In conclusion, the results suggest that the combination of oxygen-carrying microbubbles with an ultrasound-responsive therapeutic sensitiser provides the basis for a novel treatment option for recalcitrant tumours such as those seen in pancreatic cancer and for which existing therapeutic options are extremely limited.

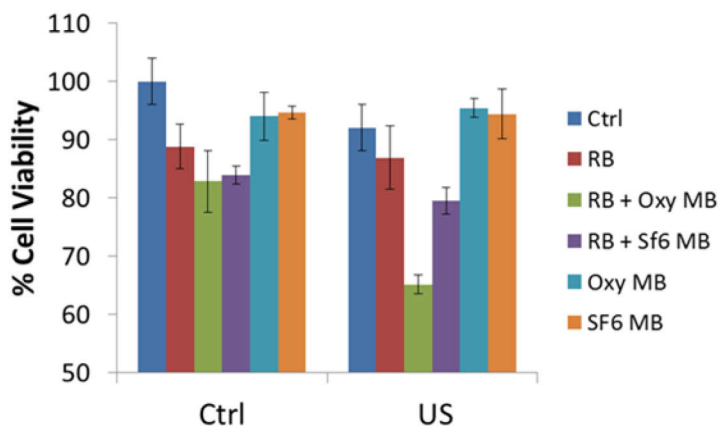


Figure 1: Plot of % cell viability for BxPc-3 cells grown in hypoxic conditions treated with 5 μ M Rose Bengal (RB), O₂-RB microbubbles or SF₆-RB microbubbles. Controls for untreated cells and those treated with just O₂ or SF₆ microbubbles are also included (n = 3).

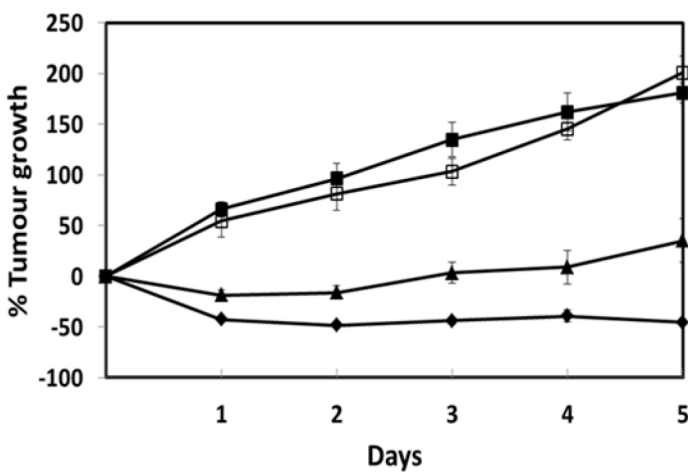


Figure 2: Plot of % tumour growth against time for mice bearing BxPc-3 tumours and treated with (i) O₂-RB microbubbles and ultrasound (filled diamonds) (ii) O₂-RB microbubbles only (open squares) (iii) SF₆-RB microbubbles and ultrasound (filled triangles) (iv) SF₆-RB microbubbles only (filled squares) (n = 3).

Estimation of local contrast-enhanced ultrasound signals from non-uniform temporal samples

Avinoam Bar-Zion¹, Melissa Yin², Elizabeth Kuczynski^{3, 4}, Dan Adam¹ and F. Stuart Foster^{2, 4}

¹Department of Biomedical Engineering, Technion - Israel Institute of Technology, Haifa, Israel

²Physical Sciences, Sunnybrook Research Institute, Toronto, Ontario, Canada

³Biological Sciences, Sunnybrook Research Institute, Toronto, Ontario, Canada

⁴Department of Medical Biophysics, University of Toronto, Toronto, Ontario, Canada

Background

Dynamic contrast-enhanced ultrasound (d-CEUS) imaging enables the measurement of changes in the concentration of the contrast agents within the vasculature of the imaged tissue. However, in many cases respiratory movements change the position of the scanned tissue relative to the transducer, causing in-plane and out-of-plane motion artifacts. Therefore, motion compensation is important for reliable quantitative analysis of d-CEUS movies. Although image registration can compensate for in-plane movement, groups of consecutive frames acquired outside of the main imaging plane contain non-relevant information and should be excluded. Currently due to the incompatibility of standard d-CEUS processing methods with non-uniformly sampled data, study scans containing considerable motion artifacts are discarded. This work aims to facilitate the estimation of perfusion parameters and visualization of vasculature even when a significant percentage of frames are excluded. To this end, this work presents a method for the estimation of ultrasound contrast agent (UCA) concentration from d-CEUS signals sampled at a non-uniform temporal grid.

Methods

In this work, adopting a multiplicative noise model, log-transformed single-pixel d-CEUS signals were processed in the temporal domain. These signals were processed within the framework of *reconstruction of non-uniformly sampled signals in shift-invariant (SI) spaces*. The Gaussian kernel (a popular generator for SI spaces) was used because it is compactly supported and can represent time-intensity curves produced using widely accepted perfusion models. In addition, d-CEUS signals that are incompatible with simple perfusion models, such as mouse tumor perfusion scans that have an extended wash-out phase, can be represented well using the Gaussian kernel. An efficient iterative algorithm was used for the estimation of the representation coefficients. The proposed method was validated in a series of numerical simulations and *in-vivo* scans. Two tumor models were used in this study. Static hind-limb LS174T tumor scans ($n=6$) were used in order to test the stability of the algorithm over different proportions of missing frames. An orthotropic mouse model of hepatocellular carcinoma (HCC, $n=22$)

was used in order to test the algorithm under substantial motion artifacts. In all cases a bolus injection was administered and the wash-in and wash-out phases were imaged.

Results

The width of the selected Gaussian kernel was narrow enough to enable proper depiction of the fast UCA wash-in, but still sufficiently broad to remove the speckle noise from the data. The theoretical perfusion curves (without noise) were represented with $R^2=0.99$, and the normalized root mean square error (NRMSE, norm of the estimation error divided by the norm of the signal) was equal to 0.01. The proposed method was able to estimate the noisy simulated time-intensity curves with mean NRMSE of 0.14 at 25 frames per second. When 50% of the samples were removed, the NRMSE of the estimated curves increased by only 0.05 to 0.19 (Figure 1). In addition, the reconstructed HCC scans, originally containing up to 55% out-of-plane frames, showed a low spatial coefficient of variance in the homogeneous liver tissue and well resolved blood vessels in the core of the tumor (Figure 2). The methods presented in this paper enabled the processing of d-CEUS scans containing substantial motion artifacts, thus extending the usability of d-CEUS imaging. Moreover, the results showed that increasing the frame rate can compensate for the decreased reconstruction quality resulting from the removal of groups of consecutive frames.

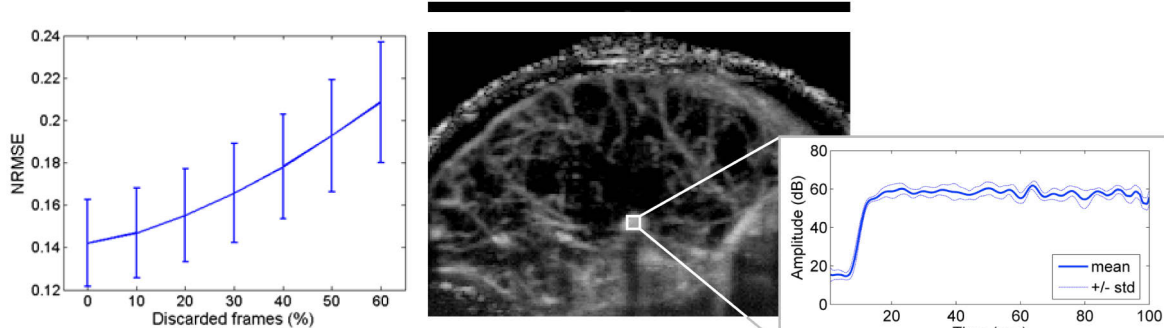


Figure 1: NRMSE VS. discarded frames

Figure 2: Processed HCC scan, with 40% frame removal. The mean time intensity curve inside a vessel and its STD are presented.

Phase-Shift protein-polymer nanodroplets for targeted drug delivery and ultrasound imaging

Jeong Yu Lee, Dario Carugo, Calum Crake, Joshua Owen and Eleanor Stride

Institute of Biomedical Engineering, Department of Engineering Science, Old Road Campus Research Building, University of Oxford, Oxford, OX3 7DQ, UK

Over the past decade numerous studies have demonstrated the considerable potential of ultrasound responsive phase-shift nanoemulsions as cavitation nuclei for both diagnostic and therapeutic applications. Compared with microbubble contrast agents they offer improved stability during storage and the ability to permeate the endothelium to enable extravascular imaging and/or therapeutic delivery [1-3].

There remain, however several challenges in their development. In particular, their stability *in vivo* and their conversion efficiency (i.e. proportion of the droplets undergoing a phase change) for a given set of ultrasound exposure conditions. The aims of this study were to investigate first the use of a hybrid protein and polymer coating to improve stability at 37°C and second incorporation of solid nanoparticles into the droplets to improve conversion efficiency.

The nanodroplets were prepared from hydrophobic perfluoropentane (PFP) and coated with human serum albumin and polyethylene glycol (PEG) modified N-hydrosuccinimide conjugated in dichloromethane using an oil-in-water emulsification method. The resulting nanodroplets had an average diameter of 344 nm and were stable at 37°C for several days. Upon exposure to ultrasound (continuous wave, frequency = ~1.8 MHz, peak-to-peak voltage = 40 V, estimated acoustic pressure = 0.4 MPa, exposure time range = 0 ~ 45 s) the nanodroplets underwent a phase change, generating microbubbles. The efficiency of this process was increased by a factor of 2.8 when iron oxide nanocrystals (IONCs, 5 nm) were added to the PFP core (Figure 1).

To explore their therapeutic potential, paclitaxel was incorporated into the droplet core and the release characteristics studied. The rate of drug release of the nanodroplets was found to increase 70.7 % compared to the control formulation without PFP upon exposure to ultrasound for 180 seconds. Finally the effect of the nanoparticles on breast cancer cells was compared with that of the free drug.

Keywords: Nanodroplets; Microbubbles; Ultrasound; Chemotherapy; Breast cancer

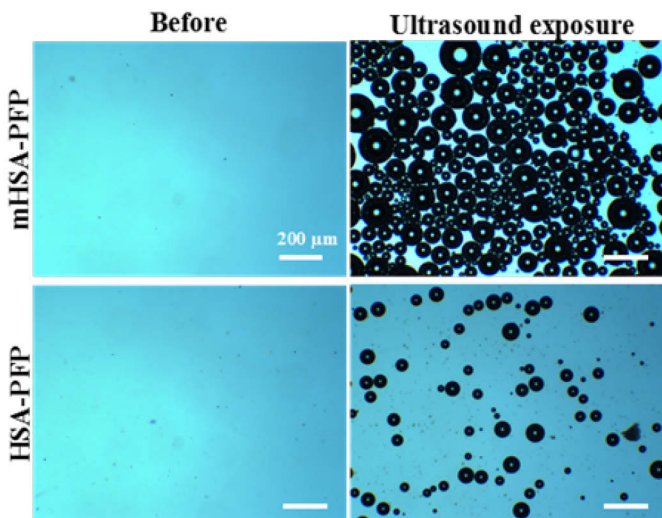


Figure 1: Optical images of the mHSA-PFP and HSA-PFP nanodroplets before ultrasound exposure and after ultrasound exposure for 45 sec. Scale bars represent 200 μm .

References

1. O.D. Kripgans, J.B. Fowlkes, D.L. Miller, O.P. Eldevik, P.L. Carson, *Acoustic droplet vaporization for therapeutic and diagnostic applications*, *Ultrasound in medicine & biology*, 26 (2000) 1177-1189
2. N. Rapoport, K.H. Nam, R. Gupta, Z. Gao, P. Mohan, A. Payne, N. Todd, X. Liu, T. Kim, J. Shea, C. Scaife, D.L. Parker, E.K. Jeong, A.M. Kennedy, *Ultrasound-mediated tumor imaging and nanotherapy using drug loaded, block copolymer stabilized perfluorocarbon nanoemulsions*, *Journal of controlled release : official journal of the Controlled Release Society*, 153 (2011) 4-15
3. C.C. Chen, P.S. Sheeran, S.Y. Wu, O.O. Olumolade, P.A. Dayton, E.E. Konofagou, *Targeted drug delivery with focused ultrasound-induced blood-brain barrier opening using acoustically-activated nanodroplets*, *Journal of controlled release : official journal of the Controlled Release Society*, 172 (2013) 795-804.

Optimization of multi-pulse sequences for nonlinear contrast agent imaging using a CMUT array

Anthony Novell¹, Christopher B. Arena¹, Mathieu Legros², Sandeep Kasozi¹, Paul A. Dayton¹

¹Joint Department of Biomedical Engineering, The University of North Carolina and North Carolina State University, Chapel Hill, NC 27599, USA

²Vermon SA, Tours, France

Background, motivation and objectives

Over the past few years, Capacitive Micromachined Ultrasonic Transducers (cMUTs) have emerged as a promising alternative to traditional piezoelectric transducers [1]. One notable advantage of cMUTs is their wide frequency bandwidth, however, their use in nonlinear imaging approaches such as those used to detect contrast agents has been challenging due to their intrinsic nonlinear character [2]. To this purpose, we have recently developed a new multi-pulse sequence, called bias voltage modulation (BVM). During BVM, three successive pulses are transmitted with different pressure amplitudes [3]. The modulation (by a factor 1, 2 and 3) was implemented on the bias voltage (V_{dc}) applied to the cMUT while the excitation voltage (v_{ac}) remained the same. Previous results showed that a complete cancellation of the nonlinear signal from the source could be reached when the BVM sequence was implemented [3]. BVM was originally developed to adapt the well-established power modulation (PM) sequence to arrays based on cMUT technology. Nevertheless, the efficiency of other multi-pulse imaging schemes, such as pulse inversion (PI) and CR, remains limited because of the cMUT nonlinear behavior. Moreover, it had been previously demonstrated [4, 5] that combining several approaches (e.g., PIPM, CRPM) increased the sensitivity to detect nonlinear responses from microbubbles. In this context, our objective was to combine the BVM sequence with these approaches to (i) suppress the undesirable harmonic component generated by the cMUT, (ii) optimize the contrast agent detection.

Material and methods

Gaussian apodized sine burst excitations and Gaussian chirps centered at 4 MHz were used as excitation signals for the diverse multi-pulse sequences. For both pulse and chirp signals, a fractional bandwidth at – 6 dB of 42% was chosen to avoid the frequency band overlapping between fundamental and 2nd harmonic components. For sequence using chirp excitations, a specific compression filter was designed to extract both the fundamental (f_0) and the 2nd harmonic ($2f_0$) components while at the same time avoiding side-lobe artifacts. Multi-pulse sequences were evaluated using 9 inter-connected elements of a cMUT linear array centered at 6.5 MHz. Excitation signals were designed using Matlab and then transferred to an arbitrary function generator. Signal amplitudes were then amplified to reach 75 V_{peak} while the V_{dc} (set to 30 V, 60 V or 90 V according to the firing) was delivered by a programmable power supply. A 7.5 MHz single-element piezoelectric transducer was used in receive

mode to reach a satisfactory level of sensitivity. Contrast-enhanced imaging techniques were compared by injecting lipid microbubbles into a microcellulose tube (250 μm) embedded in a tissue mimicking phantom. The efficiency of the different approaches was compared in terms of CTR, contrast-to-noise ratio (CNR) and axial resolution.

Results, discussion and conclusion

Experimental results showed that a satisfactory cancellation of the nonlinear signal from the source could be reached when the BVM sequence was combined with PI and CR. For sequences based on BVM, the backscattered signal from a linear reflector (silver wire) was reduced by 28 dB and 15 dB at f_0 and $2f_0$ levels, respectively. Using microbubbles, a substantial increase of the CNR was measured when BVM was combined with CR and PI as shown in Figure 1. This enhancement can be attributed to a better conservation of the different non-linear components (f_0 , $2f_0$ and $3f_0$) induced by both CR and PI methods. Furthermore, in comparison with PI and CR imaging modes, the use of sequences based on BVM resulted in a CTR increase of 10.0 dB and 4.6 dB, respectively. After chirp compression, the axial resolution at -3 dB was quasi-similar (+0.08 mm) for method based on chirp excitations (e.g. CR) in comparison with pulse excitation.

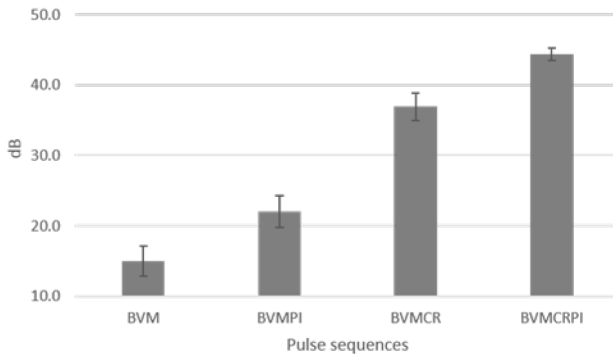


Figure 1: Contrast-to-noise ratio as a function of the pulse sequence.

These results demonstrate improvements in both CTR and CNR when BVM imaging is performed in combination with PI and CR. This detection method allows the recovery of several non-linear components contained within contrast agent responses and suggests that this approach may substantially improve performance of cMUTs for contrast ultrasound imaging.

References

1. A.S. Savoia, G. Caliano, and M. Pappalardo, *A CMUT probe for medical ultrasonography: from microfabrication to system integration*, *IEEE Trans Ultrason Ferroelectr Freq Control*, Jun. 2012, 59(6), pp. 1127-38
2. A. Novell, M. Legros, N. Felix and A. Bouakaz, *Exploitation of Capacitive Micromachined Transducers for nonlinear ultrasound imaging*, *IEEE Trans Ultrason Ferroelectr Freq Control*, Dec. 2009, 56(12), pp. 2733-43
3. A. Novell, M. Legros, J.M. Gregoire, P. Dayton and A. Bouakaz, *Evaluation of bias voltage modulation sequence for nonlinear contrast agent imaging using a capacitive micromachined ultrasonic transducer array*, *Physics in medicine and biology*, Sep. 2014, 59(17), pp. 4879-4896
4. R. J. Eckersley, C. T. Chin, and P. N. Burns, *Optimising phase and amplitude modulation schemes for imaging microbubble contrast agents at low acoustic power*, *Ultrasound Med Biol*, Feb 2005, 31(2), pp. 213-9
5. A. Novell, C. A. Sennoga, J. M. Escoffre, J. Chaline, and A. Bouakaz, *Evaluation of chirp reversal power modulation sequence for contrast agent imaging*, *Phys Med Biol*, Sep. 2014, 59(17), pp. 5101-17

The influence of binding on the radial excursions of lipid-coated microbubbles

Tom van Rooij¹, Antonius F.W. van der Steen^{1,2}, Nico de Jong^{1,2}, Klazina Kooiman¹

¹*Department of Biomedical Engineering, Thorax Center, Erasmus MC, Rotterdam, the Netherlands*

²*Laboratory of Acoustical Wavefield Imaging, Faculty of Applied Sciences, Technical University Delft, Delft, the Netherlands*

Introduction

One of the main challenges for ultrasound molecular imaging is acoustically distinguishing non-bound microbubbles from those that have bound to their molecular target. In this in vitro study we used the Brandaris 128 ultrahigh-speed camera to compare the acoustical responses of two types of targeted lipid-coated microbubbles (biotinylated DPPC and DSPC-based) in a bound and non-bound configuration, aiming to acoustically discriminate bound from non-bound microbubbles. We previously showed that biotinylated DPPC-based microbubbles (16 C-atoms) had a larger binding area and a more domed shape upon binding than DSPC-based microbubbles (18 C-atoms). Based on these differences we hypothesize a difference in acoustical properties.

Materials & Methods

Biotinylated lipid-coated microbubbles with a C₄F₁₀ gas core were made by sonication [1,2]. The coating was composed of 59.4 mol% DPPC (1,2-dipalmitoyl-*sn*-glycero-3-phosphocholine) or DSPC (1,2-distearoyl-*sn*-glycero-3-phosphocholine), 35.7 mol% PEG-40 stearate, DSPE-PEG(2000), and 0.8 mol% DSPE-PEG(2000)-biotin. For the non-bound targeted microbubbles, an OptiCell was blocked with 1% bovine serum albumin to prevent unspecific binding and the microbubbles were subsequently injected in the OptiCell. For the bound microbubbles, a 25 µm thick polyester membrane was mounted on a rectangular polyvinylchloride holder and was custom coated with a 1-2 µm thick polycarboxylate hydrogel (XanTec bioanalytics GmbH, Düsseldorf, Germany). The hydrogel was activated and streptavidin was subsequently covalently attached to the hydrogel using the amine coupling kit according to the instructions of the manufacturer.

The acoustical responses of the bound and non-bound targeted microbubbles were captured using the Brandaris 128 ultrahigh-speed camera operated at ~15 million frames per second [3]. Single microbubbles were investigated using the microbubble spectroscopy technique [4]. A broadband single element transducer transmitted a Gaussian tapered 8 or 10-cycle sine wave burst at transmit frequencies swept from 1 to 4 MHz (increment steps of 200 kHz) at a peak-negative driving pressure (P_A) of 30 or 50 kPa.

Results

We studied 34 bound microbubbles (17 DPPC, 17 DSPC) at a pressure of 30 and 50 kPa. For the non-bound microbubbles we analyzed 29 microbubbles (14 DPPC, 15 DSPC) at a driving pressure of 50 kPa. We found lower radial excursions at the fundamental frequency for bound microbubbles than for non-bound microbubbles (Fig. 1A). The resonance frequencies were equal for bound and non-bound microbubbles at a pressure of 50 kPa, whereas at a lower pressure of 30 kPa the resonance frequencies of bound DPPC-based microbubbles were lower than those of bound DSPC-based microbubbles. Nonlinear behavior in terms of subharmonic responses was the same for bound and non-bound microbubbles, whereas at the second harmonic frequency the radial excursions for bound DSPC-based microbubbles were higher (Fig. 1B).

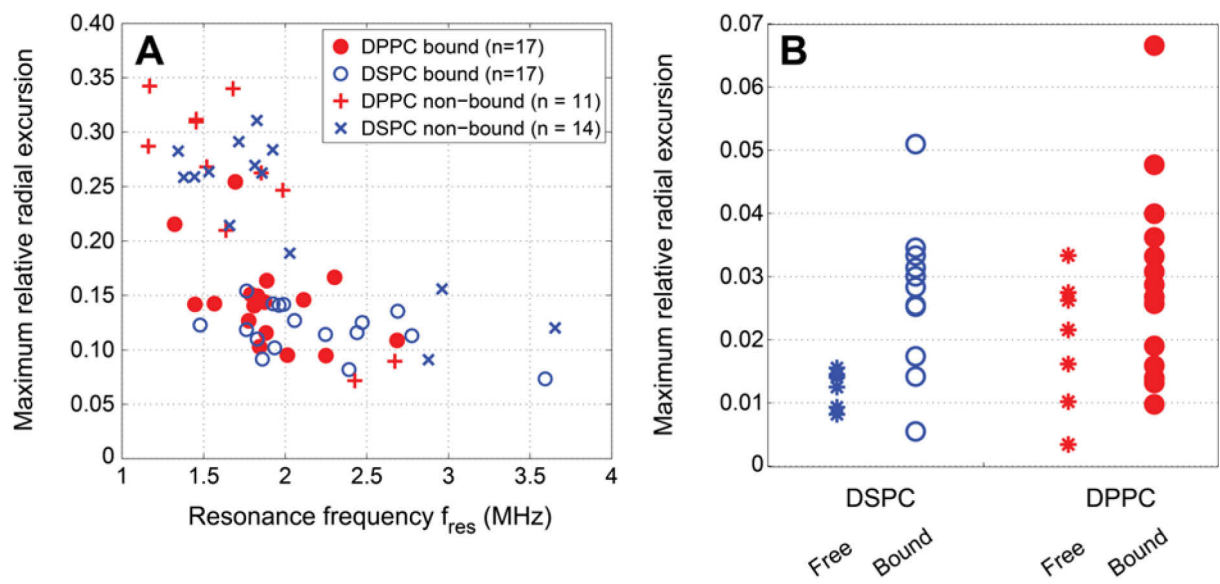


Figure 1: Maximum relative radial excursions **A**) at the resonance frequency of bound and non-bound DPPC and DSPC microbubbles plotted versus the resonance frequency at a pressure of 50 kPa. **B**) Maximum relative radial excursions at the second harmonic frequency of bound and non-bound DPPC and DSPC microbubbles at a pressure of 50 kPa.

Conclusions

This study reveals that the main difference between bound and non-bound microbubbles is the lower radial excursion at the fundamental frequency for bound microbubbles. Another main finding was that the resonance frequency was the same for bound and non-bound microbubbles, except for the driving pressure of 30 kPa. Subharmonic responses were also the same for bound and non-bound microbubbles. Finally, at the second harmonic frequency we found higher relative radial excursions for bound DSPC-based microbubbles than for non-bound DSPC microbubbles, whilst there was no difference for DPPC-based microbubbles. The main difference that we found between DPPC and DSPC-based microbubbles were the higher radial excursions of bound DSPC microbubbles at the second harmonic frequency than for non-bound DSPC microbubbles. This change in acoustic signal for bound DSPC-based

microbubbles might provide opportunities to acoustically discriminate them from non-bound DSPC microbubbles.

References

1. Kooiman et al, *DSPC or DPPC as main shell component influences ligand distribution and binding area of lipid-coated targeted microbubbles*, Eur J Lipid Sci Technol 2014, 116:1217-1227
2. Klibanov et al, *Detection of individual microbubbles of ultrasound contrast agents: imaging of free-floating and targeted bubbles*, Invest Radiol 2004, 39:187-195
3. Chin et al, *Brandaris 128: A digital 25 million frames per second camera with 128 highly sensitive frames*, Rev Sci Instrum 2003, 74: 5026-5034
4. van der Meer et al, *Microbubble spectroscopy of ultrasound contrast agents*, JASA 2007, 121: 648-656

Sonoporation for local and targeted delivery of a therapeutic antibody in colorectal cancer: in vivo proof of concept

**Thomas Barré¹, Emilie Dalloneau², Thierry Lecomte^{3,4}, Valérie Gouilleux-Gruart^{4,5},
Nathalie Heuzé-Vourc'h², Ayache Bouakaz¹**

¹UMR Inserm U930, Université François Rabelais de Tours, 10 ter Bd Tonnellé, F-37032 Tours,
France

²Université François Rabelais, EA6305, F-37032 Tours, France, Centre d'Etude des Pathologies
Respiratoires, UMR 1100/EA6305, F-37032 Tours, France

³Service Hépato-Gastro-Onco-Entérologie – CHRU Tours

⁴Université François Rabelais de Tours, CNRS, GICC UMR 7292, F-37032 Tours, France

⁵CHRU de TOURS, laboratoire d'immunologie, F-37032 Tours, France

Introduction

Therapeutic antibodies have changed the monitoring and treatment of many diseases, including some hematological malignancies. Regarding solid tumors, the results are more modest and this may be explained by the limited and heterogenous intratumoral distribution of these macromolecules after their systemic administration. Sonoporation is an innovative process coupling ultrasound with gas microbubbles leading to transient permeability of endothelial layers, thus facilitating the passage of molecules. The objective of this study is to determine whether sonoporation enhances the bioavailability of a therapeutic antibody into the tumor. Hence, we evaluated the potential of sonoporation to improve the delivery of cetuximab, an anti-EGFR antibody indicated in the treatment of metastatic colorectal cancer.

Material & Methods

HT29 cells were inoculated subcutaneously with matrigel in nude mice and the tumor growth was monitored every two days using high resolution ultrasound imaging. Ultrasound B-scans were used to calculate tumor volume using the following formula:

$$\text{tumor volume} = \frac{\text{length} \times \text{width} \times \text{height}}{2}$$

Contrast-Enhanced Ultrasound Imaging (CEUS) was performed once a week after retro orbital administration of microbubbles (MM1 Bracco ®). Both tumor vasculature growth and tumor perfusion were assessed using VevoCQ® software (Figure 1).

The antibody Cetuximab was conjugated to AlexaFluor-750 (Cetux-AF750, 30 µg) and administered systemically in animals bearing tumors of $\pm 153 \text{ mm}^3$ with or without sonoporation treatment. Sonoporation was applied using three different ultrasound settings: (i) exposure time of 3 minutes with a repetition period (RP) of 100µs, a 40% duty cycle and a acoustic pressure of 600 kPa; (ii) 5 min,

10ms RP, 20% duty cycle, and a pressure of 500 kPa; (iii) 15 min, 1s RP, 5% duty cycle, and a pressure of 350 kPa. Quantitative tumor uptake of cetuximab AF 750 was carried out by fluorescence imaging in the near infrared (Figure2). The uptake of the antibody was measured at different times post sonoporation up to 6 hours. Its intratumor distribution was determined by immunohistochemistry. To evaluate the effectiveness on tumor growth of Cetuximab delivery assisted by microbubbles and ultrasound, the treatment (100 μ g of cetuximab) was performed twice per week with the condition of sonoporation described in (i).

Results

The uptake of fluorescently labeled Cetux-AF750 in the tumors is shown in Fig. 2 for a control group (a) and for a treated group (b). Based on these fluorescence data, the results showed that Cetux- AF750 uptake was increased up to three folds within the tumor depending on the applied ultrasound settings. Moreover, the fluorescence signal persisted significantly longer after sonoporation compared to control (Figure 3). These results indicate that cetuximab accumulated more efficiently and durably in the tumor after sonoporation. Histological analysis should assess the intratumoral distribution of cetux-AF750 in the tumor. In addition, the bioavailability of the Cetux-AF750 was only slightly different between the three groups of animals.

Conclusion

This study highlighted the interest of sonoporation to improve the local delivery of anti-tumor antibodies to their target site. Further studies are required to evaluate whether the increased tumor delivery of monoclonal antibodies into the tumor by sonoporation is associated with improved therapeutic response.

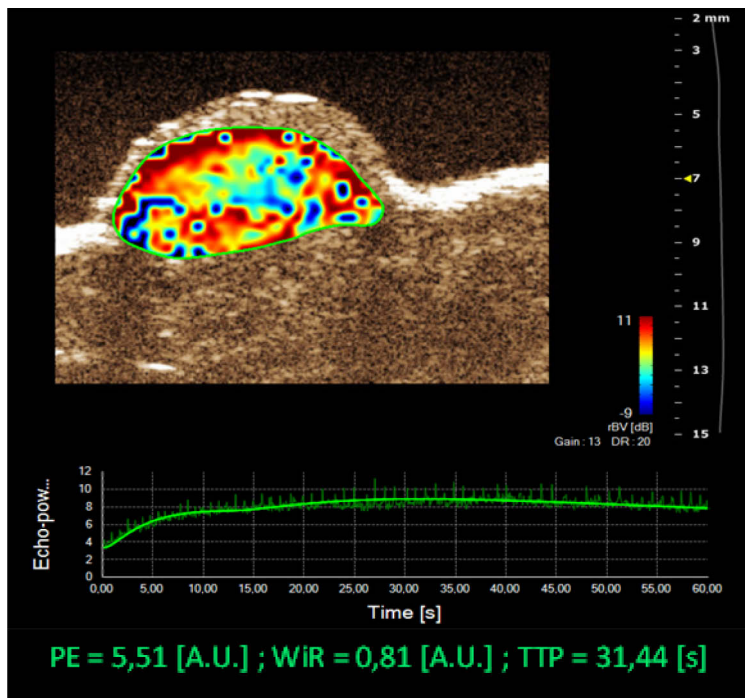


Figure 1: Quantification of tumor perfusion with VevoCQ® software after bolus injection of MM1 contrast microbubbles to obtain typical values of Peak Enhancement (PE), Wash-in Rate (WiR) and Time To Peak (TTP).

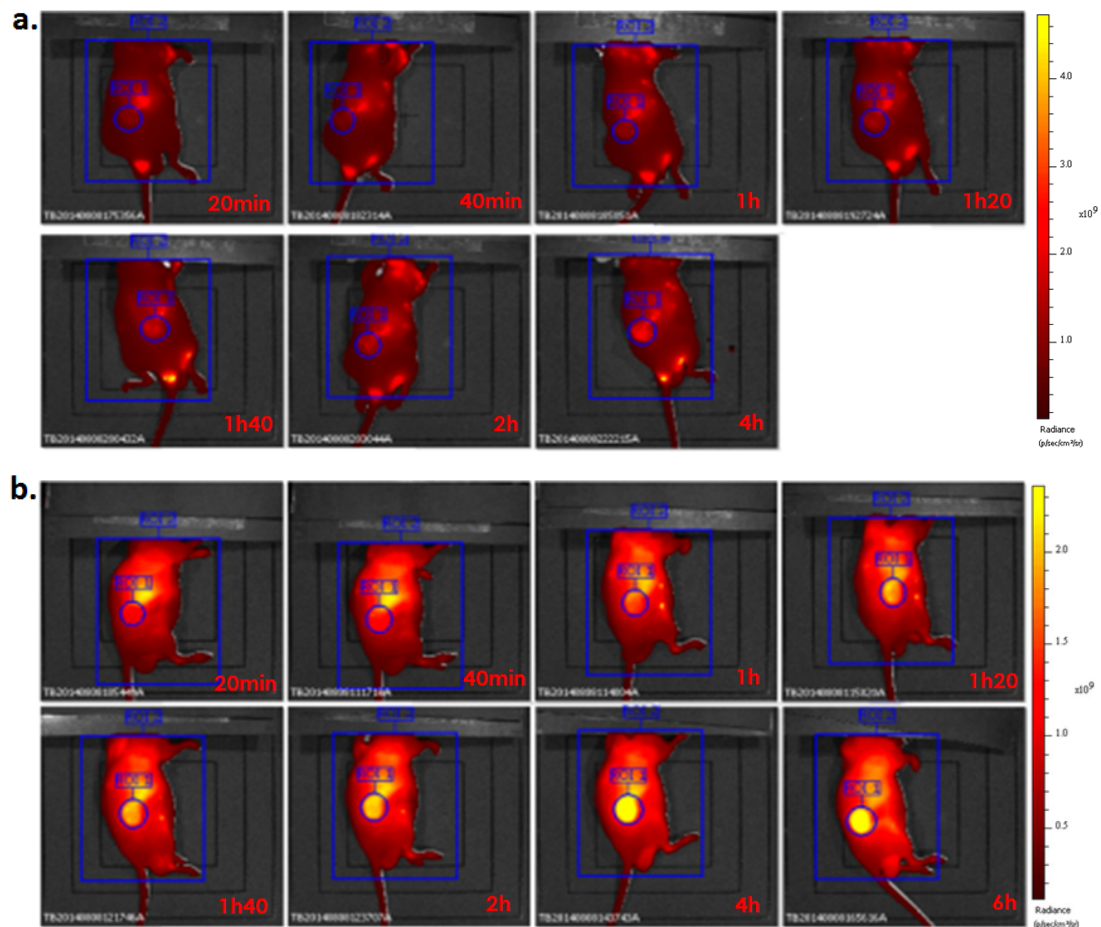


Figure 2: Comparison of bio-distribution kinetics of Cetuximab-AlexaFluor (r) 750 between a control mouse (a) and sonopored mouse (b) by fluorescence imaging

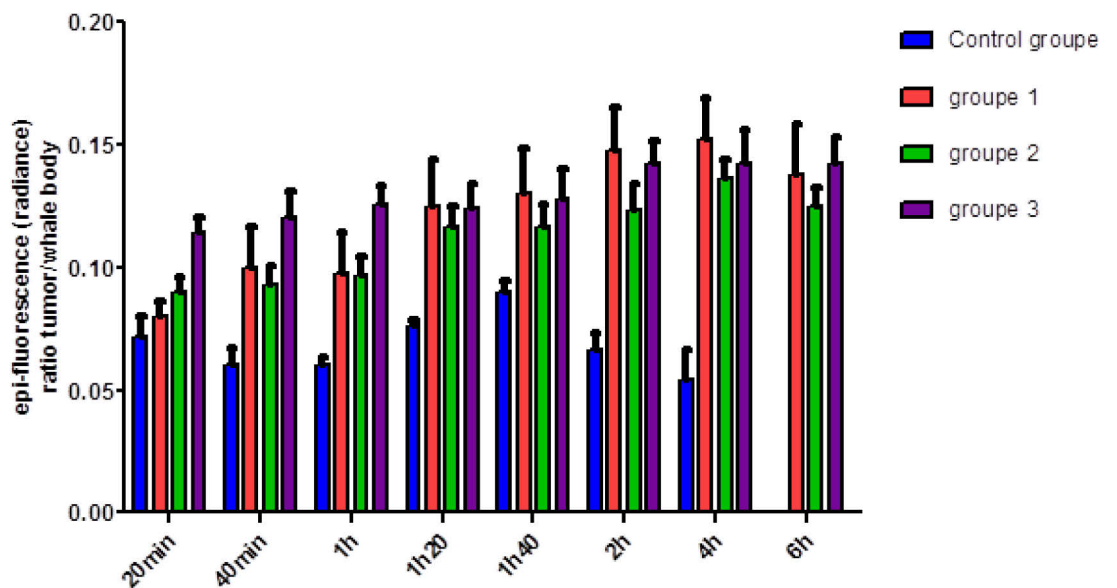


Figure 3: Kinetics of Cetuximab-AlexaFluor(r) 750 bio-distribution for the control group and the treated groups

Threshold characterization of volatile phase-shift perfluorocarbon nanodroplets at pre-clinical frequencies

***Yasaman Daghighi¹, Paul Sheeran², Ross Williams¹, E. Cherin¹, F.S. Foster^{1, 2}
and Peter Burns^{1, 2}***

¹Sunnybrook Research Institute, Toronto, ON, Canada

²Department of Medical Biophysics, University of Toronto, Toronto, ON, Canada

The potential of volatile phase-shift nanodroplets as an ultrasound contrast agent has attracted special consideration in many branches of medicine (e.g., cancer imaging, drug delivery, targeted molecular imaging). Nanodroplets, with sizes of ~100-300 nm, can diffuse into the extravascular extracellular space of tumors due to their leaky vasculature. By exposing these nanodroplets to ultrasound of sufficient pressure, their phase can be converted from liquid into gas [1] to form microbubbles (which have long been used as an intravascular contrast agent for ultrasound imaging). To date, characterization of droplets has largely been done *in vitro* and at clinical ultrasound frequencies; however, an understanding of the behaviour of these droplets at frequencies relevant to pre-clinical studies is essential to their clinical translation. In this study, we present vaporization thresholds of decafluorobutane (DFB) nanodroplets measured *in vitro* at 20-40 MHz, with complementary examples of *in vivo* vaporization in mouse tumours following intravenous administration.

DFB droplets were prepared by condensation of lipid-coated microbubbles generated by mechanical agitation [2]. The mean diameter of the droplets measured by dynamic light scattering was 255±15 nm. *In vitro* experiments were performed on polyacrylamide gel (PA) phantoms containing dilute concentrations of droplets (100µL/L); *in vivo* experiments were performed on C3H mice with KHT-C hind limb tumours, with 100µL of droplets administered through the tail vein followed by a saline flush. Droplet-free phantoms and mice injected with only saline were used as controls. All experiments were performed at physiological temperature. A VisualSonics Vevo2100 system with 20, 30, and 40 MHz probes was used to measure the vaporization thresholds. Thresholds were measured *in vitro* by exposing PA phantoms to a range of 2-cycle pulses of increasing pressure and noting the point at which image contrast at the focal depth began to rise significantly. *In vivo* tumour experiments were performed in a similar way to demonstrate that the *in vitro* thresholds are relevant to *in vivo* application. The experiments were repeated independently in 8 PA phantoms and 3 mice at each frequency. Measurements of peak negative pressure were provided by the manufacturer.

Vaporization thresholds were observed to occur at low transmit pressures with all probes, typically at 5-10% transmit power, corresponding to peak negative pressures of ~2-3 MPa. Above these thresholds a great amount of vaporization was visible, while below these thresholds very little spontaneous vaporization was evident. The mechanical indices at which vaporization occurred at 20, 30 and 40 MHz were 0.7, 0.6, and 0.4, respectively. These values support trends observed in the work of Kripfgans *et al.* [3] and Shpak *et al* [4], in which the vaporization thresholds were found to generally decrease with increasing frequency. It should be noted that these pressure values rely on hydrophone measurements performed by the manufacturer, the details of which were undisclosed, and as such should be considered preliminary. *In vivo* measurements of the threshold in tumours 5-30 minutes after administration agreed very closely with *in vitro* results and demonstrated a substantial degree of vaporization throughout the tumour.

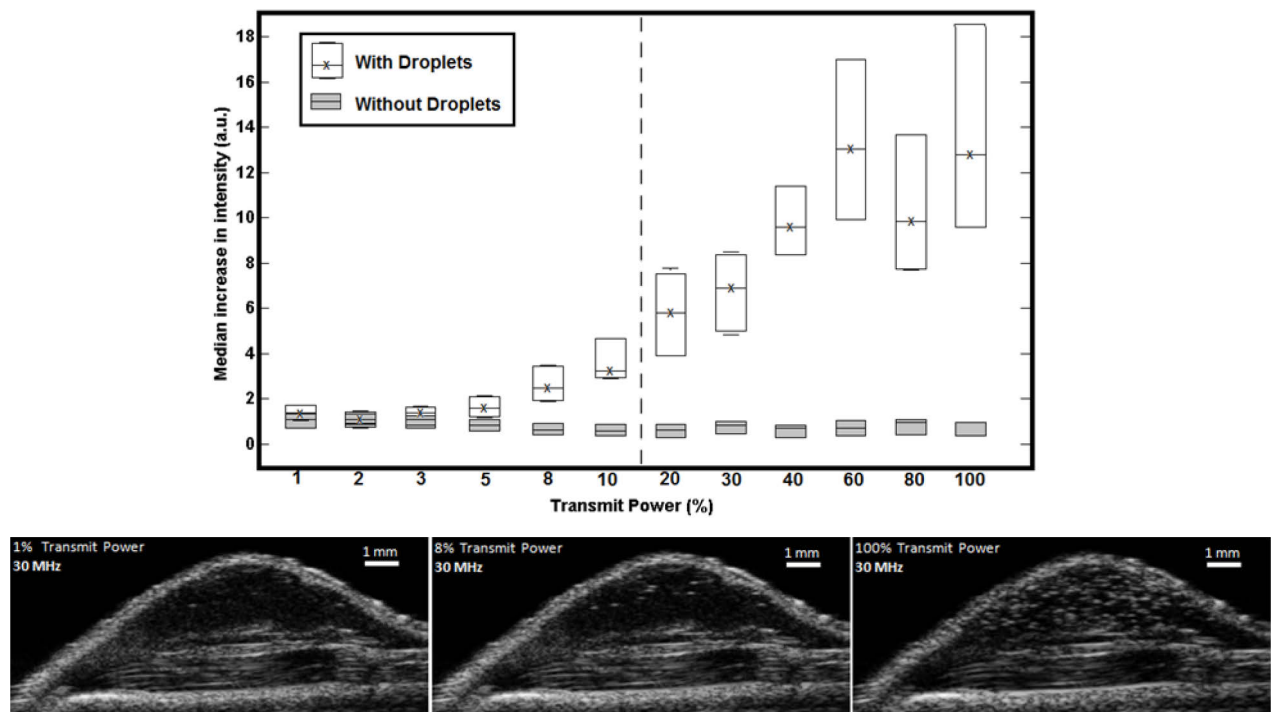


Figure 1: (Top) *In vitro* measurement of the change in image intensity as a function of pulse pressure at 30 MHz, for a polyacrylamide phantom containing decafluorobutane nanodroplets. The vaporization threshold occurs at a transmit power of 8%. (Bottom) B-mode images at 30 MHz of a mouse tumor at transmit pressures of 1, 8 and 100% after administration of nanodroplets. Vaporization begins to occur at 8% transmit power, in agreement with *in vitro* measurements.

References

1. Williams R, Wright C, Cherin E, Reznik N, Lee M, Gorelikov I, Foster FS, Matsuura N, Burns PN. Characterization of submicron phase-change perfluorocarbon droplets for extravascular ultrasound imaging of cancer. *Ultrasound Med Biol*. 2013;39(3):475-89
2. Sheeran PS, Luois SH, Mullin LB, Matsunaga TO, Dayton PA. Design of ultrasonically-activatable nanoparticles using low boiling point perfluorocarbons. *Biomaterials*. 2012;33(11):3262-9
3. Kripfgans OD, Fowlkes JB, Miller DL, Eldevik OP, Carson PL. Acoustic droplet vaporization for therapeutic and diagnostic applications. *Ultrasound Med Biol*. 2000;26(7):1177-89
4. Shpak O, Verweij M, Vos HJ, de Jong N, Lohse D, Versluis M. Acoustic droplet vaporization is initiated by superharmonic focusing. *Proc Natl Acad Sci*. 2014;111(5):1697-702

Plane wave ultrasound imaging and tracking of microbubbles in large vessels for flow quantification: Methods and initial evaluation on a carotid bifurcation phantom

Chee Hau Leow¹, Robert J. Eckersley², Alfred C.H. Yu³, Meng-Xing Tang¹

¹*Department of Bioengineering, Imperial College London, United Kingdom, Department of Biomedical Engineering*

²*King's College London, United Kingdom*

³*Medical Engineering Program, University of Hong Kong, Pokfulam, Hong Kong*

Background, Motivation and Objective

Ultrasound imaging velocimetry (UIV) quantifies flow fields in optically opaque medium by tracking microbubble contrast agents between ultrasound imaging frames and has shown great promising in imaging arterial vascular flow (Poelma et al. 2012). Comparing with conventional ultrasound Doppler Velocimetry, UIV is independent of flow angles and the use of microbubbles significantly increases SNR from with the flow. However, UIV using conventional line-by-line scanning generates errors (Zhou et al. 2013) making quantifying fast flow a challenge. Recent development of high frame rate ultrasound imaging technology offers new possibilities for fast flow visualisation and quantification. In this work, an UIV system combining plane wave ultrasound imaging, microbubble contrast agents, pulse inversion imaging and UIV data processing has been developed. The system performance was evaluated with a carotid bifurcation flow phantom.

Statement of Contribution/Methods

An anatomically realistic carotid bifurcation model was used to evaluate the performance of the system (Lai et al. 2013). The flow was driven by a pulsatile pump, delivering 3ml diluted microbubbles solution per stroke and running at 80 strokes per minute. For image acquisition, contrast images of the intraluminal flow were acquired using a Verasonics ultrasound system. A compounded plane wave-pulse inversion scheme was implemented. A temporal resolution of 2000 frames per second was achieved. For each compounding angle, a 1 cycle pulse followed by its phase inverted counterpart with a central frequency of 4MHz was transmitted and the radio-frequency data were acquired and post-beamformed into contrast images for UIV analysis. Cross-correlation of consecutive image frames was used to track microbubbles over time and their velocities calculated.

Results/Discussion

Figure 1(a)-(d) shows the flow pattern at time point indicated in Figure 1(e). In Figure 1(a), uniform flow moving forward from the common carotid artery can be clearly seen in the lumen during the peak systole phase (t1). A vortex subsequently emerged near vessel wall at the carotid bulk during post systolic phase (t2) in Figure 1(b). During the deceleration phase, the vortex slowly dissipated until it reached the peak dicrotic wave (t3) where the forward flow dominates again in Figure 1(c). In Figure 1(d), the vortex near the carotid bulk appears again during the post-dicrotic wave (t4). As visualized, plane wave UIV highlighted the key flow disturbance phenomenon in a normal carotid bifurcation model which cannot be revealed using conventional ultrasound imaging.

Conclusion

The results in this study shows high frame-rate UIV as a potentially valuable flow visualisation and quantification tool *in vivo*. With time resolution of 0.5ms under current setting, the system shows promise to accurately measure highly dynamic flow in both space and time *in vivo* and is currently being evaluated on imaging rabbit abdominal aorta.

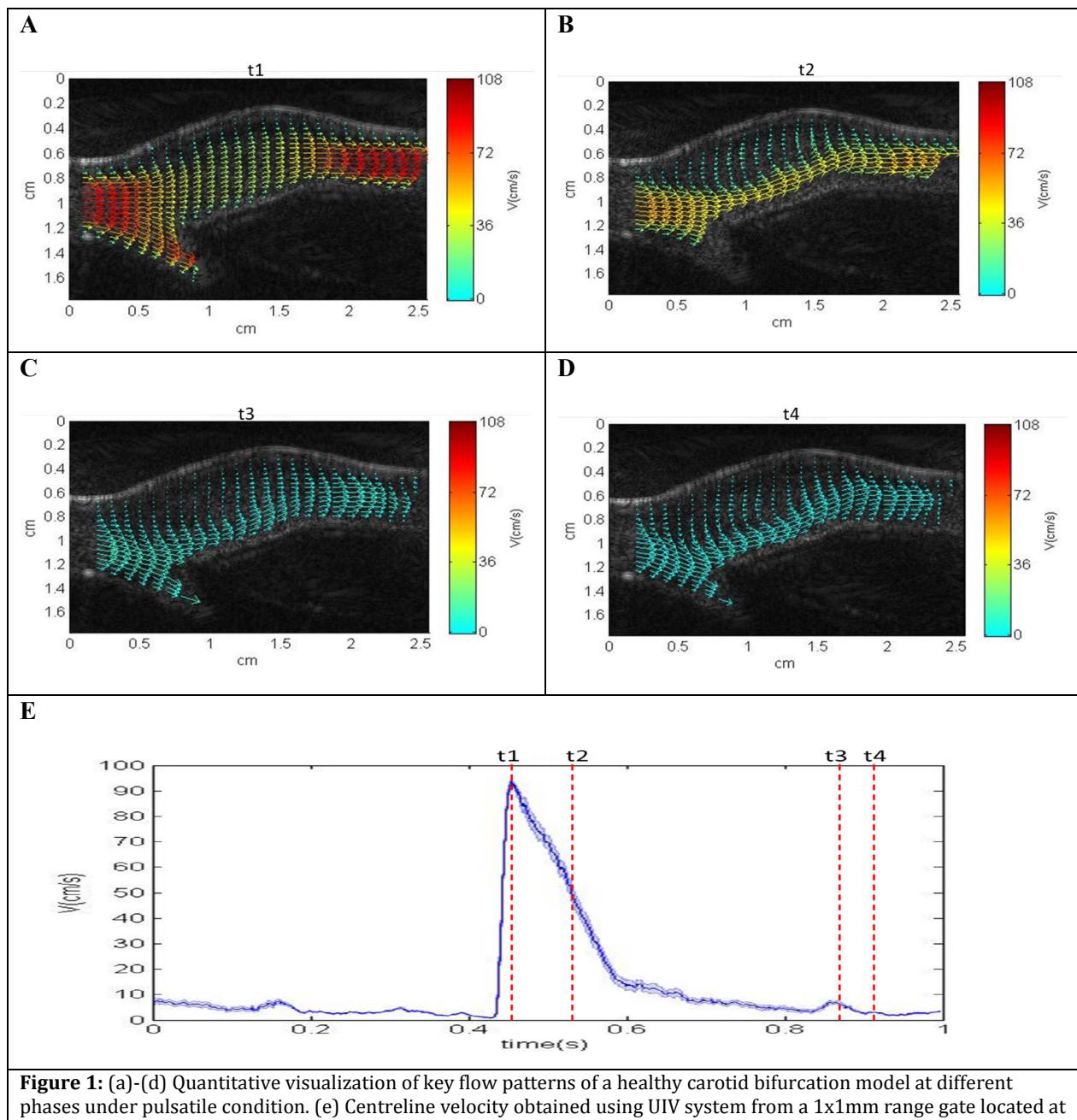


Figure 1: (a)-(d) Quantitative visualization of key flow patterns of a healthy carotid bifurcation model at different phases under pulsatile condition. (e) Centreline velocity obtained using UIV system from a 1x1mm range gate located at the common carotid artery. Note that the relative positions of each flow pattern are marked in the velocity plot.

References

1. Lai SSM, Yiu BYS, Poon AKK, Yu ACH. Design of Anthropomorphic Flow Phantoms Based on Rapid Prototyping of Compliant Vessel Geometries. *Ultrasound Med Biol* 2013;39:1654–1664
2. Poelma C, van der Mijle RME, Mari JM, Tang M-X, Weinberg PD, Westerweel J. Ultrasound imaging velocimetry: Toward reliable wall shear stress measurements. *Eur J Mech - B Fluids* 2012;35:70–75
3. Zhou B, Fraser KH, Poelma C, Mari J-M, Eckersley RJ, Weinberg PD, Tang M-X. Ultrasound Imaging Velocimetry: Effect of Beam Sweeping on Velocity Estimation. *Ultrasound Med Biol* 2013;39:1672–1681

Implicit dosimetry model for doxorubicin sonotransfer in vitro

M. Maciulevičius¹, M. Tamošiūnas¹, R. Jurkonis², S. Šatkauskas¹, M. Venslauskas¹

¹*Biophysical research group, Vytautas Magnus University, Kaunas, Lithuania*

²*Biomedical Engineering Institute, Kaunas University of Technology, Lithuania*

Introduction

In order to achieve high sonotransfer efficiency with low cell toxicity extent of ultrasound (US) induced microbubble (MB) cavitation must be precisely controlled, implying the necessity for a dose-planning sonoporation dosimetry. In present study, we have simultaneously performed quantitative evaluation of three main sonoporation elements: microbubble concentration measurements, microbubble scattered signal analysis and doxorubicin sonotransfer into Chinese hamster ovary cells. This complex research has led, not only to preexisting metrics inertial cavitation dose (ICD) (Chen et al., 2003) and MB sonodestruction rate (Tamosiūnas et al., 2012) relation explanation, but also to development of two new sonoporation metrics: 1/ time to peak of (root mean square) RMS and coefficient of RMS rising part. All these metrics were successfully used for doxorubicin sonotransfer prediction ($R^2 > 0.8$, $p < 0.05$) and therefore exhibit a possibility to be used for dosimetric applications.

Materials and methods

1. SonoVue® (Bracco diagnostics Inc., Switzerland) concentration was evaluated using spectroscopic method. MB concentration vs time curves were used for MB sonodestruction rate, abbr. $1/\tau$ of MB decay, calculation. 2. Passive cavitation detection system was used to record MB scattered signals. US excitation waveform was 1 MHz central frequency, 1 kHz pulse repetition frequency, 10 % duty cycle (100 μ s on and 900 μ s off). Center US excitation frequency was 1MHz. Overall 5 s exposure duration was recorded in 25 frames of 10 ms length each. Differential RMS was calculated for each frame in 1.5 – 1.75 MHz frequency window by subtracting – MB group from + MB group. Differential RMS was used to calculate the following estimates: 1/ time to maximum value of diff. RMS (abbr. $1/t$ of RMS); coefficient of diff. RMS rising part, approximated as straight line (abbr. k of RMS); integral of diff. RMS vs. time curve – ICD. 3. Sonoporation experiment was performed using Chinese hamster ovary cells, divided into three groups, according to exposure conditions: US + DOX, US + MB and US + MB + DOX. Cell viability was evaluated using cell colony test. DOX sonotransfer was evaluated as (US + MB + DOX) – (US + MB) – (US + DOX).

Results and discussion

Cavitation experiments. MB concentration assay showed exponential MB decrease in time at different acoustic peak negative pressure (PNP) values (Fig. 1a). As the acoustic pressure increases, MB decay exponents have faster falling phase, indicating faster MB concentration decline and lower τ values.

MB scattered US signals were recalculated to RMS vs. time curves (Fig. 1b). PNP values beginning for 150 kPa have expressed rising part, peak and falling part, indicating different processes of US + MB interaction: 50 and 100 kPa PNP values exhibit no expressed peak values, indicating steady MB response during exposure time.

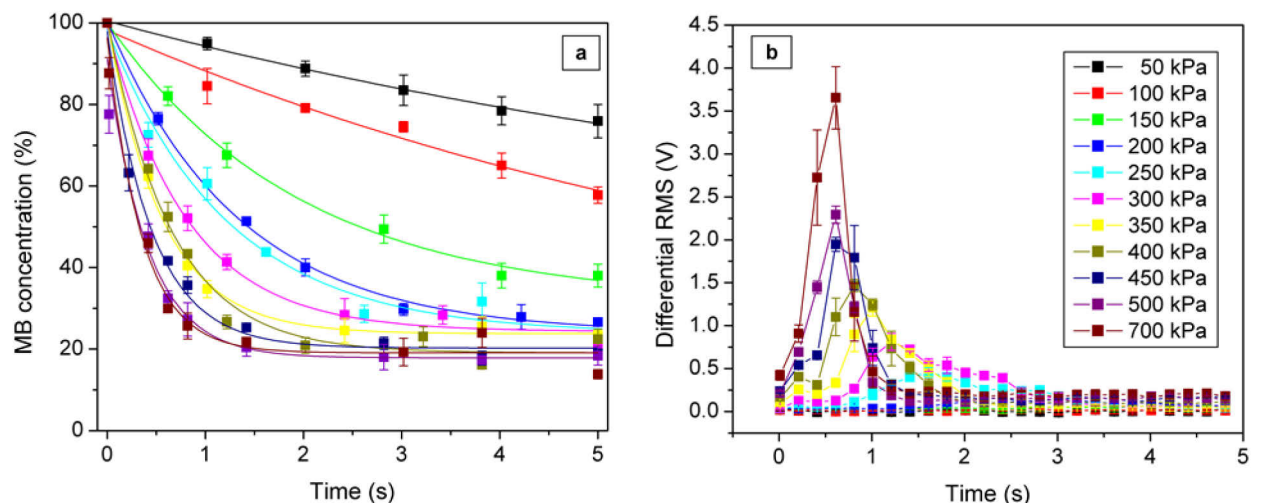


Figure 1: Dynamics of exponential SonoVue® MB concentration decay (a) and RMS (b) at different PNP values.

Estimate quantification. Investigated estimates of sonoporation dosimetry: ICD, $1/\tau$ of MB decay, $1/t$ of RMS and k of RMS were normalised (Fig. 2) to exhibit their similarity.

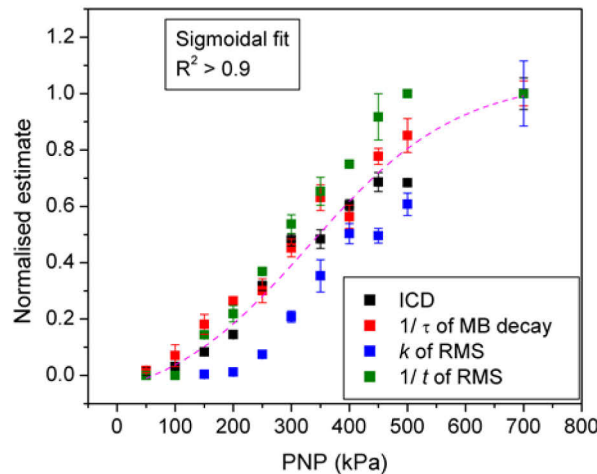


Table 1. Metric and DOX sonotransfer correlation

Metric	ICD	$1/\tau$ of MB decay	k of RMS	t of RMS
Correlation	$R^2 > 0.9$; $p < 0.01$	$R^2 > 0.9$; $p < 0.01$	$R^2 > 0.8$; $p < 0.05$	$R^2 > 0.95$; $p < 0.001$

Figure 2: Dependence of normalised estimates: $1/\tau$ of MB decay, $1/t$ of RMS, k of RMS and ICD on PNP.

All parameters have dose-response sigmoidal shape ($R^2 > 0.9$), indicating their suitability to be used for sonoporation dosimetry. Strong significant correlation, determined between $1/\tau$ of MB decay, ICD and new parameters, $1/t$ of RMS and k of RMS implies their interdependencies and metric features. Linear regression, performed between every evaluated estimate and the rate of DOX intracellular delivery (Table 1), suggested their ability to be used as dosimetrics for intracellular molecular sonotransfer.

Acknowledgements

This work was supported by the grant (MIP-034/2013) from the Research Council of Lithuania.

References

1. Chen WS, Brayman AA, Matula TJ, Crum LA. Inertial cavitation dose and hemolysis produced in vitro with or without Optison. *Ultrasound Med Biol*. 2003 May; 29(5):725-37
2. Tamasiunas M, Jurkonis R, Mir LM, Lukosevicius A, Venslauskas MS, Satkauskas S. Microbubble sonodestruction rate as a metric to evaluate sonoporation efficiency. *J Ultrasound Med*. 2012 Dec; 31(12):1993-2000

Cumulative phase delay imaging – a new contrast enhanced imaging modality

**Libertario Demi¹, Ruud J.G. Van Slooten¹, Xinran Zhao¹, Hessel Wijkstra^{2,1},
Massimo Mischi¹**

¹*Department of Electrical Engineering, Laboratory of Biomedical Diagnostics,*

Eindhoven University of Technology, the Netherlands

²*AMC University Hospital, Amsterdam, the Netherlands*

Introduction

Recently, a new marker for ultrasound contrast agents (UCAs) has been introduced [1-2]. A cumulative phase delay (D) between the second harmonic and fundamental pressure component is in fact observable for ultrasound propagating through UCAs. This phenomenon is absent in the case of tissue nonlinearity and is dependent on insonating pressure and frequency, UCA concentration, and propagation path length through UCAs. In this paper, the first ultrasound image based on this marker is presented.

Methods

The ULA-OP research platform [3], in combination with a LA332 linear array probe (Esaote, Firenze Italy), has been used to image a gelatin phantom containing a PVC plate (used as a reflector) and a cylindrical cavity with a diameter of 7 mm (placed in between the observation point and the PVC plate), see Figure 1.

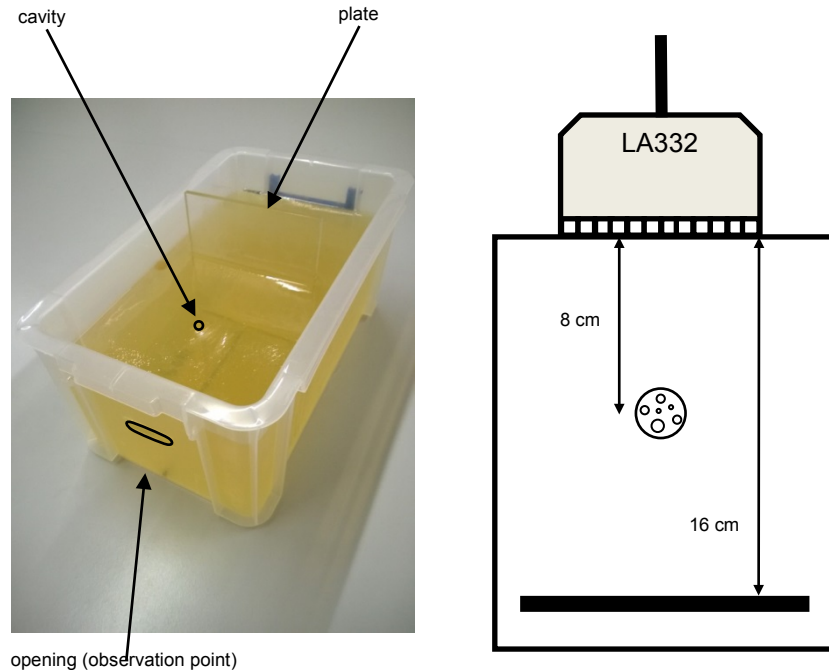


Figure 1: Picture (left) and schematic top view (right) of the phantom.

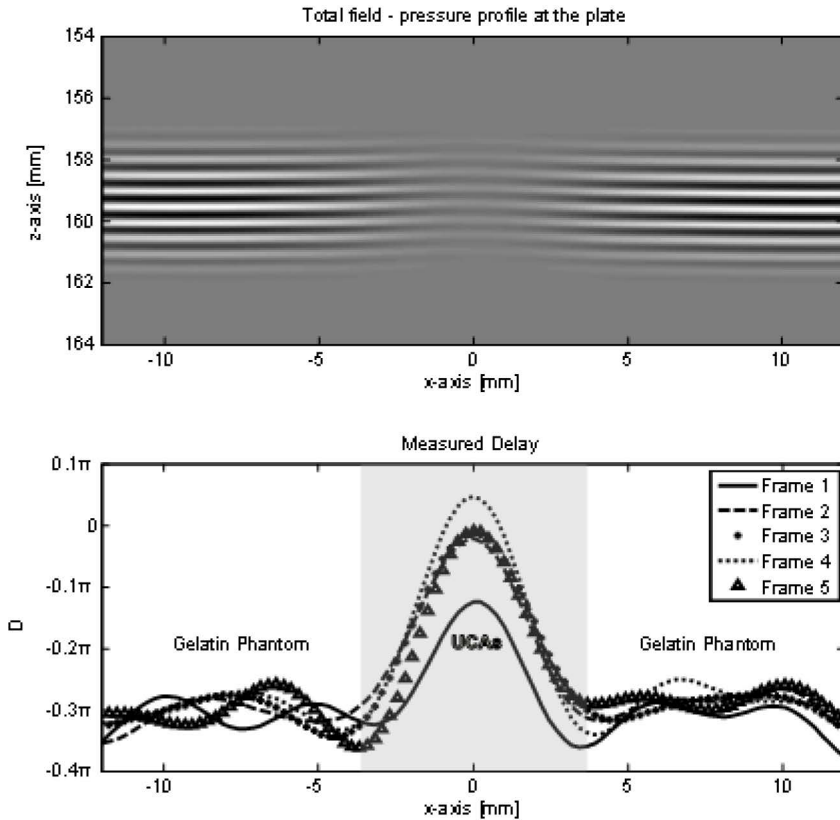


Figure 2: Total field backscattered at the plate (top) and estimated second harmonic to fundamental component cumulative phase delay profile from five consecutive frames (bottom).

The cavity contained a 240 $\mu\text{L/L}$ SonoVue® UCA concentration. The gelatin phantom was scanned with an insonating frequency $f_0 = 3$ MHz and a mechanical index MI = 0.05, measured in water at the cavity location with a HGL-0400 hydrophone (Onda, Sunnyvale, CA). The echoes obtained from the PVC plate were processed as described in [1-2] in order to obtain, for each line imaged, a measure of the cumulative phase delay $D=2\pi\Delta tf_0$, with Δt being the time delay between the second harmonic and the fundamental component. Exploiting the employed linear array, as shown in Figure 2, D can be estimated as a function of space in the lateral direction. The axis of the cylindrical cavity was positioned at $(z,x)=(80 \text{ mm}, 0 \text{ mm})$, with z and x being the axial and lateral direction, respectively, and with the center of the linear array aperture coinciding with the center of the coordinate system.

For this particular in-vitro configuration, we can exploit the symmetry of the target and assume consecutive frames as if acquired from different observation angles. Consequently, a sinogram can be constructed, and an ultrasound image generated in a tomographic fashion using the filtered back-projection method [4].

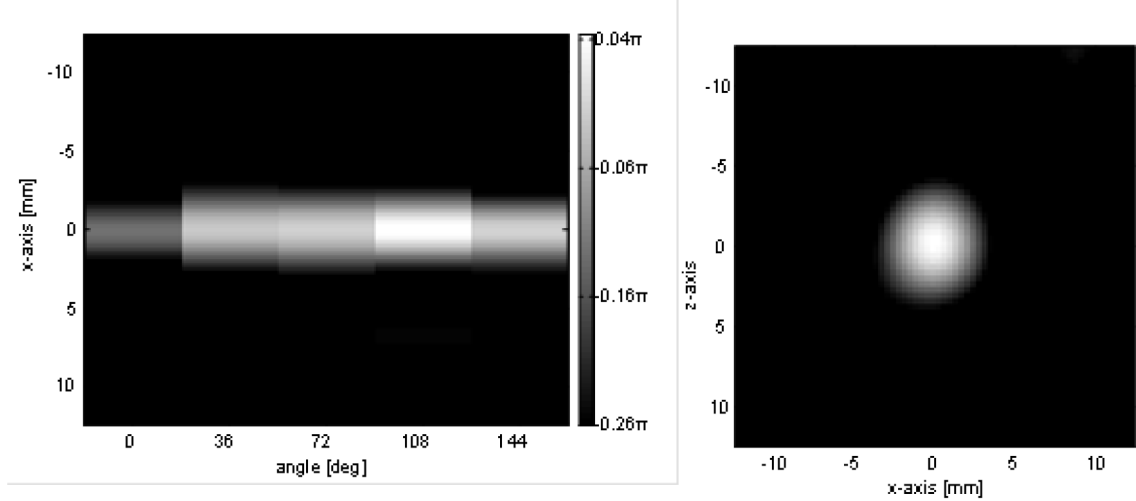


Figure 3: Sinogram (left) and corresponding ultrasound D -image (right) obtained by imaging a 7-mm diameter cavity filled with a 240 $\mu\text{L/L}$ concentration of SonoVue® contrast agent.

Results

Figure 2 (top) shows the total field backscattered at the plate. Attenuation of the total field due to the presence of UCAs in the propagation path can be observed. The bottom plot shows the estimated second harmonic to fundamental cumulative phase delay D from five consecutive frames, as a function of x . This plot shows variations of D in the presence of UCAs along the propagation path, with D increasing for longer propagation path length through UCAs. In particular, a measure of D of approximately -0.3π has been always observed in the absence of UCAs.

Figure 3 shows the sinogram (left) and obtained ultrasound D -image (right) using the filtered back-projection method. Five consecutive frames have been used, and assumed to be acquired at an angle of 0, 36, 72, 108, and 144 degree, respectively.

Conclusion and Discussion

We presented the first ultrasound image based on the cumulative phase delay between second harmonic and fundamental component observed for ultrasound propagating through UCAs. Although a simple set-up was adopted, where the symmetry of the imaged target facilitated the image formation, this result confirms the applicability of the presented cumulative delay as an UCA marker for imaging.

Comparison with standard contrast-enhanced ultrasound imaging modalities, together with the optimization of the acquisition parameters will be the focus of future work. Imaging in the presence of flowing rather than static UCAs will also be investigated.

References

1. L. Demi, G. Russo, H. Wijkstra, and M. Mischi "Observed Cumulative Time Delay Between Second Harmonic and Fundamental Component of Pressure Wave Fields Propagating Through Ultrasound Contrast Agents", *Proceedings of Meetings on Acoustics 20*, San Francisco, 075002, 2013
2. L. Demi, H. Wijkstra, and M. Mischi "Cumulative phase delay between second harmonic and fundamental components - A marker for ultrasound contrast agents", *Journal of the Acoustical Society of America*, 136, pp. 2968 - 2975, 2014
3. E. Boni, L. Bassi, A. Dallai, F. Guidi, A. Ramalli, S. Ricci, R. Housden, and P. Tortoli, "A Reconfigurable and Programmable FPGA based System for non-standard Ultrasound Methods", *IEEE Transactions on Ultrasonics Ferroelectrics and Frequency Control*, 59, pp. 1378—1385, 2012
4. Paul Suetens. *Fundamentals of medical imaging*. Cambridge University Press, 2009

Microbubble-assisted ultrasound induced transient phosphatidylserine translocation

Jean-Michel Escoffre, Marc Derieppe, Bart Lammertink, Clemens Bos, Chrit Moonen

Imaging Division, University Medical Center Utrecht, Utrecht, the Netherlands

Rationale and aim

Membrane sonopermeabilization relies on the transient permeabilization of the plasma membrane of cells exposed to microbubble-assisted ultrasound. This method is currently used *in-vitro* and *in-vivo* due to its efficiency to deliver exogenous molecules while limiting loss of cell viability. However, very little is known about the consequences of membrane sonopermeabilization at the molecular and cellular levels. Progress in the knowledge of the mechanisms involved is a biophysical challenge. The aim of the present study is to investigate the influence of microbubble-assisted ultrasound on the transversal mobility of phospholipids, especially the phosphatidylserines (PS).

Material & Methods

Rat glioma C6 cells were seeded into OptiCell™ culture chambers and were grown as a monolayer until cell confluence for the ultrasound experiments. Fresh complete medium containing 2 µM SYTOX Green (*i.e.*, membrane permeabilization assay) or 20 µM FM 1-43 (*i.e.*, PS externalization assay) and 700 µL of SonoVue® microbubbles (microbubble-to-cell ratio of 20) was injected into the OptiCell™ chamber 15 min before ultrasound exposure. The OptiCell™ chamber was positioned at 8 mm of the mono-element transducer in a deionized water tank at 37°C. The cell-coated surface of the OptiCell™ chamber was on top such that the buoyancy favored contact between the microbubbles and the cells. Subsequently, the cell monolayer was exposed to 1.4 MHz sinusoid ultrasound waves for 30 s with a pulse repetition period of 100 µs, 20 cycles per pulse (*i.e.*, optimal acoustic parameters for transient and efficient membrane permeabilization)². The peak-to-peak acoustic pressure was selected at 200 kPa. After 15 min incubation at 37°C, the percentage of permeabilized cells was evaluated using epifluorescence microscope. The real-time assessment of PS externalization was performed using fibered confocal fluorescence microscopy. The post-sonopermeabilization evolution of PS externalization was monitored using a conventional Annexin-V assay.

² Derieppe M *et al.*, (2012) Mol. Imaging Biol., 15:3-11.

Results

In the present study, *in-vitro* results showed that microbubble-assisted ultrasound induced a significant increase in membrane permeability of C6 cells to non-permeant molecule, SYTOX Green (Data not shown). In our ultrasound conditions, the percentage of permeabilized and living C6 cells were of $45 \pm 4\%$.

To further investigate PS externalization in C6 cells after the exposure of microbubble-assisted ultrasound, C6 cells were stained with the FM 1-43 dye. The membrane insertion of FM 1-43 is a fast process controlled by an electrostatic process whereby negatively charged PS attract the positively charged FM 1-43 from the medium into the plasma membrane. The increase in FM 1-43 membrane insertion induces a fluorescence enhancement. As shown in the Fig. 1, PS externalization was monitored by real-time FM 1-43 fluorescence at the living cell population level using fibered confocal fluorescence microscope. The exposure of cells to microbubble-assisted ultrasound induced a fast increase in fluorescence intensity over time (Figure 1). This result suggested that microbubble-assisted ultrasound induced PS externalization.

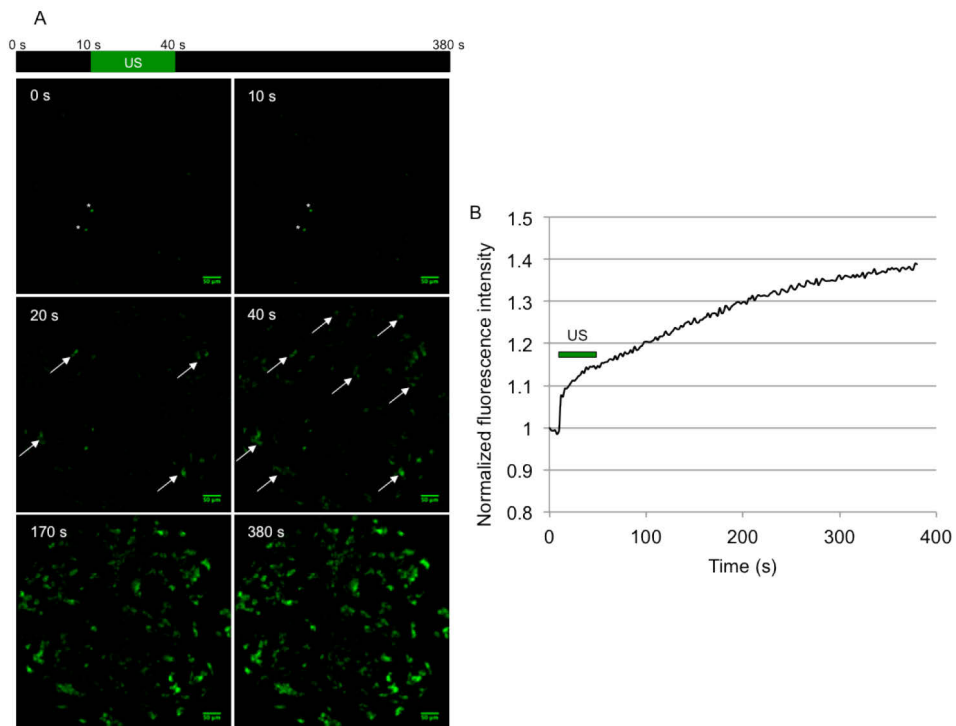


Figure 1: Real-time assessment of PS externalization.

To assess the post-sonopermeabilization evolution of PS externalization, C6 cells were stained with FITC-conjugated Annexin-V at different time points after their exposure to microbubble-assisted ultrasound. As shown in the Fig. 2, the percentage of PS-externalizing cells significantly decreased in the

hours following the sonopermeabilization. This phenomenon was positively correlated to membrane resealing (Pearson's correlation coefficient, 0.99) (Figure 2, insert). Altogether, these results suggest that sonopermeabilization-mediated PS externalization is a transient process. The activation of aminophospholipid translocase during the membrane resealing phase might explain the transient character of this process.

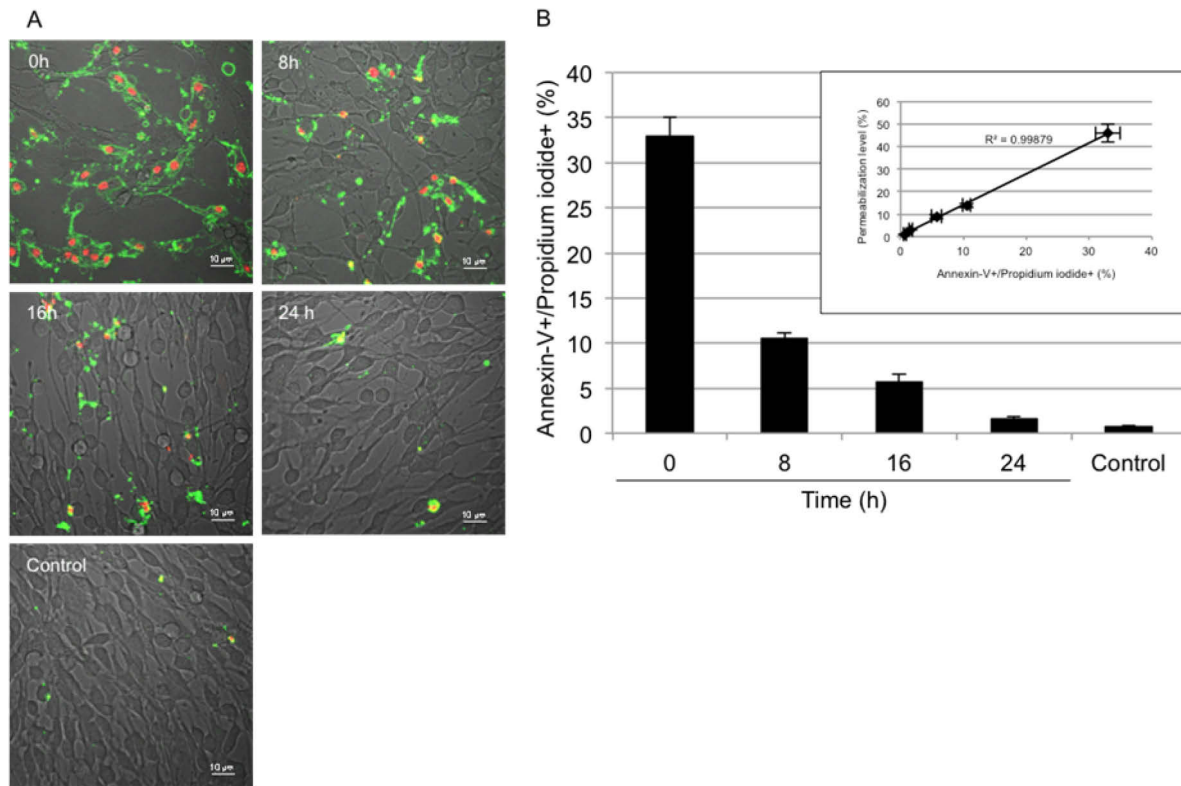


Figure 2: Post-sonopermeabilization evolution of PS externalization.

Conclusions

Microbubble-assisted ultrasound induced a transient phosphatidylserine translocation. The mechanisms involved in such a phenomenon are under investigation.

Acknowledgement

This project was funded by the ERC Advanced Grant – 268906 (CM).

Changes in the physical properties of lipid membranes interacting with ultrasound-activated microbubbles

Dario Carugo^{1*}, Erdinc Sezgin^{2*}, Jorge Bernardino de la Serna^{2*}, Marina Kuimova³, Christian Eggeling² and Eleanor Stride¹

¹*Institute of Biomedical Engineering, University of Oxford, Old Road Campus Research Building, Oxford OX3 7DQ, UK*

²*MRC Human Immunology Unit, Weatherall Institute of Molecular Medicine, University of Oxford, Oxford OX3 9DU, UK*

³*Department of Chemistry, Imperial College London, London SW7 2AZ, UK*

Gas microbubbles stabilised by a surfactant or polymer shell have been extensively used as contrast agents for echocardiography [1], and have demonstrated potential for application in targeted drug delivery of therapeutic compounds [2]. The behavior of a microbubble in an ultrasound (US) field is highly dependent on both the characteristics of the bubble and the US wave. At lower acoustic pressures, microbubbles undergo stable volumetric oscillations which drive the motion of the surrounding fluid (also known as micro-streaming). At higher pressures, microbubbles may collapse generating shock waves and fluid jets [3]. The perturbations of the local hydrodynamic environment caused by US-activated microbubbles are known to cause temporary permeabilisation of cell membranes [4], which can be exploited for intra-cellular delivery of therapeutic compounds, including anti-cancer drugs and genetic material. This technique has enormous potential in the treatment of various pathologies; its translation in the clinical environment is however limited by the lack of quantitative information about the governing bio-physical mechanisms [3]. Insights about the interaction between oscillating microbubbles and cell membranes have been revealed by means of high-speed microscopy [5-7] and fluorescence microscopy [8, 9]; however, there is no available quantitative information about the effect of this interaction on the physical properties of cell membranes.

In the present study we employed advanced microscopy techniques to investigate changes in the physical properties of phospholipid membranes interacting with lipid-shelled microbubbles, either in the presence or in the absence of ultrasound. Multi-layered microfluidic systems were developed to generate an ultrasound field within a confined microenvironment. A piezoelectric element (PZ26, Ferroperm, Denmark) was coupled with the devices, and actuated by a power amplifier driven by a sine-wave from a programmable signal generator (33220A, Agilent Technologies, USA), at a frequency of ~1 MHz (continuous wave).

Dioleoyl-sn-glycero-phosphocholine (DOPC) giant unilamellar vesicles (GUVs) produced by electroformation [10] were employed as model cell membranes [11]. Microbubbles coated with 1,2-distearoyl-sn-glycero-3-phosphocholine (DSPC) and PEG-40 stearate (molar ratio = 9:1) and containing sulphur hexafluoride (SF_6) were produced by sonication, and suspended in phosphate buffered saline (PBS) solution. Quantitative fluorescence microscopy techniques and environmentally sensitive lipid analogue dyes were employed for measuring changes in (i) membrane viscosity and (ii) lipid packing, as a result of the interaction with ultrasound and/or microbubbles. Membrane viscosity was measured by applying fluorescence lifetime imaging microscopy (FLIM) to exploit the viscosity-sensitive photophysical properties of a molecular rotor (BODIPY-C₁₂) [12, 13]. Changes in rotor lifetime were measured under varying experimental conditions, using the Leica TCS SP8 confocal microscope. Membrane lipid packing was indirectly quantified using an environment sensitive fluorophore (C-Laurdan, a derivative of Laurdan [14]), which emission spectrum varies depending on the polarity of the microenvironment. C-Laurdan has two emission peaks, at 440 nm and 490 nm, whose relative intensity changes in ordered *vs* disordered membranes [15]. Membrane lipid/packing order was indirectly measured *via* a relative index called generalized polarization (GP) [16], which has been adopted previously to quantify lipid packing in both bilayered (GUVs and cells) [15, 17] and monolayered [18] systems. Spectral lambda imaging was performed using the Zeiss 780 LSM/FCS confocal microscope.

The results obtained indicate that due to the interaction with DSPC:PEG microbubbles, the viscosity of DOPC membrane bilayers increased, as manifested by the increased lifetime of the BODIPY-C₁₂ rotor (Figure 1a). This effect is enhanced by the application of US but US-alone did not cause statistically significant changes in membrane viscosity (Figure 1a). These observations were corroborated by measurements of lipid packing using C-Laurdan, showing increased packing density for membranes interacting with microbubbles (Figure 1b). Results suggest that there may be a reorganisation of the membrane and/or a compositional change due to lipid exchange between lipid-shelled microbubbles and model membranes. This observation could open exciting perspectives in the field of microbubble-mediated drug delivery, and help understanding the mechanisms governing microbubble-cell interaction and microbubble-mediated delivery of therapeutic compounds. Future work will focus on correlating changes in membrane physical properties with membrane diffusion coefficient and permeability to bioactive molecules, and membrane potential.

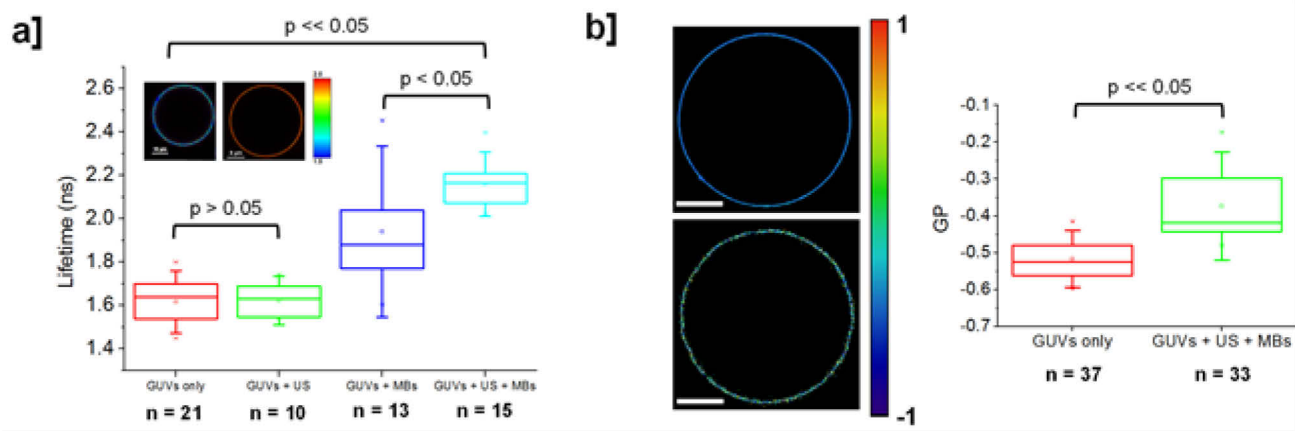


Figure 1: [a] Average BODIPY-C₁₂ rotor lifetime for DOPC GUVs under different experimental conditions. Box plots (with standard deviation) are reported [MBs = Microbubbles]. The inset shows representative contours of lifetime for a GUV in the absence of US and microbubbles (left) and after exposure to US and microbubbles (right). [b] Representative contours of Generalized Polarization (GP) for a GUV in the absence of US and microbubbles (top-left; scale bar = 7.5 μ m) and a GUV exposed to US in the presence of microbubbles (bottom-left; scale bar = 10 μ m). Average GP values are reported on the right. One-way ANOVA was performed among different experimental groups to assess statistical significance.

References

- Stride, E. and N. Saffari, Microbubble ultrasound contrast agents: a review. *Proceedings of the Institution of Mechanical Engineers, Part H: Journal of Engineering in Medicine*, 2003. **217**(6): p. 429-447
- Ferrara, K., R. Pollard, and M. Borden, Ultrasound microbubble contrast agents: fundamentals and application to gene and drug delivery. *Biomedical Engineering*, 2007. **9**
- Lentacker, I., et al., Understanding ultrasound induced sonoporation: Definitions and underlying mechanisms. *Advanced drug delivery reviews*, 2014. **72**: p. 49-64
- Karshafian, R., et al., Sonoporation by ultrasound-activated microbubble contrast agents: effect of acoustic exposure parameters on cell membrane permeability and cell viability. *Ultrasound in medicine & biology*, 2009. **35**(5): p. 847-860
- Hu, Y., J.M. Wan, and A.C. Yu, Membrane perforation and recovery dynamics in microbubble-mediated sonoporation. *Ultrasound in medicine & biology*, 2013. **39**(12): p. 2393-2405
- Moosavi Nejad, S., et al., Optical observation of cell sonoporation with low intensity ultrasound. *Biochemical and biophysical research communications*, 2011. **413**(2): p. 218-223
- Kooiman, K., et al., Sonoporation of endothelial cells by vibrating targeted microbubbles. *Journal of Controlled Release*, 2011. **154**(1): p. 35-41
- Qin, P., et al., Sonoporation-Induced Depolarization of Plasma Membrane Potential: Analysis of Heterogeneous Impact. *Ultrasound in medicine & biology*, 2014. **40**(5): p. 979-989
- Kudo, N., K. Okada, and K. Yamamoto, Sonoporation by single-shot pulsed ultrasound with microbubbles adjacent to cells. *Biophysical journal*, 2009. **96**(12): p. 4866-4876
- Angelova, M.I. and D.S. Dimitrov, Liposome electroformation. *Faraday discussions of the Chemical Society*, 1986. **81**: p. 303-311
- Bagatolli, L. and E. Gratton, Two photon fluorescence microscopy of coexisting lipid domains in giant unilamellar vesicles of binary phospholipid mixtures. *Biophysical journal*, 2000. **78**(1): p. 290-305
- López-Duarte, I., et al., A molecular rotor for measuring viscosity in plasma membranes of live cells. *Chemical Communications*, 2014. **50**(40): p. 5282-5284
- Hosny, N.A., et al., Mapping microbubble viscosity using fluorescence lifetime imaging of molecular rotors. *Proceedings of the National Academy of Sciences*, 2013. **110**(23): p. 9225-9230
- Weber, G. and F.J. Farris, Synthesis and spectral properties of a hydrophobic fluorescent probe: 6-propionyl-2-(dimethylamino) naphthalene. *Biochemistry*, 1979. **18**(14): p. 3075-3078
- Sezgin, E., T. Sadowski, and K. Simons, Measuring lipid packing of model and cellular membranes with environment sensitive probes. *Langmuir*, 2014
- Parassassi, T., et al., Quantitation of lipid phases in phospholipid vesicles by the generalized polarization of Laurdan fluorescence. *Biophysical journal*, 1991. **60**(1): p. 179-189

17. Gaus, K., et al., *Visualizing lipid structure and raft domains in living cells with two-photon microscopy*. *Proceedings of the National Academy of Sciences*, 2003. **100**(26): p. 15554-15559
18. Bernardino de la Serna, J., et al., *Compositional and structural characterization of monolayers and bilayers composed of native pulmonary surfactant from wild type mice*. *Biochimica et Biophysica Acta (BBA)-Biomembranes*, 2013. **1828**(11): p. 2450-2459

Effectiveness and limits of plane wave contrast imaging for moving contrast agents

Jacopo Viti^{1,2}, Francesco Guidi², Hendrik J. Vos¹, Nico de Jong¹, Piero Tortoli²

¹*Biomedical Engineering, ErasmusMC, Rotterdam, The Netherlands*

²*Information Engineering Dept., Università degli Studi di Firenze, Italy*

Plane wave ultrasound imaging inherently couples high frame rate with low peak pressure. It thus represents an interesting candidate to perform nondestructive detection of ultrasound contrast agents (UCA) flowing in a vessel. As multiple angled plane waves (APW) can be compounded to create a single, higher-resolution frame, plane wave imaging can offer a resolution similar to traditional (focused) contrast imaging, while delivering a superior SNR when operating in a nondestructive regime. In this work, the ULA-OP research platform is programmed to allow comparing the contrast-to-background ratio (CBR) obtainable by focused (F) and APW imaging combined with amplitude modulation (AM), when very low pressure ultrasound is used. In an AM image, we define as “background” the signal detected in regions where UCAs are not present. This signal originates from the combination of both random noise and undesired contributions such as artefacts and residual tissue echoes. The influence of both the number of compounded plane waves and the flow speed of the UCA are investigated to identify an optimal tradeoff for CBR performance.

BR-14 UCA (Bracco Medical Imaging, Switzerland) with 1:2000 dilution was forced to flow in a flow phantom (ATS 524 flow phantom, ATS Laboratories, Inc. Bridgeport, CT. USA), containing a wall-less vessel with a diameter of 6 mm, surrounded by tissue mimicking material (TMM).

A linear array probe LA332 (Esaote, Italy) was placed on top of the phantom and connected to the ULA-OP system to perform F-AM and APW-AM contrast imaging. 4-cycle, Gaussian weighted pulses at 3.5 MHz were transmitted, using an active aperture of 64 elements. In F-AM, the transmission (TX) was focused on the vessel, located at 25 mm depth; in APW-AM a programmable number of angled transmissions (N, range: 1-63) was used, covering a total scanning angle of 13 degrees.

The peak-negative pressure (PNP) was 140 kPa at the vessel’s location for both methods, which was low enough to avoid destruction. For each line (in F-AM) or each scan angle (in APW-AM) a 3-pulse AM sequence (50/100/50% TX amplitude) was transmitted at a 166 µs inter-pulse interval.

Raw RF data were processed offline to produce 64-line B-Mode AM images, see Figure 1. Note that the appearance of the speckle pattern is very different between APW and Focused, due to the different reconstruction strategies: in F-AM, each image line is reconstructed from a separate TX/RX. This is not the case for APW, where image lines are acquired simultaneously, and thus contributions from one line can influence the neighboring lines as well. This determines a different speckle pattern, as well as a worse lateral resolution in APW where compounding is not applied. Two equal-sized regions of interest (ROIs) were selected in the images, covering the UCA and a region of TMM, respectively. The CBR was calculated as the ratio of the RMS pixel brightness measured for each ROI.

The CBR measured in different experimental conditions is reported in Table 1. F-AM performs similarly to single angle APW-AM; this is consistent with the fact that in both cases each image pixel is hit by the same AM set (three TX). Compounding significantly improves the CBR, as the random noise component of the background is averaged out until only the residual tissue contribution remains, increasing the SNR, and thus the CBR. When using a low flow speed, compounding up to 63 angles is possible, albeit increasing N from 9 to 63 brings only minor gradual improvements, if any, on the final CBR. This is due to decorrelation of the UCA signal over consecutive scan angles, which partly destroys the UCA signal when compounding many angles, negating the SNR gain. As the UCA decorrelation is proportional to UCA motion, using a large N is even more detrimental to CBR when a high flow speed is used, with performance degrading steadily for $N > 15$: after the random noise in the background is suppressed, the residual tissue component of background is a coherent signal, whereas the UCA is not; therefore only the latter is progressively reduced by angle compounding, resulting in a net CBR degradation. In Figure 1, using $N=63$ is visibly worse than $N=9$, as the decreased UCA signal results in reduced image contrast, after normalization; on the other hand, a compound of 9 angles can be used to simultaneously achieve a good image resolution and a CTB increase of 5-8 dB over F-AM.

In conclusion, collected data indicate that APW-AM can usually be more sensitive than F-AM when performing detection of UCA in a low pressure regime. Moreover a few compounding angles (in the range of 10) may be sufficient to guarantee good performance in terms of resolution and offer a high CBR in both low and fast flow conditions, thus making high frame rate contrast imaging actually feasible. Finally, a high number of compounded angles could be conceivably used to discriminate between slow and fast moving contrast when imaging a complex network of vessels.

CBR (dB) @ 140kPa PNP		
	55 mm/s flow	20 mm/s flow
APW-AM 1-angle (N=1)	26.1	25.8
APW-AM 3-angles (N=3)	30.0	29.1
APW-AM 9-angles (N=9)	33.1	32.9
APW-AM 15-angles (N=15)	33.2	33.6
APW-AM 31-angles (N=31)	31.6	34.9
APW-AM 63-angles (N=63)	28.6	33.3
Focused AM	25.7	25.5

Table 1 : Measured CTB for 140kPa PNP, when two different mean flow speed are imposed.

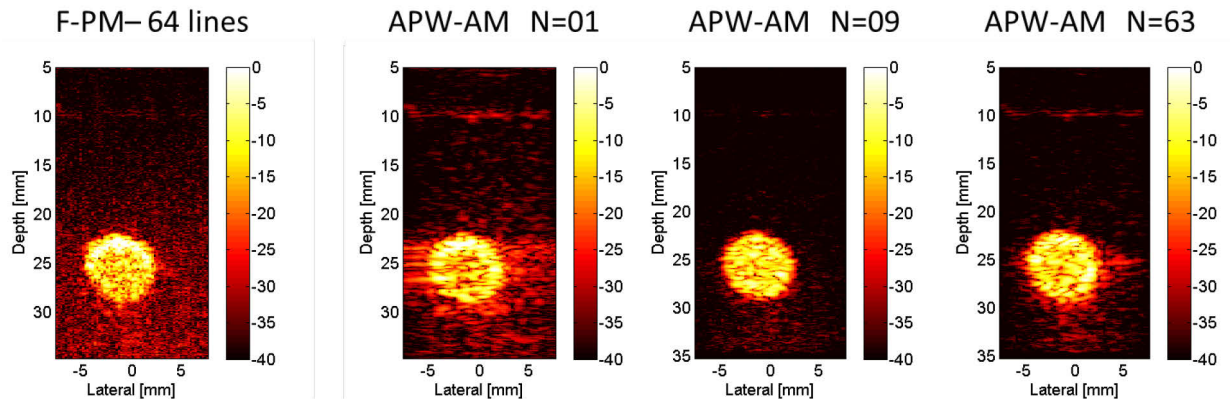


Figure 1 : B-Mode AM frames at 140kPa PNP and 110 mm/s peak flow speed. Frames are normalized, with a 40 dB dynamic range.

Dual frequency acoustic droplet vaporization detection for medical imaging

Christopher B. Arena, Anthony Novell, Paul S. Sheeran, Connor Puett, Linsey C. Moyer, and Paul A. Dayton

Joint Department of Biomedical Engineering, The University of North Carolina and North Carolina State University, Chapel Hill, NC 27599, USA

Background, motivation and objectives

Liquid-filled droplets emit a unique acoustic signature when vaporized into gas-filled microbubbles using ultrasound [1]. We have developed a system to generate ultrasound images from vaporization events using a dual frequency transducer design that receives signals at 1/8 the insonification frequency. Here, a pilot study was conducted by imaging a tissue-mimicking flow phantom to explore the spatial aspects of droplet vaporization and investigate the effects of applied pressure and droplet concentration on image contrast and resolution.

Material and Methods

Droplets were generated by condensing microbubbles with an octafluoropropane gas core according to established techniques [2]. The tissue-mimicking phantom tested was constructed by embedding a microcellulose tube (250 µm outer diameter) inside a gellan gum base material. A 0.3% concentration of droplets diluted in PBS was continuously infused through the tube at 50 µl/min using a syringe pump. The ‘pulse high, listen low’ methodology, previously described in [1], was implemented to isolate vaporization signals. To this purpose, a confocal, dual-frequency transducer was used to transmit at 8 MHz and passively receive at 1 MHz. LabVIEW was used to raster the transducer in the elevational (4 mm, 121 µm step size) and lateral (3 mm, 125 µm step size) dimensions. At each location, five radiofrequency (RF) lines were acquired and stored offline for analysis. In the tissue phantom, the peak negative pressures (PNP) at the focus were 160, 450, 640, 700, and 770 kPa (after accounting for phantom attenuation).

Results, discussion and conclusion

At low pressures, droplet signals were of significantly higher energy than microbubble signals (Figure 1a). This resulted in improved signal separation and high contrast-to-tissue ratios (CTR) (Figure 1b). A steep increase in CTR occurred when the PNP rose above the threshold pressure for droplet activation (between 160 and 450 kPa). Specifically, when a PNP of 450 kPa was transmitted, the CTR was 17.7 dB for droplets and -0.3 dB for microbubbles. In post-processing, time-domain averaging was used to improve the detection of droplet vaporization signals. Droplet vaporization signals varied in amplitude,

frequency, and phase to a greater extent than microbubble signals and tissue signals received at 1/8 the insonification frequency. This is due to the stochastic nature of droplet activation (i.e., not all transmit events induce vaporization, even when the PNP is above the threshold for activation) as well as the dependence of the vaporization signal on droplet size.

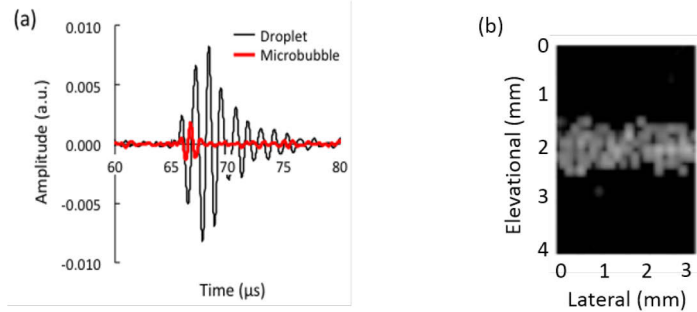


Figure 1: (a) Acoustic signals from different contrast agents infused through the tissue-mimicking phantom. The concentration of droplets and microbubbles was 0.3%, and the peak negative pressure (PNP) at the focus was 700 kPa. (b) Example of images formed from droplet vaporization signals in the tissue mimicking phantom.

The axial resolution in droplet images was related to the size of the initial droplet and the center frequency of the receive transducer. In general, smaller droplets exhibit higher frequency signals that decay faster and correlate with improved axial resolution. With the transducer and droplet population tested here, the axial resolution at 450 kPa was 3.86 mm. The lateral resolution was dictated by the droplet activation area. Lower pressures resulted in smaller activation areas and correlated with improved lateral resolution. At 450 kPa, the lateral resolution for droplets was 0.67 mm.

Taken together, these results indicate that it is possible to generate high-sensitivity, high-contrast images of vaporization events, providing a unique method of imaging phase change contrast agents. In the future, this imaging approach has the potential to be applied in combination with droplet-mediated therapy to track treatment outcomes or as a stand-alone diagnostic system to monitor the physical properties of the surrounding environment.

References

1. P. S. Sheeran, T. O. Matsunaga, and P. A. Dayton, 'Phase Change Events of Volatile Liquid Perfluorocarbon Contrast Agents Produce Unique Acoustic Signatures', *Phys Med Biol*, 59 (2014), 379-401
2. P. S. Sheeran, S. H. Luo, L. B. Mullin, T. O. Matsunaga, and P. A. Dayton, "Design of ultrasonically-activatable nanoparticles using low boiling point perfluorocarbons," *Biomaterials*, vol. 33, pp. 3262-3269, Apr 2012

A multi-technique investigation of the effect of coating composition on microbubble behaviour

Paul Rademeyer¹, Dario Carugo¹, Erdinc Sezgin², Jorge Bernardino de la Serna², Cen Zhang¹, Joshua Owen¹, Eleanor Stride¹

¹ Institute of Biomedical Engineering, University of Oxford, United Kingdom

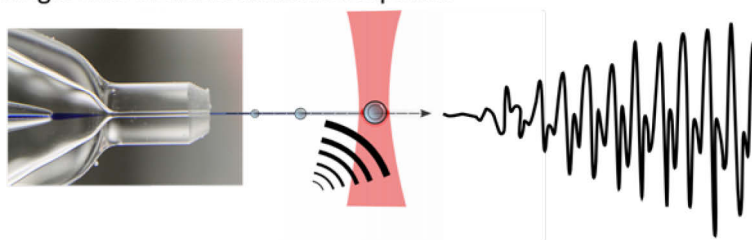
² MRC Human Immunology Unit, Weatherall Institute of Molecular Medicine, University of Oxford, United Kingdom

The composition of a microbubble's coating is known to influence both its physical and biological properties, affecting its response to ultrasound excitation, stability and circulation dynamics *in vivo*. Unfortunately, the underlying mechanisms are poorly understood and there is currently little empirical evidence to support or characterise the effect of composition. Better understanding and methods for assessing this effect are crucial for the optimisation of microbubbles for current contrast enhanced ultrasound imaging techniques and particularly for quantitative diagnostic and therapeutic applications, such as sonothrombolysis and drug delivery.

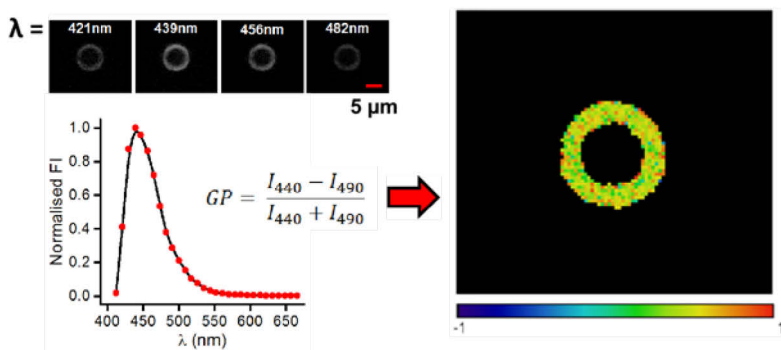
In this study we present and compare data from three characterisation techniques recently developed in house, Fig 1: (i) large sample analysis of single microbubble acoustic response [1], (ii) analysis of lipid surface concentration using quantitative fluorescence microscopy [2] and (iii) observation of quasi-static microbubble response in a pressure chamber. The combination of these techniques allows for a systematic study of the effect of microbubble coating composition as well as to examine the variation in properties within a microbubble population. In this work we specifically investigated the effect of varying the ratios of phospholipid (DSPC) to emulsifier (PEG-40 stearate), and the addition of functional components such as cholesterol or targeting vehicles (i.e., magnetic nanoparticles). For comparison, data were also obtained for the commercial contrast agent SonoVue® (Bracco Imaging s.P.A.).

The results obtained indicate that coating composition can significantly affect a microbubble's acoustic response; however, the manufacturing techniques investigated in this work generate microbubble populations with significant variability between individual bubbles.

(i) Single microbubble acoustic response



(ii) Quantitative fluorescence microscopy



(iii) Quasi-static microbubble response in a pressure chamber

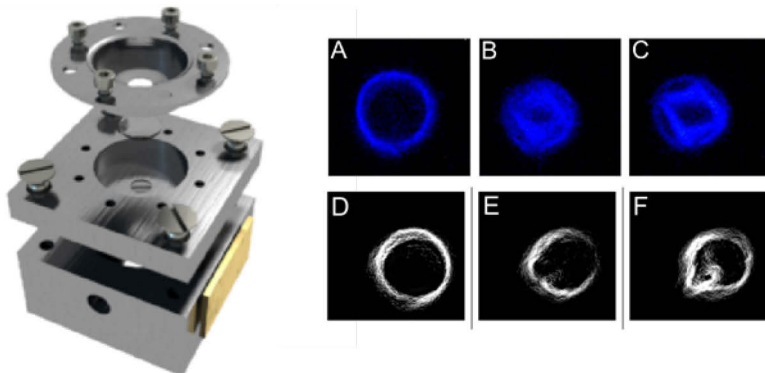


Figure 1: Techniques to investigate the effect of coating composition of microbubble behaviour: (i) Unconstrained single microbubble response to ultrasound is obtained using a hydrodynamically focussed flow through a focussed laser beam, high throughput ($n > 10,000$) enables statistical analysis, (ii) Lipid packing estimation using fluorescence microscopy and (iii) the observation of microbubbles under quasi-static pressure changes provides a method for estimating the coating stiffness and behaviour of the lipid (bottom right images: A-C demonstrate buckling, D-F demonstrate lipid shedding or 'budding', enhanced using edge detection).

References

1. Rademeyer, P., Carugo, D., Lee, J. and Stride, E., Microfluidic System for High Throughput Characterisation of Echogenic Particles, *Lab on a Chip*, 2014, DOI: 10.1039/C4LC01206B
2. Sezgin, E., Sadowski, T. and Simons, K., Measuring lipid packing of model and cellular membranes with environment sensitive probes. *Langmuir*, 2014, DOI: 10.1021/la501226v

Effect of the acoustic pressure on the uptake kinetics of sytox green model drug in sonopermeabilization

Marc Derieppe¹, Bart Lammertink¹, Baudouin Denis de Senneville^{1,2}, Clemens Bos¹, Chrit Moonen¹

¹*Imaging Division, University Medical Center Utrecht, Utrecht, the Netherlands*

²*IMB, UMR 5251 – CNRS – Université Bordeaux 1 – INRIA, Bordeaux, France*

Introduction

Ultrasound (US)-activated microbubbles (MB) can be used to enhance intracellular delivery of (model) drugs, a process termed sonopermeabilization. The underlying mechanisms remain to be fully understood, but there is evidence that pore-like structures are formed and endocytosis is up-regulated upon ultrasound exposure. Current belief is that higher acoustic pressures induce a greater number and larger sized pore-like structures. In this study, we hypothesize that higher acoustic pressures also induce a faster delivery of Sytox Green model drug, and investigate it using Fibered Confocal Fluorescence Microscopy (FCFM).

Methods

C6 rat glioma cells were seeded in Opticell™ culture chambers to reach confluence at the time of the US experiment. For the real-time monitoring of sonopermeabilization, uptake of Sytox Green fluorescent dye (600 Da) was triggered with 1.5 MHz US (Duty Cycle 10%, Pulse Repetition Frequency 1 kHz, Exposure Time 10 seconds) with acoustic pressures from 0.1 MPa to 1.2 MPa peak-to-peak, in the presence of Sonovue® MB. This has been conducted at 2 µM and 20 µM of Sytox Green. Uptake in each nucleus was monitored in real-time using FCFM, as described in [1] and [2]. After detecting and tracking the nuclei, the uptake rates were obtained from fitting a two-compartment model to the fluorescence intensity data with the 3 following parameters: asymptotic signal (maximum signal intensity), signal onset and uptake rate [1]. Statistical analysis of the uptake kinetics was performed using the Kruskall-Wallis test, and magnitudes are expressed as median (\pm interquartile range). Right after the real-time monitoring of the model drug uptake, the number of permeabilized cells in the sonicated area was assessed using a Keyence epifluorescence microscope (Keyence International, Belgium) with the mosaicing module. The number of permeabilized cells in the sonicated area are presented as mean (\pm standard deviation).

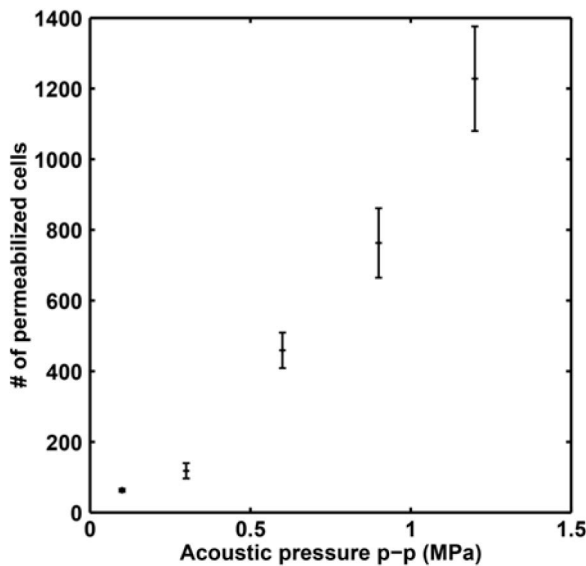


Figure 1: Impact of the acoustic pressure on the number of permeabilized cells in the sonicated area, (epifluorescence microscope).

Results

Cells subjected to higher acoustic pressures displayed a significantly increased number of permeabilized cells, from 63 ± 4 cells at 0.1 MPa, to 1228 ± 147 cells at 1.2 MPa (Fig. 1). For the real-time monitoring of the uptake, within one Sytox Green concentration, the pharmacokinetic parameters displayed non-significant differences of the asymptotic signal from 0.1 MPa to 1.2 MPa (Fig. 2). At the same acoustic pressure, a greater asymptotic signal was observed at 20 μ M of Sytox Green compared to 2 μ M.

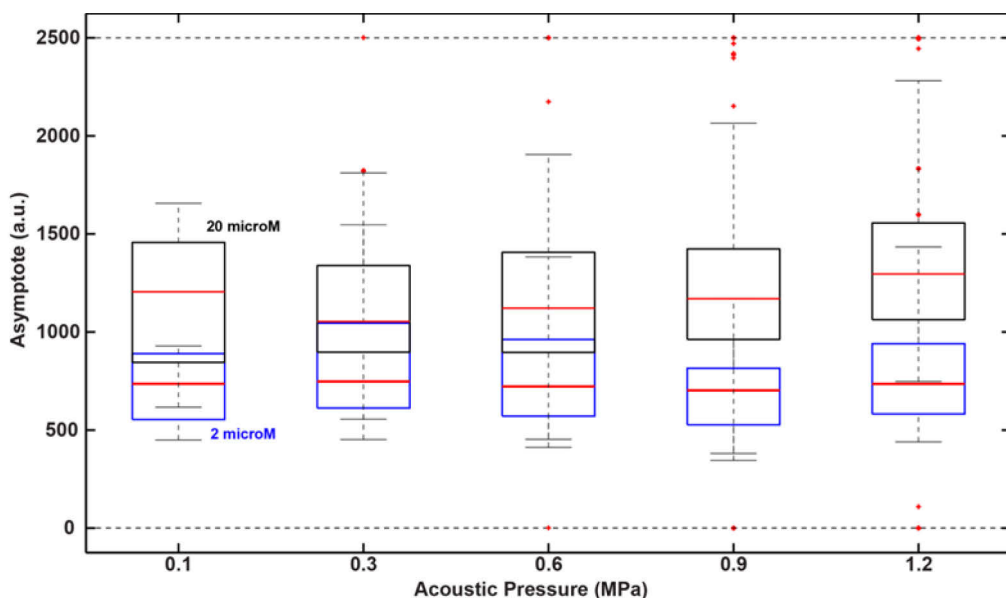


Figure 2: Impact of the acoustic pressure (0.1 MPa to 1.2 MPa) on the asymptotic fluorescence signal, at 2 μ M (blue boxes) and 20 μ M (black boxes) of Sytox Green.

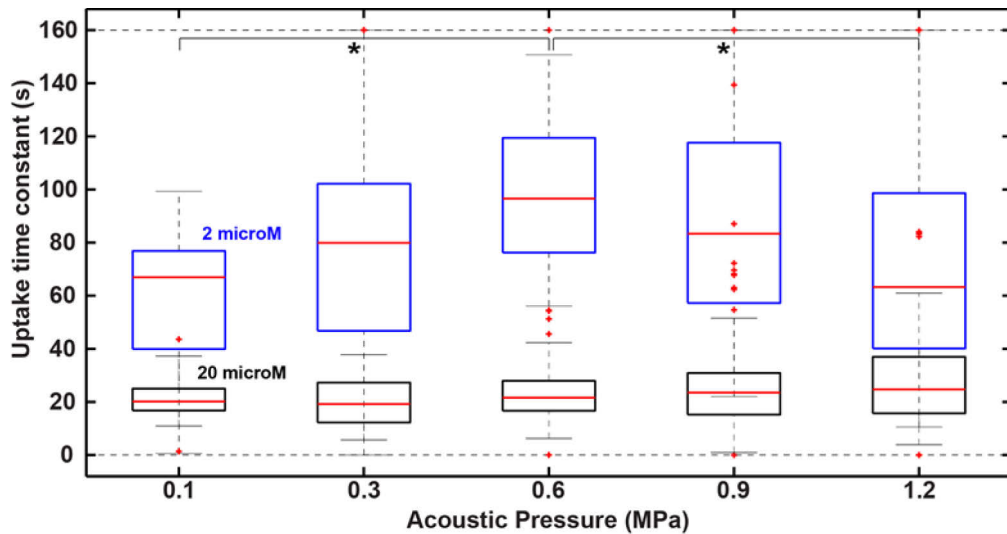


Figure 3: Impact of the acoustic pressure (0.1 MPa to 1.2 MPa) on the uptake rate $1/k$, at 2 μM (blue boxes) and 20 μM (black boxes) of Sytox Green. * $p < 0.05$.

At 2 μM of Sytox Green (Fig. 3), the uptake rate $1/k$ showed no clear trend as a function of the acoustic pressure, with a small but significant difference at 0.6 MPa: 1'37" (43"). At 20 μM , no significant difference could be observed between the time constants for the different acoustic pressures: 20" (8"), 19" (15"), 22" (11"), 23" (16"), and 25" (21").

Conclusion

US-induced uptake of Sytox Green occurred in more cells with higher acoustic pressure, as also found in [3], but did not show a clear variation in the uptake kinetics. Since it is known that larger pores are formed with increasing acoustic pressure in the presence of MBs, the finding that uptake rates do not depend on acoustic pressure indicates that the size of the pores does not limit the uptake rate of the model drug.

References

1. Derieppe et al. 2013, *Mol. Im. Biol.*
2. Derieppe et al. 2014, *Mol. Im. Biol.*
3. De Cock et al. 2014, *J. Control. Rel.*

ON-CHIP production and characterization of nanometer sized bubble populations

Sally A. Peyman*, James McLaughlan, ** Gemma Marston,[§] Steven Freear, ** P. Louise Coletta[§] and Stephen D. Evans*

*School of Physics and Astronomy, University of Leeds, UK. LS2 9JT

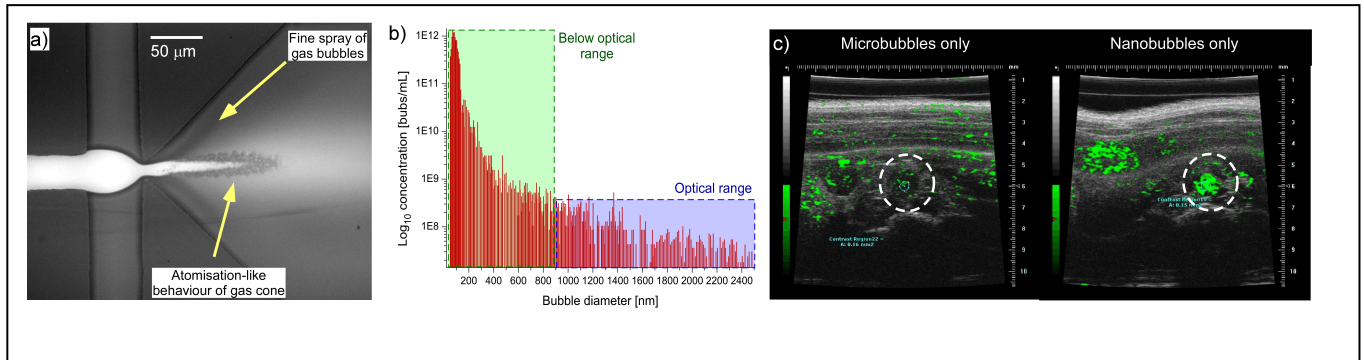
**School of Electronics and Electrical Engineering, University of Leeds, UK. LS2 9JT

[§]Leeds Institute for Molecular Medicine, St James's Hospital, Leeds, UK LS9 7TF

Lipid stabilized, micron sized gas-in-water emulsions have been utilised for many years as contrast agents for ultrasound (US). Due to their compressibility, sound waves are reflected and scattered from the gas / liquid interface, enhancing imaging. Ultra-fine populations of pico- and nano- sized bubbles have also found use as highly effective cleaning agents in floatation techniques in the mining and microfabrication industries.

Microfluidics has already been demonstrated for producing monodisperse microbubble populations by utilizing flow focusing geometries.[1-3] We have reported the use of a 3D expanding geometry for the preparation of high concentrations of microbubble contrast agents using a new ‘microspray’ production regime. [4] Recently, the microspray production regime has been investigated as a potential method for producing nano-meter sized, ‘ultra-fine’ bubble populations. The microspray regime produces bubbles in an atomization-like method generated by the high velocities inside the chip nozzle being subjected to a sudden and severe pressure drop as the outlet expands in the 3D planes (Figure 1a). As mentioned, this has successfully and robustly produced very high concentrations of microbubbles previously; however the histograms produced when counting optically indicated that a high number of bubbles were not being counted due to limitations in optical resolution. An alternative method for sizing and counting particles utilizing nanopore technology (qNano, Izon, UK) was used to characterize populations below the optical resolution. Larger, microbubble populations were separated over time by allowing bubbles to rise after formation and the subnatant collected. The qNano detected large numbers of particles (10^{10} - 10^{11} particles / mL) with diameters $< 1\mu\text{m}$ (See figure 1b). In order to determine whether these particles were acoustically active (bubbles) or not (liposomes) the samples were investigated using a 15 MHz transducer and compared to commercially available contrast agents (Sonovue) and liposomes of a similar diameter. The subnatant sample showed large amounts of backscatter at higher frequencies compared to liposomes of a similar size, suggesting the presence of a gas core. Further *in vitro* investigations in mouse aorta compared the nanobubble subnatant to 1) the whole bubble sample (micro- and nano- mixed) and also 2) micron sized bubbles only. The nanobubble sample showed greater contrast intensity compared to microbubbles alone using a 40 MHz transducer

(figure 1c), and a similar contrast intensity to the whole bubble sample, suggesting the presence of nanobubbles contributes significantly to the observed contrast intensity in contrast agents.



References

1. K. Hettiarachchi, E. Talu, M. L. Longo, P. A. Dayton and A. P. Lee, *Lab on a Chip*, 2007, 7, 463-468
2. E. Castro-Hernandez, W. van Hoeve, D. Lohse and J. M. Gordillo, *Lab on a Chip*, 2011, 11, 2023-2029
3. M. Seo, I. Gorelikov, R. Williams and N. Matsuura, *Langmuir*, 2010, 26, 13855-13860
4. S. A. Peyman, R. H. Abou-Saleh, J. R. McLaughlan, N. Ingram, B. R. G. Johnson, K. Critchley, S. Freear, J. A. Evans, A. F. Markham, P. L. Coletta and S. D. Evans, *Lab on a Chip*, 2012, 12, 4544-4552

Modeling of the dynamics of volatile phase-change contrast agents

Alexander A. Doinikov¹, Paul S. Sheeran², Ayache Bouakaz¹ and Paul A. Dayton²

¹INSERM U930, Université François Rabelais, Tours 37032, France

²Joint Department of Biomedical Engineering, University of North Carolina at Chapel Hill, Chapel Hill, NC 27599

Background

Interest in perfluorocarbon (PFC) phase-change contrast agents (PCCAs) is motivated by the fact that they can be triggered to transition from the liquid state to the gas state by an externally applied acoustic pulse. This property opens up new approaches to ultrasound imaging and therapy. Insight into the physics of this process is vital for effective use of PCCAs and for anticipating bioeffects. The aim of our study was (i) to develop an improved theoretical model that describes the conversion of a PFC droplet into a vapor bubble and subsequent bubble evolution and (ii) to validate this model by comparison with *in vitro* experimental data. The development of the model was specifically aimed at exploring the complex behavior which is demonstrated by volatile PFC droplets experimentally but has not been well-described theoretically so far.

Methods

The derivation of the model is based on applying the mathematical methods of fluid dynamics and thermodynamics to the process of the acoustic vaporization of PFC droplets. The validation of the model was carried out by comparing simulated results with *in vitro* experimental data acquired by ultra-high-speed video microscopy for octafluoropropane (OFP) and decafluorobutane (DFB) microdroplets of different sizes.

Results

The developed model describes the following processes: the growth of a vapor bubble, triggered by an US pulse, inside a PFC droplet until the droplet is completely converted into the bubble, the over-expansion of the vapor bubble and subsequent damped oscillations of the bubble until settling to a final diameter. The model consists of the following equations: (1) Equation for the radius of the vapor bubble, (2) Equation for the radius of the PFC droplet, (3) Equation for vapor pressure inside the bubble, (4) Equation for vapor temperature inside the bubble, (5) Equation for vapor density inside the bubble, (6) Equation for mass flux through the bubble surface, (7) Equation for temperature inside the droplet. The conversion of the PFC droplet into the vapor bubble and subsequent bubble evolution is modeled by numerically solving the above equations. The numerical solution is realized by the collocation method with the use of Chebyshev polynomials. An example of comparison of simulated

and experimental results is shown in Fig.1.

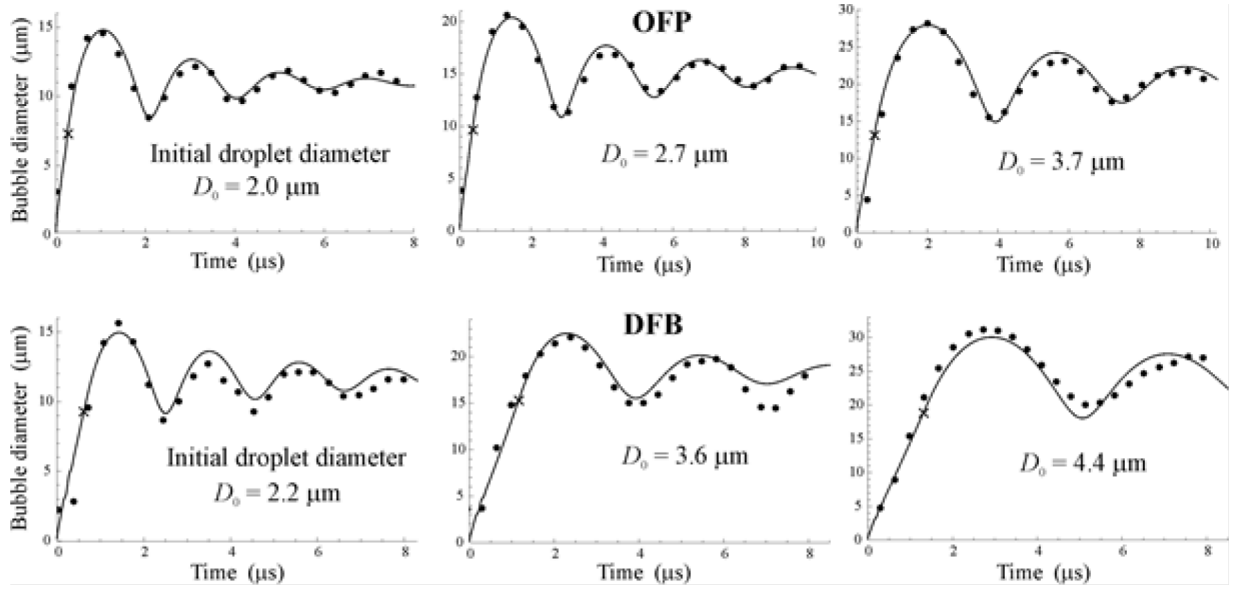


Figure 1: Comparison of simulated and experimental results for OFP and DFB droplets with different initial diameter D_0 .

Figure 1 shows the evolution of the diameter of the vapor bubble in time. The circles correspond to the experimental data and the solid lines show the simulated results. The crosses on the solid lines show the moment when, as the model predicts, the droplet completely turns into vapor. The simulated results were fitted to the experimental data by the least squares method. The fitting was carried out by varying two model parameters: viscosity and surface tension of the liquid surrounding the PFC droplet. The values of other model parameters were set to correspond to the material properties of gaseous and liquid PFC (OFP and DFB, respectively) and were kept invariable during fitting.

Conclusions

The good agreement between the theoretical and experimental results suggests that the developed model is able to correctly describe the key physical processes underlying the vaporization dynamics of volatile PFC droplets. The necessity of varying the parameters of the surrounding liquid for fitting the experimental curves can be explained by the fact that the parts of the initial phospholipid shell of PFC droplets remain on the surface of vapor bubbles at the oscillatory stage and their presence affects the bubble dynamics.

3D contrast-ultrasound dispersion imaging by mutual information analysis in prostate cancer

Stefan G. Schalk^{1,*}, Libertario Demi¹, Martijn Smeenge², Jean J.M.C.H de la Rosette², Hessel Wijkstra^{1,2}, Massimo Mischi¹

¹Eindhoven University of Technology, Dept. of Electrical Engineering, Eindhoven, the Netherlands

²Academic Medical Center, Dept. of Urology, Amsterdam, the Netherlands

Introduction

A major problem in prostate cancer (PCa) is the invasiveness and the low sensitivity of the most commonly used diagnostic tool: systematic biopsy [1], [2]. Currently, many researchers are developing new techniques for PCa localization based on MRI or ultrasound to enable targeting the biopsy needle to a tumor to reduce the number of biopsy samples required for a diagnosis, while boosting the diagnostic sensitivity [3]–[5]. Ultrasound imaging has the advantages over MRI of being less expensive, applicable at the bedside, and more practical for biopsy guidance.

Recently, contrast-ultrasound dispersion imaging (CUDI) [6] has been developed as a new ultrasound-based technique to detect angiogenesis in PCa. In CUDI, a bolus of ultrasound contrast agent (UCA) is intravenously injected and its kinetics recorded over time by transrectal contrast-enhanced ultrasound (CEUS). Initially, a local density random walk model was fitted to the resulting indicator dilution curves (IDCs) in each pixel, resulting in a map of a dispersion-related parameter κ [6]. Later, the similarity between neighboring IDCs was proven to be strongly related to κ [7]. Following this theory, temporal correlation r and spectral coherence ρ have been adopted as similarity measures to localize PCa [7]–[9]. In a recent publication, a similar approach has been investigated while using mutual information as a more general, statistical similarity measure [10]. A preliminary validation involving 26 datasets in 15 patients resulted in a sensitivity, specificity, and ROC curve area of 84%, 85%, and 0.92, respectively.

Until now, CUDI by mutual information has been implemented in 2D only. As a result, each imaging plane requires a separate bolus injection of UCA and out-of-plane information cannot be used for the dispersion analysis. In this work, CUDI by mutual information is implemented in 3D, following the same strategy adopted for r and ρ [11] to overcome the aforementioned issues. A preliminary validation was performed on 4D datasets from two patients.

Material and Methods

4D CEUS recordings were made in 2 patients using a LOGIQ E9 scanner (GE Healthcare, Fairfield, CT) equipped with an RIC9-5 probe after a peripheral intravenous injection of 2.4 mL SonoVue® (Bracco, Geneva). The MI was set to a low value (0.09-0.13) to reduce disruption of UCAs. All 3D CEUS recordings were preprocessed by a speckle regularization filter [11] to compensate for the depth-dependency and anisotropy of the spatial resolution. Instead of using a square or block-shaped kernel as proposed in [10], we used a hollow, shell-shaped one as proposed in [11]. In this way, a bias in similarity caused by spatial correlation of IDCs due to the intrinsic limited resolution of the CEUS data is avoided. Different from 2D CUDI, no temporal filtering was applied in 3D CUDI and the time window of 9 s proposed in [10] was extended to 25 s, because of the low temporal resolution (0.26 Hz) of 4D CEUS. For the same reason, the number of quantization levels was reduced from 256 to 64 to deal with grey level sparsity prior to the statistical analysis. As a preliminary validation, the mutual information maps obtained by 3D CUDI were compared with results from 12-core systematic biopsies.

Results

Figures 1 and 2 show the 3D CUDI maps by mutual information for one plane in patient 1 and 2, respectively. Additionally, the biopsy results are given in the coronal plane, where the approximate locations of the imaging planes (almost perpendicular to the coronal plane) are indicated by the green dashed lines. Overall, we observe a higher value for mutual information in the patient with the most positive biopsy samples. In particular the 3D mutual information maps agree well with the biopsy results for both patients. The average values and standard deviation calculated over the entire prostate for mutual information by 3D CUDI were 0.62 ± 0.25 and 0.26 ± 0.14 for patient 1 and 2, respectively. A double-tailed Student's *t*-test showed a significant difference with $p < 0.001$.

Conclusion

The 3D CUDI maps by mutual information showed good agreement with the biopsy results in two patients. When optimized and validated using a more extensive dataset, possible applications of the method could be found in biopsy and focal-treatment targeting.

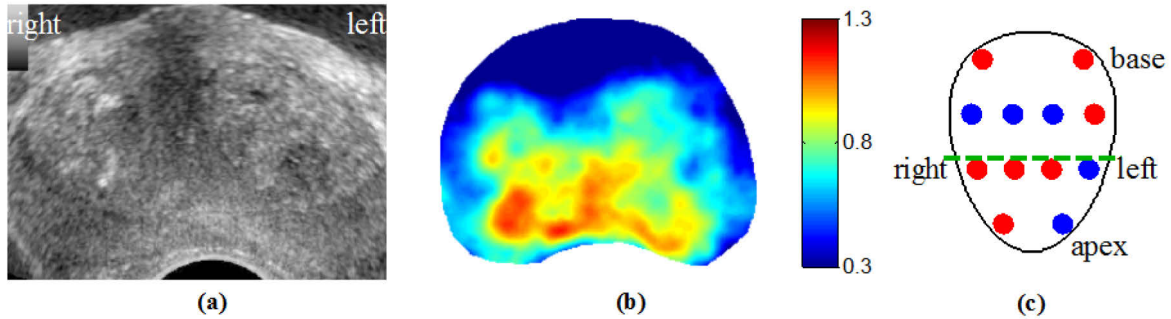


Figure 1: (a) B-Mode and (b) 3D CUDI by mutual information for patient 1 in corresponding planes. Subfigure (c) contains the biopsy results in the coronal plane, where red dots represent positive biopsy samples (Gleason 4+3 in 10–50% of the tissue). The green dashed line indicates the estimated location of the imaging plane.

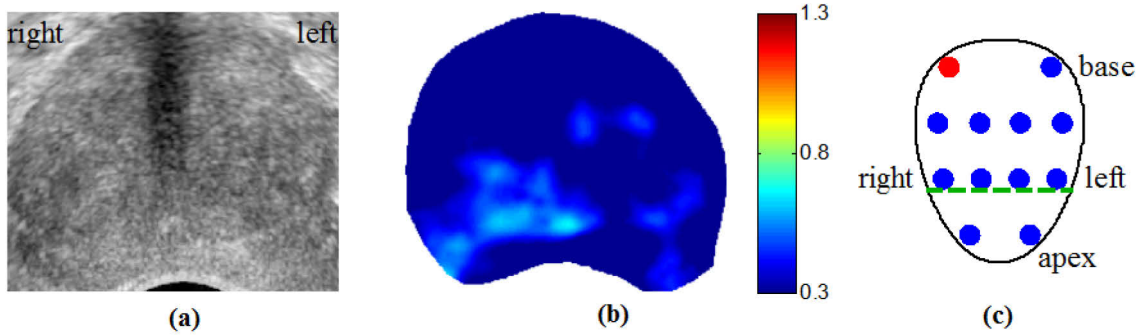


Figure 2: (a) B-Mode and (b) 3D CUDI by mutual information for patient 2 in corresponding planes. Subfigure (c) contains the biopsy results in the coronal plane, where the red dot represents a positive biopsy sample (Gleason 3+3 in <10% of the tissue). The green dashed line indicates the estimated location of the imaging plane.

References

1. V. Scattoni, A. Zlotta, R. Montironi, C. Schulman, P. Rigatti, and F. Montorsi, “Extended and saturation prostatic biopsy in the diagnosis and characterisation of prostate cancer: a critical analysis of the literature.,” *Eur. Urol.*, vol. 52, no. 5, pp. 1309–1322, 2007
2. D. J. Rosario, J. A. Lane, C. Metcalfe, J. L. Donovan, A. Doble, L. Goodwin, M. Davis, J. W. F. Catto, K. Avery, D. E. Neal, and F. C. Hamdy, “Short term outcomes of prostate biopsy in men tested for cancer by prostate specific antigen: prospective evaluation within ProtecT study.,” *Br. Med. J.*, vol. 344, no. January, ID d7894, 2012
3. J. V Hegde, R. V Mulkern, L. P. Panych, F. M. Fennessy, A. Fedorov, S. E. Maier, and C. M. C. Tempany, “Multiparametric MRI of prostate cancer: an update on state-of-the-art techniques and their performance in detecting and localizing prostate cancer.,” *J. Magn. Reson. Imaging*, vol. 37, no. 5, pp. 1035–1054, 2013
4. G. Russo, M. Mischi, W. Scheepens, J. J. De la Rosette, and H. Wijkstra, “Angiogenesis in prostate cancer: onset, progression and imaging.,” *Br. J. Urol. Int.*, vol. 110, no. 11 Pt C, pp. E794–808, Dec. 2012
5. C. J. Harvey, J. Pilcher, J. Richenberg, U. Patel, and F. Frauscher, “Applications of transrectal ultrasound in prostate cancer.,” *Br. J. Radiol.*, vol. 85 Spec No, pp. S3–17, 2012
6. M. P. J. Kuenen, M. Mischi, and H. Wijkstra, “Contrast-ultrasound diffusion imaging for localization of prostate cancer,” *IEEE Trans. Med. Imaging*, vol. 30, no. 8, pp. 1493–1502, 2011
7. M. P. J. Kuenen, T. a Saidov, H. Wijkstra, and M. Mischi, “Contrast-ultrasound dispersion imaging for prostate cancer localization by improved spatiotemporal similarity analysis.,” *Ultrasound Med. Biol.*, vol. 39, no. 9, pp. 1631–1641, 2013
8. M. Mischi, M. P. J. Kuenen, and H. Wijkstra, “Angiogenesis imaging by spatiotemporal analysis of ultrasound contrast agent dispersion kinetics.,” *IEEE Trans. Ultrason. Ferroelectr. Freq. Control*, vol. 59, no. 4, pp. 621–629, 2012
9. M. P. J. Kuenen, T. A. Saidov, H. Wijkstra, J. J. M. C. H. De Rosette, and M. Mischi, “Spatiotemporal Correlation of Ultrasound Contrast Agent Dilution Curves for Angiogenesis Localization by Dispersion

- Imaging,” IEEE Trans. Ultrason. Ferroelectr. Freq. Control, vol. 60, no. 12, pp. 2665–2669, 2013*
- 10. *M. Mischi, N. Bouhouche, L. Demi, M. P. J. Kuenen, A. Postema, J. J. de la Rosette, T. J. Tjalkens, and H. Wijkstra, “Contrast-ultrasound dispersion imaging of cancer neovascularization by mutual-information analysis,” in Proc. IEEE International Ultrasonics Symposium, Chicago (IL), Sep. 3-6, 2014, pp. 1148–1151*
 - 11. *S. Schalk, L. Demi, M. Smeenge, J. de la Rosette, H. Wijkstra, and M. Mischi, “Three-dimensional contrast-ultrasound dispersion imaging for prostate cancer localization, a feasibility study,” in Proc. IEEE International Ultrasonics Symposium, Chicago (IL), Sep. 3-6, 2014, pp. 616–619*

In vivo contrast enhancement and circulation kinetics of low-boiling point phase-change contrast agents

**Paul S. Sheeran¹, Juan D. Rojas¹, Connor Puett¹, Jordan Hjelmquist²,
Christopher B. Arena¹ and Paul A. Dayton¹**

¹*Joint Graduate Department of Biomedical Engineering, University of North Carolina and
North Carolina State University, NC, USA*

²*Undergraduate Department of Biomedical Engineering, North Carolina State University, NC,
USA*

Introduction and Background

Ultrasound phase-change contrast agents PCCAs have been proposed for different medical applications [1], [2]. PCCAs based on perfluorocarbon (PFC) droplets have been used for therapy enhancement over the last two decades, but few studies have explored their diagnostic potential or *in vivo* contrast-enhancement. Conventional PCCAs employ PFCs with boiling points close to body temperature that can be activated using ultrasound. However, small droplets, in the order of 100s of nm, have a considerably higher vaporization threshold than micron-sized droplets due to an increase in Laplace pressures, which is caused by the decrease in the agent's diameter [3]. This boiling point increase limits vaporization efficiency and *in vivo* use often requires therapeutic pressures that are not suitable for diagnostic applications. Recent studies have shown that PCCAs composed of low-boiling point PFCs such as decafluorobutane (DFB, boiling point -2°C) and octafluoropropane (OFP, boiling point -37°C) can overcome the limitations associated with conventional PCCAs [3], [4]. These PCCAs can be activated using pressures safe for diagnostic imaging, and can be tuned for different applications by mixing the PFC compounds to balance the trade-off between activation efficiency and thermal stability. However, to date little is known about the circulation and wash-out characteristics of these low-boiling point nanoscale PCCAs.

In this study, our goal was to evaluate wash-out and circulation kinetics of DFB and OFP nanodroplets vs traditional microbubble (MB) contrast agents *in-vivo*. We used a Verasonics Ultrasound platform to create a custom pulse sequence for imaging PCCAs with a single clinical transducer, and performed activation and imaging in the kidneys of rats.

Materials and Methods

PFC microbubbles and PCCAs were prepared using previously described protocols [4], [5]. MBs with a DFB core and PCCAs with both DFB and OFP cores were used. Imaging and activation of droplets was performed with an ATL L12-5 38mm linear array and a Verasonics research system. A B-mode imaging sequence was first used to locate the kidney, and was followed by a nonlinear contrast-specific

imaging sequence to obtain a baseline. An activation sequence was then used to vaporize droplets inside a rectangular region of interest, and the resulting contrast was captured using the contrast imaging sequence. The B-mode sequence consisted of the coherent angular compounding of 7 different frames obtained by delivering 9 MHz plane-waves and using the Verasonics reconstruction algorithms to envelope detect and beam form the RF signal. The contrast sequence consisted of a Pulse Inversion [6] approach that incorporated the angular compounding described for the B-mode sequence. The pulse inversion sequence used 3 angles for the frame compounding, and 4.5 MHz plane waves. Activation was accomplished by delivering several 5 MHz, 2-cycle focused pulses to an activation region of interest.

Three groups of Fischer 344 rats were included in the study: DFB PCCAs, OFP PCCAs, and MBs. 60 μ L of the agent was diluted in 60 μ L of saline and injected into the tail vein. 10 baseline frames were captured at a rate of 10 Hz, followed by droplet activation, and the resulting contrast was imaged for 10 seconds at a rate of 10 Hz. This process was repeated every 3 minutes for 19 minutes, starting 1 minute after injection, and once before the introduction of the agents to obtain a pre-injection baseline.

Results

Contrast Enhancement- very little signal was present in the pre-injection baseline. The activation sequence produced high contrast for both DFB and OFP (Figure 1). DFB exhibited a patterned appearance, while OFP produced uniform activation. However, OFP is less stable due to its low boiling point and so, spontaneous vaporization can be seen in the pre-injection baseline (Figure 1). Additionally, droplets demonstrated a distinct phase over 10 to 20 seconds where the contrast washed out of the imaging plane. The mean pixel intensity within and ROI placed in the area of higher contrast was used to calculate the contrast enhancement over the pre-injection baseline (Figure 2). One minute after injection, DFB and OFP produced mean values of 7.29 ± 3.65 dB and 18.24 ± 3.14 dB, respectively, and MB produced a value of 12.63 ± 3.64 .

Half-life- The contrast enhancement obtained diminishes over time as the difference in circulation between the agents becomes apparent (Figure 3). The data was normalized and fitted to a mono-exponential and the half-life was calculated. MB and OFP PCCAs exhibited similar contrast half-lives, 3.26 ± 0.37 min for MB and $3.67 \pm .37$ min. DFB PCCAs circulated significantly longer than MBs, with a half-life of 10.84 ± 1.63 min.

Wash-out- As the contrast generated by the activation sequence is cleared from the imaging plane, the contrast enhancement decreases for several seconds during a wash-out phase (Figure 2). Since the contrast enhancement can be monitored in real-time, a measure of blood perfusion can be obtained. The

washout-rate for each type of agent was measured by fitting the decay curve of the 1 minute time point to a monoexponential. OFP produced a mean wash-out rate of $.13 \pm .03 \text{ sec}^{-1}$, and DFB a rate of $.17 \pm .04 \text{ sec}^{-1}$.

Discussion

The results show that contrast enhancement similar or greater than MBs can be obtained with PCCAs. It was also demonstrated that despite the high volatility of low-boiling point PFCs, PCCAs exhibit similar or substantially longer circulation half-life than MBs, depending on the filling gas. Additionally, the results show that PCCAs can be used to measure contrast wash-out.

The parameters for activation were kept constant in order to compare the performance of the different compounds, and this led to under-activation of DFB and over-activations of OFP. However, the activation parameters can be optimized to enhance activation efficiency of the compound used for a given application.

We have shown that contrast produced by PCCAs can be captured using custom pulse sequences, and that different species of PFCs perform differently, which allows for tuning of the PCCA formulation to better fit a specific application.

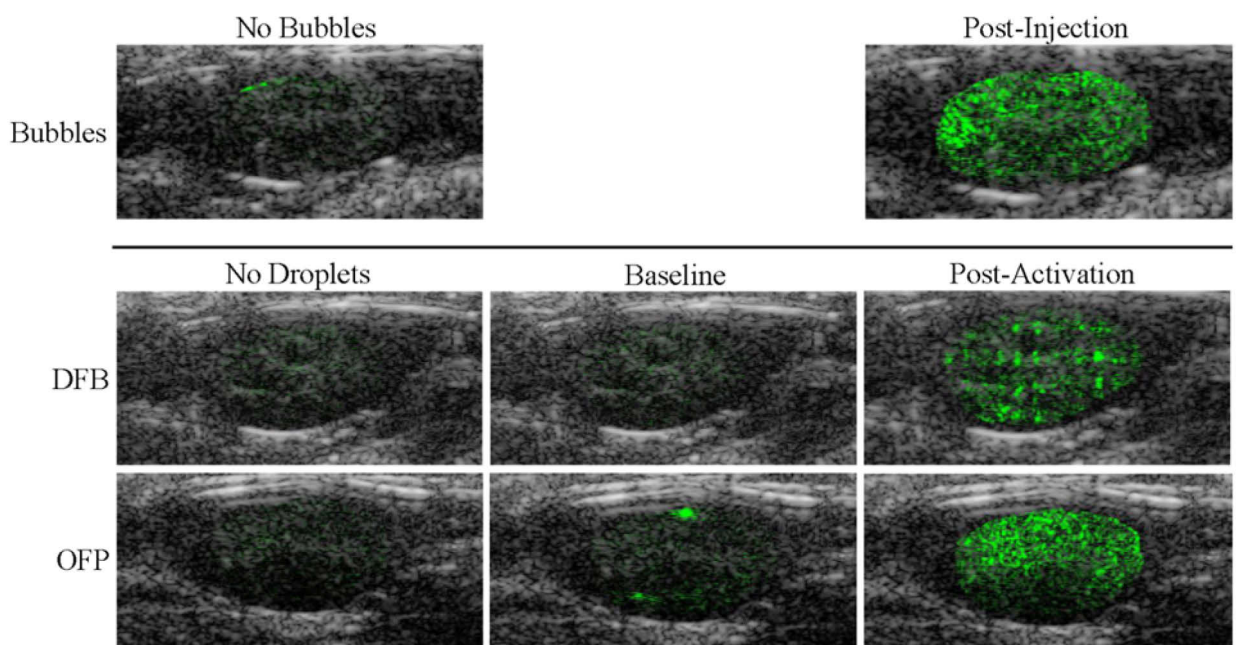


Figure 1: Overlay of B-mode images (grey) and pulse-inversion scans (green).

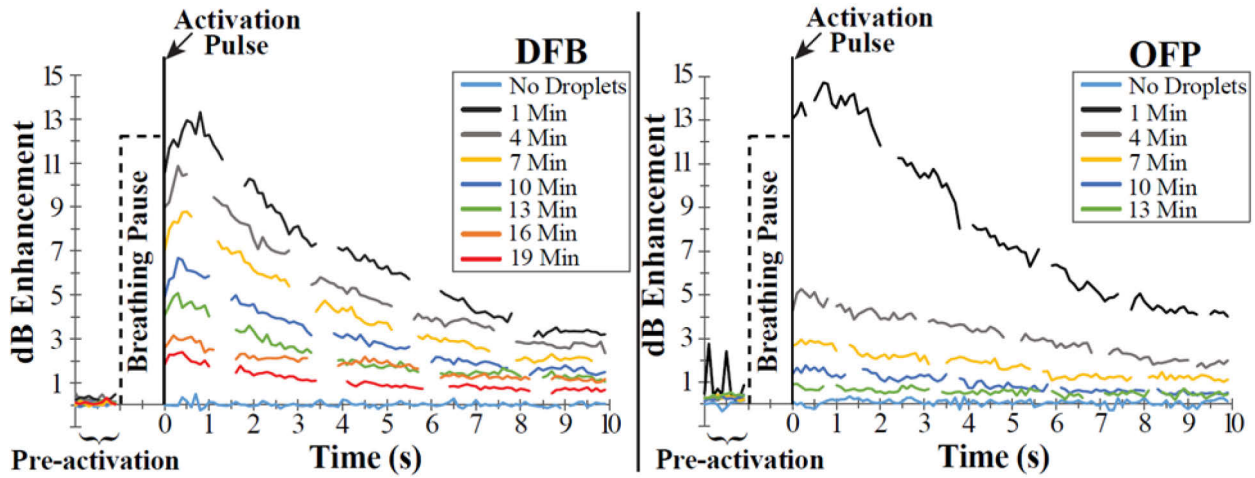


Figure 2: Contrast Enhancement for DFB (A) and OFP(B).

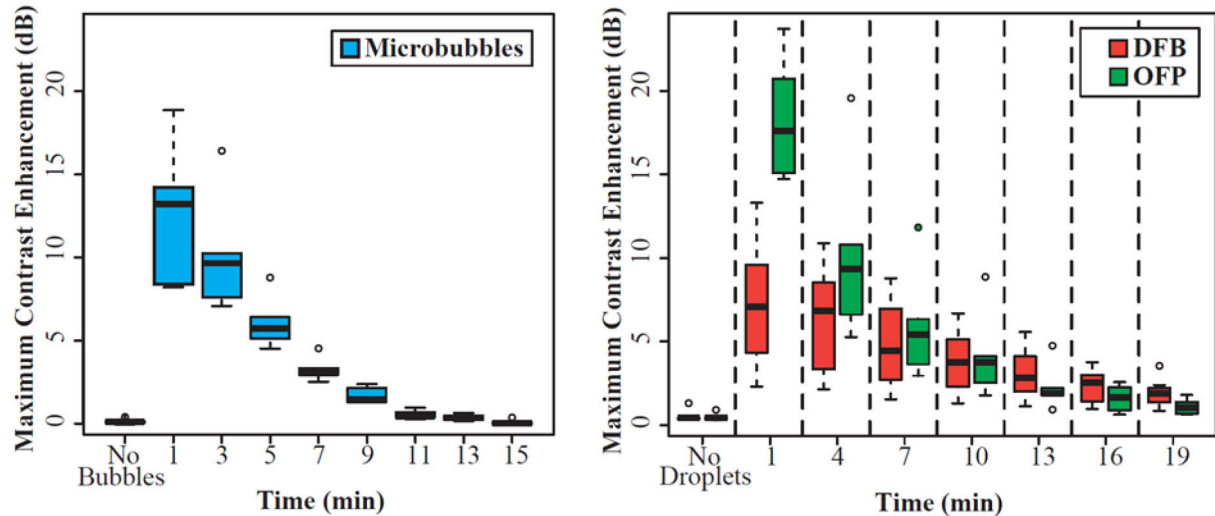


Figure 3: Maximum contrast enhancement relative to the pre-injection baseline for MB (left) and PCCAs (right).

References

1. A. Droplet, V. For, and D. Applications, "Acoustic Droplet Vaporization for Therapeutic and Diagnostic Applications," *Ultrasound Med. Biol.*, vol. 26, no. 7, pp. 1177–1189, 2000
2. P. S. Sheeran and P. A. Dayton, "Phase-change contrast agents for imaging and therapy," *Curr. Pharm. Des.*, vol. 18, no. 15, pp. 2152–65, Jan. 2012
3. P. S. Sheeran, V. P. Wong, S. Luois, R. J. McFarland, W. D. Ross, S. Feingold, T. O. Matsunaga, and P. a Dayton, "Decafluorobutane as a phase-change contrast agent for low-energy extravascular ultrasonic imaging.," *Ultrasound Med. Biol.*, vol. 37, no. 9, pp. 1518–30, Sep. 2011
4. P. S. Sheeran, S. H. Luois, L. B. Mullin, T. O. Matsunaga, and P. A. Dayton, "Design of ultrasonically-activatable nanoparticles using low boiling point perfluorocarbons.," *Biomaterials*, vol. 33, no. 11, pp. 3262–9, Apr. 2012
5. P. S. Sheeran, S. Luois, P. A. Dayton, and T. O. Matsunaga, "Formulation and acoustic studies of a new phase-shift agent for diagnostic and therapeutic ultrasound," *Langmuir*, vol. 27, no. 17, pp. 10412–20, Sep. 2011
6. D. H. Simpson, C. T. Chin, and P. N. Burns, "Pulse inversion Doppler: a new method for detecting nonlinear echoes from microbubble contrast agents.," *IEEE Trans. Ultrason. Ferroelectr. Freq. Control*, vol. 46, no. 2, pp. 372–82, Jan. 1999

Acoustic interaction between a coated microbubble and a rigid boundary

K. Efthymiou and N. Pelekasis

Dpt. Mechanical Engineering, University of Thessaly, Greece

It is of interest to identify the dynamic behavior and acoustic signature of coated microbubbles during insonation in the vicinity of nearby boundaries. Experimental studies identify asymmetric pulsations of microbubbles adherent to tissue [1,2], accompanied by a decrease in their acoustic signal [1]. We present a numerical investigation of the nonlinear interaction between a microbubble that is coated by a polymeric or phospholipid shell and a nearby rigid boundary. The response to a step or sinusoidal change in the far field pressure is investigated. Owing to the dominant shell viscosity, to a first approximation, we ignore viscous and acoustic damping, while accounting for nonlinearity in the elastic behaviour of the shell. The boundary element method is employed for the solution of the velocity potential in the surrounding fluid, coupled with the appropriate dynamic and kinematic conditions at the microbubble/liquid and boundary/liquid interfaces taken to be axisymmetric [3]. Benchmark simulations are first conducted in order to recover the dynamic behavior of free bubbles in the vicinity of a rigid boundary [4]. The simulations capture the basic aspect of this flow arrangement, namely jet formation directed towards the boundary (fig. 1a). Simulations of the acoustic response of a coated microbubble whose shell behaves as a neo-Hookean solid with significant dilatational viscosity, in the vicinity of a rigid boundary, reveal the stabilizing effect of the viscoelastic coating with respect to volume pulsation when a step change disturbance is applied (fig. 1b). However the fluid in its aft region retains its accelerating motion and, for large enough initial disturbance, it penetrates the bubble without forming a jet (fig 1b). Rather, it causes rapid shell bending in the aft region where break-up occurs as a result of stress concentration. When a sinusoidal pressure change is applied the microbubble is attracted to the boundary and performs volume pulsations at the forcing frequency. For moderate amplitudes shape deformation occurs as a result of resonance that is more pronounced along the direction of translation (fig. 1c). When the amplitude further increases shape deformation and break-up occurs in a fashion similar to the case with step change illustrated in fig 1b, where the balance between inertia and bending dominates (fig. 1d) generating a region of very small radius of curvature.

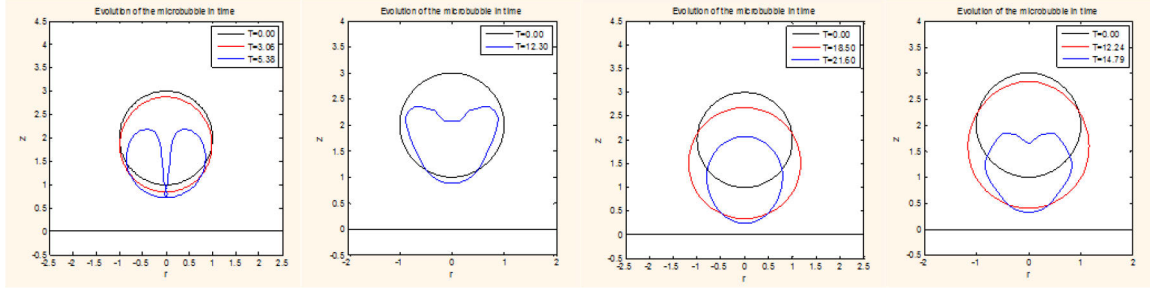


Figure 1: (a) Shape sequence of a free bubble and (b) a coated microbubble approaching a rigid wall, subject to a step pressure change. Shape sequence of a coated microbubble approaching a rigid wall, subject to a sinusoidal pressure change for (c) a relatively small ($\varepsilon=2$) and (d) a large amplitude ($\varepsilon=3$) of the acoustic disturbance; simulation parameters are set to: $R_0=3.6\text{ }\mu\text{m}$, $G_s=80\cdot10^6$, $\mu_s=20\text{ Pa}\cdot\text{s}$, $k_B=3\cdot10^{-14}\text{ N}\cdot\text{m}$, $b=0$ (Mooney-Rivlin shell), $v_0=1\text{ MHz}$, $v_t=1.7\text{ MHz}$, $\gamma=1.07$, $P_{st}=101325\text{ Pa}$, $\delta=1\text{ nm}$.

References

1. Zhao S., Ferrara K.W., Dayton P.A., "Asymmetric oscillation of adherent targeted ultrasound contrast agents", *Appl. Phys. Lett.*, 87:ref. 134103, 2008
2. Vos H. J., Dollet B., Bosch J. G., Versluis M. & de Jong N. "Nonspherical vibrations of microbubbles in contact with a wall—a pilot study at low mechanical index", *Ultrasound in Med. & Biol.*, Vol. 34 (4), pp. 685–688, 2008
3. K. Tsiglifis & N. Pelekasis, "Dynamic simulations of insonated contrast agents". *Phys. Fluids*, 2013.
4. Blake J. R., Taib B. B. and Doherty G., "Transient cavities near boundaries. I. Rigid boundary", *J. Fluid Mech.*, 170, 479-497, 1986

Physical insights into ultrasound-stimulated microbubble sonoporation

Brandon Helfield, Xucai Chen, Bin Qin and Flordeliza S. Villanueva

*Center for Ultrasound Molecular Imaging and Therapeutics, University of Pittsburgh Medical Center,
Pittsburgh, PA, United States*

There has been recent interest in employing ultrasound and microbubbles to elicit therapeutic benefit, applications of which include the site-specific delivery of drugs and/or genetic materials. Sonoporation, the transient increase in cell membrane permeability induced by ultrasound-stimulated microbubbles, is considered a potential mechanism by which successful delivery in this manner may be achieved. The majority of studies on sonoporation, however, are conducted over a range of acoustic parameters, cell types, microbubble distributions and microbubble-cell ratios, which render a physical understanding of sonoporation difficult. The objective of this work is to gain insight into the underlying physical mechanisms responsible for sonoporation, by attempting to correlate individual microbubble oscillation behavior with the corresponding cell membrane permeability dynamics.

Individual phospholipid encapsulated perfluorobutane gas microbubbles ($n=70$) were allowed to rest adjacent to a cultured human umbilical vein endothelial cell (HUVEC) monolayer within an OpticellTM at 37°C. Propidium iodide (PI) and calcein-AM were injected before ultrasound exposure into the surrounding media (100 μM and 0.25 μM , respectively) as a set of fluorescent markers capable of providing real-time information on cell membrane permeability (*i.e.* sonoporation), as defined by PI uptake and/or cellular calcein retention. Individual microbubble-cell complexes (*i.e.* bubble to cell ratio = 1:1) were insonicated with a single 1 MHz, 8-cycle Hanning windowed pulse at peak negative pressures ranging from 0.2-0.8 MPa. The UPMC-Cam (Chen et al. *Rev. Sci. Instrum.* 2013), an ultrafast imaging system capable of recording 128 frames at a frame rate up to 25 million frames per second (Mfps), was employed to capture microbubble dynamics, while a second, standard CCD camera (15 fps) was simultaneously employed to record the subsequent fluorescent marker activity for an approximate duration of three minutes. Microbubble oscillation characteristics were extracted from the ultrafast recordings, and the corresponding fluorescent marker dynamics were placed within a physical diffusion model framework in order to estimate membrane pore features.

Microbubble excursion was determined to be strong indicator of cell membrane poration. Specifically, sonoporation of a given cell (presence of PI uptake) was observed when the maximum absolute expansion of the adjacent bubble, defined as $D_{\max}-D_0$, reached a threshold value of approximately 3 μm (Figure 1), independent of initial bubble size. Among the subset of microbubble-cell complexes that

exhibited sonoporation ($n=32$), distinctly different PI uptake dynamics were observed. In the majority of cases ($n=29$), PI intensity within the nucleus increased exponentially until reaching a constant value. A two parameter 2-D diffusion model was applied to a subset of the data resulting in an inverse relation between the maximum PI uptake intensity and the maximum relative microbubble expansion D_{max}/D_0 . The remaining sonoporated cells ($n=3$) exhibited PI uptake only at the site of entry in the cytoplasm, the intensity of which decreased back to baseline by the three minute time point. The amount of cellular calcein retention was shown to be less in the former case ($n=29$) as compared to the latter ($n=3$), resulting in relative retentions of up to 23% and 80%, respectively.

These results highlight that the occurrence of sonoporation is physically related to absolute maximum microbubble expansion, and can be achieved with a variety of transmit pressures and microbubble initial sizes. This work contributes to the pursuit of the understanding of the governing physical principles of sonoporation, as opposed to an empirical determination of an “optimal” set of ultrasound/microbubble parameters that elicit sonoporation.

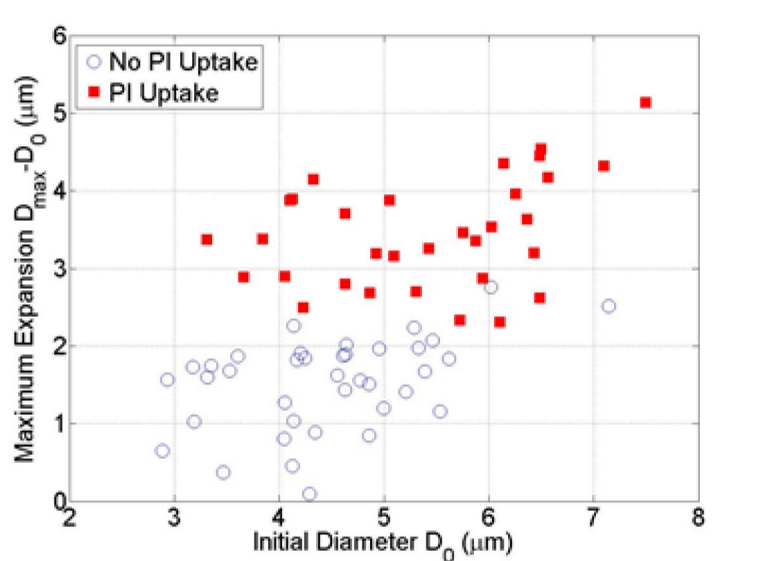


Figure 1: Maximum absolute radial expansion as a function of initial diameter for individual microbubbles adjacent to a HUVEC cell monolayer, insonicated with a single 1 MHz, 8-cycle Hanning window tapered pulse at peak negative pressures between 0.2-0.8 MPa. Circles denote no corresponding PI activity, while squares denote PI uptake. This suggests a threshold in maximum radial expansion above which sonoporation occurs.

A new denoising method for improved parameter estimation in DCE-US

S.Turco¹, A. Bar-Zion², H. Wijkstra^{1,3}, D. Adam², M. Mischi¹

¹*Eindhoven University of Technology, Eindhoven, the Netherlands*

²*Technion - Israel Institute of Technology, Haifa, Israel*

³*Academic Medical Center, Amsterdam, the Netherlands*

Background

The major role of angiogenesis in cancer growth has led to the development of dynamic contrast enhanced (DCE) imaging methods to probe tumor angiogenic vasculature. In DCE-ultrasound (DCE-US), fitting mathematical perfusion models to measured time intensity curves (TICs) describing the echo power as a function of time enables the estimation of quantitative hemodynamic parameters. Quantification is facilitated by the linear relationship between contrast concentration and echo power (TIC) at typical contrast concentrations found in tissue [1]. When log-compression is applied by the scanner, data linearization is still possible, provided that sufficient dynamic range is used for acquisition [2]. However, parameter estimation remains challenging due to the noisy nature of DCE-US data. As a result, prior to applying curve fitting, a preprocessing step for TIC denoising is necessary and widely employed.

DCE-US images present the same type of speckle noise observed in conventional B-mode images [3]. In amplitude, noise can be described by a multiplicative noise model following a Rayleigh distribution [3]. In time, noise in consecutive frames can be considered to be independent due to the Brownian motion of DCE-US contrast particles over time [1]. By log-transforming the ultrasound data, the original multiplicative noise becomes additive, and the noise distribution can be approximated by a Gaussian distribution [4], enabling the application of standard low-pass linear filters for temporal denoising.

Recently, contrast ultrasound dispersion imaging (CUDI) was proposed and tested for prostate cancer (PCa) localization with promising results [5]. In CUDI, fitting the modified local density random walk (mLDRW) model to DCE-US TICs enables the estimation of the local dispersion parameter κ , which provides a characterization of the microvascular architecture. However, parameter estimation after standard low-pass filtering in time-domain has shown limited results, requiring the addition of spatial filtering, and therefore reducing the spatial resolution of the method. Motivated by the model fitting limitations caused by high noise levels, here we propose a novel preprocessing method for DCE-US based on wavelet denoising, and we evaluate the ability of this method to improve parameter estimation

in CUDI.

Methods

Based on the convective dispersion equation, the evolution of the contrast agent concentration at each pixel over time, $C(t)$, is described by the mLDRW model as [5]

$$C(t) = \alpha \sqrt{\frac{\kappa}{2\pi(t-t_0)}} e^{-\frac{\kappa(t-t_0-\mu)^2}{2(t-t_0)}}, \quad (1)$$

with $\kappa = v^2/D$ being the dispersion-related parameter, t_0 the theoretical injection time, μ the contrast mean transit time, and α the time integral of $C(t)$. Fitting the measured TICs by (1) enables the estimation of the dispersion parameter κ , which characterizes the microvascular architecture.

In CUDI, before curve fitting, a preprocessing step is applied to reduce the TIC noise level. Up until now, this consisted of a FIR (finite impulse response) low-pass filter in time domain with cut-off frequency of 0.5 Hz, proven sufficient to represent any perfusion TIC in the prostate [5]. In this work, we propose a novel preprocessing method, based on wavelet denoising. By this method, an outlier removal procedure is first performed to locally remove low value outliers. This enables the use of standard denoising methods, optimized for Gaussian white noise, based on the approximation of the log-transformed signal amplitude to a Gaussian distribution [4]. The noise level is then estimated at each wavelet decomposition scale. Lastly, the wavelet coefficients at each scale are thresholded, removing low-value noise-related coefficients and preserving dominant signal coefficients.

In order to evaluate the ability of the proposed denoising method to improve parameter estimation, 95 noisy TICs were simulated by the mLDRW model with multiplicative noise obeying a Rayleigh distribution. The signal-to-noise ratio (SNR) of the simulated TICs was -1.4 dB, and the parameter κ was varied from 0.1 s^{-1} to 2 s^{-1} , covering the range of values typically found in the prostate [5]. The estimation performance was evaluated by calculating the determination coefficient R^2 of the fit with respect to the clean simulated TIC, and the normalized mean error (NME) in the estimation of the parameter κ .

The proposed method was also tested on DCE-US loops from 6 patients with biopsy-proven PCa, acquired after an intravenous peripheral bolus injection of 2.4-mL SonoVue® (Bracco, Milan, Italy) with an iU22 ultrasound scanner (Philips Healthcare, Bothell, WA) in power modulation mode at low mechanical index (MI=0.06). The data was collected at the Academic Medical Center, University of Amsterdam, the Netherlands. All the patients signed informed consent. The fitting performance on patient data was evaluated by calculating the mean R^2 of the fit with respect to the filtered TIC, and the

percentage of voxel with successful fit ($R^2 > 0.75$).

Results

Table 1 reports the results of the simulations, comparing the estimation performance of wavelet denoising (WD) filtering with FIR low-pass (FIR-LP) filtering. Table 2 reports the results obtained in patient data, comparing the fitting performance obtained after WD filtering, FIR-LP filtering, and without any preprocessing. Figures 1a and 1c show an example of TIC together with the corresponding FIR-LP and WD filtered curves for simulated and patient data, respectively. Figures 1b and 1d compare the fit obtained after FIR-LP and WD filtering with the clean TIC, for simulated data, and with the filtered TIC, for patient data.

Table 1. Results in simulated data

Filtering	FIR-LP	WD
R^2	0.74 ± 0.1	0.98 ± 0.1
NME (%)	-4.71 ± 16.4	-0.91 ± 6.16

Table 2. Results in patient data

Filtering	none	FIR-LP	WD
R^2	0.78 ± 0.04	0.86 ± 0.06	0.88 ± 0.06
Percentage fit (%)	0.04	42.7	54.7

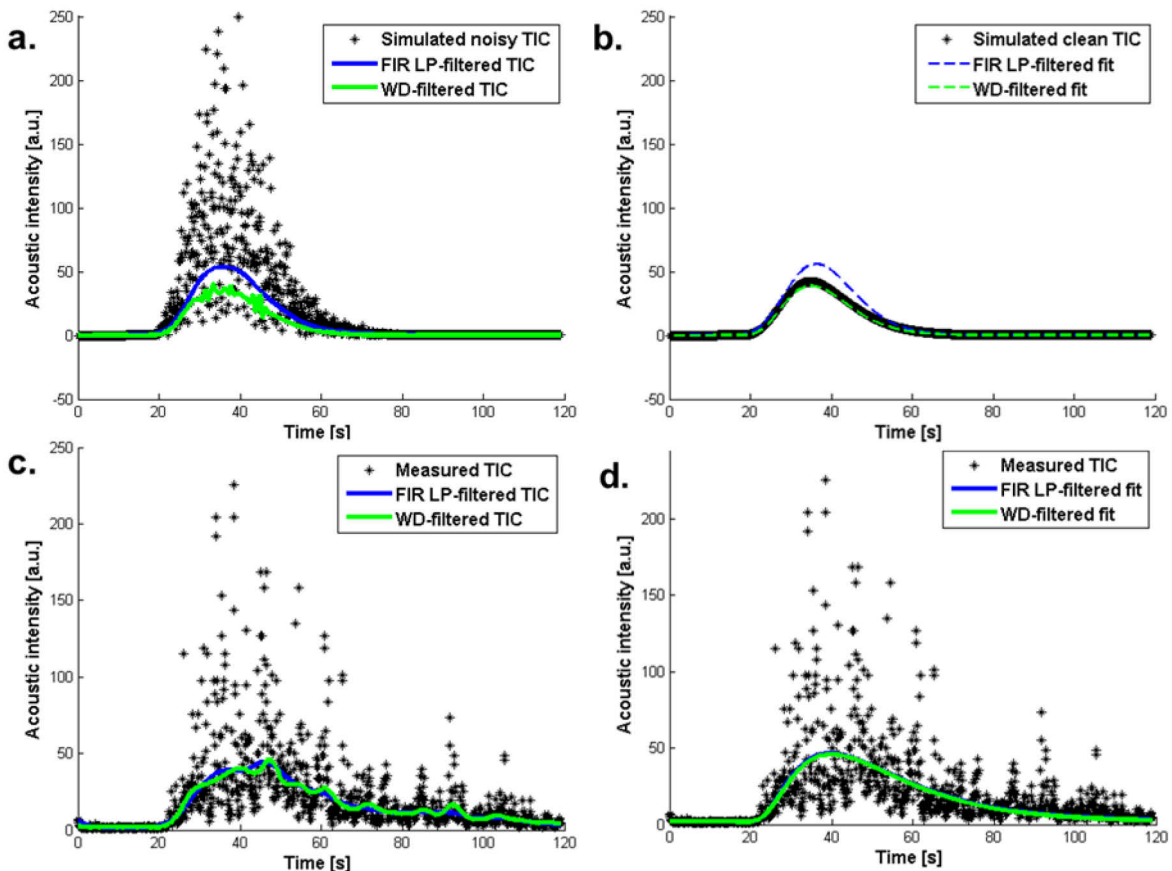


Fig. 1 **a.** Simulated noisy TIC with corresponding TIC after FIR-LP and WD filtering. **b.** Simulated clean TIC with corresponding fits obtained after FIR-LP and WD filtering. **c.** Experimental TIC with corresponding TIC after FIR-LP filtering and WD filtering. **d.** Experimental TIC with corresponding fits obtained after FIR-LP filtering and WD filtering.

Discussion and conclusions

Denoising in the temporal domain is a necessary step for parameter estimation in DCE-US, as demonstrated by the very low (0.04%) percentage of pixel TICs which can be fit without any filtering in time-domain. In this work, a novel preprocessing step based on wavelet denoising was presented and tested for improved parameter estimation in CUDI; a comparison with standard FIR-LP filtering is also provided. By simulations, the proposed method showed a significant reduction in the estimation error and a significant R^2 increase ($p\text{-value}<0.01$). Moreover, the analysis in patient data showed a significant improvement in R^2 and in the percentage of pixels with successful fit ($p\text{-value}<0.01$). The promising results suggest that time filtering based on wavelet decomposition might be well suited for temporal denoising of DCE-US loops, reducing the need for spatial low-pass filtering and thus leading to a better compromise between fit accuracy and spatial resolution.

References

1. Mischi, M., *Contrast Ecocardiography for Cardiac Quantifications*. 2004, Eindhoven University of Technology
2. Rognin, N.G., et al., *In-vivo Perfusion Quantification by Contrast Ultrasound: Validation of the Use of Linearized Video Data vs. Raw RF Data*. IEEE International Ultrasonics Symposium Proceedings, 2008: p. 1690-1693
3. Barrois, G., et al., *A multiplicative model for improving microvascular flow estimation in dynamic contrast-enhanced ultrasound (DCE-US): theory and experimental validation*. IEEE Trans Ultrason Ferroelectr Freq Control, 2013. 60(11): p. 2284-2294
4. Michailovich, O. and D. Adam, *Robust estimation of ultrasound pulses using outlier-resistant de-noising*. Medical Imaging, IEEE Transactions on, 2003. 22(3): p. 368-381
5. Kuenen, M.P.J., M. Mischi, and H. Wijkstra, *Contrast-Ultrasound Diffusion Imaging for Localization of Prostate Cancer*. IEEE Trans Med Imag, 2011. 30(8): p. 1493-1502

A numerical study on the natural frequency of a microbubble bound to a surface

Naohiro Sugita, Toshihiko Sugiura

Department of Mechanical Engineering, Keio University, 3-14-1, Hiyoshi, Kohoku-ku, Yokohama, 223-8522, Japan

Background

The natural frequency of a microbubble bound to a surface was numerically investigated in order to discriminate the acoustical properties of a bound microbubble. The dynamics of a microbubble constrained to a rigid or compliant wall is of great importance for effective medical treatments. When the targeted microbubbles are attached to the specific site due to the binding force, the contact area between the bubble and the wall surface changes depending on the ligand distribution [1]. Since the boundary condition at the bubble-wall interface is significantly changed, it is necessary to distinguish the vibrational behavior of the bound microbubble from that of a freely floating one. The purpose of this study is to investigate the effect of the fixed contact boundary condition on the natural frequency of a bound microbubble in an ultrasound field.

Methods

We employed the direct boundary element method in order to simulate shape deformation and translational motion of an oscillating microbubble. The host liquid was assumed to be incompressible and the gravity force was ignored due to the small size of the bubble. The flow out of the boundary layer was assumed to be irrotational (potential flow), and the weakly viscous effect was introduced into the boundary condition applying the modified Bernoulli equation [2]. Figure 1 shows the schematic model of the 2D axisymmetric flow domain. We assumed that the bubble was constrained to a rigid plane wall with the contact line fixed. θ_c and R_{bind} denote the initial contact angle and the radius of the contact area, respectively. The radius of curvature of the bubble surface in the equilibrium state was set $2\mu\text{m}$. The physical properties of water and air were used. In this study, we focused only on the natural frequency of the volumetric or breathing mode.

Results

We obtained time-volume curve responding to a gaussian sine wave for various initial contact angles, θ_c , and calculated the natural frequency using FFT spectra of the time-volume curves (shown in Figure 2). The natural frequency is a linear function of the initial contact angle. When the bubble is tangentially in contact with the wall, $\theta_c=0$, the natural frequency is about one thirds of that of a freely floating microbubble. Increase of the initial contact angle leads to linear growth of the natural frequency.

Conclusion

The volumetric natural frequency of the bound microbubble attached to a solid surface is a linear function of the initial contact angle, θ_c .

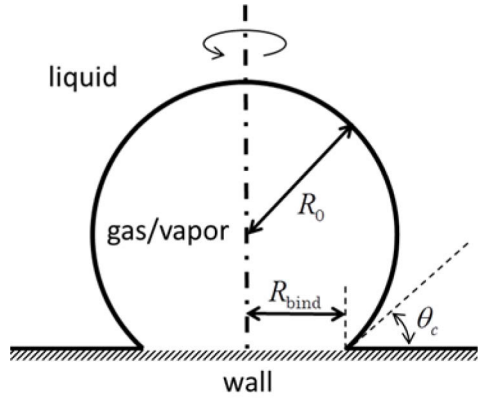


Figure 1: Shematic model of the 2D axisymmetric flow domain.

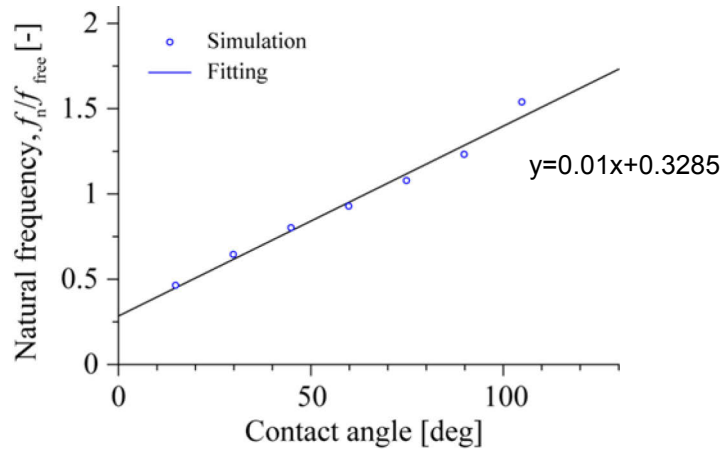


Figure 2: The natural frequency of the bound microbubble as a function of the initial contact angle. The vertical axis is normalized by the natural frequency of a $2\mu\text{m}$ -radius free bubble.

References

1. K. Kooiman, T. J. A. Kokhuis, T. van Rooij, I. Skachkov, A. Nigg, J. G. Bosch, A. F. W. van der Steen, W. A. van Cappellen and N. de Jong, "DSPC or DPPC as main shell component influences ligand distribution and binding are of lipid-coated targeted microbubbles", *Eur. J. Lipid Sci. Technol.* 2014, 116, 1217–1227
2. T. S. Lundgren and N.N. Mansour, "Oscillation of drops in zero gravity with weak viscous effects." *J. Fluid Mech.*, 1988, 194, 479-510

An automated algorithm for quantification of tissue perfusion in contrast enhanced ultrasound images: Initial evaluation in quantification of lower limb perfusion

¹**W.K. Cheung, ²K.J. Williams, ³K. Christensen-Jeffries, ³R.J. Eckersley, ²A.H. Davies,
¹M.X. Tang**

¹*Department of Bioengineering, Imperial College, Exhibition Road, London, SW7 2AZ*

²*Section of Surgery, Imperial College, Exhibition Road, London, SW7 2AZ*

³*Division of Imaging Sciences, King's College London, WC2R 2LS*

Background and aim

An accurate and automated technique for quantification of tissue perfusion is desirable for a wide-range of clinical applications. Contrast-enhanced ultrasound (CEUS) has shown a great potential in imaging perfusion but quantification has been affected by a number of factors [1, 2]. Many existing studies still use qualitative visual assessment. In a recent study, contrast signals were quantified by tracking individual bubbles within the 2D imaging plane[3] but it is difficult to deal with bubbles travelling through the imaging plane. In this study, we aim to develop a pixel-based automated bubble detection algorithm which is capable of separating contrast signals from both tissue signals and noise through temporal intensity features and generating a quantitative measure of vascular density.

Methods

The automated bubble detection algorithm processes contrast enhanced ultrasound image sequences and consists of two steps. Firstly, a rigid motion correction algorithm is applied to correct bulk motion effects in the CEUS images. Secondly, histogram thresholding is employed to capture the bubble activities on a pixel-by-pixel basis and separating them from tissue signals and noise. The thresholding is based on a number of features in the time intensity curve related to its amplitude and spatial and spectral variations. The algorithm was evaluated both in vitro and on clinical limb perfusion data acquired from healthy volunteers. In the in vitro study microbubble solutions of different dilutions were imaged and contrast signals quantified. For the in-vivo work, five healthy subjects were recruited and CUES image sequences were acquired from the lower limb with a clinical scanner (Philips iU22 with a 13 MHz broadband linear array transducer). Sequences were acquired both before and after physical exercise for each subject. Two repeated scans were performed on each subject. Five Regions of interests (ROIs) were selected manually, one to segment the micro-vessels above the main vessels within lower limb where quantification is required. A relative vascular density measure within ROIs were calculated and compared before and after exercise. Statistical analysis was conducted to evaluate the difference in contrast enhancement before and after exercise.

Results

The In vitro study demonstrated a good agreement between known bubble concentrations and quantification measures generated by the algorithm. For in vivo data the quantification results were calculated and compared before and after exercise by the subjects. An example of microbubble signal segmentation before and after exercise is shown in Figure 1. Initial analysis showed a significant difference in average vascular density measure before ($31.33\% \pm 8.34\%$) and after ($44.78\% \pm 10.65\%$) exercise ($p<0.004$).

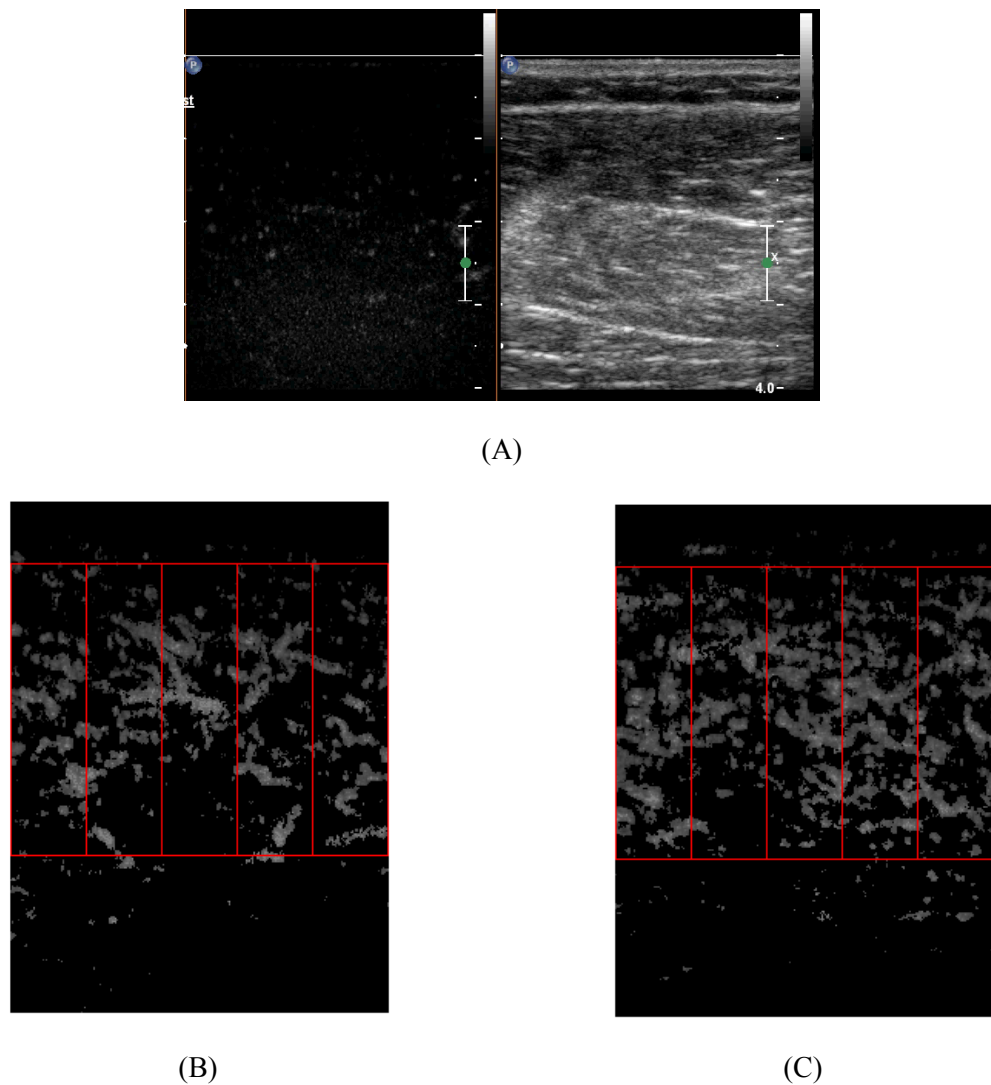


Figure 1: Bubble capture before exercise (A) side by side CEUS and B-mode image (B) by our automated bubble detection algorithm (C) after exercise by our automated bubble detection algorithm.

Conclusions

The proposed bubble detection and quantification method is shown to be a promising tool for detecting and quantifying microbubble signals both in vitro and in vivo.

References

1. MX. Tang, H. Mulvana, T. Gauthier, A. K. P. Lim, D. O. Cosgrove, R. J. Eckersley, and E. Stride, *Quantitative contrast-enhanced ultrasound imaging: a review of sources of variability*, *Interface Focus*, August 6, 2011 1:520-539
2. E Stride, MX Tang and RJ Eckersley, *Physical phenomena affecting quantitative imaging of ultrasound contrast agents*, *Applied Acoustics*, 2009 Vol 70(10), Special Issue: Sp. Iss. SI Pages: 1352-1362
3. Akkus Z, Hoogi A, Renaud G, van den Oord SC, Ten Kate GL, Schinkel AF, Adam D, de Jong N, van der Steen AF, Bosch JG. *New quantification methods for carotid intra-plaque neovascularization using contrast-enhanced ultrasound*. *Ultrasound Med Biol* 2014;40:25-36

Modifications of perfluorocarbon-loaded PLGA particles for ultrasound imaging

*Edyta Swider, Olga Koshkina, Eric van Dinter, Carl Figdor, I. Jolanda M. de Vries,
Mangala Srinivas*

*Radboud University Medical Center (RadboudUMC), Department of Tumor Immunology,
Radboud Institute for Molecular Life Sciences (RIMLS), 6500HB Nijmegen, The Netherlands*

Ultrasound (US) is an efficient imaging method to monitor cell therapy. Ultrasound contrast agents (USCAs) are typically gas-filled microbubbles or perfluorocarbon (PFC) droplets that vaporize before imaging. Although these agents can demonstrate contrast and be further applied to the release of drugs at targeted sites in a noninvasive manner, they have limited active lifetimes both *in vitro* and *in vivo*. This drawback severely limits their efficacy for advanced personalized medicine applications.

We report on PFC-encapsulated poly(lactic-co-glycolic acid) (PLGA) USCAs, which can be used for long-term US imaging [1]. In particular, we study the US properties of particles in a size range of 400-1000 nm and focus on their structure-function relationship. We describe the impact of various formulation parameters, including the effects of surfactant and polymer concentration and sonication input on physicochemical properties of particles. We characterized particles using several methods, including dynamic light scattering, transmission electron microscopy, ¹⁹F NMR and mass spectrometry. Finally, we studied the relation between particle properties and US contrast using high resolution US (Visualsonics Inc.). Preliminary results indicate that changing formulation parameters leads to particles with different properties, which appear to have strong impact on the US contrast. Moreover, our findings show that PFC-loaded PLGA particles are suitable for both *in vitro* and *in vivo* US imaging.

Another advantage of PFC-PLGA contrast agents is that they can be lyophilized and stored as a powder. Furthermore, they can be used for imaging with ¹⁹F MRI in addition to US and be further adapted for multimodal imaging applications by introducing additional functionalities, such as fluorescent dyes [2]. After further modifications their application in targeted drug delivery can be envisioned in the near future.

References

1. *M. Srinivas, I. J. de Vries, J. L. Cruz, C. G. Figdor. Contrast agents for imaging (pending patent application, filed Sep. 14, 2012). Application Number 12184562.2-1216*
2. *M. Srinivas, L. J. Cruz, F. Bonetto, A. Heerschap, C. G. Figdor, I. J. de Vries, Biomaterials 2010, 31, 7070-77*

Correction of nonlinear propagation artefact in contrast enhanced ultrasound imaging: in vitro and in vivo evaluation

Y Yildiz¹, R.J. Eckersley², Adrian Lim³, R Senior⁴, S Li⁵, D. Cosgrove⁶, M.X. Tang¹

¹*Department of Bioengineering, Imperial College, London, SW7 2AZ*

²*Division of Imaging Sciences, King's College London*

³*Charing Cross Hospital, Imperial College London*

⁴*Royal Brompton Hospital, Imperial College London*

⁵*Department of Diagnostic Ultrasound & Echocardiography, Sir Run Run Shaw Hospital, Zhejiang University, College of Medicine, Hangzhou, China*

⁶*Hammersmith Hospital, Imperial College London*

Background

Contrast enhanced ultrasound (CEUS) imaging which detects nonlinear microbubble echoes over background tissue signal is a proven tool in a wide range of clinical applications. The detection of these agents is hindered when nonlinear propagation of ultrasound in tissue containing bubbles causes tissue echoes to become nonlinear and leads to misclassification of tissue as bubble echoes [1-2]. Nonlinear propagation artefact has been observed in both high frequency vascular imaging [4] and low frequency deep tissue imaging [6] and significantly affects both qualitative and quantitative CEUS imaging [3]. Other studies have reported the clinical presence of such artefacts [4-6] and some strategies to reduce the artefacts [7-9] without any in vivo evaluation. In this study an artefact correction algorithm is evaluated both in vitro and in vivo on carotid artery CEUS images.

Methods

Ultrasound image formation is described as a convolution between a tissue scattering distribution (TSD) and the point spread function (PSF) of the imaging system with added measurement noise. It is assumed that a B-mode image at fundamental frequency contains mostly tissue signal.

Given the artefact is generated by tissue scattering and desirable nonlinear signals are generated by microbubble scattering, the proposed method estimates the unwanted nonlinear tissue signal by convolving an estimated tissue scattering distribution with an optimized nonlinear point spread function. This tissue signal is then removed from the original Pulse Inversion (PI) image to improve Contrast-to-Tissue Ratio (CTR).

The method was tested both in-vitro and in-vivo. Using a clinical scanner (Toshiba AplioXG), RF data was acquired from a tissue mimicking material (TMM) with a large (8mm) and a small (600 microns) wall-less vessel filled with microbubble suspension. The TMM is imaged at an MI of 0.3 with a

transmit center frequency of 4 MHz with SonoVue dilutions of 0.5 mL/L and 0.2 mL/L in the large and small vessel respectively.

Longitudinal images of the carotid artery during administration of a bolus injection of Sonovue (2 mL) were also acquired from four patients at an MI of 0.3 with transmit center frequency of 4 MHz.

To study the performance of the algorithm at low frequencies, a recent clinical case where pseudoenhancement was observed in gallbladder sludge was reproduced in vitro and correction applied.

Results

Figure 1 shows the original and corrected PI images of the TMM. In the original PI image the intensity of the tissue region below the large vessel, representing artefact, is comparable to the intensity of the microbubble region and the smaller vessel signal is buried in the tissue artefact. In the corrected image the intensity of the tissue is significantly reduced while the strength of the microbubble signals remain relatively unchanged. The increase in CTR for the large and small vessels is 8.7 ± 1 dB and 5.6 ± 0.84 dB respectively.

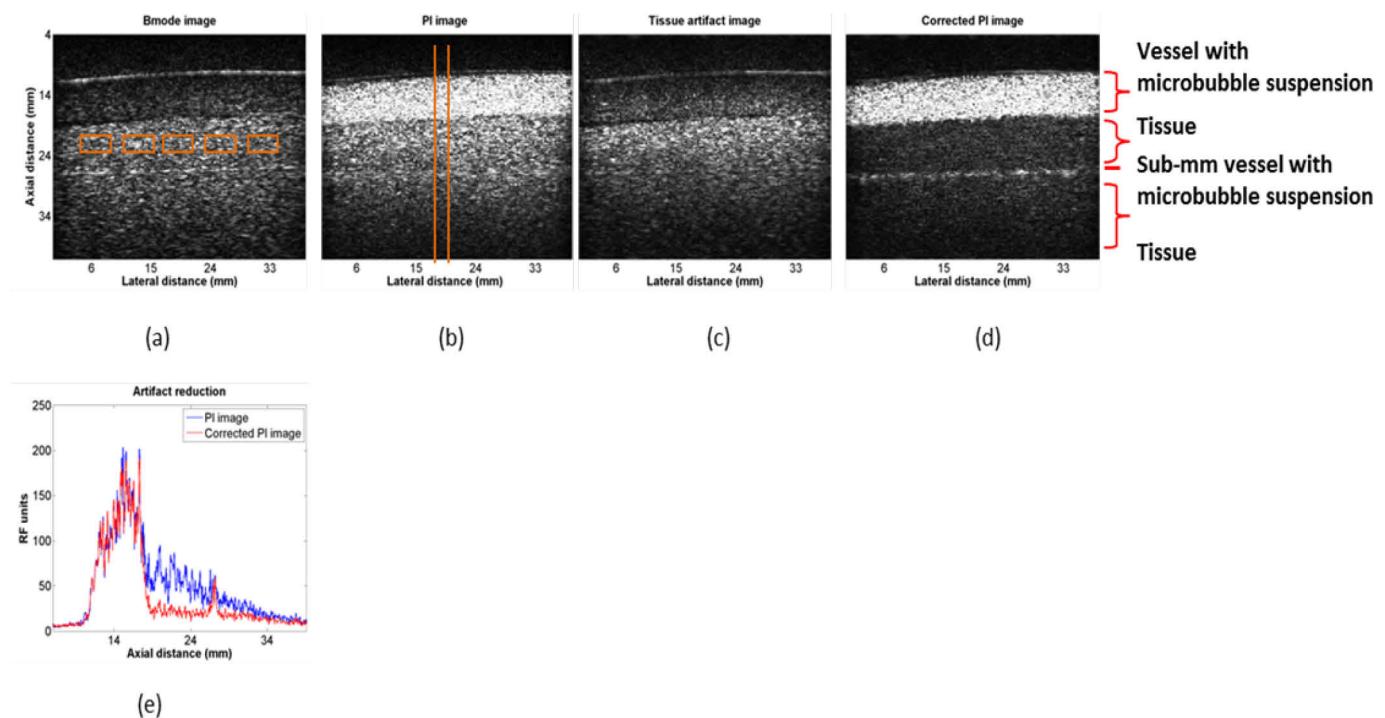


Figure 1: Images of a flow phantom acquired at an MI of 0.3 with SonoVue dilution of 0.5 mL/L in the large and 0.2 mL/L in the small vessel: Bmode image (a), PI image (b), estimated tissue artefact image (c), corrected PI image (d), demodulated RF data averaged over the columns indicated in orange lines showing artefact reduction. In the corrected image, CTR is increased 8.7 ± 1 dB for tissue region deep to the large vessel and 5.6 ± 0.84 dB for the small vessel in the ROIs indicated on the Bmode image.

To validate the algorithm's in vivo performance, contrast free images of a carotid artery were evaluated and resulted in an increase in CTR of 7.9 ± 0.6 dB along the far-wall. Since there is no contrast administered, the ground truth is known as the PI image results purely from tissue nonlinearity and all the signals in the PI image are artefacts.

Figure 2 shows original and corrected PI images of a patient's carotid artery with contrast. Lumen and tissue regions are indicated in the corrected PI image. The tissue artefact image is the artefact image estimated by the algorithm and subtracted from the original PI image to obtain the corrected PI image. It can be observed that the signal all along the far-wall is significantly reduced in the corrected PI image compared to the original. Specifically, the increase in CTR at the far-wall in the corrected PI image is 7 ± 1.5 dB. The displayed RF data corresponds to the brightest region of the far-wall as indicated by the orange lines on the original PI image. The average signal in the lumen after correction is nearly unchanged as can be seen from the RF data and the non-existence of signals in the lumen region of the estimated tissue artefact image.

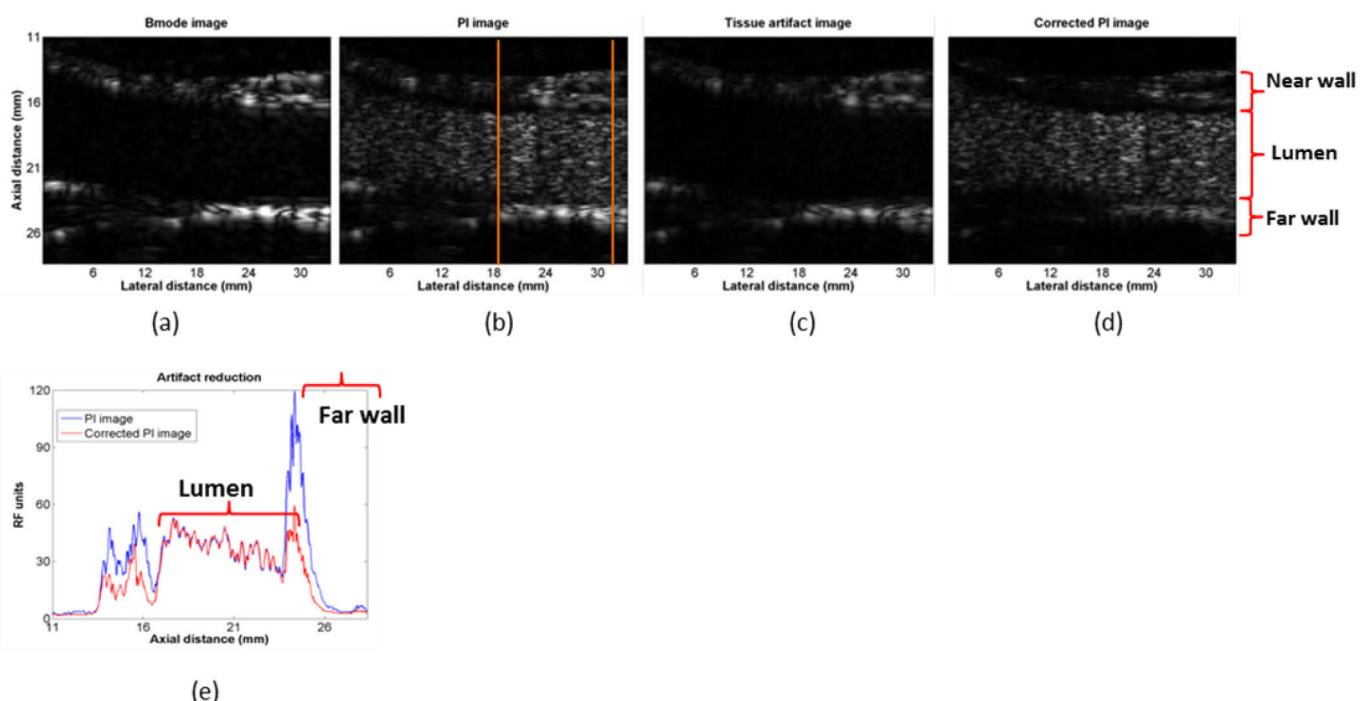


Figure 2: Carotid artery images with contrast acquired at an MI of 0.3 with a bolus injection of SonoVue: +Bmode image (a), original PI image (b), tissue artefact image estimated by the algorithm (c), corrected PI image (d) and demodulated RF data averaged over the columns indicated in orange lines showing artefact reduction (e). The corrected PI image shows significant artefact reduction along the far-wall with an increase in CTR in the corrected PI image of 7 ± 1.5 dB.

Initial evaluation of the algorithm in the in vitro reproduction of the gallbladder case gives 8.4 dB suppression of tissue artefact at a transmit center frequency of 2 MHz and an MI of 0.08 with microbubble concentration of 0.35 mL/L. Further in vitro and in vivo evaluation is under way.

Conclusion

The correction technique reduced nonlinear propagation artefacts in CEUS imaging of the carotid artery and showed an improvement in CTR of up to 11 dB in-vitro and 7dB in-vivo. Contrast signal from a small vessel of 600 micron in diameter buried in tissue artefacts prior to correction was recovered after the correction.

References

1. Tang, M.X. and R.J. Eckersley, *Nonlinear propagation of ultrasound through microbubble contrast agents and implications for Imaging*. *Ieee Transactions On Ultrasonics Ferroelectrics and Frequency Control*, 2006. 53(12): p. 2406-2415
2. Tang, M.X., N. Kamiyama, and R.J. Eckersley, *Effects of nonlinear propagation in ultrasound contrast agent imaging*. *Ultrasound In Medicine and Biology*, 2010. 36(3): p. 459-466
3. Tang, M.X., et al., *Quantitative contrast-enhanced ultrasound imaging: a review of sources of variability*. *Interface Focus*, 2011. 1(4): p. 520-539
4. ten Kate, G.L., et al., *Far-Wall Pseudoenhancement During Contrast-Enhanced Ultrasound of the Carotid Arteries: Clinical Description and In Vitro Reproduction*. *Ultrasound in Medicine & Biology*, 2012. 38(4): p. 593-600
5. Stijn C.H. et al, *Far wall pseudo-enhancement: A neglected artefact in carotid contrast-enhanced ultrasound? Atherosclerosis*, volume 229 issue 2 Pages 451-452, 2013
6. Yu, H.J., et al., *Pseudoenhancement Within the Local Ablation Zone of Hepatic Tumors Due to a Nonlinear Artefact on Contrast-Enhanced Ultrasound*. *American Journal Of Roentgenology*, 2010. 194(3): p. 653-659
7. G Renaud et al [Counter-propagating wave interaction for contrast-enhanced ultrasound imaging](#), 2012 *Phys. Med. Biol.* 57 L9
8. Pasovic, M, et al., *Second harmonic inversion for ultrasound contrast harmonic imaging*. *Physics in Medicine and Biology*, 2011.56(11): p. 3163-3180
9. Olivier C, Jean-François A, Gabriel M, Mickael T, Mathias F. *Suppression of tissue harmonics for pulse-inversion contrast imaging using time reversal*. *Physics in Medicine and Biology* 2008;53:5469
10. Yesna O Yildiz; Robert J Eckersly; Roxy Senior; Adrian Lim; David Cosgrove; Meng-Xing Tang. *Correction of nonlinear propagation artifact in contrast enhanced ultrasound imaging of carotid arteries: methods and in vitro evaluation*, *Ultrasound in Medicine and Biology* (under review)

A new non-destructive method for the visualization and quantification of targeted microbubbles in ultrasound molecular imaging

Jean-Marc Hyvelin, Peter Frinking, Emmanuel Gaud, Maria Costa, Sylvie Henrioud, Thomas Fresneau, Thierry Bettinger and François Tranquart

*Bracco Suisse S.A., Geneva Research Center and Manufacturing Site,
Plan-les-Ouates / Geneva, Switzerland*

Objectives

Ultrasound molecular imaging (USMI) is gaining momentum in preclinical research. Upon injection of targeted microbubbles (MB), those MB circulate in the blood stream, providing first an enhancement of tissue perfusion, and subsequently, during a late phase when most of the unbound MB have been eliminated from the bloodstream, specific areas show a prolonged enhancement due to the binding of the MB to the selected targets expressed on the surface of endothelial cells. Effective USMI requires the capacity to differentiate between bound MB and freely circulating unbound MB. This is usually achieved during the late phase several minutes (5-10min) after MB injection, when the enhancement of bound MB can be easily assessed. Despite the substantial clearance of unbound MB, the late phase enhancement usually still comprises remaining circulating MB. A classical approach to discriminate bound MB from remaining circulating ones, is to destroy all the MB (bound and unbound) in the field of view during late phase using high mechanical index (MI) pulses, and then to return to low MI imaging to record signals from only circulating MB. This so-called differential targeted enhancement (dTE) approach suffers from several limitations, *viz.* the binding cannot be assessed after destruction and the signal from circulating MB might be under/over-estimated. Moreover, despite some controversies, there are concerns of potential adverse effect of MB destruction with regards to the integrity of endothelial layer. To avoid these limitations of dTE, we recently developed an image processing method that improves the conspicuity of bound MB by suppressing the echoes originating from the remaining circulating MB. This method is based on a minimum intensity projection algorithm which preserves the minimum pixel value between subsequent imaging frames. Thus, it is based on the analysis of low MI data.

The aims of the present study were first to validate the quantitative aspect of the new method in an *in vitro* model, and then to compare it with the classical dTE method in an *in vivo* model.

Material and Methods

In vitro imaging of bound microbubbles. An in-house developed flow-cell chamber was used to assess the quantifiability of bound MB using the new image processing method. The bottom plate of the flow cell was coated with mouse P-selectin-Fc receptor at concentrations ranging from 1 to 10 $\mu\text{g}/\text{mL}$. Clinically translatable P-selectin-targeted MB were incubated by decantation for 30 min under static condition, and bubble density was measured optically at 5 random locations as a function of P-selectin concentration using an Olympus IX51 inverted microscope equipped with a 40x objective. In vitro imaging of bound MB was performed using a Sequoia ultrasound system equipped with a 15L8 linear array transducer with and without the presence of non-targeted MB (BR38) acting as freely flowing MB. CPS image sequences of 25 s were acquired at a frame rate of 4 Hz at 5 random locations in the flow cell and stored as DICOM clips. Data were processed off line with the new method implemented in VueBoxTM.

In vivo imaging of bound microbubbles. In vivo imaging of bound MB was performed in the orthotopic colorectal HCT116 tumor mouse model. Briefly, imaging was performed using BR55, a clinically translatable VEGFR2-targeted agent. Late phase enhancement of BR55 at 10 min post-injection was compared pre- and post-inhibition of VEGFR2 using free anti-VEGFR2 antibody, and to that of two different types of control MB. Qualitative and quantitative analysis of late phase enhancement was performed using the classical dTE approach and the new image processing method. A 50 s wash-in sequence was recorded at low MI and then the acquisition was frozen. After ten minutes, images were acquired at a frame rate of 4 Hz during 10 seconds. Then, high MI (1.9) destructive pulses were applied during 10 sec at 1 Hz. Finally, low MI acquisition was continued at 4 Hz during 10 s to measure signals from remaining circulating MB. From the pre- and post-destruction sequences, dTE was determined using VueBoxTM. The exact same pre-destruction sequence was used for the analysis with the new method, also using VueBoxTM.

Results

In vitro data. Figure 1 summarizes the in vitro results. In Figure 1A, the optically measured bubble density (mean \pm sd of the 5 random fields-of-view) is plotted as a function of the P-Selectin concentration. As can be observed, bubble density increased linearly with receptor concentration ($R^2 = 0.99$). Moreover, Figure 1B demonstrates that the USMI signal as measured with the new method is directly proportional to receptor concentration ($R^2 = 0.96$), indicating the quantifiability of the method.

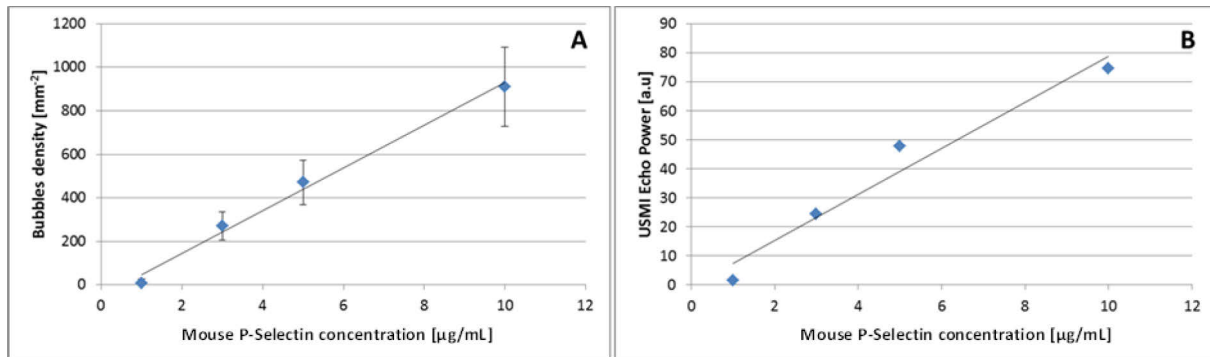


Figure 1: a) Optically measured mean bubble density \pm sd a.f.o. P-Selectin receptor concentration; b) USMI mean Echo Power a.f.o. P-Selectin receptor concentration measured with the new image processing method.

In vivo results. In the orthotopic HCT116 tumor model, 10 min after BR55 injection, late-phase enhancement was higher within the tumor compared to the surrounding tissue. Contrast enhancement within the tumor was mostly comprised of bound BR55 MB, whereas unbound circulating MB were observed within the surrounding tissue. In some cases, the presence of circulating MB within the surrounding tissue reduced the visual assessment of the tumoral lesion (Figure 2A). The use of the new image processing method for late phase enhancement analysis significantly improved the qualitative assessment of the bound MB within the tumor by effectively suppressing the echoes originating from the unbound circulating MB and therefore offering better delineation of the tumoral lesion (Figure 2B). Conversely, dTE was not able to fully suppress the echoes originating from circulating MB though it did improve tumor visualization (Figure 2C).

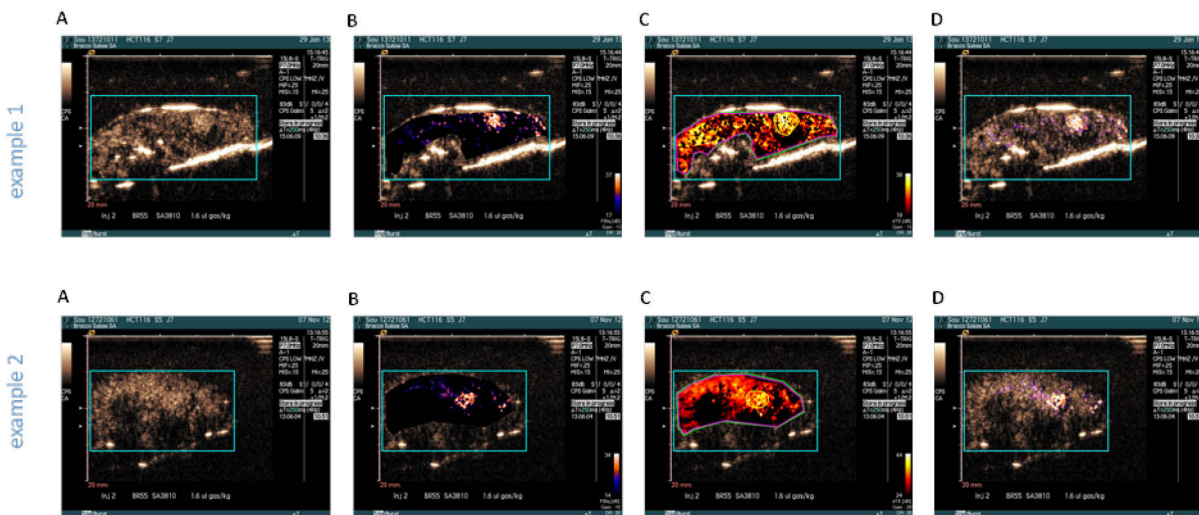


Figure 2: Typical examples of USMI of VEGFR2 in HCT116 colorectal tumor mouse model with BR55. A) CPS image of late phase enhanced signal as shown on the ultrasound scanner; B) new image processing method showing improved conspicuity of bound MB; C) similar image as B after using the classical dTE analysis; D) similar image as B but overlaid on the original CPS image.

We next quantified the late phase enhancement within the tumor applying either dTE or the new method. In a first series of animals ($n=5$), late phase enhancement of BR55 was compared to that of the first control MB, i.e. streptavidin MB functionalized with an antibody against FLK-1 (mouse VEGFR2

receptor). Quantification revealed no difference between BR55 and this control MB, whatever the method used. In a different group of animals ($n=6$), we compared late phase enhancement of BR55 to that of a second control MB (i.e. MB lacking the lipopeptide specific for VEGFR2 recognition). As expected, these MB produced a negligible late phase enhancement within the tumor. However, quantitative analysis of the same sequence indicated that late phase enhancement of these control MB was $9.8 \pm 8.5\%$ compared to BR55 when using the new method, and $24.2 \pm 13.2\%$ compared to BR55 when applying the classical dTE analysis. This is in agreement with a better suppression of the circulating MB by the new method. Finally, in a third series of experiment ($n=4$), we assessed the inhibition of binding of BR55 using the free anti-VEGFR2 antibody. Within the same mice, late phase enhancement of BR55 was quantified pre- and post-inhibition after 1 h. Quantitative analyses indicated that after inhibition, late-phase enhancement of BR55 decreased by more than 98% using the new method, and about 70% using dTE (Figure 3). These results support the use of the new image processing method for effectively suppressing the unbound circulating MB.

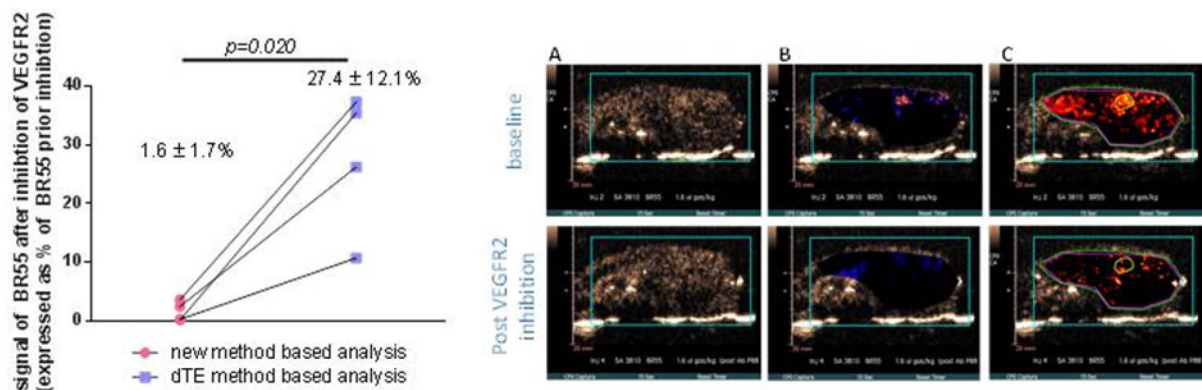


Figure 3: Quantitative analysis of late phase enhancement after injection of BR55 pre- and post-inhibition of VEGFR2 in HCT116 colorectal tumor. A) typical CPS images before and after inhibition; B) results obtained with the new method before and after inhibition; C) results obtained with dTE before and after inhibition.

Conclusion

With USMI, accurate detection of bound MB remains a prerequisite for accurately quantifying target expression. In the present study, we developed and validated a new non-destructive image processing method that allows automatic detection of bound MB. Compared to the classical dTE approach, this new method showed a better suppression of remaining circulating MB. These results suggest that the new method provides a more accurate estimation of the amount of bound MB therefore offering: 1) a reliable approach to detect and quantify bound MB without the need of MB destruction using high-MI pulses, a situation that might potentially cause endothelial cell damage; 2) a method of choice for comparing USMI of specific markers to their expression as assessed by immunostaining. Finally, a better suppression of circulating MB also allows improved delineation of the area of interest, an added value for the detection of a lesion within an organ.

Acoustic characterization and modeling of sorted bubbles and the implications for contrast imaging

Tim Segers, Maarten Kok, Nico de Jong* and Michel Versluis

*Physics of Fluids Group, MIRA Institute of Biomedical Technology and Technical Medicine and MESA+ Institute of Nanotechnology, University of Twente, The Netherlands
Biomedical Engineering, Thoraxcentrum, Erasmus MC, Rotterdam, The Netherlands

Conventional ultrasound contrast agent production methods result in bubble suspensions with a wide size distribution. Clinical ultrasound systems typically operate at a single frequency, therefore only a small fraction of the bubbles will resonate to the driving ultrasound pulse. Thus, the sensitivity of diagnostic imaging and molecular imaging with targeted microbubbles can be improved by narrowing down the size distribution¹. Moreover, a fully resonant bubble population of drug-loaded agents will be much more efficient in the local delivery to target cells.

Recently, we showed that contrast agents can be sorted to size with a novel microfluidic technique called pinched flow fractionation^{2,3} (PFF) (Fig. 1A). However, bubbles of the same size can have a different acoustic behavior through a varying phospholipid shell packing density. Enriched contrast bubble suspensions can also be obtained by acoustic bubble sorting where resonant bubbles are sorted from a polydisperse bubble suspension using the primary radiation force⁴ (Fig. 1B).

Here we show experimentally the increased sensitivity of narrow size distribution bubble populations obtained by size-selective sorting and by acoustic sorting. The responses of the enriched bubble suspensions were compared to the response of the native agent by their scattering-to-attenuation ratio (STAR). The scattering and attenuation were measured simultaneously using narrowband 16-cycle ultrasound pulses with a frequency ranging from 1.0 MHz to 5.5 MHz at acoustic peak negative pressures of 10, 25, 50 and 100 kPa. The echo of individual bubbles was modeled by a Rayleigh-Plesset type equation accounting for buckling and rupture of the viscoelastic bubble shell⁵. The frequency-dependent volume pulsations of all bubble sizes in the suspension are modeled from which the scattered pressure and attenuation are calculated. Inclusion of the position-dependent acoustic pressure distribution turned out to be essential for an accurate description of the pressure dependent nonlinear bubble response within the monodisperse suspension.

The STARs of the sorted agents ($R = 2.7 \mu\text{m} \pm 0.35 \mu\text{m}$) were 10 times larger at the fundamental frequency and 20 times larger at the second harmonic as compared to the native agent. A good agreement was found between the modeled and the measured scattering and attenuation curves (Fig. 2) for the acoustically sorted agent using a unique set of shell parameters, which confirms acoustic

monodispersity of the acoustically sorted bubbles. The initial surface tension of the bubbles in the suspension determines the acoustic crossover pressure where the bubble oscillations become non-linear and where the frequency of maximum response starts to decrease. The precise pressure dependence was measured by attenuation measurements over a pressure range from 5 to 75 kPa with pressure steps of 2.5 kPa (Fig. 3). A full characterization measurement was performed in less than 30 seconds. The measured pressure dependence of the resonance behavior of the acoustically sorted agent can potentially be employed in contrast-enhanced imaging to minimize shadowing effects in deep-tissue imaging, where imaging frequency and pressure can be selected such that bubbles resonate only in the acoustic focus where the pressure is at maximum. The characterization procedure provides valuable insight into an optimized bubble response obtained from contrast enrichment strategies in addition to fundamental insight into bubble shell parameters.

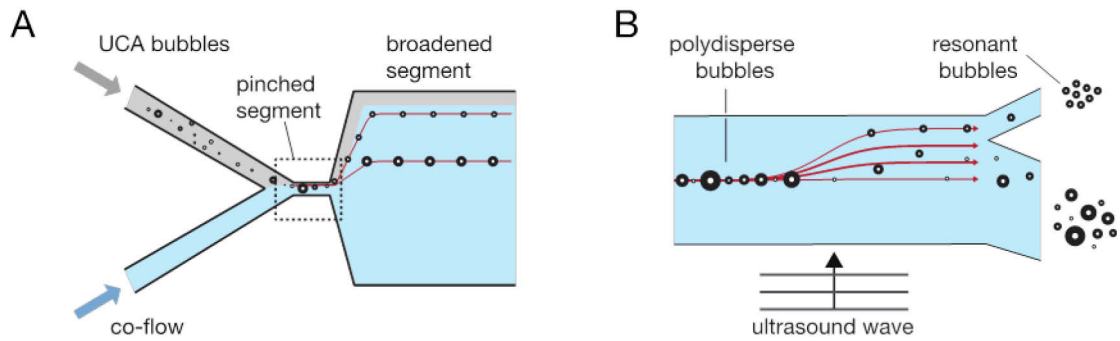


Figure 1: A) In a pinched microchannel bubbles are pinned against the top wall of the pinched segment. The distance between the bubble center on the wall is amplified when the pinched segment expands into the broadened segment sorting bubbles to size. B) In acoustic bubble sorting the resonant bubbles are separated from a stream of polydisperse bubbles by the primary radiation force.

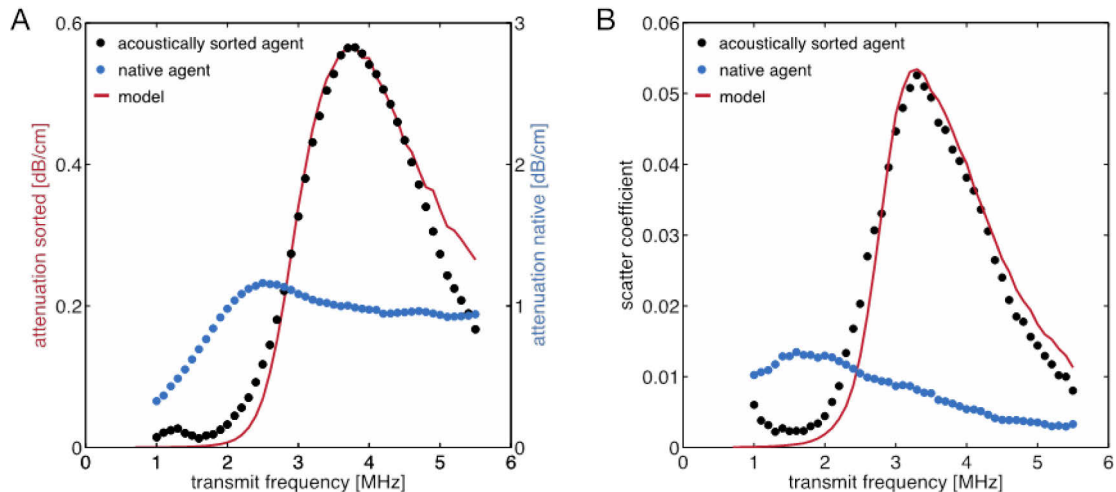


Figure 2: A) Attenuation as a function of the insonation frequency of acoustically sorted agent (black dots) and the native agent (blue dots) at 10 kPa. The red curve shows the modeled attenuation of the acoustically sorted bubbles. B) Scatter coefficient at the fundamental of acoustically sorted bubbles and the native agent. The red curve shows the modeled backscatter coefficient.

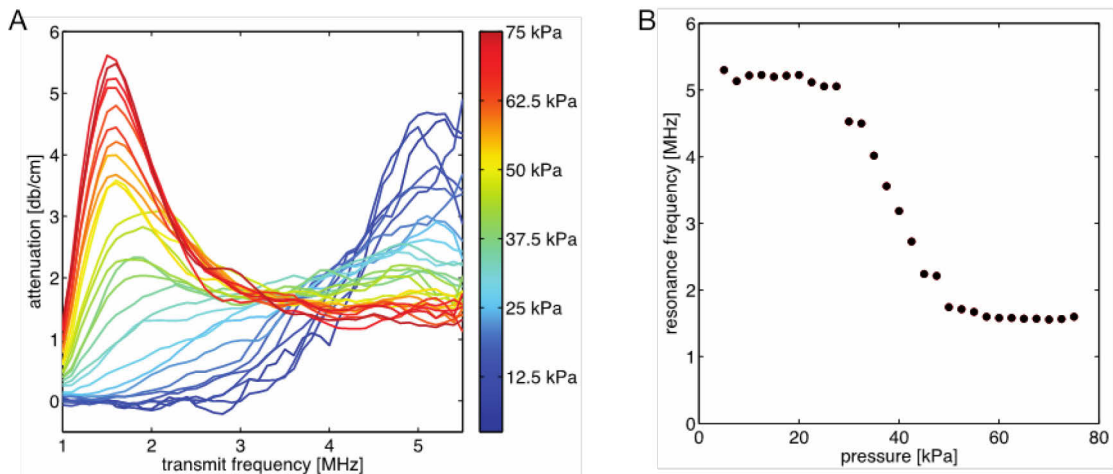


Figure 3: A) Attenuation of acoustically sorted bubbles as a function of the insonation frequency for acoustic pressures ranging from 5 to 75 kPa. B) The frequency of maximum response in figure 2A plotted as a function of the insonation pressure.

References

1. Hettiarachchi *et al.*, “On-chip generation of microbubbles as a practical technology for manufacturing contrast agents for ultrasonic imaging”, *Lab Chip*, 2007
2. Kok *et al.*, “Pinched flow fractionation for ultrasound contrast agent enrichment”, *Lab Chip*, to be submitted
3. Yamada *et al.*, “Pinched flow fractionation: continuous size separation of particles utilizing a laminar flow profile in a pinched microchannel”, *Anal. Chem.*, 2004
4. Segers *et al.*, “Acoustic bubble sorting for ultrasound contrast agent enrichment”, *Lab Chip*, 2014
5. Marmottant *et al.*, “A model for large amplitude oscillations of coated bubbles accounting for buckling and rupture”, *JASA*, 2005

To buckle or not to buckle, that is the question – a fluorescence high-speed camera study

**Klazina Kooiman^{1,2,3}, Tom van Rooij³, Flordeliza S. Villanueva¹, Bin Qin¹, Frits Mastik³,
Hendrik J. Vos^{3,4}, Alexander L. Klibanov⁵, Nico de Jong^{3,4}, Xucai Chen¹**

¹*Center for Ultrasound Molecular Imaging and Therapeutics, University of Pittsburgh Medical Center,
Pittsburgh, PA, USA*

²*Interuniversity Cardiology Institute of the Netherlands, Utrecht, the Netherlands*

³*Dept. of Biomedical Engineering, Thoraxcenter, Erasmus MC, Rotterdam, the Netherlands*

⁴*Laboratory of Acoustical Wavefield Imaging, Faculty of Applied Sciences, Technical University Delft,
Delft, the Netherlands*

⁵*Dept. of Biomedical Engineering, School of Engineering and Applied Science, University of Virginia,
Charlottesville, VA, USA*

Background

The nonlinear behavior of microbubbles is exploited in many contrast-enhanced ultrasound imaging modalities [1]. An example of such nonlinearity is “compression-only” behavior, where a microbubble compresses significantly more than it expands [2]. This phenomenon was first observed in an ultra-high-speed optical study on lipid-coated microbubbles in 2007 [2], and was later confirmed by other ultra-high-speed optical studies [3,4]. It was hypothesized that compression-only behavior is related to buckling of the lipid shell [5]. Also, the initial lipid concentration on the microbubble surface was thought to play a role, as microbubbles with a high initial lipid concentration are more likely to exhibit compression-only behavior as they can reach the buckling regime more easily [5]. The complex interplay is predicted by the Marmottant model [5], a mathematical description of microbubble dynamics. However, buckling of the lipid shell during ultrasound excitation has not been experimentally demonstrated. Up till now, optical high-speed imaging necessary to resolve microbubble oscillations in the MHz range could heretofore only be performed in bright field, allowing visualization of the gas core, but not the lipid coating. In this study we used high speed fluorescence imaging and fluorescence microbubbles to record the lipid distribution during microbubble oscillation. We hypothesized that focal high intensities of fluorescence (hot spots) reflect high localized concentration of lipids as a result of lipid buckling.

Methods

Microbubbles were made using the Vial Shaker method with a coating of DSPC and DSPE-PEG(2000)-Oregon Green 488, thus fluorescently labeling the lipid coating. Microbubbles were insonified at a frequency of 0.5 or 1.0 MHz with a 10-cycle sine wave. The peak negative acoustic pressure was varied between 25 kPa and 50 kPa. Fluorescence microscopic recordings were obtained with the UPMC Cam [6], an ultra-high-speed imaging camera at the University of Pittsburgh Medical Center. Frame rates

were 4-5 million frames per second. High speed fluorescence movies were analyzed for the degree of microbubble expansion and compression as well as formation of hot spots, defined as a focal area of increased fluorescence intensity. Compression-only behavior was previously defined when $E/C < 0.50$ [2], where $E = (\text{maximum diameter} - \text{initial diameter})/\text{initial diameter}$ is the relative expansion of the microbubble, and $C = (\text{initial diameter} - \text{minimum diameter})/\text{initial diameter}$ is the relative compression of the microbubble. At 25 kPa and 0.5 MHz, 50 microbubbles were studied. At 50 kPa and 0.5 MHz, 29 microbubbles were studied. At 50 kPa and 1.0 MHz, 40 microbubbles were studied.

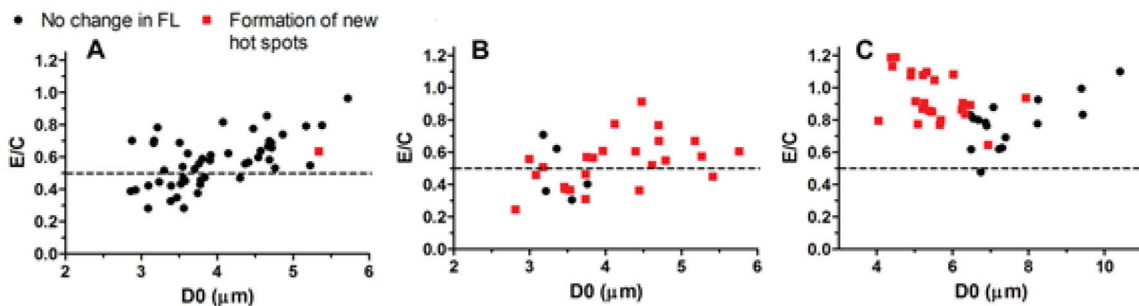


Fig. 1. E/C as function of the diameter of the studied microbubbles. A) 25 kPa, 0.5 MHz insonification; B) 50 kPa, 0.5 MHz insonification; C) 50 kPa, 1.0 MHz insonification. Dashed lines indicate defined cut-off level for compression-only behavior ($E/C \leq 0.50$). FL = fluorescence.

Results

At 50 kPa and 0.5 MHz, the majority of microbubbles formed new hot spots during the compression phase (see Fig 1 and 2). The same was observed for microbubbles $< 6.5 \mu\text{m}$ in diameter at 50 kPa and 1.0 MHz. We observed the formation of new hot spots for microbubbles that showed compression-only behavior as well as microbubbles that showed more symmetrical oscillations (i.e. $E/C \approx 1.00$). Compression-only behavior was observed in 36% of all microbubbles at 25 kPa and 0.5 MHz ($n=18$), in 41% of all microbubbles at 50 kPa and 0.5 MHz ($n=12$), and in 3 % of all microbubbles at 50 kPa and 1.0 MHz ($n=1$) (Figure 1). At 25 kPa and 0.5 MHz, newly formed hot spots during the oscillation of the microbubble were only observed in one microbubble, having an $E/C > 0.50$. In about half of all studied microbubbles, hot spots were already present before insonification. Interestingly, microbubbles without any hot spots before insonification showed stronger compression-only behavior than microbubbles that already had a hot spot before insonification. On the other hand, the fluorescence ultra-high-speed recordings revealed that formation of new hot spots occurred when the relative compression of the microbubbles was higher than 20% at 0.5 MHz (see Fig. 3A,B). MHz (see Fig. 3A,B). At 50 kPa and 1.0 MHz, the one microbubble showing compression-only behavior did not form hot spots. Similarly, hot spots were observed at this pressure and insonification frequency when the relative compression of the microbubble was higher than 15% (see Fig. 3C).

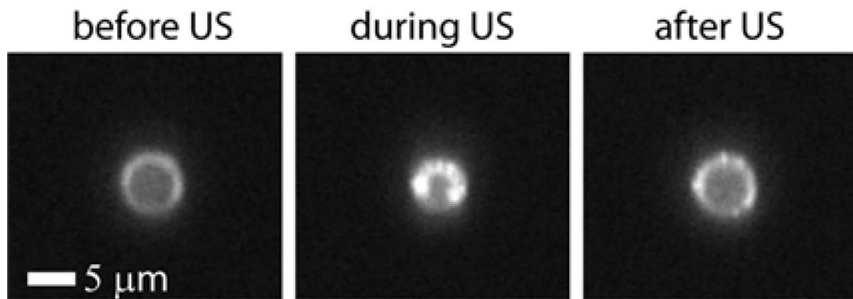


Fig. 2. Formation of hot spots during microbubble vibration. Selected frames from fluorescence high-speed recordings (~4 Mfps) of an insonified DSPEC/DSPE-PEG(2000)-Oregon Green 488 lipid-coated microbubble. The microbubble insonified at 50 kPa (0.5 MHz) formed hot spots that persisted after insonification; this microbubble showed compression-only behavior ($E/C = 0.45$).

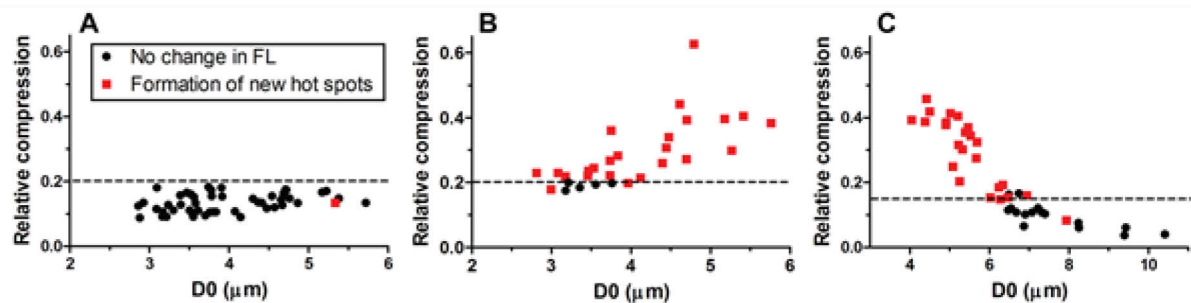


Fig. 3. Relative compression as function of the diameter of the studied microbubbles. A) 25 kPa, 0.5 MHz insonification; B) 50 kPa, 0.5 MHz insonification; C) 50 kPa, 1.0 MHz insonification. Dashed lines indicate threshold for formation of hot spots. FL = fluorescence.

Discussion and Conclusion

This experimental study reveals for the first time the formation of hot spots in the lipid shell of oscillating microbubbles during the compression phase of the oscillation cycle. However, hot spots were not correlated to compression-only behavior, but were related to the level of compression of the microbubbles during insonification. When a lipid microbubble is compressed, the surface density of the lipid increases and the surface tension at the microbubble/water interface decreases. At a certain compression threshold, no further reduction in surface tension is possible and the lipid monolayer becomes unstable. This leads to buckling/folding of the lipid monolayer [7]. For our microbubbles, this compression threshold was 15-20%. As the formation of new hot spots always occurred during the compression phase of the microbubble, these are considered as buckles/folds in the lipid monolayer. The specific microbubble characteristics that favor compression-only behavior have to be further investigated. However, the observations from our study can improve our understanding of microbubble behavior in an acoustic field which in turn may help optimize imaging strategies that exploit non-linear behavior.

Acknowledgments

This research was financially supported by the Interuniversity Cardiology Institute of the Netherlands (fellowship to K.K.), the Center for Ultrasound Molecular Imaging and Therapeutics, University of Pittsburgh Medical Center, and the Center for Translational Molecular Medicine and the Dutch Heart Foundation (PARISK). The authors would like to thank Brandon Helfield, Jianjun Wang, Regeant Pandy, and Linda Lavery from the Center for Ultrasound Molecular Imaging and Therapeutics, University of Pittsburgh Medical Center, and Michiel Manten, Geert Springeling, Robert Beurskens, Ying Luan, Tom Kokhuis, and Ilya Skachkov from the Dept. of Biomedical Engineering, Erasmus MC for technical assistance.

References

1. *Qin et al, Phys Med Biol 2009; 54: p. R27*
2. *de Jong et al, Ultrasound Med Biol, 2007; 33: p. 653*
3. *Overvelde et al, Ultrasound Med Biol, 2010; 36: p. 2080*
4. *Sijl et al, J Acoust Soc Am 2011; 129: p. 1729*
5. *Marmottant et al, J Acoust Soc Am 2005; 118: 3499*
6. *Chen et al, Rev Sci Instrum 2013; 84: p. 063701*
7. *Baoukina et al, PNAS 2008; 105:p. 10803*

The biophysical facet of sonoporation: Dynamics at the cellular level

Alfred C. H. Yu

Medical Engineering Program, The University of Hong Kong

In the biomedical acoustics community, sonoporation is nowadays a well heard phenomenon whereby ultrasound-triggered microbubble collapse would generate a cavitational force that is supposedly strong enough to puncture cellular membrane. Our current scientific understanding of sonoporation is however quite inadequate. Perhaps paradoxically, even the membrane dynamics involved in the process have not been characterized. Using real-time confocal microscopy techniques and a single-site sonoporation protocol, we have acquired a new series of epitomizing evidence at a single-cell level, and have demonstrated that sonoporation is a highly dynamic course of action with distinct periods of pore formation and resealing. We also show that membrane resealing is not a definite event, as its success depends on both physical and biochemical factors. Even if resealing is successful, subcellular structures such as the actin cytoskeleton may be concomitantly disrupted, and membrane herniations in the form of blebs may emerge. These findings serve to underscore that sonoporation is a biophysically active process. Its course of action at the cellular level is by no means trivial.

Contrast enhanced ultrasound parametric imaging for the detection of prostate cancer

***Postema AW, Frinking PJA, Smeenge M, De Reijke TM, De la Rosette JJMCH,
Tranquart F, Wijkstra H***

Introduction

The lack of adequate imaging is a major deficit in the diagnostic pathway of prostate cancer (PCa). The current standard of systematic random biopsies results in both misdiagnosis and a high number of negative biopsies. Dynamic Contrast Enhanced-Ultrasound (DCE-US) has shown improved detection of PCa over conventional greyscale-ultrasound. Perfusion parameters can be extracted from DCE-US recordings by dedicated software analysis and displayed in the form of parametric maps. These perfusion imaging techniques are aimed at improving diagnostic accuracy and decreasing user-dependency. The aim of the present study is to investigate the value of DCE-US and the added value of parametric map interpretation in predicting biopsy outcome and their potential to reduce the amount of negative biopsy cores.

Methods

For 651 prostate biopsy locations (82 consecutive patients referred for prostate biopsies) we correlated the interpretation of DCE-US recordings with and without parametric maps with biopsy results.

The parametric maps were generated by software under development by Bracco Suisse SA (Geneva, Switzerland) that analyses time-intensity curves (TIC) representing the echo-power as a function of time, on a pixel-by-pixel basis. For each pixel of the parametric map, histograms of Wash-in Rate (WiR) are calculated in small areas around this pixel, and statistical parameters such as the Mode (most occurring WiR value) and Standard Deviation (SD, dispersion of WiR values) are determined from the histograms. Classification between malignant and benign tissue is based on combinations of the Mode and SD of the WiR, and the thus calculated probability of PCa occurrence is displayed in the form of a colour-coded map(1).

We performed separate analyses including all tumours (“stringent analysis”) or only clinically significant tumours (“clinical analysis”). We determined the potential reduction in biopsies (negative on imaging) and associated missed tumor (false negatives). Additionally, we calculated sensitivity, specificity, NPV (Negative Predictive Value) and PPV (Positive Predictive Value) on the per-patient level.

Results

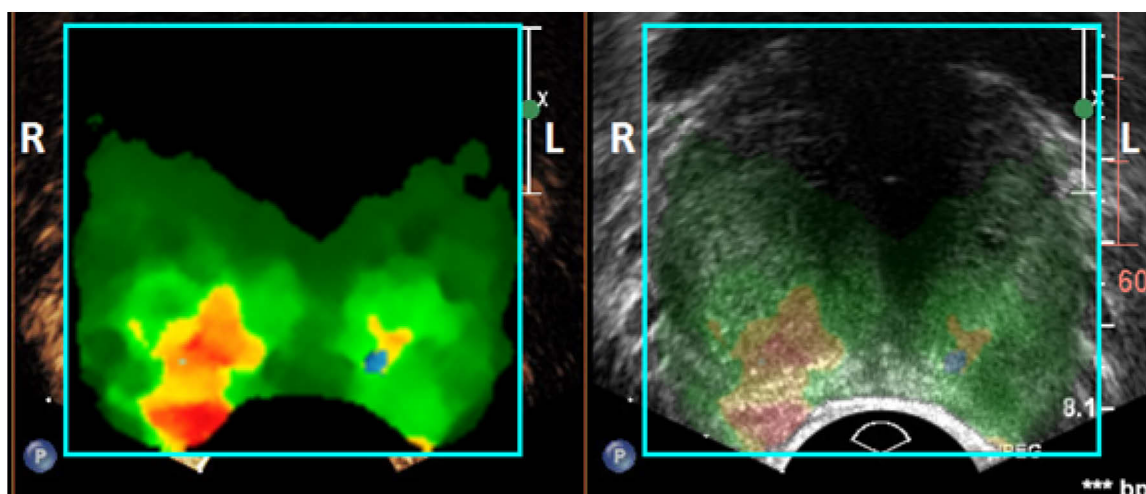
Based on DCE-US alone, 470/651 (72.2%) of biopsies were benign resulting in 40 clinical false-negatives (8.5%). Including parametric map interpretation, 411/651 (63.1%) of the biopsies locations

were classified benign, resulting in 23 clinical false-negatives (5.6%). On the per-patient level, the clinical analysis showed that DCE-US alone identified 38/82 patients as benign but missed the diagnosis in 8 patients. Including parametric map interpretation, 31/82 patients were identified as not needing biopsies missing 3 diagnoses. Sensitivity, specificity, PPV and NPV for clinically significant tumours were 73%, 58%, 50% and 79% for DCE-US alone and 91%, 56%, 57% and 90% when parametric map interpretation was included.

Conclusion

With DCE-US interpretation aided by parametric maps a good prediction can be made which biopsy cores can be safely omitted. The consequence is that the amount of biopsy cores could be lowered by almost two-thirds with a modest decrease in cancer diagnosis.

Figure 1. Parametric Map. Left: In this parametric map a high probability of prostate cancer is displayed red, intermediate probability yellow and low probability green. Right: the parametric map is displayed as a semi-transparent overlay over the greyscale TRUS image, allowing localization of lesions relative to prostate zonal borders. Biopsy cores from the right side confirmed Gleason 4+3 Prostate Carcinoma while the left side was benign.



References

Frinking P, Mercier L, Rognin N, Arditi M, Tranquart F. Real-Time Contrast-Enhanced Ultrasound Parametric imaging in the Prostate. 15th European Symposium on Ultrasound Contrast Imaging [Internet]. Rotterdam; 2010. Available from: <http://www-fgg.eur.nl/thorax/contrast/frames/ABSTRACTS/Orals/26.Frinking.pdf>

Assessment of the influence of propofol and butorphanol on contrast-enhanced ultrasonography of the feline kidney

E. Stock¹, K. Vanderperren¹, E. Van der Vekens¹, H. Haers¹, L. Duchateau², I. Polis³, M. Hesta⁴, J.H. Saunders¹

¹*Department of Veterinary Medical Imaging and Small Animal Orthopaedics, Faculty of Veterinary Medicine, Ghent University, Merelbeke, Belgium*

²*Department of Comparative Physiology and Biometrics, Faculty of Veterinary Medicine, Ghent University, Merelbeke, Belgium*

³*Vakgroep Geneeskunde en Klinische Biologie van de Kleine Huisdieren, Faculty of Veterinary Medicine, Ghent University, Merelbeke, Belgium*

⁴*Department of Nutrition, Genetics and Ethology, Faculty of Veterinary Medicine, Ghent University, Merelbeke, Belgium*

Introduction

Contrast-enhanced ultrasound (CEUS), using gas-filled microbubbles, has been proven a promising technique to evaluate tissue perfusion.¹ The CEUS technique as well as the contrast agents are extremely safe and well-tolerated.² Quantitative information about renal perfusion can be valuable in the diagnosis of diffuse renal disorders. As up to 30% of the older cats suffer from renal disease, accurate and early diagnosis is of major importance in veterinary medicine.³ Renal perfusion parameters in healthy cats are established, but these results are achieved in sedated or anesthetized cats.^{4,5} However, anesthetic and sedative agents may affect renal blood flow, altering the perfusion variables measured with CEUS.⁶

Therefore, the objectives of this study are (1) to compare the renal perfusion patterns of healthy cats that were imaged awake, sedated with butorphanol and anesthetized with propofol, (2) to investigate whether anesthesia leads to a decrease in variance in quantitative parameter values, due to more stable cardiovascular parameters when the effect of stress is reduced.

Materials and methods

Contrast-enhanced ultrasound of the left kidney was performed in 6 healthy purpose-bred cats, using a linear transducer of 12–5 MHz (iU22 xMATRIX, Philips) with contrast-specific software. Three 0.15 mL boluses of a commercial contrast agent (Sonovue®, Bracco) were administered, immediately followed by a 1 mL saline bolus. A cross-over design was used to compare 3 protocols: awake, butorphanol (Dolorex®, MSD AH, 0.4 mg/kg IM), and propofol (Propovet®, Abbott Lab, 3.5-7.7 mg/kg IV boluses on effect). The image clips obtained by the second and third injections were used for further evaluation.

Time-intensity curves were created from 2 regions-of-interest drawn in the renal cortex. The curves were analyzed for blood flow parameters representing blood volume (base intensity (BI), peak intensity (PI), area-under-curve (AUC)) and blood velocity (arrival time (AT), time-to-peak (TTP), wash-in/out (W_{in}/W_{out})) using a mixed model with cat as random effect.

A mixed model with protocol and injection sequence as categorical fixed effects and cat and time period nested in cat as random effects was used (SAS Version 9.3). The F-test at the 5% significance level was performed. The Bonferroni's adjustment technique was used for multiple comparisons and adjusted P-values are reported.

The study protocol was approved by the Local Ethical Committee of Ghent University (EC2013/36).

Results

There was no difference in the qualitative enhancement pattern between the 3 protocols. The microbubbles were first imaged in the renal artery and the interlobar arteries, followed by the renal cortex. While there was already decreasing intensity in the cortex, a heterogeneous enhancement of the medulla occurred (figure 1).

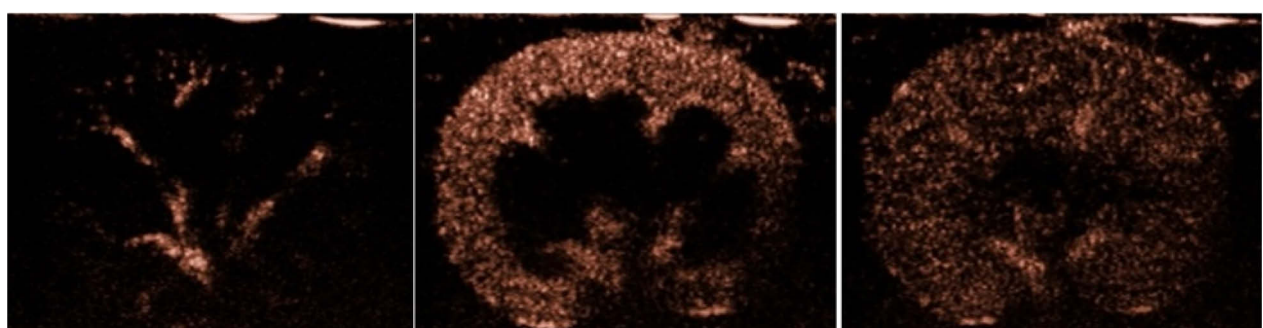


Figure 1: Enhancement pattern of the feline kidney: early phase with enhancement of the interlobar arteries, followed by the cortical phase. Later, there is a mild, heterogeneous enhancement of the medulla.

No significant effect of butorphanol compared to awake cats was observed in any of the perfusion parameters ($P>0.05$). Propofol induced a significant increase in AT, TTP compared to awake and sedated with butorphanol cats, and a significant increase in W_{in} compared to awake cats. Mean \pm standard error values of the renal blood flow parameters for the different protocols are summarized in Table 1. Figure 2 illustrates the time-intensity curves.

Anesthesia with propofol markedly reduced motion artifacts, although motion artifacts occurred at the same rate in sedated and awake cats. Sedation or anesthesia did not lead to a reduced variance.

None of the cats had adverse reactions during or after contrast medium administration.

Perfusion parameter	Awake	Butorphanol	Propofol
BI	0.77 ± 0.19	1.20 ± 0.18	0.69 ± 0.18
PI	60.66 ± 5.08	53.73 ± 4.88	51.47 ± 4.88
AT	3.83 ± 0.41	3.85 ± 0.40	5.14 ± 0.40^a
TTP	6.19 ± 0.40	6.18 ± 0.40	7.90 ± 0.40^a
W_{in}	27.55 ± 2.12	23.94 ± 2.05	19.93 ± 2.05^b
W_{out}	-0.45 ± 0.04	-0.39 ± 0.04	-0.39 ± 0.04
AUC	792.80 ± 139.74	695.55 ± 136.90	722.42 ± 136.90

Table 1 Means and Standard Errors of perfusion parameters calculated from the renal cortex in awake cats, cats sedated with butorphanol, or anesthetized with propofol

^a value represents a significant ($P<0.05$) effect in respect to awake and butorphanol group; ^b value represents a significant ($P<0.05$) effect in respect to awake group (BI base intensity, PI peak intensity, AT arrival time, TTP time-to-peak, W_{in} wash-in, W_{out} wash-out, AUC area-under-the-curve)

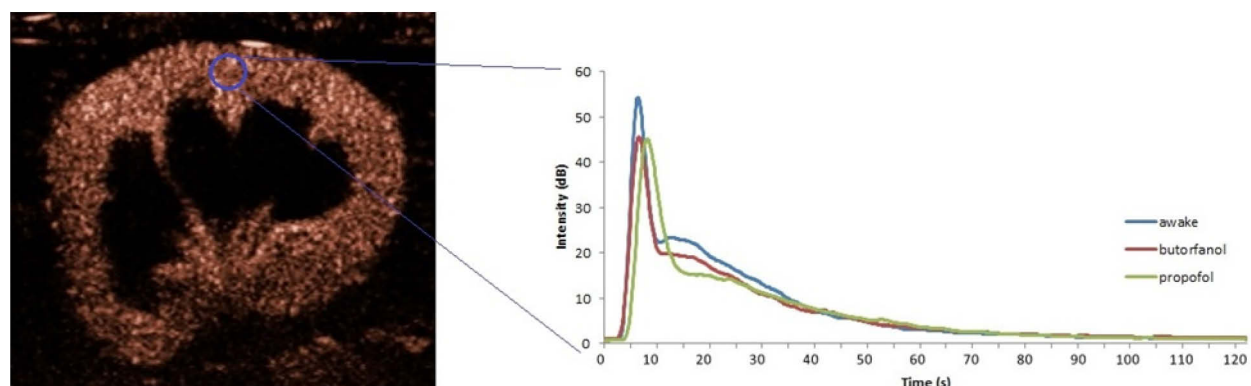


Figure 2: Mean time-intensity curves calculated from the renal cortex in awake cats, cats sedated with butorphanol, or anesthetized with propofol. Butorphanol has no significant influence on CEUS parameters.

Discussion

In this study, no subjective enhancement differences were observed in the kidney between the sedation/anesthesia protocols. Anesthesia with a combination of butorphanol and propofol induced an increase in the heterogeneity of the spleen in cats, which is probably related to the anesthesia-induced splenic congestion.⁷ Congestion following anesthesia is not observed on the renal parenchyma. Despite the absence of effect on subjective enhancement pattern, there were clear differences in the quantitative perfusion parameters between the propofol-group and the butorphanol- and awake-group.

Butorphanol is an opiate with agonistic effects on the κ -receptor. It has only minor effects on the μ -receptor. This explains its analgesic and sedative properties with minor cardiovascular and pulmonary effects.⁸ There were no significant differences in the perfusion parameters obtained after sedation with butorphanol compared with awake cats. Nevertheless, the variable and low sedation level obtained after the administration of butorphanol as a single agent makes it of limited use for sedation in healthy cats

for CEUS procedures. Butorphanol is still a valuable sedative agent for use in cats that are in a very bad general condition or suffer from severe cardiovascular disease.

Propofol is an anesthetic agent and acts by enhancing the function of GABA-receptors in the central nervous system. In contrast to butorphanol, propofol has well-known cardiovascular influences. The combined effect of a depression of the baroreceptor response and central sympathetic depression induces a decrease in cardiac output and systemic vascular resistance resulting in a depression of systolic and diastolic blood pressure.⁹ There was a significant delay in blood velocity parameters such as AT and TTP, with a less steep wash-in. A decrease of blood velocity is likely to be caused by systemic hypotension due to propofol anesthesia. Our findings correspond with a previous study on the feline spleen. An increase in AT was seen for CEUS of the spleen after anesthesia with butorphanol and propofol.⁷ In contrast, propofol anesthesia caused a reduction in TTP without a change in wash-in when performing CEUS of the liver in dogs.¹⁰ This finding was explained by an increased hepatic arterial blood flow which has been described after induction of anesthesia with propofol in dogs.¹¹

In conclusion, sedation with butorphanol has favorable cardiovascular properties without significant influence on renal perfusion parameters. Unfortunately, its sedative properties are often insufficient in healthy cats. Propofol causes a decrease in renal blood velocity and hence, quantitative blood velocity parameters. Taking this effect into account, because the most important perfusion parameter (AUC) was not influenced, propofol can be used for CEUS studies.

References

1. Haers H, Daminet S, Smets PMY, Duchateau L, Aresu L, Saunders JH: Use of quantitative contrast-enhanced ultrasonography to detect diffuse renal changes in Beagles with iatrogenic hypercortisolism. *Am J Vet Res* 2013;74: 70-77
2. Seiler GS, Brown JC, Reetz JA et al.: Safety of contrast-enhanced ultrasonography in dogs and cats: 488 cases (2002-2011). *J Am Vet Med Ass* 2013;242: 1255-1259
3. Lulich JP, Osborne CA, Obrien TD, et al.: Feline Renal-Failure - Questions, Answers, Questions. *Compendium on Continuing Education for the Practicing Veterinarian* 1992;14: 127-152
4. Leinonen MR, Raekallio MR, Vainio OM et al.: Quantitative contrast-enhanced ultrasonographic analysis of perfusion in the kidneys, liver, pancreas, small intestine, and mesenteric lymph nodes in healthy cats. *Am J of Vet Res* 2010;71: 1305-1311
5. Kinns J, Aronson L, Hauptman J et al. : Contrast-Enhanced Ultrasound of the Feline Kidney. *Vet Radiol Ultrasound* 2010;51: 168-172
6. Greene SA, Grauer GF. Renal disease. In: Tranquilli WJ, Thurmon JC and Grimm KA (eds) *Lumb & Jones' Veterinary anesthesia and analgesia*, Oxford, Blackwell Publishing, 2007; 915-919
7. Leinonen MR, Raekallio MR, Vainio OM et al.: Effect of anaesthesia on contrast-enhanced ultrasound of the feline spleen. *Vet J* 2011;190: 273-277
8. Hosgood G. Pharmacologic Features of Butorphanol in Dogs and Cats. *J Am Vet Med Ass* 1990;196: 135-136
9. Short CE, Bufalari A. Propofol anesthesia. *Vet Clin North Am Small Anim Pract* 1999;29: 747-778
10. Nyman HT, Kristensen AT, Kjelgaard-Hansen M et al. Contrast-enhanced ultrasonography in normal canine liver. Evaluation of imaging and safety parameters. *Vet Radiol Ultrasound* 2005;46: 243-250
11. Wouters PF, Vandevelde MA, Marcus MAE et al. Hemodynamic Changes During Induction of Anesthesia with Eltanolone and Propofol in Dogs. *Anesth Anal* 1995;81: 125-131

Evaluation of placental perfusion using contrast enhanced ultrasound imaging

Chloé J Arthuis^{1,2}, Anthony Novell¹, Jean Michel Escoffre¹, Franck Perrotin^{1,2}, Ayache Bouakaz¹

¹*UMR Inserm U 930, University François Rabelais Tours, 10 bd ter Tonnellé, 37032 Tours Cedex 1, France*

²*Department of Obstetrics and Gynecology CHRU Tours, 2 bd Tonnellé, 37044 Tours Cedex 9, France*
³*CNRS – TAAM UPS44, Centre d’Imagerie du Petit Animal, 45071 Orléans cedex 2, France*

Background, motivation and objectives

During pregnancy several complications are associated with the reduced uteroplacental blood flow and are the major cause of maternal and fetal morbidity and mortality. The uteroplacental perfusion is commonly assessed by measuring Doppler resistance index of the uterine and umbilical arteries but their application as screening tools for intrauterine growth restriction, preeclampsia and perinatal death remains controversial. In this context, contrast enhanced ultrasound (CEUS) offers a new opportunity to monitor the uteroplacental circulation and to quantify the intervillous space flow velocity.

Statement of contribution, methods

Five rats were examined by CEUS on days 14, 17 and 20 of pregnancy. For each rat, a 200 µl solution of Vevo Micromarkers was intravenously injected in rat tail. CEUS was performed using a LZ250D probe connected to a Vevo 2100 ultrasound scanner. Data were post-processed using Vevo CQ software and Matlab. Time-intensity curves were 5 minutes and quantitative perfusion parameters during wash-in and wash-out were calculated in 3 regions: whole placenta, placenta maternal face (PMF), placenta fetal face (PFF) and compared to each other.

Results, discussion and conclusion:

After injection, the contrast agents first appeared in the uterine artery supplying the placenta in blood and in the PFF (Fig. B). Then, the ultrasound signal increased slowly (Fig. C) in the placenta, filling the maternal face. Finally, the signal intensity decreases after few minutes (Fig. D) in the whole placenta. A faster and more intense wash-in was observed in PFF than in PMF. Between day 14 and 20, the peak enhancement increased by a factor 6.1 for both the PFF and PMF ($p<0.01$) whereas the whole placenta size increased by a factor 3 ($p<0.01$). In the same way, the wash-in rate increased by a factor 18 and 7 for PFF and PMF, respectively ($p<0.01$). These results suggest that a rapid expansion of the blood vessels supplying the placenta occurs during the last gestational week. During wash-out, contrast is more persistent in the PMF. At day 20, the fall time was 177s and 56s for PMF and PFF respectively.

Perfusion of the PFF can be distinguished from that of PMF by CEUS in both wash-in and wash-out phase. Noninvasive quantification of placental low velocity microcirculation by CEUS could be useful to manage placental insufficiency in the earlier stage of the pregnancy.

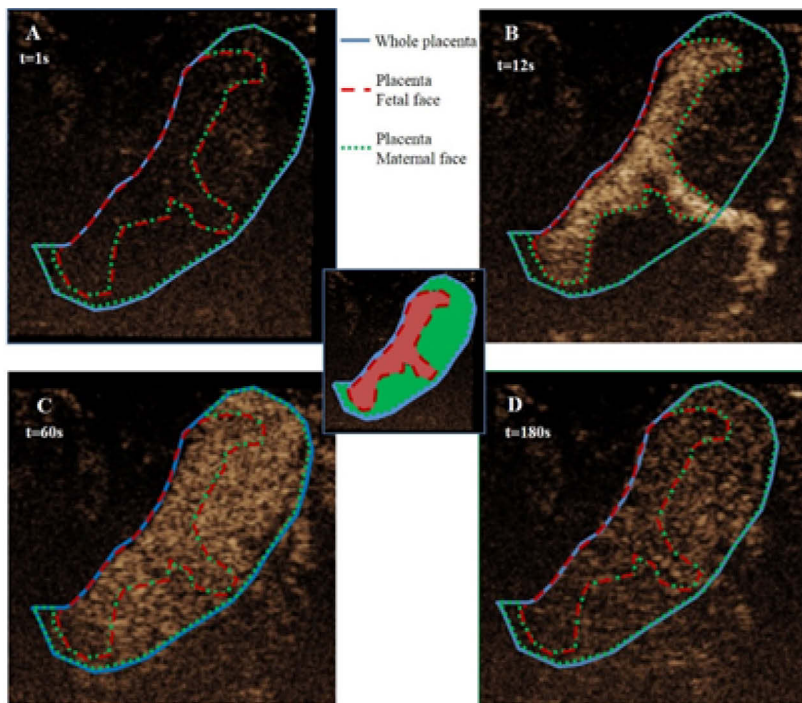


Figure 1. Monitoring of the contrast agents in the uteroplacental unit by CEUS on the 20th gestational day

Nitric oxide contributes to effective sonoreperfusion of microvascular obstruction

Francois TH Yu, Michelle Wolf, Mathea G Tenwalde, Frederick Schnatz, Xucai Chen,
Flordeliza S Villanueva and John J Pacella

Center for Ultrasound Molecular Imaging and Therapeutics,
University of Pittsburgh School of Medicine, Pittsburgh, PA, USA

Background

Despite successful reperfusion therapy with percutaneous coronary intervention for acute myocardial infarction, distal microembolization of atherothrombotic debris into the microcirculation causes microvascular obstruction and limits myocardial salvage, which is associated with worse prognosis and increased mortality. We have previously shown that microbubbles (MB) and ultrasound (US) therapy (termed “sonoreperfusion” or “SRP”) can restore microvascular perfusion during MVO *in vitro* (1) and *in vivo* (2), using long tone burst US producing prolonged inertial cavitation activity. However, the mechanisms implicated in SRP efficacy remain largely unknown. While inertial cavitation correlated in a dose dependent manner with SRP efficacy *in vitro* – suggesting physical chiseling (disintegration, degradation) of the clots by MB activity – we posit that biological mechanisms could also be implicated in the *in vivo* efficacy of SRP. Building on our previous experience and the literature suggesting the US+MB may modulate endothelial nitric oxide (NO) release (3-5), we sought to explore the importance of NO in SRP efficacy. NO has multiple beneficial microvascular effects which could ultimately culminate in a reduction in microvascular resistance and an increase in perfusion. Accordingly, we hypothesized that MB oscillations, through endothelial shear stress and mechanotransduction (6-7), would release NO (5) and contribute to SRP efficacy. We thus studied SRP efficacy in a hindlimb model of MVO during blockade of NO with L-N-nitroarginine methyl ester (L-NAME).

Methods

Using our previously described rat hindlimb model of MVO (2), we compared SRP efficacy with and without the addition of LNAME. Blood perfusion in the hindlimb before and after SRP therapy was measured by contrast specific ultrasound imaging (CPS with 15L8 probe, Sequoia, Siemens) using a burst replenishment sequence. Briefly, the rat was placed in right lateral position and an imaging probe was positioned just anterior to the left hindlimb to scan the long axis plane of the limb muscle. Imaging MB (Definity, Lantheus) were infused through a catheter placed in the jugular vein at a flow rate of 2 mL/h during imaging sequences. Microclots were prepared from clotted recalcified porcine blood (1 h at room temperature) followed by fractionation using successive passage through decreasing needles gauges (down to 30G) and filtering (200 µm pore mesh). The filtered microclots (range 15-30 µm) were injected into the femoral artery to cause MVO. A 1 MHz single element treatment transducer was

positioned perpendicularly to the imaging plane to deliver a 5000 cycle 1.5 MPa treatment pulse every 3 seconds. Treatment MB were perfluorobutane filled lipid encapsulated MB made in house (DSPC/mPEG2000-DSPE/polyoxyethylene(40)stearate, 3 μ m diameter), which were infused into the femoral artery at a concentration of 2×10^9 MB/mL at a flow rate of 3 ml/h. Treatment consisted of two successive 10 min SRP sessions. LNAME (50 mg/kg) or saline control was intravenously injected before ultrasound therapy. Video-intensity (VI) of hindlimb muscle over time was modeled by an exponential function $A(1-\exp(-\beta t))$ where A is a measure of microvascular blood volume and $A \times \beta$ is a measure of volume flow rate (8). Volume and flow rate at different time points were compared using Student's t-tests.

Results

Twelve rats were studied, with 6 receiving MB+US+saline (controls) and 6 receiving MB+US+LNAME (blockade of NO). Typical frames at 10s into burst replenishment imaging sequence are displayed in Figure 1. Microthrombi injection significantly reduced microvascular blood volume (A) compared to baseline (>85% reduction) in both groups ($p < 0.05$) (Figure 2). Microvascular blood volume was restored to baseline in the MB+US control group after SRP (65 VI, $p < 0.05$), but remained low in the LNAME (NO blockade) group after treatment 1. After treatment 2, microvascular blood volume remained at baseline levels (67 VI) in the MB+US control group. It increased to 28 VI in the MB+US+LNAME group, however, microvascular blood volumes in the LNAME animals after either treatment 1 or treatment 2 were not statistically different compared to the MVO stage. Perfusion rates ($A \times \beta$), corresponding to the initial slope of the intensity-time curve, followed similar patterns, but the differences were not statistically significant.

Discussion and Conclusions

In this preliminary study, our findings suggest that NO played an important role in SRP efficacy. Following MVO, reperfusion was blunted in the group receiving LNAME before SRP therapy. Further studies are needed to confirm these findings. Investigating the efficacy of other pulsing regimes, including shorter inertial cavitation pulses or stable cavitation regimes, are warranted.

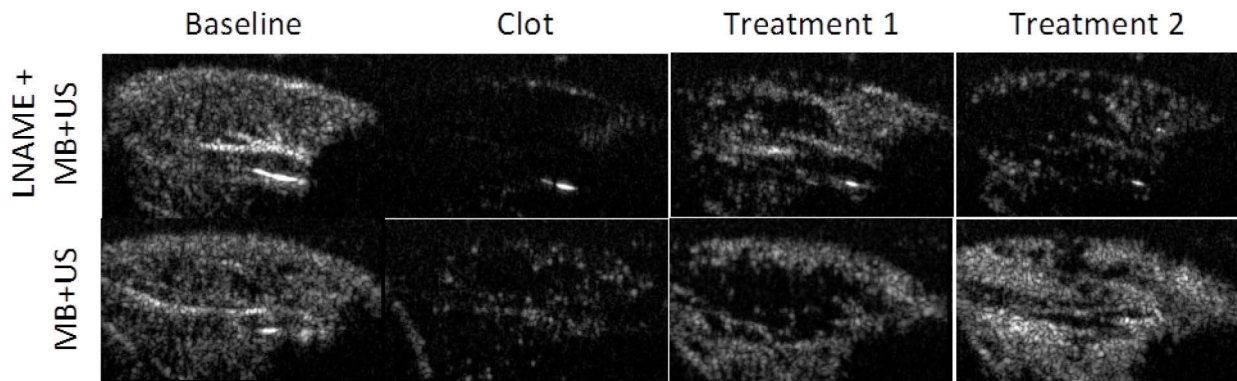


Figure 1: Typical perfusion image at 10s during burst replenishment imaging of the hindlimb at baseline, after clot injection, and after 1 and 2 sessions of SRP (10 min each).

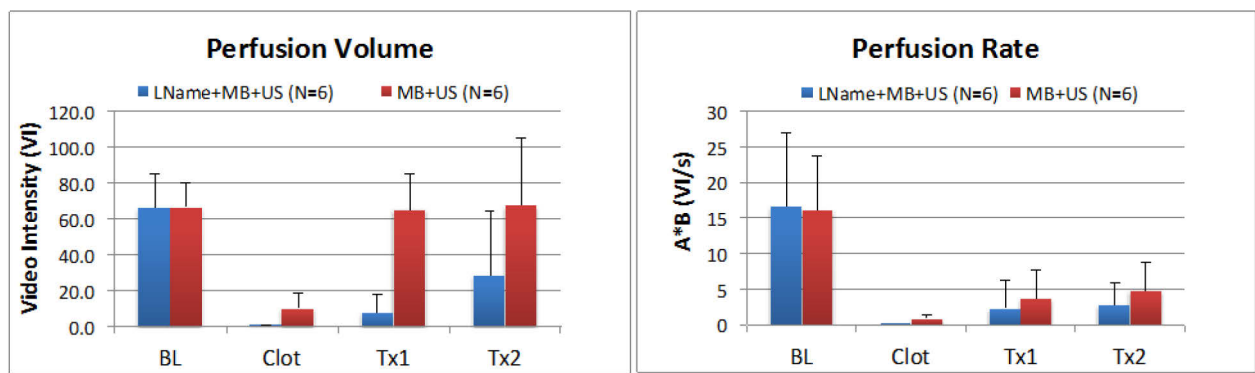


Figure 2: Perfusion volume and perfusion rate measured using burst reperfusion imaging at baseline (BL), after clot injection (Clot), and after 1 10 min (Tx1) and 2 sonoreperfusion therapy sessions (Tx2).

References

1. Leeman JE, Kim JS, Yu FT, Chen X, Kim K., Wang J, Villanueva FS. Effect of acoustic conditions on microbubble-mediated microvascular sonothrombolysis. *Ultrasound Med Biol* 2012;38(9): 1589-1598
2. Pacella JJ, Brands J, Schnatz FG, Black JJ, Chen X, Villanueva FS. Treatment of microvascular microembolization using microbubbles and long tone burst ultrasound: an in vivo study. *Ultrasound Med Biol.* 2014; In press
3. Siegel RJ, Suchkova VN, et al. Ultrasound energy improves myocardial perfusion in the presence of coronary occlusion. *J Am Coll Cardiol* 2004; 44(7): 1454-1458
4. Suchkova VN, Baggs RB, et al. Ultrasound improves tissue perfusion in ischemic tissue through a nitric oxide dependent mechanism. *Thromb Haemost* 2002; 88: 865-870
5. Belcik T, Mott B, Xie A, Kim S, Ammi A, Yan Z, Lindner JR. Ultrasound-mediated augmentation of tissue blood flow is potentiated by microbubble cavitation which acts through eNOS activation. *Circulation.* 2013; 128: A13325
6. White CR, Frangos JA. The shear stress of it all: The cell membrane and mechanochemical transduction. *Philos T R Soc B.* 2007;362:1459-1467
7. Sonkusare SK, Dalsgaard T, et al. AKAP150-dependent cooperative TRPV4 channel gating is central to endothelium-dependent vasodilation and is disrupted in hypertension. *Sci Signal* 2014;7(333): ra66
8. Wei K, Tong KL, Belcik T, Rafter P, Ragosta M, Wang XQ, Kaul S. Detection of coronary stenoses at rest with myocardial contrast echocardiography. *Circulation.* 2005; 112:1154-1160

Theranostic mRNA-loaded microbubbles in the lymphatics of dogs: Implications for ultrasound-guided cancer vaccination

**Heleen Dewitte^{a,*}, Katrien Vanderperren^{b,*}, Hendrik Haers^b, Emmelie Stock^b,
Luc Duchateau^c, Myriam Hesta^d, Jimmy H. Saunders^b, Stefaan C. De Smedt^a and
Ine Lentacker^a**

^a*Laboratory for General Biochemistry and Physical Pharmacy, Faculty of Pharmacy, Ghent University,
Ghent, Belgium*

^b*Department of Veterinary Medical Imaging and Small Animal Orthopaedics, Faculty of Veterinary
Medicine, Ghent University, Merelbeke, Belgium*

^c*Department of Comparative Physiology and Biometrics, Faculty of Veterinary Medicine, Ghent
University, Merelbeke, Belgium*

^d*Department of Animal Nutrition, Faculty of Veterinary Medicine, Ghent University, Heidestraat 19,
Merelbeke, Belgium*

Introduction & aim

Recently, we developed mRNA-loaded microbubbles, which could be used to transfect primary dendritic cells (DCs) *in vitro* with mRNA encoding tumor antigens and immunostimulants^{1,2}. This resulted in the generation of highly immunogenic cells that could be used as potent cancer vaccines². The overall aim of these mRNA-loaded microbubbles, however, is to deliver the mRNA to DCs *in vivo*. The ideal locations where this should occur are the lymph nodes, as these harbor large numbers of DCs and are the anatomical hot-spots for the induction of immune responses^{3,4}. Therefore, the aim of this study was to evaluate (a) whether mRNA-loaded microbubbles can reach the lymph nodes after subcutaneous injection; (b) if mRNA-loading influences microbubble drainage and (c) the potential of these nucleic acid-loaded microbubbles as intralymphatic theranostics.

Study design

The lymphatic drainage of unloaded and mRNA-loaded microbubbles was evaluated in a cross-over study after subcutaneous injection of the contrast agents in 6 healthy research beagles. The migration of the microbubbles from the injection site towards the lymph nodes was studied via contrast-enhanced ultrasound imaging (CEUS) using a 12.5 MHz linear transducer of a Philips iU-22 US scanner (MI=0.08). To reach intranodal microbubble destruction, the acoustic power was set at the highest level (MI=0.61).

Image analysis was performed using QLAB quantification software (Philips) and ImageJ. Measurements were performed by 2 independent, blinded observers.

Results & Discussion⁵

Using CEUS, we observed fast (<1 min) and extensive drainage of the injected microbubbles towards the draining lymph nodes for both unloaded and mRNA-loaded microbubbles, as exemplified in **Figure 1**. We could not detect significant differences in migration distance, intralymphatic stability or maximal echo intensity between both types of microbubbles.

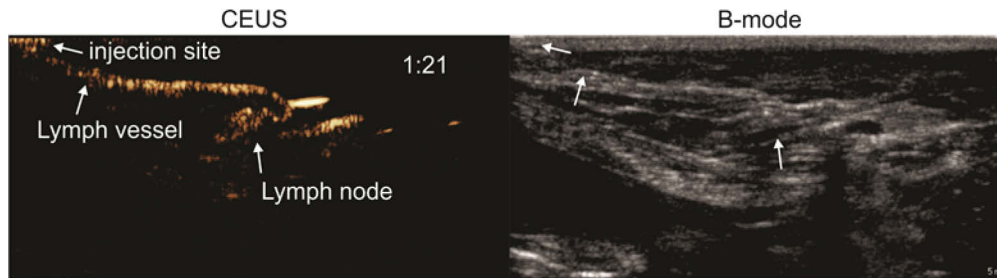


Figure 1: Contrast agent migration from the injection site into the lymph vessels and nodes. Upon microbubble injection, unidirectional transport of microbubbles away from the injection site, through an afferent lymph vessel into a draining lymph node can be observed with CEUS. Images were obtained after injection of mRNA-loaded microbubbles in female dogs. Time after microbubble injection is noted on the CEUS images (in min:s).

Interestingly, the images revealed detailed information on the lymphatic anatomy. It could point out the location of draining lymph nodes, as well as the number of afferent and efferent lymph vessels connected to that node. Moreover, different patterns of contrast agent presence within the node could be detected: Some nodes were completely filled with contrast agent, whereas others showed a “hollow” appearance, with contrast only appearing at the outer rim of the node, as shown in **Figure 2**. This can be explained by the fact that afferent lymph vessels can either directly discharge their content into the draining lymph nodes, or the afferent lymph vessels run through or over the nodes, without effectively discharging the lymph within the node⁶.

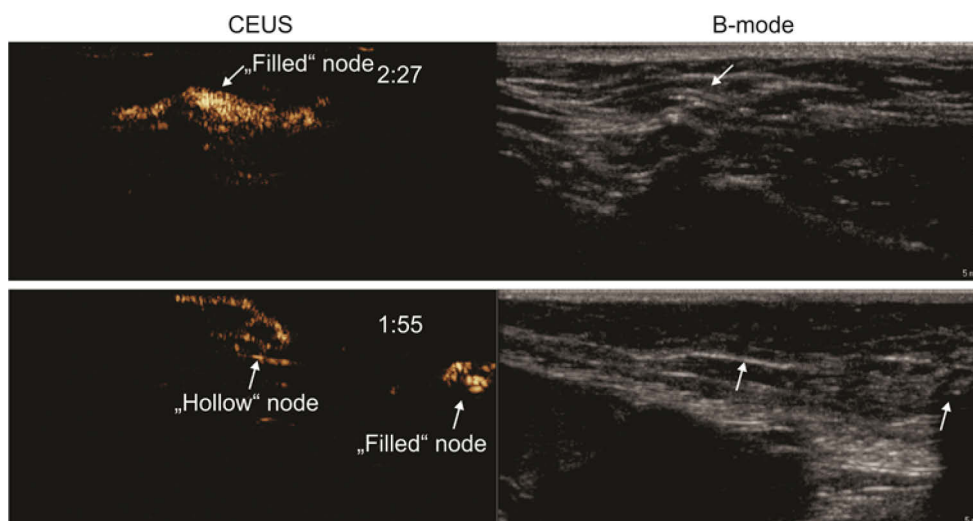


Figure 2: Lymph node anatomy observed by CEUS. CEUS can be used to identify the relation between afferent lymph vessels and draining lymph nodes. Lymph vessels either distribute their content within the lymph node (“filled” nodes) or they go around the lymph nodes without discharging its contents into the node (“hollow” nodes). In the latter scenario, we always observed a node with a “hollow” appearance, followed by a more distant “filled” node.

Lastly, we by delivering higher-intensity ultrasound bursts, the intranodal microbubbles could be imploded, as indicated by a significant reduction in the microbubble echo intensity. However, it is likely that the use of lower-frequency transducers that can emit higher ultrasound powers, could be better suited for effective mRNA delivery.

Conclusions

In conclusion, we were able to show that homemade unloaded as well as mRNA-loaded microbubbles efficiently reach the lymph vessels and nodes upon subcutaneous injection in dogs. mRNA-loading of the microbubbles had no significant effect on the distance of microbubble migration from the injection site, nor on the intensity of the observed contrast signals. This shows that theranostic mRNA-loaded microbubbles could have potential for the ultrasound-guided, ultrasound-triggered intranodal delivery of mRNA. However, it is beyond doubt that careful optimization of the acoustic parameters will be required to effectively sonoporate the cells of interest, and locally deliver the mRNA.

Acknowledgements

Heleen Dewitte is a doctoral fellow of the Institute for the Promotion of Innovation through Science and Technology in Flanders, Belgium (IWT-Vlaanderen). Ine Lentacker and Katrien Vanderperren are postdoctoral fellows of the Research Foundation-Flanders, Belgium (FWO-Vlaanderen). This project was funded through the FWO grant G016513N. The authors would also like to thank Prof.dr. Jean-Paul Remon for providing the animals, and Prof.dr. Mike Averkiou and dr. Ying Luan for the helpful discussions.

References

1. De Temmerman, M.L. et al. *mRNA-Lipoplex loaded microbubble contrast agents for ultrasound-assisted transfection of dendritic cells*. *Biomaterials* 32, 9128-9135 (2011)
2. Dewitte, H. et al. *The potential of antigen and TriMix sonoporation using mRNA-loaded microbubbles for ultrasound-triggered cancer immunotherapy*. *Journal of Controlled Release* 194, 28-36 (2014)
3. Randolph, G.J., Angeli, V. & Swartz, M.A. *Dendritic-cell trafficking to lymph nodes through lymphatic vessels*. *Nature Reviews Immunology* 5, 617-628 (2005)
4. Dewitte, H., Verbeke, R., Breckpot, K., De Smedt, S.C. & Lentacker, I. *Nanoparticle design to induce tumor immunity and challenge the suppressive tumor microenvironment*. *Nano Today* In press (2014)
5. Dewitte, H. et al. *Theranostic mRNA-loaded microbubbles in the lymphatics of dogs: implications for drug delivery*. *Theranostics* 5, 97-109 (2015)
6. Tanis, P.J., Nieweg, O.E., Olmos, R.A.V. & Kroon, B.B.R. *Anatomy and physiology of lymphatic drainage of the breast from the perspective of sentinel node biopsy*. *Journal of the American College of Surgeons* 192, 399-409 (2001)

Microvascular thrombolysis: From in vitro to in vivo to clinical trials

Thomas Porter, Feng Xie, John Lof

University of Nebraska Medical Center, Omaha, NE, USA

Background

Although both ultrasound induced inertial cavitation (IC) of microbubbles has been associated with vascular and microvascular thrombus dissolution (sono-thrombolysis) in the acute setting, the importance of other parameters (acoustic radiation, ultrasound stimulated nitric oxide release, etc.) has been difficult to determine. The purpose of this study was to determine the role of NO release in restoring microvascular blood volume (MBV) in acute thromboembolism.

Methods

Using a 1.7 MHz modified diagnostic ultrasound transducer (Philips S5-1), we quantified skeletal MBV changes in a rat hind limb ($n=16$ rats) after microvascular obstruction was created by injecting <200 micron diameter thrombi into the common iliac artery. Occlusion was confirmed with low MI non-destructive imaging (NDI) at 0.2 MI during a continuous intravenous infusion of 3% Definity microbubbles. Ten of the 16 rats then had a 10 minute treatment with intermittent IC inducing impulses from the same transducer, with four of these getting pre-treatment with a nitric oxide inhibitor (L-NAME). NDI imaging alone served as a control group ($n=6$).

Results

IC inducing impulses in the presence or absence of the nitric oxide inhibitor produced improved MBV when compared to NDI alone (Figure), but the addition of L-NAME resulted in a lower recovered MBV when compared to IC impulses without L-NAME ($p<0.01$).

Conclusions

IC inducing impulses from a modified diagnostic transducer can improve MBV in acute arterial thromboembolism by both dissolving thrombi and improving nitric oxide production. Other factors, such as ultrasound induced nitric oxide release and acoustic radiation, may have a role in both vascular and microvascular recanalization. Clinical data supporting this hypothesis will be presented.

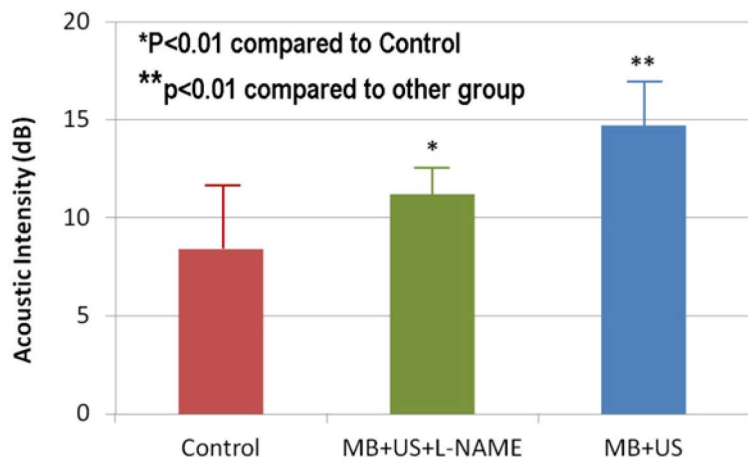


Figure Abbreviations: L-NAME: Nitric oxide synthase inhibitor; MB: Systemic intravenous infusion of 3% Definity; US=Modified 1.7 MHz diagnostic transducer

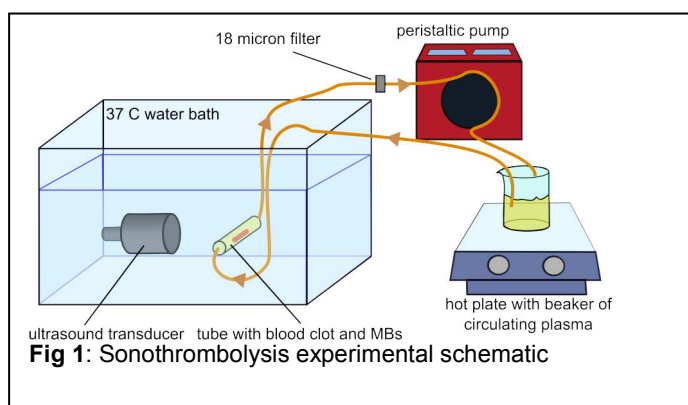
Microbubbles produced by a catheter-based flow-focusing microfluidic device for sonothrombolysis

Adam J Dixon*, Joseph P Kilroy*, Alexander L Klibanov*†, John A Hossack*

*Dept. of Biomedical Engineering, University of Virginia, Charlottesville, VA USA
†School of Medicine, Cardiovascular Division, University of Virginia, Charlottesville, VA USA

Introduction

Therapeutic approaches that enhance thrombolysis by combining tissue plasminogen activator (tPA), ultrasound (US), and/or microbubbles (MBs) are known generally as sonothrombolysis techniques. To date, sonothrombolysis clinical trials and experimental investigations have primarily utilized commercially available MB formulations (or derivatives thereof) with MB diameters between 1 – 4 μm [1]–[4]. The restriction on MB diameter is due to a risk of gas emboli formation, which has left MBs outside of this diameter range virtually unexplored for sonothrombolysis applications. However, it is broadly understood that large MBs confer larger bioeffects when excited acoustically, as has been shown in sonoporation [5], blood brain barrier disruption [6], and sonothrombolysis [7] applications. In support of the hypothesis that large MBs confer enhanced therapeutic effects, we demonstrate that MBs with diameters between 10 – 20 μm achieve a 4.5-fold increase in *in vitro* sonothrombolysis rates compared to MBs with diameters between 1 – 4 μm . In addition, we present the development of a catheter (1.5 mm diameter) containing a flow-focusing microfluidic device (FFMD) capable of producing large-diameter MBs suitable for catheter-directed sonothrombolysis applications. The microfluidically-produced MBs are comprised of N_2 gas and a weak albumin/dextrose shell, which confers MB half-lives on the order of 30 s and reduces the risk of gas emboli formation [8].



Methods

A schematic of the experimental sonothrombolysis system is shown in Figure 1. A flow-focusing microfluidic device (FFMD) produced monodisperse MBs comprised of 99.9% N_2 gas with a 10% (w/v) dextrose and 4% (w/v) bovine serum albumin (BSA) shell. MBs were produced within an *in vitro*

flow-loop that also contained a clot formed from 40% Hct human blood. Human plasma and tPA [0, 0.1, or 1 µg/ml] were circulated within the flow loop at 35 ml/min and the water bath was kept at 37 °C. Ultrasound (1 MHz, 10% duty cycle, 250 or 500 kPa PNP) was applied to the blood clot by a focused 1" diameter Panametrics transducer. Clot lysis rates were determined by measuring the concentration of hemoglobin in the re-circulating flow loop as a function of time.

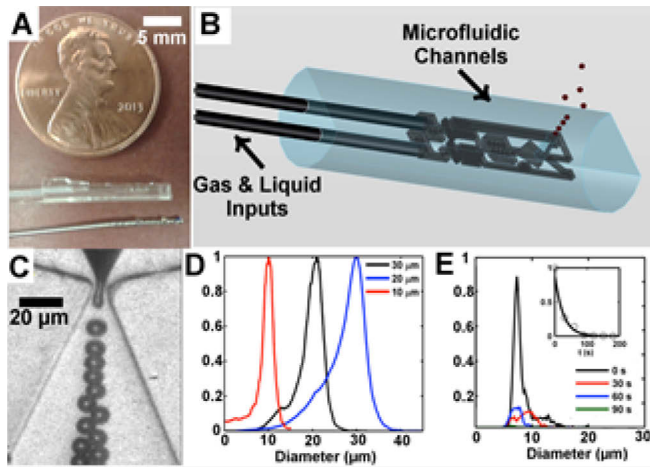


Figure 2: (a) 1.5 mm diameter microfluidic catheter shown next to a penny and 1 mm diameter IVUS for scale. (b) Schematic of microfluidic device catheter showing inlet lines and microfluidic channels. (c) Production of 10 µm diameter MBs at microfluidic device nozzle. (d) Size distributions of 10, 20, and 30 µm MBs. (e) Lifetime curves of a 10 µm diameter MB population. Greater than 99% of all MBs have disintegrated by 90 s.

Results

(a) MB Properties and Catheter-sized FFMD: Transiently stable MBs with diameters between 10 – 20 µm were produced by a FFMD at rates between 0.1 – 0.95×10^6 per second by adjusting either the gas pressure or the liquid flow-rate. All MBs were monodisperse at the device nozzle with a polydispersity index less than 6 % (Figure 2C, D). This MB formulation has previously been shown to have half-lives less than 30 s (Figure 2E) [9], [10]. In addition, Figure 2A,B,C shows our progress on miniaturizing the FFMD design to a catheter dimension suitable for catheter-directed sonothrombolysis (device diameter of 1.5mm)

Table 1

Parameter	Low	Med	High	Notes
tPA Conc. ($\mu\text{g/ml}$)	0	0.1	1	1 $\mu\text{g/ml}$ is clinical dose [1]
US PNP (kPa)	0	250	500	
FFMD MB Diameter (μm)	10	15	20	
FFMD MB Prod. Rate (MB/s)	5E4	25E5	95E5	
Sonication MB Conc. (MB/ml)	1E6		90E6	90E6/ml matches volume of 15 μm FFMD MBs @ 250,000 MB/s

(b) Sonothrombolysis: Clot lysis rates were evaluated across a range of tPA, US, and MB parameters, as shown in Table 1. This table utilized a design of experiments (DOE) approach to sample the extents of the parameters space with the intent of finding a global maximum that achieved maximal clot lysis. A subset of representative results are shown in Figure 3. Group B, representing the clinical tPA-only condition, has been normalized to a relative sonothromboysis rate of 1.0. Group A represents clot volume loss with no tPA, US, or MBs. Group C, which shows an 80% improvement over Group B, is sonothrombolysis using clinical tPA dose, clinical-MBs (average diameter 2.1 μm), and clinical ultrasound. Groups G, H, and I utilize 15 μm diameter FFMD MBs produced at 0.25×10^6 MBs/s with decreasing tPA dose. Group G achieves an approximate 8-fold improvement over tPA-alone (Group B) and a 4.5-fold improvement over Group C. Decreasing tPA dose is associated with a reduction in sonothrombolysis rates when using FFMD MBs, but in all cases, the FFMD MBs outperform the smaller diameter clinical MBs.

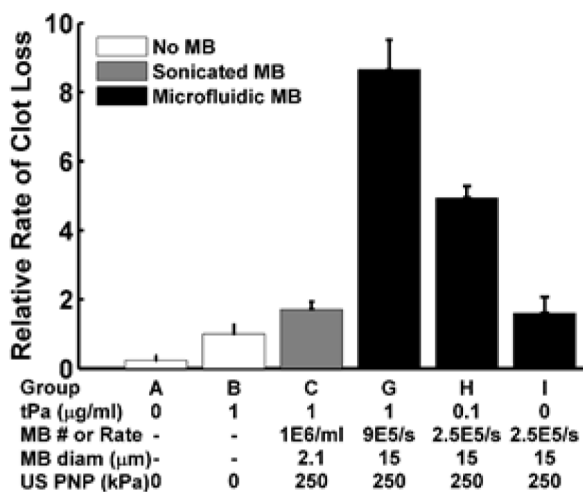


Figure 3: Results of *in vitro* clot lysis assay. Groups: (A) No treatment, (B) clinical tPA dose, (C) clinical tPA dose + clinical MBs + clinical US, (G,H,I) FFMD MBs with clinical US and decreasing tPA dose.

Conclusions

This is the first demonstration of *in vitro* sonothrombolysis with MBs dimensioned significantly outside of the 1 – 4 μm size range. Our results demonstrate a significant increase (~4.5X) in sonothrombolysis rates when using 10 – 20 μm diameter MBs rather than smaller MBs. We propose that safe use of these MBs can be achieved by specifically designing the MBs to dissolve within 90 s of fabrication by a catheter positioned in close proximity of the thrombus. To this end, we demonstrate operation of a catheter-sized FFMD with 1.5 mm diameter that produces MBs with 10 – 20 μm diameter half-lives of less than 30 s.

References

1. A. V. Alexandrov, C. a Molina, J. C. Grotta, Z. Garami, S. R. Ford, J. Alvarez-Sabin, J. Montaner, M. Saqqur, A. M. Demchuk, L. a Moyé, M. D. Hill, and A. W. Wojner, “Ultrasound-enhanced systemic thrombolysis for acute ischemic stroke.,” *N. Engl. J. Med.*, vol. 351, no. 21, pp. 2170–8, Nov. 2004
2. C. A. Molina, M. Ribo, M. Rubiera, J. Montaner, E. Santamarina, R. Delgado-Mederos, J. F. Arenillas, R. Huertas, F. Purroy, P. Delgado, and J. Alvarez-Sabin, “Microbubble administration accelerates clot lysis during continuous 2-MHz ultrasound monitoring in stroke patients treated with intravenous tissue plasminogen activator.,” *Stroke J. Cereb. Circ.*, vol. 37, no. 2, pp. 425–9, Feb. 2006
3. B. Petit, E. Gaud, D. Colevret, M. Ardit, F. Yan, F. Tranquart, and E. Allémann, “In vitro sonothrombolysis of human blood clots with BR38 microbubbles.,” *Ultrasound Med. Biol.*, vol. 38, no. 7, pp. 1222–33, Jul. 2012
4. K. E. Hitchcock and C. K. Holland, “Ultrasound-assisted thrombolysis for stroke therapy: better thrombus break-up with bubbles.,” *Stroke J. Cereb. Circ.*, vol. 41, no. 10 Suppl, pp. S50–3, Oct. 2010
5. Z. Fan, H. Liu, M. Mayer, and C. X. Deng, “Spatiotemporally controlled single cell sonoporation,” *Proc. Natl. Acad. Sci. U. S. A.*, vol. 109, no. 41, pp. 1–4, Sep. 2012
6. J. J. Choi, J. A. Feshitan, B. Baseri, S. Wang, Y.-S. Tung, M. A. Borden, and E. E. Konofagou, “Microbubble-size dependence of focused ultrasound-induced blood-brain barrier opening in mice in vivo,” *IEEE Trans. Biomed. Eng.*, vol. 57, no. 1, pp. 145–154, Jan. 2010
7. M. J. Borrelli, W. D. O'Brien, E. Hamilton, M. L. Oelze, J. Wu, L. J. Bernock, S. Tung, H. Rokadia, and W. C. Culp, “Influences of microbubble diameter and ultrasonic parameters on in vitro sonothrombolysis efficacy.,” *J. Vasc. Interv. Radiol. JVIR*, vol. 23, no. 12, pp. 1677–1684.e1, Dec. 2012.
8. A. H. Dhanaliwala, A. J. Dixon, D. Lin, J. L. Chen, A. L. Klibanov, and J. A. Hossack, “In vivo imaging of microfluidic-produced microbubbles,” *Biomed. Microdevices*, In Press
9. A. J. Dixon, A. H. Dhanaliwala, J. L. Chen, and J. A. Hossack, “Enhanced intracellular delivery of a model drug using microbubbles produced by a microfluidic device,” *Ultrasound Med. Biol.*, vol. 39, no. 7, pp. 1267–1276, 2013
10. J. L. Chen, A. H. Dhanaliwala, A. J. Dixon, A. L. Klibanov, and J. A. Hossack, “Synthesis and Characterization of Transiently Stable Albumin-Coated Microbubbles via a Flow-Focusing Microfluidic Device,” *Ultrasound Med. Biol.*, vol. 40, no. 2, pp. 400–409, Feb. 2014

Real-time control of ultrasound cavitation applied to extracorporeal ultrasound thrombolysis

Adrien Poizat^{1,2}, Bruno Gilles¹, Jean-Christophe Bera¹, Christian Cachard²

¹LabTAU, U1032, INSERM, Université Claude Bernard Lyon 1 FRANCE

²CREATIS, CNRS UMR 5220, INSERM U1044, INSA, Université Claude Bernard Lyon 1 FRANCE

Focused ultrasound enables targeted therapeutic treatments in human body. It has been successfully applied to extracorporeal ultrasound thrombolysis without any thrombolytic agent or any ultrasound contrast agent: In that case, cavitation activity is directly responsible for the thrombolysis, and either short pulses with high negative peak pressure [1,2] or longer pulses with lower negative peak pressure can be used [3]. In this latter case, problems of reproducibility related to the random aspect of cavitation process are encountered. Therefore a better control of cavitation activity during ultrasound treatment is necessary for clinical implementation of ultrasound thrombolysis devices.

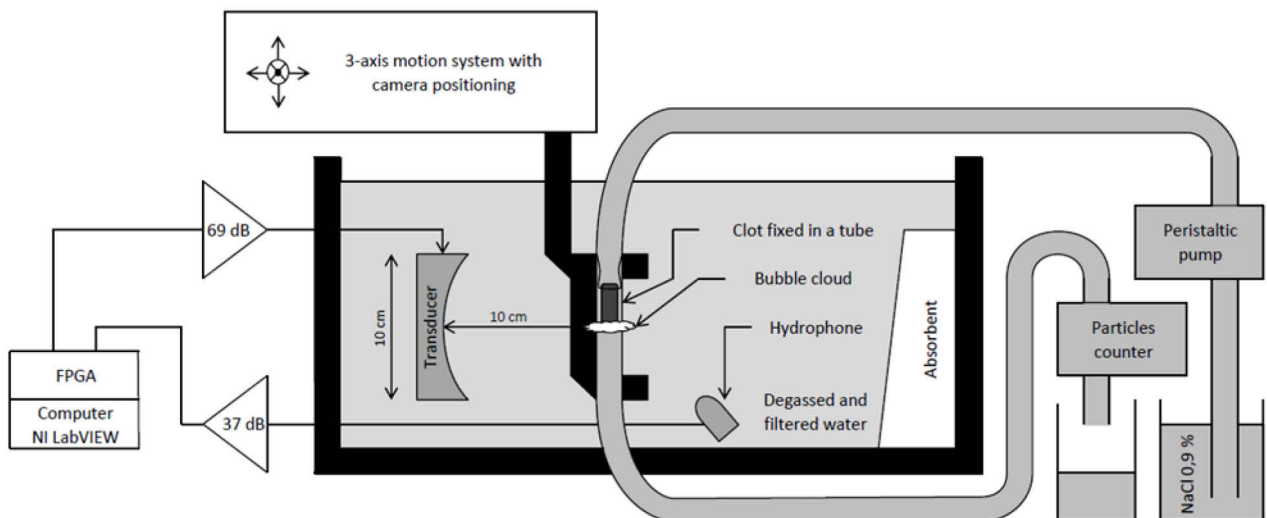


Figure 1

A system for temporal control of ultrasound cavitation was implemented for in vitro ultrasound thrombolysis experiments (*Figure 1*). A focused transducer (500 kHz or 1MHz) was used in pulsed mode (period 250 to 3000 ms, duty-cycle 0.01 to 0.1) to generate cavitation in the focal region, where a blood clot is placed. Ultrasound cavitation activity (CI) was quantified in real time from the acoustic signal measured by a hydrophone by averaging dB-power spectra of scattered signals. A feedback loop implemented by a field-programmable gate array (FPGA) controlled the cavitation activity with a 0.4 ms time delay (*Figure-2*). This device was applied on in vitro human blood clot model. Clots obtained with blood from different anonymous healthy volunteers were tested and clot lysis efficiency was

measured for each clot. Several parameters were assessed such as acoustic intensities in open loop and cavitation activities in closed loop, as well as the clot sweep velocity.

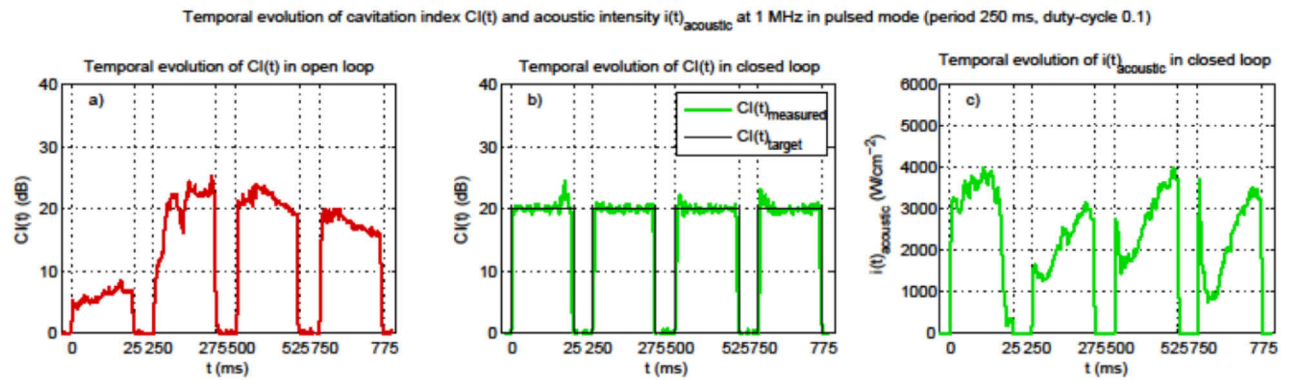


Figure 2

Tests performed (Figure-3) show an excellent efficiency in closed loop for sufficient cavitation activity. Without regulation, a very low reproducibility in clot destruction efficiency was observed at moderate intensities (45 W/cm^2). The real-time regulation permits us to set a stable and reproducible cavitation activity leading to complete clot lysis at lower intensities with a much better reproducibility.

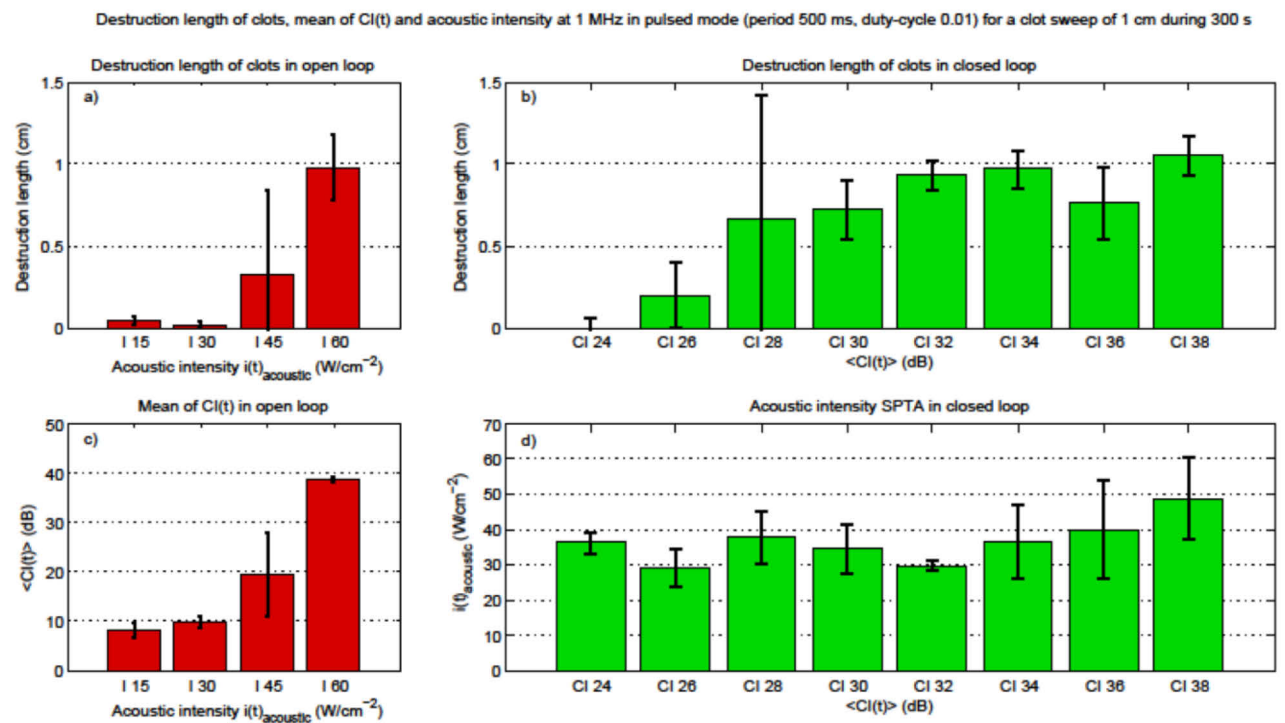


Figure 3

References

1. A. D. Maxwell, G. Owens, H. S. Gurm, K. Ives, D. D. Myers Jr., and Z. Xu, « Noninvasive treatment of deep venous thrombosis using pulsed ultrasound cavitation therapy (histotripsy) in a porcine model », *Journal of Vascular and Interventional Radiology*, vol. 22, no. 3, pp. 369–377, 2011
2. C. Wright, K. Hynynen, and D. Goertz, « In vitro and in vivo high-intensity focused ultrasound thrombolysis », *Investigative Radiology*, vol. 47, no. 4, pp. 217–225, 2012
3. I. Saletes, B. Gilles, V. Auboiron, N. Bendridi, R. Salomir, and J. C. Béra, « In Vitro Demonstration of Focused Ultrasound Thrombolysis Using Bifrequency Excitation », *BioMed Research International*, vol. 2014, 518787, 2014

Safety and feasibility of diagnostic ultrasound high mechanical index impulses in restoring epicardial flow in acute ST segment elevation myocardial infarction in humans

Miguel Osmam Aguiar, Jeane Mike Tsutsui, Bruno Garcia Tavares, Diego Garcia, Alessandra Gomes de Oliveira, José A.F. Ramires, Roberto Kalil Filho, Thomas R. Porter, Wilson Mathias Junior

*Sao Paulo University Medical Center, Sao Paulo, Brazil and
University of Nebraska Medical Center; Omaha, Nebraska, USA*

Objective

Intravenous microbubbles (MB) and transthoracic ultrasound have been utilized to recanalize both the microvasculature and epicardial vessels in animal models of ST segment elevation myocardial infarction (STEMI). The feasibility and safety of such an ultrasound guided approach in humans with STEMI has not been studied.

Methods

In 20 patients (16 male; mean age 57 \pm 9 years) with acute STEMI (14 anterior wall, one lateral wall, five inferior wall) at the Sao Paulo Medical Center Cardiovascular Emergency Room (InCor), diagnostic ultrasound guided high mechanical index impulses were applied within and outside the risk area during a continuous infusion of intravenous 3% Definity. Patients either received a custom designed high mechanical index (MI) impulses at 4-20 usec and >1.0 MI (n=6) designed for the Philips 1.7 MHz S5-1 transducer, or repeated high diagnostic high mechanical index impulses (all <2 usec pulse duration; MI 1.0; n=7) whenever very low mechanical index perfusion imaging detected microbubbles within the microvasculature. A control group (n=5) received limited diagnostic high mechanical index impulses (<5) just to analyze perfusion within the risk area at various intervals of treatment. All patients received ultrasound treatments before and immediately after emergent percutaneous intervention (PCI). Comparisons between groups on survival during the treatment period, angiographic recanalization rates at the time of the initial angiography, ST segment changes in EKG, and reduction in infarct size (salvagability index) at magnetic resonance imaging 48-72 hours post STEMI.

Results

There were no deaths during the initial treatment period pre-PCI in any group. No delays in door to dilation time were observed in any group, or when compared to patients receiving no therapy. Angiographic recanalization rates at the time of the initial angiogram were 6/7 (86%) in the repeated high diagnostic high mechanical index impulse group, 2/6 (33%) in the custom designed high mechanical index longer pulse duration group, and 0/7 in the control group ($p=0.02$; Fisher's Exact Test). Salvagability index was also reduced in the group receiving repeated diagnostic high mechanical index impulses.

Conclusions

Utilization of a modified diagnostic ultrasound transducer to apply high mechanical index impulses to the microvasculature in acute STEMI is safe and feasible in a large emergency department setting. The acoustic radiation forces generated by repeated diagnostic high mechanical index impulses applied to the entire myocardium may be a method of achieving early recanalization in acute STEMI, and improving the salvagability index.

Sonoreperfusion therapy for microvascular obstruction using microbubbles and low dose tPa

***Sebastiaan T. Roos, Francois T. Yu, Xucai Chen, Otto Kamp, Albert C. van Rossum,
Flordeliza S. Villanueva, John J. Pacella***

Introduction

Current therapy to achieve epicardial coronary patency in acute ST-elevation myocardial infarction (STEMI) is percutaneous coronary intervention. Despite successful epicardial recanalization, adequate microvascular perfusion is often not achieved due to distal embolization of atherothrombotic debris, resulting in microvascular obstruction

We previously reported that long tone burst high mechanical index ultrasound (US) + microbubbles (MB) restored microvascular perfusion (sonoreperfusion, SRP) in an in vitro flow model using PBS perfusate. We sought to demonstrate SRP efficacy in whole blood perfusate with and without low dose tPa.

Methods

The model comprised a 4 mm diameter phantom vessel with a 40 μm pore mesh to simulate a microvascular cross section and upstream pressure reflecting thrombus burden. Bovine whole blood and $2 \times 10^6/\text{ml}$ lipid MB ($\sim 3 \mu\text{m}$) infused at 0.75 ml/min simulated microvascular flow. Bovine blood microthrombi were injected onto the mesh until upstream pressure was 30 mmHg. US was delivered for 20 min (1 MHz, 1.5 MPa peak negative pressure, 3 sec pulse interval, 1000-5000 cycles) with and without low dose tPa (2.5 $\mu\text{g}/\text{ml}$) during measurement of upstream pressure to assess SRP efficacy ($n=3-7$). Lytic rate (rate of pressure drop in the first 4 min) and lytic index (1/area under pressure-time curve) quantified SRP efficacy.

Results

In whole blood, lytic rate was $2.6 \pm 1.5 \text{ mmHg}/\text{min}$ at 1000 cycles US+MB increasing to $7.3 \pm 3.2 \text{ mmHg}/\text{min}$ at 5000 cycles US+MB ($p<0.01$) without tPa. The lytic index was similar for tPa only ($2.0 \pm 0.5 \times 10^{-3} \text{ mmHg}^{-1} \cdot \text{min}^{-1}$) and 5000 cycles US + MB without tPa ($2.3 \pm 0.5 \times 10^{-3} \text{ mmHg}^{-1} \cdot \text{min}^{-1}$) ($p=0.5$) but increased to ($3.6 \pm 0.8 \times 10^{-3} \text{ mmHg}^{-1} \cdot \text{min}^{-1}$) ($p<0.01$) for 5000 cycles US+MB+tPa, indicating an additive effect of tPa with US + MB therapy (See figure 1).

Conclusions

In whole blood, US + MB therapy restored microvascular perfusion. Similarly to our previous findings with PBS perfusate, SRP efficacy varied with cycle length in the presence of MB. The addition of tPa increased SRP efficacy in blood, suggesting a potential additive effect of low dose tPa and US + MB therapy *in vivo*.

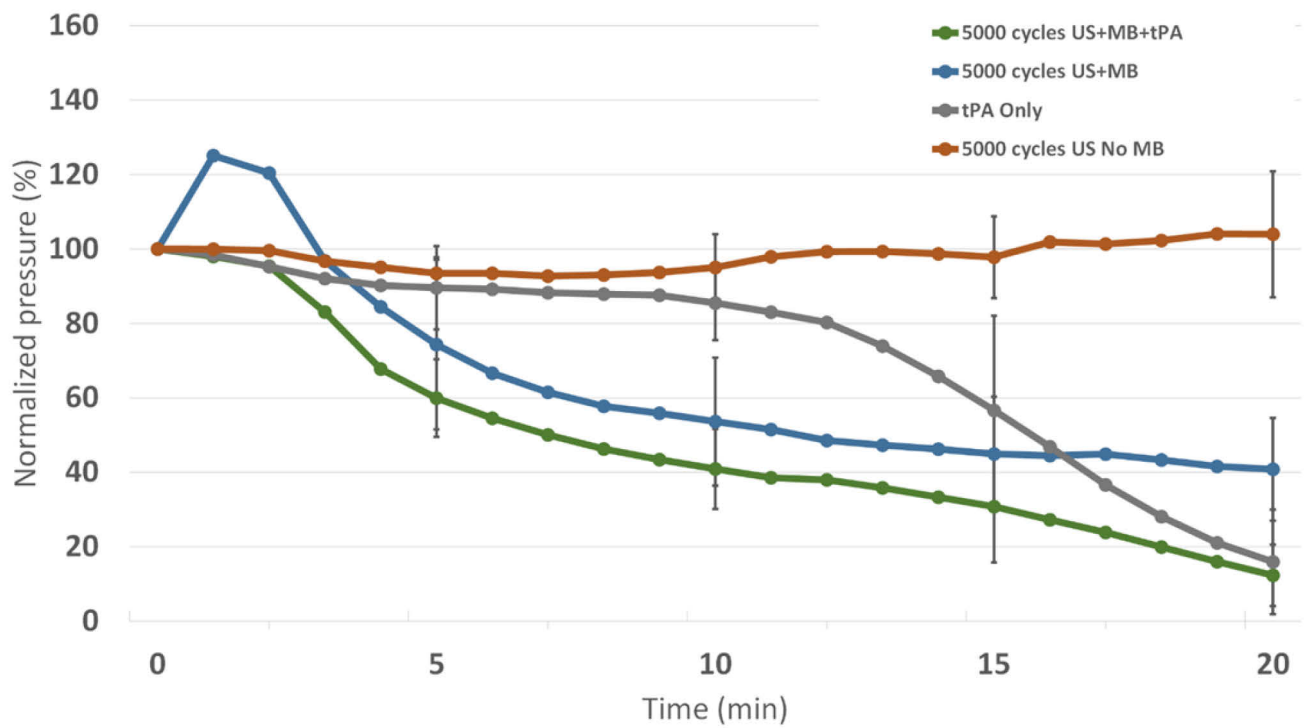


Figure 1: Pressure kinetics during SRP therapy (mean \pm standard deviation).

A study of the micro-scale evolution of the erosion front of blood clots subjected to ultrasound stimulated microbubble treatments

Christopher Acconcia^{1,2,*}, Ben Y.C. Leung² and David E Goertz^{1,2}

¹*Department of Medical Biophysics, University of Toronto, Toronto, M5S 1A1, Canada*

²*Sunnybrook Research Institute, 2075 Bayview Avenue, M4N 3M5, Toronto, Canada*

Objectives

There is a considerable body of work establishing the ability of ultrasound stimulated microbubbles (USMBs) to degrade blood clots, both in the presence and absence of lytic agents[1]–[3]. A range of mechanisms have been proposed or implicated, though a detailed understanding of this process remains both elusive and necessary in order to provide a more rational basis for the development improved sonothrombolysis (STL) techniques.

In previous work, we examined micro-scale interactions between USMBs and fibrin clots[4], [5], motivated by the recognition that fibrin networks are the primary constituent responsible for the mechanical integrity of whole blood clots. It was demonstrated that microbubbles could enter into the (transparent) clots and, under the appropriate exposure conditions, damage fibrin networks and promote external fluid uptake. This work suggested that these mechanisms may be prominent factors in STL, but their relative role in whole blood clot lysis remained to be established. The objective of the present study was to examine the evolution of whole blood clot surfaces at a micro-scale to gain an improved understanding of the USMB STL process. In particular, we employed a combination of high speed white light photography and 3D 2-photon microscopy to assess both the clot surface and potential modifications to the fibrin network.

Methods

Clots were formed from arterial rabbit blood, where prior to initiating clot formation fluorescent fibrinogen was added in order to visualize the fibrin network. Clots were formed with flat interfaces that were adjacent to a flow channel containing Definity (1:5000 dilution in PBS) flowing at a velocity of ~6 mm/s. 1 MHz pulsed ultrasound was applied with a pulse duration of 1 ms and a 15% duty cycle. Exposures, based on our previous studies, were comprised of 20 repetitions of the 1 ms pulses which occurred every 800 ms to allow for bubble replenishment within the beam. For each train of 20 pulses, the first 4 were of lower amplitude while the following 16 were of higher amplitude. The pressure combinations employed were either 200/400 kPa or 400/1000 kPa. In one set of experiments, high speed (10 kf/s) photography was used to evaluate the interaction of bubbles with the interface of whole

blood clots or fibrin clots. In a second set of experiments, serial 3D 2-photon microscopy of the clot fibrin network was performed at 2-5 minute time intervals during exposure.

Results

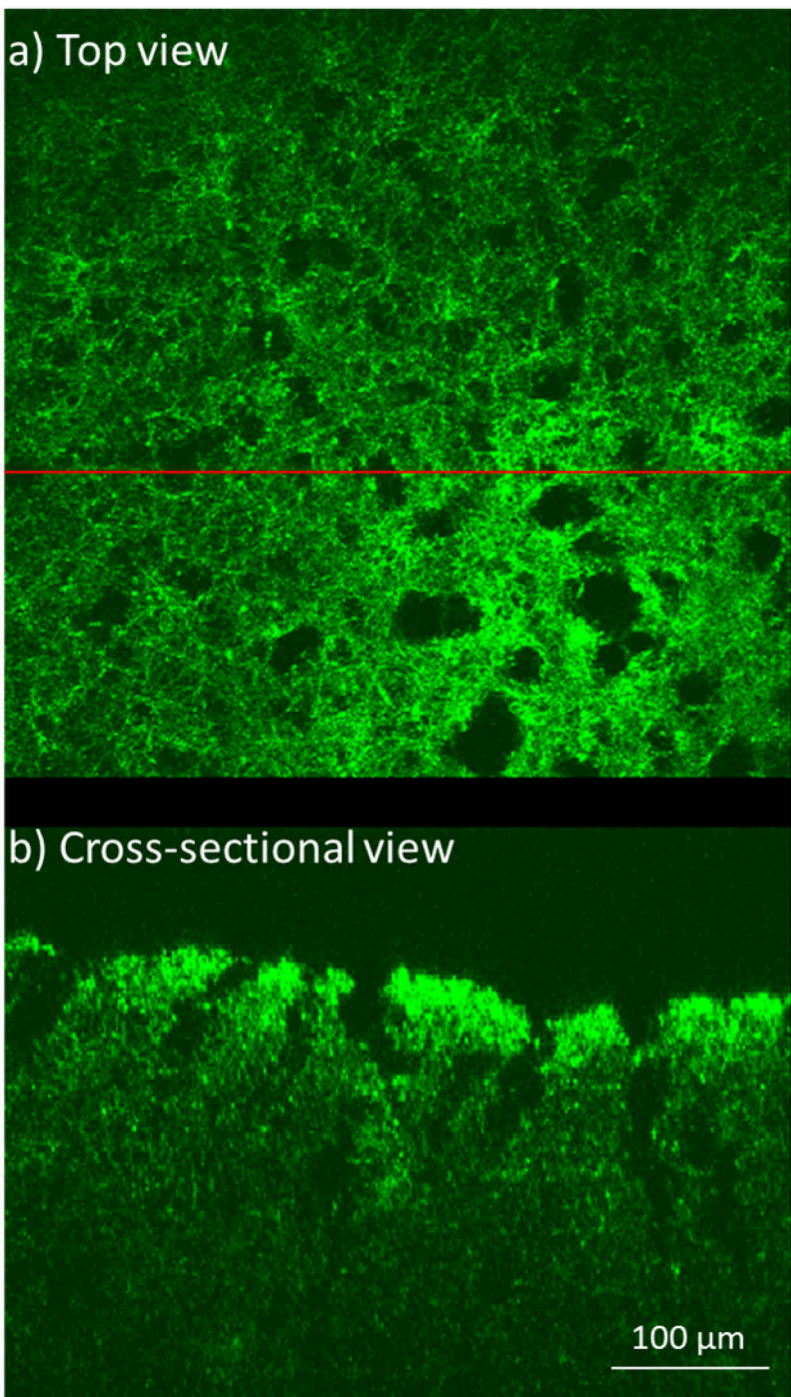
High speed white light imaging of the blood clots revealed the ejection of red blood cells (RBCs) from the clot boundary region, which was accompanied by its gradual recession. 2-photon experiments of control clots revealed only surface fibrin, with deeper network rendered undetectable due to the attenuating effects of RBCs. Upon exposure, the clot developed an RBC depleted zone (up to 100s of microns), which consisted of an ‘empty’ fibrin network. For the 200/400 kPa exposure condition, the depth of this zone increased with time and was comprised of a predominantly intact fibrin network. For the 400/1000 kPa exposures the zone was comprised of a fibrin network that has been substantially damaged, characterized by a multitude of tunnels on the order of 30-50 μm s in diameter (see Figure). With continued exposure this surface receded indicating that clot erosion was occurring. This pattern of tunnel development is consistent with our previous work with fibrin clots, which indicated that tunnels can form under sufficient pressure amplitudes particularly in the presence of bubble clustering. In additional high speed imaging experiments of fibrin clots it was observed that tunnels, once initiated, act in subsequent exposures as a conduit for bubbles to enter and act at deeper points within the clots.

Conclusions

These results provide new evidence of the complex nature of an eroding whole blood clot interface, which involves the ejection of RBCs leaving behind a zone of bare fibrin network. The strong dependence of the erosion front characteristics on exposure conditions indicates that further examination of these effects are of relevance to the development of improved STL exposure schemes.

References

1. B. Petit, E. Gaud, D. Colevret, M. Ardit, F. Yan, F. Tranquart, and E. Allémann, “*In vitro sonothrombolysis of human blood clots with BR38 microbubbles.*,” *Ultrasound Med. Biol.*, vol. 38, no. 7, pp. 1222–33, Jul. 2012
2. J. E. Leeman, J. S. Kim, F. T. H. Yu, X. Chen, K. Kim, J. Wang, X. Chen, F. S. Villanueva, and J. J. Pacella, “*Effect of acoustic conditions on microbubble-mediated microvascular sonothrombolysis.*,” *Ultrasound Med. Biol.*, vol. 38, no. 9, pp. 1589–98, Sep. 2012
3. S. Datta, C.-C. Coussios, A. Y. Ammi, T. D. Mast, G. M. De Courten-Myers, and C. K. Holland, “*Ultrasound-enhanced thrombolysis using definity as a cavitation nucleation agent.*,” *Ultrasound Med. Biol.*, vol. 34, no. 9, pp. 1421–1433, 2008
4. C. Acconcia, B. Y. C. Leung, K. Hynynen, and D. E. Goertz, “*Interactions between ultrasound stimulated microbubbles and fibrin clots.*,” *Appl. Phys. Lett.*, vol. 103, no. 5, p. 053701, 2013
5. C. Acconcia, B. Y. C. Leung, A. Manjunath, and D. E. Goertz, “*Interactions between individual ultrasound stimulated microbubbles and fibrin clot.*,” *Ultrasound Med. Biol.*, vol. 40, no. 9, pp. 2134–50, 2014



A single slice (a) and cross sectional view (b) of 2-photon whole blood clot imaging after exposure to 10 minutes of ultrasound at pressure amplitudes of 400/1000 kPa. The network has been largely cleared of red blood cells with tunnels present on the order of 50 μm in diameter. Here it is also apparent that the clot has been eroded over continual exposure. In panel (a) the direction of ultrasound propagation is into the page and the red line indicates the location of the cross-sectional view presented in panel (b).

Lowering acoustic requirements for effective sonoreperfusion of microvascular obstruction using ultra low dose tPA

**Akash Goyal, Francois T. H. Yu, Mathea G. Tenwalde, Xucai Chen,
Flordeliza S. Villanueva and John J. Pacella**

*Center for Ultrasound Molecular Imaging and Therapeutics
University of Pittsburgh School of Medicine, Pittsburgh, PA*

Background

Percutaneous coronary intervention (PCI) to restore epicardial coronary artery patency during acute myocardial infarction (AMI) is generally successful, but often results in hypoperfusion of the distal microvasculature due to embolization of atherothrombotic debris. This phenomenon, known as microvascular obstruction (MVO), is a major contributor to the ‘no-reflow’ phenomenon, occurs in up to 80% of cases, and remains an important obstacle for fully successful reperfusion^{1,2}. We have previously demonstrated the efficacy of long tone burst high mechanical index (MI) ultrasound (US) and microbubble (MB) therapy for relieving MVO and restoring perfusion³, through direct mechanical effects on thrombus⁴. Ultra low dose local fibrinolytic treatment, such as with tissue plasminogen activator (tPA), could potentially address the thrombotic component of MVO, and decrease the US requirements to achieve effective reperfusion, without significantly increasing the risk of systemic bleeding. It has been shown that low MI US + MB therapy may enhance the efficacy of tPA by facilitating the penetration of tPA into the clot structure to cause fibrinolysis⁵. The purpose of the present study was to determine whether the addition of ultra low dose tPA would lower the US requirements for effective reperfusion of MVO.

Methods

MVO was created in a previously described *in-vitro* model (Figure 1)³. Briefly, phosphate-buffered saline loaded with 3µm-diameter lipid-encapsulated MBs (2×10^6 MB/mL) was perfused in a constant flow (1.5 mL/min) driven system. Venous microthrombi were infused into a phantom vessel comprising a 40 µm pore mesh until upstream pressure reached 40 ± 5 mmHg, which is a measure of thrombus burden on the mesh and the degree of MVO³. A 1 MHz US treatment transducer (Olympus NDT, A302S, 1 inch diameter, 1.63 inch focus, Waltham, MA) was used to deliver treatment US for 20 minutes with the following two regimes: (1) inertial cavitation (IC): 1.0 MPa, 1000 cycles, 0.33 Hz pulse repetition frequency (PRF) and (2) stable cavitation (SC): 0.23 MPa, 20% duty, 0.33 Hz PRF. Our previously used high MI US dose of 1.5 MPa and 5000 cycles (without tPA) was also tested as a positive control. Passive cavitation signal was obtained from a confocally aligned 3.5 MHz transducer

(Olympus NDT, V383, 0.375 inch diameter, 1 inch focus), band pass filtered (2-20 MHz) and digitized for offline processing. Ultra low dose tPA (3 μ g/mL, ~1/6 of clinical dose) was added to the perfusate upon the start of US treatment. Pressure upstream of the MVO was monitored continuously as an indicator of clot burden. The following treatment groups were tested: tPA alone, SC US+MB alone, IC US+MB alone, tPA with SC US+MB, and tPA with IC US+MB. Lytic index was defined as the inverse of the area beneath the pressure versus time curve and lytic rate was defined as the slope of the pressure versus time curve for the first three minutes of treatment. ANOVA was used to identify differences among the groups and any differences detected were compared using Student's t-tests (n=2-5 per conditions).

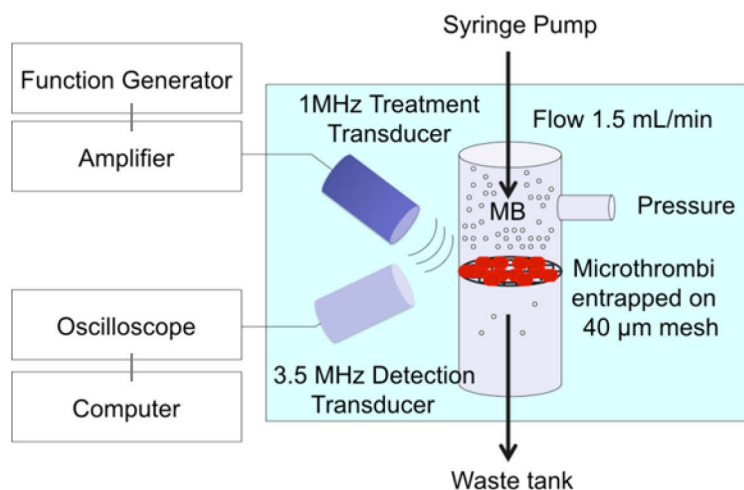


Figure 1: *In-vitro* model of microvascular obstruction (MVO).

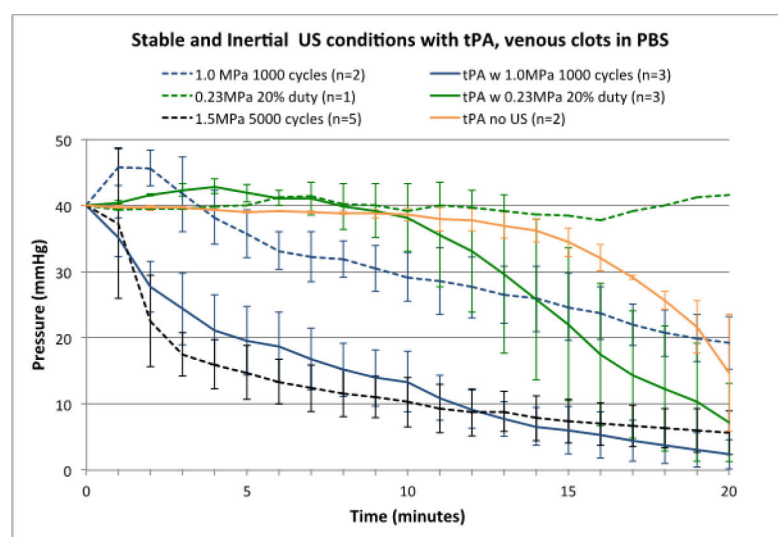


Figure 2: Pressure-time curves through 20 minutes of treatment. Stable and inertial cavitation regimes were compared with and without tPA.

Results

The clot burdens for various treatment conditions are shown in **Figure 2**. Lytic index and lytic rate were significantly greater for tPA + IC US+MB when compared to either tPA alone or IC US+MB alone ($p<0.05$ for all comparisons). Furthermore, the lytic index and lytic rate were greater with tPA+IC US+MB versus tPA+SC US+MB ($p<0.05$). Importantly, similar reperfusion efficacy was seen between lower MI IC (1.0 MPa, 1000 cycles) with tPA vs higher MI IC (1.5 MPa, 5000 cycles) *without* tPA. This corresponds to 10 times less ultrasound energy. As shown in Figure 2, with SC US+MB alone, no reperfusion occurred. With tPA alone, the pressure began to decline at 14 minutes and reached 15 mmHg. When SC US+MB was applied with tPA, pressure drop began at 10 minutes and ended at 7 mmHg at 20 minutes

Discussion and conclusions

We found that US induced MB activity enhanced thrombolysis in the presence of tPA^{6,7} in a clinically relevant *in vitro* model of MVO. Clot burden kinetics could be used to quantify the efficacy of sonothrombolysis for various ultrasound conditions. Our findings demonstrate that IC US+MB with ultra low dose tPA increased sonothromolytic efficacy when compared to either tPA alone or IC US+MB without tPA. Moreover, a lower MI IC regime with tPA (1.0 MPa) was equally efficacious compared to a high MI IC regime (1.5 MPa) without tPA, demonstrating that tPA lowers the acoustic requirements for effective sonoreperfusion. Overall, these data suggest that a sub-clinical dose of tPA can be used synergistically with IC US+MB to achieve a greater degree of fibrinolysis, perhaps by increasing mechanical interaction of tPA with clot fibrin, in addition to mechanical effects of US+MB on microthrombi. Future studies in an *in-vivo* model may help inform novel therapies for MVO post-PCI.

References

1. Wu KC, Zerhouni EA, Judd RM, Lugo-Olivieri CH, Barouch LA, Schulman SP, Blumenthal RS, Lima JA. Prognostic significance of microvascular obstruction by magnetic resonance imaging in patients with acute myocardial infarction. *Circulation.* 1998;97:765-772
2. Costantini CO, Stone GW, Mehran R, Aymong E, Grines CL, Cox DA, Stuckey T, Turco M, Gersh BJ, Tcheng JE, Garcia E, Griffin JJ, Guagliumi G, Leon MB, Lansky AJ. Frequency, correlates, and clinical implications of myocardial perfusion after primary angioplasty and stenting, with and without glycoprotein IIb/IIIa inhibition, in acute myocardial infarction. *J Am Coll Cardiol.* 2004;44:305-312
3. Leeman JE, Kim JE, Yu FT, Chen X, Kim K, Wang J, Chen X, Villanueva FS, Pacella JJ. Effect of Acoustic Conditions on Microbubble-Mediated Microvascular Sono-thrombolysis. *Ultrasound Med Biol.* 2012;38.9:1589-598
4. Chen X, Leeman JE, Wang J, Pacella JJ, and Villanueva FS. New insights into mechanisms of sono-thrombolysis using ultra-high-speed imaging. *Ultrasound Med Biol.* 2014;40.1: 258-62
5. Datta S, Coussios CC, Ammi YA, Mast TD, De Courten-Myers GM, and Holland CK. Ultrasound-enhanced thrombolysis using Definity® as a cavitation nucleation agent. *Ultrasound Med Biol.* 2008;34.9: 1421-433
6. Bader KB, Gruber MJ and Holland CK. Shaken and stirred: mechanisms of ultrasound-enhanced thrombolysis. *Ultrasound Med Biol.* 2014.
7. Wu J, Xie F, Kumar T, Liu J, Lof J, Shi W, Everbach EC and Porter TR. Improved sono-thrombolysis from a modified diagnostic transducer delivering impulses containing a longer pulse duration. *Ultrasound Med Biol.* 2014;40:1545-53

On the controlled and directed local release from drug-loaded microbubbles for sonothrombolytic therapy

Guillaume Lajoinie*, **Ying Luan[†]**, **Erik Gelderblom***, **Benjamin Dollet[‡]**, **Ine Lentacker[§]**,
Heleen Dewitte[§], **Nico de Jong[†]** and **Michel Versluis***

**Physics of Fluids Group, MIRA Institute for Biomedical Technology and Technical Medicine and MESA+ Institute for Nanotechnology, University of Twente, P.O. Box 217, 7500 AE Enschede, The Netherlands*

[†]*Biomedical Engineering, Erasmus MC, P.O. Box 2040, 3000 CA Rotterdam, The Netherlands*

[‡]*Institut de Physique de Rennes, UMR 6251 CNRS/Universit Rennes 1, Campus Beaulieu, Btiment 11A, 35042 Rennes cedex, France*

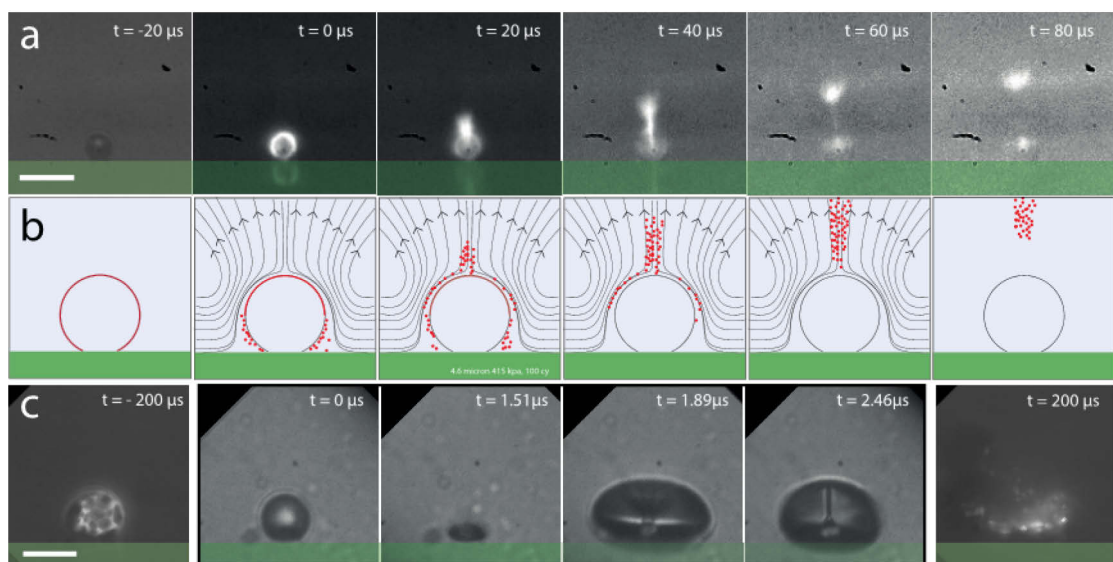
[§]*Ghent Research Group on Nanomedicines, Lab of General Biochemistry and Physical Pharmacy, Faculty of Pharmaceutical Sciences, Ghent University, Ghent, Belgium*

In developed countries, stroke is the cause of 12% of the deaths, concerning particularly the population over 65 years of age [1]. The most acute cases can provoke heavy and irreversible cerebral damage by inducing cell death by lack of oxygenation. In order to prevent such effects, it is imperative for the thrombus to be treated within the shortest time. The existing thrombolytic therapy shows a limited efficacy, and tends to provoke internal bleeding, while allowing for a limited reperfusion. Moreover, such a delicate treatment is only accessible to a selected group of patients, depending on their age and on the severity of the stroke. The limitations of the existing technology urge the development of novel therapeutic interventions.

Ultrasound in combination with a co-administration of thrombolytic agents (sonothrombolysis) is proposed to improve the efficiency of the treatment and was shown to have a significant effect in terms of reperfusion and recovery [2]. Further improvement of the treatment requires the use of agents such as microbubbles already widely used in medical ultrasound diagnostic and therapeutic applications. The proposed method demonstrated a 13% increase of patients achieving a full recovery upon the addition of microbubbles [3]. However, the patient trials also suggested that the use of microbubbles could increase the bleeding around the site of the thrombus, which is a consequence of the insufficient control over the microbubbles activity in situ. Here we study the behavior of individual microbubbles irradiated with 1-MHz ultrasound bursts at a pressure ranging from 150 to 500 kPa. The bubbles can be loaded both with targeting ligands and with encapsulated (liposomal) drugs in order to assist the local dissolution of the clot.

The microbubbles used here were loaded with DiI in the phospholipid shell in order to understand the controlled release from the coating of the microbubble. Ultra high-speed imaging of the acoustic response of the microbubbles is recorded in bright-field at a frame rate of 5 million frames per second,

combined with simultaneous high-speed fluorescence imaging at a frame rate ranging from 5,000 to 50,000 frames per second. We show the existence of two regimes with different release mechanisms. The first one is a direct effect of the resonance of the microbubbles targeted to the substrate leading to asymmetrical bubble oscillations. In this regime, the microbubbles generate a strong acoustic streaming field, inducing first of all intense shear to the neighboring clot, and secondly a local recirculation of the flow which promotes flushing away of deactivated reagents and mixing in freshly released model drug. In the second regime, dominant for the larger bubbles, we observe the quasi-systematic formation of a high-speed jet toward the substrate that is well known to create a strong and very localized mechanical damage. When the jet is formed, the load of the microbubble is directly deposited on the membrane, which is expected to promote a highly localized clot dissolution efficacy.



a. Release of the fluorescent coating material from an oscillating microbubble showing a transport by the streamlines seen at 50,000 frames per second. b. Schematic of the streamlines generated by the microbubble and subsequent shedding. c. Fluorescence images taken before and after the ultrasound exposure that show the release of the fluorescent material on the membrane and snapshots of the ultra-high-speed recording of the formation of a jet in the bubble toward the membrane. The scale bars represents 10 μm .

References

1. Ricci S et al., *Sonothrombolysis for acute ischaemic stroke*, The Cochrane Library 2012, Issue 10
2. Ishibashi T, Akiyama M, Onoue H, Abe T, Furuhata H. Can transcranial ultrasonication increase recanalization flow with tissue plasminogen activator? *Stroke* 2002;33(5): 1399–404
3. Molina CA, Ribo M, Rubiera M, Montaner J, Santamarina E, Delgado-Mederos R, et al. Microbubble administration accelerates clot lysis during continuous 2-MHz ultrasound monitoring in stroke patients treated with intravenous tissue plasminogen activator. *Stroke* 2006;37(2):425–9

The 30th Annual ADVANCES In CONTRAST ULTRASOUND

www.bubbleconference.com

**Thursday all day and Friday morning
September 10-11, 2015
8:00AM Thursday until noon on Friday**

**Basic CEUS Training Sessions:
Saturday morning
September 12, 2015
8:00 AM to 1:30 PM**



The Drake Hotel, Chicago, IL

The 2015 Bubble Conference

FIRST ANNOUNCEMENT 2016

21th EUROPEAN SYMPOSIUM ON ULTRASOUND CONTRAST IMAGING

21-22 JANUARY 2016

ROTTERDAM, THE NETHERLANDS

Course Directors: **Nico de Jong**
Arend Schinkel
Edward Leen

Information on the 21th EUROPEAN SYMPOSIUM ON ULTRASOUND CONTRAST IMAGING: **Mieke Pruijsten, m.pruijsten@erasmusmc.nl**

**The 20th European Symposium on Ultrasound Contrast Imaging Rotterdam is
sponsored by:**

Philips Healthcare

Mr. John MacQuarrie
Senior Product Manager - Ultrasound
Philips Healthcare
22100 Bothell Everett Highway
Bothell, WA 98021 U.S.A.

Bracco Suisse SA

Mr. M. Graf, Congress Manager
Senior Communication Events Manager
Centro Galleria 2
Via Cantonale
CH-6928 Manno - Switzerland

GE Healthcare Ltd

Mr Francois Roche
Global Product Leader
Building 21, Ground Floor
The Grove Centre, White Lion Road,
Amersham, HP7 9LL UK

SIEMENS AG - Ultrasound Division

Mr. Richard Medley, Product Manager
H WS ES US CRM Operations
Sir William Siemens Square
Newton House
Frimley, Camberley, SY GU16 8QD – UK

Hitachi Medical Systems

Mrs. E. Bibby
European Marketing
Sumpfstrasse 24
6300 Zug – Switzerland

Visualsonics

Mr. Anil K K Amlani
Acting President and CEO
3080 Yonge Street
Toronto, Ontario - M4N 3N1 – Canada

Oldelft Ultrasound

Mr. S. Roggeveen
Commercial Manager
Elektronicaweg 10
2628 XG Delft
The Netherlands

ZONARE

Mr. Ludwig Steffgen
Manager, International Clinical Marketing
Medical Systems GmbH
Henkestraße 91
91052 Erlangen - Germany

Coeur

Mr. H. Boersma
Erasmus MC - Thoraxcenter
Dr. Molewaterplein 50
3015 GE Rotterdam
The Netherlands

Nederlandse Hartstichting

Mrs. E. Buitenhuis
Manager Research Department
P.O. Box 300
2501 CH Den Haag
The Netherlands

Tide Microfluidics B.V.

Dr. W. Van Hoeve
P.O. Box 545
7500 AM Enschede
The Netherlands



GE Healthcare



PHILIPS

SIEMENS

HITACHI
Inspire the Next

Oldelft
Ultrasound



ZONARE



tide
microfluidics

The 20th European Symposium of Ultrasound Contrast Imaging, Rotterdam is sponsored by:



PHILIPS

GE Healthcare



**Oldelft
Ultrasound**

ZONARE

HITACHI
Inspire the Next

